COASTAL LANDSLIDE AND SEA CLIFF RETREAT MONITORING FOR CLIMATE ADAPTATION AND TARGETED RISK ASSESSMENT

Final Report

SPR-807

Oregon Department of Transportation

COASTAL LANDSLIDE AND SEA CLIFF RETREAT MONITORING FOR CLIMATE ADAPTATION AND TARGETED RISK ASSESSMENT

Final Report

PROJECT SPR-807

by

Michael J. Olsen, Ben A. Leshchinsky,
Andrew Senogles, Matt O'Banion, Michael Bunn (OSU)
Jonathan Allan (DOGAMI)

for

Oregon Department of Transportation
Research Section
555 13th Street NE, Suite 1
Salem OR 97301

and

Federal Highway Administration
1200 New Jersey Avenue SE
Washington, DC 20590

July 2025

Technical Report Documentation Page

1. Report No. FHWA-OR-RD-26-01	2. Government Accession No.	3. Recipient's Catalog No.
4. Title and Subtitle Coastal Landslide and Sea Cliff Retreat Monitoring for Climate Change Adaptation and Targeted Risk Assessment		5. Report Date May 2025 6. Performing Organization Code
7. Author(s) Michael J. Olsen, Ben A. Leshchinsky, Andrew Senogles, Matt O'Banion, Michael Bunn (OSU), Jonathan Allan (DOGAMI)		8. Performing Organization Report No.
9. Performing Organization Name and Address Oregon State University 101 Kearney Hall Corvallis, OR 97331		10. Work Unit No. (TRAIS) 11. Contract or Grant No.: SPR-807
12. Sponsoring Agency Name and Address Oregon Dept. of Transportation Research Section and Federal Highway Admin. 555 13th Street NE, Suite 1 1200 New Jersey Avenue SE Salem, OR 97301 Washington, DC 20590		13. Type of Report and Period Covered: Final Report 14. Sponsoring Agency Code
15. Supplementary Notes: Curran Mohney (Project Champion), Kira Glover-Cutter (Project Manager)		

16. Abstract: This research presents new tools, methodologies, and insights obtained from an extensive 7-year monitoring campaign at five coastal sites affected by erosion and landsliding. The objective of this research is to develop a more comprehensive, data-driven framework to prioritize coastal asset management. This new research for ODOT builds upon recent smaller-scale, foundational efforts, and recommendations in order to (1) Evaluate five representative sites reflecting a combination of coastal geologic terrains, landslide types, and sea cliff erosion activities, (2) capture detailed landslide and sea cliff geometry and movement using traditional and advanced 3D technologies for quantifying displacement (e.g., lidar, UAS structure from motion Multiview stereopsis photogrammetry, in-situ GNSS receivers, and real-time, remote, in-place MEMS sensors), (3) quantify changes in landslide movement, groundwater change, and sea cliff erosion rates over an extended 7-year timeline to fully capture the episodic nature of sea cliff erosion in the context of climate change events, and (4) develop a GIS/Lidar-based management framework for targeted risk assessment and climate change adaptation planning including guidelines for future evaluations of coastal infrastructure sites. In addition to long term benefits associated with the research, the data, tools, and methods developed in this research had immediate impact at several of the sites when failures occurred during the course of the research.

17. Key Words: Climate change, coastal erosion, sea cliffs, landslides, slope stability, lidar, remote sensing	18. Distribution Statement Copies available from NTIS, and online at http://www.oregon.gov/ODOT/TD/TP_RES/		
19. Security Classification (of this report) Unclassified	20. Security Classification (of this page) Unclassified	21. No. of Pages 199	22. Price

Technical Report Form DOT F 1700.7 (8-72) Reproduction of completed page authorized Printed on recycled paper

SI* (MODERN METRIC) CONVERSION FACTORS

APPROXIMATE CONVERSIONS TO SI UNITS

Symbol	When You Know	Multiply By	To Find	Symbol
		LENGTH		
in	inches	25.4	millimeters	mm
ft	feet	0.305	meters	m
yd	yards	0.914	meters	m
mi	miles	1.61	kilometers	km
		AREA		
in^2	square inches	645.2	millimeters squared	mm^2
ft^2	square feet	0.093	meters squared	m^2
yd^2	square yards	0.836	meters squared	m^2
ac	acres	0.405	hectares	ha
mi^2	square miles	2.59	kilometers squared	km^2
		VOLUME		
fl oz	fluid ounces	29.57	milliliters	ml
gal	gallons	3.785	liters	L
ft^3	cubic feet	0.028	meters cubed	m^3
yd^3	cubic yards	0.765	meters cubed	m^3
NOTE: Volumes greater than 1000 L shall be shown in m^3.				
		MASS		
oz	ounces	28.35	grams	g
lb	pounds	0.454	kilograms	kg
T	short tons (2000 lb)	0.907	megagrams	Mg
		TEMPERATURE (exact)		
°F	Fahrenheit	(F-32)/1.8	Celsius	°C

APPROXIMATE CONVERSIONS FROM SI UNITS

Symbol	When You Know	Multiply By	To Find	Symbol
		LENGTH		
mm	millimeters	0.039	inches	in
m	meters	3.28	feet	ft
m	meters	1.09	yards	yd
km	kilometers	0.621	miles	mi
		AREA		
mm^2	millimeters squared	0.0016	square inches	in^2
m^2	meters squared	10.764	square feet	ft^2
m^2	meters squared	1.196	square yards	yd^2
ha	hectares	2.47	acres	ac
km^2	kilometers squared	0.386	square miles	mi^2
		VOLUME		
ml	milliliters	0.034	fluid ounces	fl oz
L	liters	0.264	gallons	gal
m^3	meters cubed	35.315	cubic feet	ft^3
m^3	meters cubed	1.308	cubic yards	yd^3
		MASS		
g	grams	0.035	ounces	oz
kg	kilograms	2.205	pounds	lb
Mg	megagrams	1.102	short tons (2000 lb)	T
		TEMPERATURE (exact)		
°C	Celsius	1.8C+32	Fahrenheit	°F

*SI is the symbol for the International System of Measurement

ACKNOWLEDGEMENTS

This monitoring work required a substantial amount of field work by OSU Geomatics and Geotechnical Engineering graduate students. Bryce Berrett, Fatih Sen, Dae Kun Kang, Maria Krivova, Joanie Hermann, Bipin Peethambaran, Stefano Alberti, Eve Lathrop, Kat Holtan, Peyton Pressler, Ezra Che, Marian Jamieson, Sanjaya Paudel, Mohsen Arjmand, Caleb Ogbeta, Nick Mathews, Richie Slocum, Erik Fulmer, Ezra Stockton, Chase Simpson, Richie Slocum, David Abiola, Sahar Kamalou, Charles Ghartey, Mahyar Sharifi-Mood, and Farid Javadnejad assisted with the field data collection. Joan Hermann (OSU) assisted with the progressive sea cliff failure analysis code and field work. Chase Simpson & Katherine Holtan assisted with the GNSS sensor instrument installation.

The authors acknowledge the immense support provided by Curran Mohney and Dr. Kira Glover-Cutter from ODOT throughout the course of the project. Additionally, Geoff Crook, Mike Tardiff, Mike Brinton, Katie Castelli, and Gary Pischke from ODOT; Dr. Adam Young from Scripps Institution of Oceanography at UCSD; and Ben Haines (FHWA) provided valuable feedback on the project. Jill DeKoekkoek and Collin Cunningham provided field logistical support. Chris Glantz from Geometronics helped coordinate the UAS lidar surveys. Michael Bunn and Matt O'Banion (OSU PhD students) diligently prepared and installed the SAA MEMs sensors as well as developed the initial plans for the site surveys. Emerald Shirley (ODOT), Jill Dekoekkoek, and Pete Castro (ODOT) assisted with drilling, planning the Hooskanaden UAS surveys, and selecting the locations for the GNSS sensors. We appreciate HazTech who diligently performed the drilling at the coastal sites, often in adverse weather. Oregon State Parks and Recreation Department provided the permits to conduct the field research data.

Leica Geosystems and David Evans and Associates provided equipment and software used in this research. Maptek I-Site also provided software used in this study. We also thank the developers of CloudCompare software, which was very helpful for the project analysis. The NSF Natural Hazards Engineering Research Infrastructure: Post-Disaster, Rapid Response Research (RAPID) Facility (Award CMMI-1611820) acquired and performed initial processing of the UAS lidar data to support this research. Special thanks to Jake Dafni, Michael Grilliot, and Andrew Lyda who executed those surveys.

DISCLAIMER

This document is disseminated under the sponsorship of the Oregon Department of Transportation and the United States Department of Transportation in the interest of information exchange. The State of Oregon and the United States Government assume no liability of its contents or use thereof.

The contents of this report reflect the view of the authors who are solely responsible for the facts and accuracy of the material presented. The contents do not necessarily reflect the official views of the Oregon Department of Transportation or the United States Department of Transportation.

The State of Oregon and the United States Government do not endorse products of manufacturers. Trademarks or manufacturers' names appear herein only because they are considered essential to the object of this document.

This report does not constitute a standard, specification, or regulation.

Dr. Olsen has financial interests in EZDataMD LLC, a company which commercializes the Rambo software for point cloud analysis technology, which was utilized in this research. The conduct, outcomes, or reporting of this research could benefit EZDataMD LLC and could potentially benefit Dr. Olsen.

TABLE OF CONTENTS

LIST OF TABLES

LIST OF FIGURES

LIST OF ACRONYMS

TLS	Terrestrial laser scanning
COM	Conservation of mass
GPS	Global Positioning System
GNSS	Global Navigation Satellite System
MP	Milepost
SfM	Structure from Motion
MVS	Multi-view Stereopsis
MEMs	Micro-Electrical-Mechanical-Systems
b.g.l	below ground level
VWT	Vibrating Wire Transducer
ODOT	Oregon Department of Transportation
CSZ	Cascadia Subduction Zone
JCL	Johnson Creek Landslide
lidar	light detection and ranging
RTK	Real-time kinematic
UAS	Uncrewed aircraft system
SAR	Synthetic aperture radar
DSAS	Digital shoreline analysis system

1.0 INTRODUCTION

1.1 BACKGROUND

Rising seas and extreme coastal weather events pose significant risks for the safety, reliability, and effectiveness of ODOT infrastructure and operations along the Oregon coast (Hormann, 2012). Coastal landslides and cliff erosion are particularly sensitive to climate drivers with sea-level rise, storm frequency and intensity, wave scour, and rainfall amounts influencing landslide movement and sea cliff[1] erosion. The retreat rate of sea cliffs will likely accelerate from to climate change effects and in many locations directly threatens disruption of ODOT's coastal infrastructure. Though landslides and sea cliff erosion are common processes that damage Oregon's coastal highways regularly (e.g., Figure 1.1), sea cliff retreat and rate of landslide movement are not well-characterized, particularly in context of climate change (Crozier, 2010). In 2014, ODOT's Coastal Climate Change Vulnerability Assessment identified the limited information available regarding sea cliff retreat as an issue of concern and has had continued discussions since then. Additionally, ODOT is designated as a lead implementation agency for the Governor's climate change adaptation priority.

Figure 1.1: Example Evidence of damage to Highway 101 at the Hooskanaden Slide requiring routine repaving of the road (MP344, August 2016).

[1] Coastal cliffs are steep slopes where the land and shoreline meet. They are often referred to as sea cliffs when adjacent to oceans and bluffs near lakes. However, the terms are often used interchangeably in practice. Please see Hampton and Griggs (2004) for further discussion. In this report, the term sea cliff is consistently used for clarity.

The need to systematically and reliably assess landslides and sea cliff erosion in terms of both magnitude and rates of movement and retreat will become increasingly critical, particularly given that at least 71 sites totaling nearly 34 miles along Highway 101 have already been identified as areas of concern in ODOT SPR-843 (Olsen et al., 2024). The rate and magnitude of sea cliff retreat are essential measures to be used in prioritizing highway segments situated upon those sea cliffs. These parameters would allow the agency to both prioritize sites for repair and financially plan for mitigation projects that are timed to maximize the utility of the existing facility. In this regard, the agency already knows which areas are impacted by sea cliff retreat, but without sufficient resources to address all of these locations at once, it becomes critical to determine which areas have the shortest lifespan so that they can be prioritized for repair. Research to directly address this concern is needed in order to optimize ODOT infrastructure planning, secure lifeline routes, and address the climate change adaptation focus of the Oregon Transportation Commission work plan.

The effects of sea cliff erosion and coastal landslide movements are of high societal and economic relevance beyond the Pacific Northwest of the United States, as nearly one quarter of the global population resides near coastal areas (Small and Nicholls, 2003).

Previous coastal landslide research for ODOT includes investigation of the Johnson Creek Landslide (Priest et al., 2007) and Arch Cape site in Lincoln and Clatsop counties, respectively. The Johnson Creek Landslide research study focused on the relationships between coastal sea cliff retreat, precipitation, and groundwater using standard survey methods to evaluate select cross-sectional areas of the coastal sea cliff at the toe of the landslide. In addition, ODOT Geometronics performed a brief analysis of the coastal sea cliff morphology of the Arch Cape site evaluating the use of terrestrial lidar (Light Detection and Ranging) technology for change detection. Compared to standard survey methods, terrestrial lidar provides a more accurate and efficient way to map, visualize, and quantify changes in sea cliff erosion.

Aerial-based lidar surveys undertaken by the USGS/NASA/NOAA, U.S. Army Corps of Engineers and DOGAMI/Oregon Lidar Consortium have been produced for coastal landscape-level use, which can be useful to erosional studies on the coast (e.g., Sallenger et al., 2003;Young et al., 2010). However, airborne lidar data have several limitations in accurately capturing sea cliff retreat, such as: (1) lower resolution of the data, particularly in heavily vegetated areas, (2) blockage of key features such as the slope crest from vegetation, (3) difficulty in capturing the steep or vertical sea cliff faces, the shape of which directly affects erosion rates and subsequent slope movements, and (4) limited temporal frequency (typically ~ 5-years between surveys) to enable meaningful temporal resolution of patterns in coastal sea cliff degradation. This temporal and topographic resolution is of particular importance for better understanding the timing and behavior of successive movements of coastal slopes after large storms, rainfall, and other erosion-inducing events.

In summary, given the limited research on coastal landslide movement and sea cliff retreat with respect to changing climate drivers, an increasingly long-term and in-depth monitoring study with modeling potential is critical to enable improved asset management decisions for ODOT, particularly in the face of climate change.

1.2 OBJECTIVES

The objective of this research is to develop a more comprehensive, data-driven framework to prioritize coastal asset management. This new research for ODOT builds upon recent smaller-scale, foundational efforts, and recommendations. The primary objectives of this project are to:

1. Evaluate five representative sites reflecting a combination of coastal geologic terrains, landslide types, and sea cliff erosion activities.

2. Capture detailed landslide and sea cliff geometry and movement using traditional and advanced 3D technologies for quantifying displacement (e.g., lidar, UAS structure from motion Multiview stereopsis photogrammetry, in-situ GNSS receivers, and real-time, remote, in-place Micro-Electrical-Mechanical-Systems (MEMS) sensors).

3. Quantify changes in landslide movement, groundwater change, and sea cliff erosion rates over an extended 7-year timeline to fully capture the episodic nature of sea cliff erosion in the context of climate change events.

4. Develop a GIS/lidar-based management framework for targeted risk assessment and climate change adaptation planning including guidelines for future evaluations of coastal infrastructure sites.

1.3 PRODUCTS

In addition to this final report to ODOT, the following major deliverables have been provided to ODOT throughout the course of the project:

- **Literature Review**: This document describes the geology and geohazards present along the Oregon Coast as well as provides general information on processes related to coastal landsliding and erosion. It then discusses monitoring technologies, slope stability and coastal change analysis techniques. Relevant hazard mapping and erosion studies are also summarized. The review also provides background information such as geology specific to the sites that are being monitored as part of SPR-807. This content has been adapted into Chapters 2 and 3 of the final report.

- **Research Methodology**: The Research Methodology contains detailed, specific, standard operating procedures and business rules for systematic data acquisition, storage, processing, analysis to support the analysis and model development. Volume I covers the survey work to be completed as well as data gathering activities. Volume II is specific to the instrumentation installed on site. This content has been adapted into chapters 4-6 of the report as well as Appendices A and B.

- **Hooskanaden Preliminary Analysis**: Through supplemental funds, two Uncrewed Lidar Systems (ULS) datasets have been collected at Hooskanaden after a major failure in February 2019. One ULS dataset has been processed and delivered to ODOT as well as results from the preliminary analyses. This content has been adapted into Chapter 11 of the final report.

- **Interim Report**: An interim report describing the progress of the research project as well as preliminary analysis and findings was delivered to ODOT in January 2020. This report was formally published in 2022. Materials from this report have been adapted into this final report.

    - Olsen, M.J., Leshchisnky, B.A., Senogles, A., Herrmann, J., and Allan, J. (2022). Coastal Landslide and Sea cliff Retreat Monitoring for Climate Change Adaptation and Targeted Risk Assessment, Interim Report Project SPR-807, FHWA-OR-RD-22-13.

- **RTK-GNSS STIC**: Through supplemental funds, low-cost in-situ RTK-GNSS networks were installed at both Arizona Inn and Hooskanaden in summer of 2020. A STIC report describing how these systems were installed, how they performed during their first year, and how the data could be utilized for monitoring was delivered in August 2021. A copy of this report is included in Appendix C.

- **Publications:** Many innovative scientific publications have resulted from the methodologies developed and data collected in this project. Copies of each of the following publications were provided to ODOT in conjunction with this report:

    - Leshchinsky, B., Olsen, M.J., Mohney, C., Glover-Cutter, K., Crook, G., Allan, J. Bunn, M., O'Banion, M.S., and Mathews, N. (2017). Mitigating coastal landslide damage, *Science*, 357(6355), 981-982. DOI: 10.1126/science.aao1722.

    - Che, E., and Olsen, M.J., (2017). "Fast Ground Filtering for TLS data via ScanLine Density Analysis," ISPRS Journal of Photogrammetry and Remote Sensing, 129, 226-240, http://dx.doi.org/10.1016/j.isprsjprs.2017.05.006

    - Stockton, E., Leshchinsky, B., Xie, Y., Olsen, M.J., & Leshchinsky, D. (2018). "Limit Equilibrium Stability Analysis of Layered Slopes: A Generalized approach," Transportation Infrastructure Geotechnology, 5(4), 366-378. DOI: 10.1007/s40515-018-0065-y

    - Leshchinsky, B., Olsen, M.J., Mohney, C. O'Banion, M.S.*, Bunn, M.*, Allan, J., and McClung, R. (2019). "A Framework for Quantifying Progressive Landslide Movement Stemming from Undercutting Processes and Hydrological Changes," Journal of Geophysical Research-Earth Surface, 124(2), 616-638. AGU. https://doi.org/10.1029/2018JF004833

    - Bunn, M.D., Leshchinsky, B.A., Olsen, M.J., (2020) Geologic Trends in Shear Strength Properties Inferred through Three-Dimensional Back-Analysis of Landslide Inventories, Journal of Geophysical Research – Earth Science, 125, e2019JF005461. https://doi.org/10.1029/2019JF005461

    - Bunn, M.D., Leshchinsky, B.A., Olsen, M.J., (2020). Estimates of Three-Dimensional Rupture Surface Geometry of Deep-Seated Landslides using

Landslide Inventories and High-Resolution Topographic Data, Geomorphology, 367, 107332. https://doi.org/10.1016/j.geomorph.2020.107332

- Alberti, S., Senogles, A., Kingen, K., Booth, A., Castro, P., DeKoekkoek, J., Glover-Cutter, K., Mohney, C., Olsen, M. and Leshchinsky, B., (2020). The Hooskanaden Landslide: historic and recent surge behavior of an active earthflow on the Oregon Coast. Landslides, 17, pp.2589-2602. https://doi.org/10.1007/s10346-020-01466-8

- Che, E., Senogles, A., and Olsen, M. J. (2021). "VO-SMOG: A versatile, smooth segment-based ground filter for point clouds via multi-scale voxelation," ISPRS Ann. Photogramm. Remote Sens. Spatial Inf. Sci., VIII-4/W2-2021, 59–66, https://doi.org/10.5194/isprs-annals-VIII-4-W2-2021-59-2021 *Note that this paper received the 2021 Martin Isenberg Best Paper Award.*

- Alberti, S., Olsen, M.J., Allan, J. and Leshchinsky, B., (2022). Feedback thresholds between coastal retreat and landslide activity. Engineering Geology, 301, p.106620.

- Alberti, S., Leshchinsky, B., Roering, J., Perkins, J, and Olsen, M.J., (2022). Inversions of Landslide Strength as a Proxy for Subsurface Weathering, Nature Communications, 13, 6049 https://doi.org/10.1038/s41467-022-33798-5

- Senogles, A., Olsen, M.J. and Leshchinsky, B., (2022). SlideSim: 3D landslide displacement monitoring through a physics-based simulation approach to self-supervised learning. Remote Sensing, 14(11), p.2644. https://doi.org/10.3390/rs14112644

- Senogles, A., Olsen, M.J., and Leshchinsky, B.A. (2023). LADI: Landslide Displacement Interpolation through a Spatial-Temporal Kalman Filter, Computers and Geosciences, 180. https://doi.org/10.1016/j.cageo.2023.105451

- Senogles, A., Leshchinsky, B., Olsen, M.J., Allan, J.C., and Massey, C.I. (Under Review). Hyperspatial, time series observations of morphological and climactic processes driving sea cliff erosion in Oregon, USA. Submitted to Geomorphology for peer-review.

- **Student Dissertations and Theses:** This project was foundational to support the following students towards their thesis research work:

  - Andrew Senogles (PhD. Dissertation, 2023). <u>New Techniques to Monitor and Characterize Landslide Behavior and Controls Using Digital Terrain Models</u>. Dr. Senogles developed novel techniques to track landslide movement blending remote sensing data with in-situ sensors. He also explored the relationship between erosion rates and climatic factors such as precipitation and wave contact hours.

- Maria Krivova (PhD. Dissertation, 2023). Advancing Spatial Data Engineering and Analysis: Integrative Approaches with GIS, Statistical Modelling, and Deep Learning. A chapter in Maria's dissertation explores coastal erosion forecasting using the Spencer Creek Landslide as a case study.

- Joan Hermann (MS Thesis, 2022). Tools for Evaluating Climate Change Impacts in Coastal Environments. Ms. Hermann developed physics-based techniques to forecast the evolution of sea cliffs, leveraging work. Her work was utilized in SPR-843 to identify vulnerable sites on Highway 101.

- Fatih Sen (MS Thesis 2022). Assessing the Feasibility of Utilizing UAS-Based Point Clouds for Pavement Smoothness/Roughness Quantification. The core research was funded by Pactrans; however, Fatih utilized point cloud data obtained at the Arizona Inn landslide as a case study for the roughness characterization. He also assisted in several data collections for SPR-807.

- Eve Lathrop (Honors Thesis 2020). Preliminary deployment and evaluation of geophone sensors for monitoring wave activity: *GeoMoteShield*. In this work, Ms. Lathrop experimented with geophone sensors to capture wave activity.

- Michael Bunn (PhD. Dissertation, 2019). Improving Region-Scale Landslide Inventory and Susceptibility Mapping. Dr. Bunn developed a hybrid-spline techniques to capture the 3D rupture surface of deep-seated landslides. This work was applied to landslides such as the Arizona Inn and Johnson Creek landslides. He then applied it to the mapped landslides within the Port Orford and Ophir Quadrangles. This technique was then employed to perform back analysis to evaluate the influence of geologic and mechanical trends on landslide inventories: https://ir.library.oregonstate.edu/concern/graduate_thesis_or_dissertations/70795b54f

- Ezra Stockton (MS Thesis). Stability of heterogeneous and anisotropic slopes determined by the compound logarithmic spiral limit equilibrium method. Mr. Stockton's work explored the ability to use a log spiral in limit equilibrium analysis in heterogeneous slopes such as those prevalent on the Oregon Coast. He also explored the utilization of this method to evaluate cohesion and frictional anisotropy on tension crack depth and slope stability.

- Matt O'Banion (PhD. Dissertation, 2017). Rigorous 3D Point Cloud Quality Assessment. Most of Dr. O'Banion's dissertation work was completed prior to the start of SPR-807. However, Dr. O'Banion was instrumental in organizing the initial field surveys and preparing the sensors for deployment. https://ir.library.oregonstate.edu/concern/graduate_thesis_or_dissertations/7p88cn24z?locale=en

- Bryce Berrett (PhD in progress). Title TBD. Bryce will utilize data from the Arizona Inn and Hooskanaden sites as case examples in his dissertation developing new techniques to model landslide movement and mechanics.

- Beyond the use of these data in dissertations and theses, the data collected from SPR-807 were also utilized by several students in course projects. Many current and future students will utilize these data for further analyses in their research.

- **TAC and research coordination meetings**: Site selection and survey plans were reviewed at TAC meetings at the onset of the project and periodic meetings with ODOT staff were held throughout the project.

- **Presentations** at technology transfer meetings with ODOT personnel.

  - *Coastal Landslide and Sea Cliff Retreat Monitoring for Climate Change Adaptation and Targeted Risk Assessment*. ODOT Geotechnical Working Group, Salem OR. (July 26, 2017).

  - *SPR-807 Research update*. ODOT Engineering Geology and Geotechnical Engineering Technical Transfer Meeting. Corvallis, OR. (July 16-17, 2019).

  - *Photo, rock, lasers: Analyzing rockfall activity with lidar and/or photogrammetry.* ODOT Engineering Geology and Geotechnical Engineering Technical Transfer Meeting. Corvallis, OR. (July 16-17, 2019).

  - *When the highway goes for a ride: Monitoring infrastructure traversing coastal landslides*, Northwest Transportation Conference, Corvallis, OR. (March 2020).

  - *Living on the Edge: Monitoring of erosional hazards on highway 101,* Oregon DOT GeoHazMat Geotechnical Engineering, Engineering Geology & Hazardous Materials Design Workshop, Salem, OR. (May 2023).

  - *Session 10: Here be landslides!*, Northwest Transportation Conference, Corvallis, OR (March 5, 2024), consisting of 3 presentations:

    a) Evaluating Precipitation- and Earthquake-Induced Landslide Impacts along ODOT Lifelines, Ben Leshchinsky, Michael Olsen and Nick Mathews, OSU

    b) US highway 101 coastal hazard vulnerability and risk assessment for mitigation prioritization, Michael Olsen, Steve Dundas, Jonathan Allan, Maria Krivova, Andrew Senogles, Ben Leshchinsky, Jaonie Hermman, Ashley Low and Chris Parrish, OSU

    c) Detailed monitoring and characterization of landslide displacements, Michael Olsen, Andrew Senogles, and Ben Leshchinsky, OSU

  - *Living on the edge: Advanced coastal erosion monitoring technologies*. ODOT Surveyor's Conference, Albany, OR, (April 16, 2024).

- **Presentations** at conferences, workshops, meetings, and other events.

    - Senogles, A., Leshchinsky, B., and Olsen, M.J., Slipping and Sliding on the Oregon Coast: Spatiotemporal Interpolation of Landslide Displacements Using UAS Photogrammetry, Terrestrial Lidar, In-situ GNSS Monitoring, Kalman Filtering, and Deep Learning. Surveying and Geomatics Conference, (ASCE UESI, AAGS, SaGES, and OSU), Corvallis, OR. (June 4, 2024).

    - Senogles, A., Olsen, MJ., and Leshchinsky, B. New techniques to monitor landslide behavior using digital terrain models and in-situ GNSS, World Landslide Forum, Florence, Italy. (November 2023)

    - Leshchinsky, B., Alberti, S. and M. Olsen. Three-dimensional back analysis of landslide inventories to evaluate trends in strength at large spatial scales, World Landslide Forum, Florence, Italy. (November 2023)

    - Olsen, MJ. "Play with the RAI until it ROARs when not Slidin' in da Sim", Endeavour Workshop, Lower Hutt, New Zealand. (February 2023).

    - Olsen, MJ, Leshchinsky, B., Massey C., and Ning, Z. Effective Utilization of State-of-the-art Geospatial Technology for Geotechnical Investigations and Monitoring: The Future is Now, National Academies of Science, Engineering, and Technology, Committee on Geological and Geotechnical Engineering (COGGE). (April 7, 2022).

    - Leshchinsky, B. "Will it stay or will it go? Use of Lidar to Assess Slope Instability." Canadian Geotechnical Society Chapter Meeting (Virtual). Vancouver, BC. (March 31, 2022).

    - Herrmann, J., Leshchinsky, B. A., Olsen, M. J., Parrish, C. E., Allan, J. C., Senogles, A., & Krivova, M. (2021, December). Integrating a Sea cliff Erosion Forecast Model into the State of Oregon's Climate Change Strategy. In AGU Fall Meeting 2021. (December 2021)

    - Leshchinsky, B. "Will it stay or will it go? Use of Lidar to Assess Slope Instability." American Society of Civil Engineers Oregon Geo-Institute Chapter Meeting (Virtual). Portland, OR. (October 6, 2021)

    - Olsen, MJ. Foreseeable trends in surface survey techniques including InSAR, Lidar differencing, laser scanning, Engineering value from the monitoring of slopes -current practice and the future, New Zealand Geotechnical Society 2021 Conference (Virtual Presenter), Queenstown New Zealand. (March 2021)

    - Leshchinsky, B.A., Bunn, M.D., and Olsen, M.J. (2020). Trends in Lithology Revealed through Three-Dimensional Mapping of Rupture Surface Geometry and Shear Strength Properties using Landslide Inventories. AGU Fall Meeting, NH030-022.

- Alberti, S., Senogles, A., Hermann, J.F., Olsen, M.J., Allan, J., and Leshchinsky, B.A., (2020). Feedback Between Coastal Erosion Processes and Landslide Activity on The Oregon Coast, AGU Fall Meeting, NH030-0014.

- Leshchinsky, B. and M. Olsen. "Evaluating Coastal Landslide Hazards using Lidar." ASCE Geo-Institute Web Conference. (December 10, 2020).

- Leshchinsky, B., Wartman J., Franke, K., and Olsen, MJ. Panel Session. Point the Way Photogrammetry and lidar for geo-imaging, ASCE Geo Congress, Minneapolis, MN (February 2020).

- Leshchinsky, B. "Will it stay or will it go? Use of Lidar to Assess Slope Instability." ASCE Geo-Institute Web Conference. (December 3, 2019).

- Leshchinsky, B., and Olsen, MJ. Will it Stay or Will it Go? Use of Lidar to Assess Slope Instability. AEG Oregon Chapter Meeting, Portland, OR, (December 2018).

- Leshchinsky, B. "Will it stay or will it go? Use of Lidar to Assess Slope Instability." American Society of Civil Engineers Oregon Geo-Institute Chapter Meeting. Seattle, WA. (November 15, 2018).

- Javadnejad, F., Gillins, D. T., Olsen, M. J., and O'Banion, M. S. "Application of UAS for coastal cliff mapping: A comparison between SfM and lidar." International Conference on Advances in Sustainable Construction Materials & Civil Engineering Systems (ASCMCES-17), Sharjah, UAE (April 2017).

- Che, E., Olsen, M.J. (2017). "Fast Ground Filtering for Terrestrial Laser Scanning based on Density Analysis," 2017 International Workshop on Computing in Civil Engineering (IWCCE), Seattle WA. Extended Abstract.

1.4 ORGANIZATION OF THE REPORT

This final report provides a summary of data acquisition and processing, results from analysis of those data, a risk framework model for progressive failure modeling incorporating climatic variables and enabling long-term projections along the shoreline and highlights near-term benefits and applications for ODOT. This section provides a brief overview of each section, what it contributes, and how it fits into the overall research project.

- Chapter 2 first describes the geology and geohazards present along the Oregon Coast. It then describes processes related to coastal landsliding and erosion. Next, it examines monitoring technologies, slope stability analysis techniques, and coastal change analysis techniques. Lastly, relevant hazard mapping and erosion studies are summarized.

- Chapter 3 provides geologic and other background information specific to the five sites that are being monitored as part of SPR-807: Arch Cape, Silver Point, Spencer Creek, Arizona Inn, and Hooskanaden.

- Chapter 4 describes the scope and extent of survey data collection spanning the period of Fall 2016 to Spring 2023 to support this project.

- Chapter 5 briefly summarizes the data processing procedures implemented to support the analysis.

- Chapter 6 provides the methods used for the analysis to correlate the erosion analysis with environmental variables such as precipitation, total water levels, and wave contact hours.

- Chapter 7 presents the erosion analysis results from change detection of the multi-epoch terrestrial laser scans at the slower moving landslide sites (Arch Cape, Silver Point, and Spencer Creek).

- Chapter 8 documents the installation of in-situ sensors including the MEMs arrays, piezometers, and RTK-GNSS monitoring system.

- Chapter 9 reports the analysis of the in-situ sensor data tracking landslide movement and water level changes.

- Chapter 10 describes the new methodologies developed for determining surface movements at the Hooskanaden and Arizona Inn landslides.

- Chapter 11 presents a summary of the evaluation performed of the Hooskanaden landslide following the massive surge and closure of Highway 101 in February 2019.

- Chapter 12 explores the large movements of the Arizona Inn landslide resulting in closure of Highway 101 in January 2023.

- Chapter 13 presents a novel modeling approach for modeling the progressive failure of landslides incorporating climatic variables.

- Chapter 14 considers the benefits to ODOT of this monitoring effort and opportunities for implementation of the research.

- Chapter 15 then provides conclusions and recommendations to build upon the extensive work completed in this research project.

Additionally, the report contains several appendices:

- Appendix A provides the detailed survey data collection and processing methodology employed in this research.

- Appendix B documents the installation and maintenance plan of the in-situ sensors.

- Appendix C describes the custom GNSS monitoring sensors designed, fabricated, assembled, and deployed to monitor the Arizona Inn and Hooskanaden landslides.

- Appendix D contains sample results of a low-cost geophone sensor tested in this research to capture wave activity.

- Appendix E is a digital appendix containing copies of the permits, safety plans, site maps, agreements, research papers, and other documents supporting the research. Available upon request to ODOT.

2.0 LITERATURE REVIEW

This chapter describes the current geological setting of the Oregon Coast, including a discussion of geohazards experienced in this dynamic environment. It will then describe coastal landslides and processes that lead to the unstable coastal sea cliffs. Various monitoring technologies utilized for similar studies will then be explored, followed by a review of existing slope stability analysis techniques. Lastly, challenges and future opportunities will be discussed.

2.1 THE OREGON COAST

The Oregon coast is ~590 km in length, extending from the Columbia River in the north to the California border in the south. Geomorphologically, the coastline can be divided into a series of "pocket beach" littoral cells bounded by resistant headlands (primarily basalt) interspersed with short to long stretches of beaches backed by less resistant cliffs and dunes (Allan et al., 2009; Komar, 1997). Sea cliffs are the dominant geomorphic feature, Figure 2.1, on this coast accounting for 58% of its ocean shore (Hapke et al., 2014). The sea cliffs of Oregon can be further subdivided into those that are fronted by beaches (both sand and cobble, ~33%) and those that are fronted by boulders and rocky intertidal areas (25%). The rest of the coast is characterized with dune-backed beaches (35%), with the remaining ~5.6% of shoreline comprised of mixed sand and gravel or pure gravel beaches. Recently, Burgette et al. (2023) performed detailed geomorphic mapping and geologic characterization of the Oregon Coast for the purposes of assessing telecommunication cable landings sites.

On the cliff-backed shores of the central Oregon coast, between Yachats and Lincoln City, homes are perched precariously close to the edge of receding cliffs (Figure 2.2). In some areas, the erosion has become acute requiring various forms of coastal engineering (commonly riprap) in order to mitigate the problem (Priest and Allan, 2004; Allan et al., 2015a) and in a few cases the landward removal of the homes (Komar, 1997). In other areas, critical infrastructure such as U.S. Highway 101 track close to the coast (Figure 2.3 and Figure 2.4), and in several areas, erosion of the sea cliffs has resulted in expensive remediation (Allan and Stimely, 2013; Allan et al., 2015b). While the processes driving sea cliff erosion depend on a delicate balance between the assailing forces (waves, tides, precipitation etc.) and properties of the rock (bedding, strength, jointing etc.) (Hampton and Griggs, 2004; Sunamura, 1992), increasing development pressure, a lack of quantitative information, and uncertainty of the physical processes are contributing to the need for expensive remediation in many Pacific Northwest (PNW) coastal areas (Allan et al., 2009).

Of concern to coastal managers is the rapid expansion of riprap along the eroding sea cliffs, which may be compounding the erosion problem by reducing the supply of beach sediments to the physical system (Haas, 2005; Young and Ashford, 2006). Sand is regularly redistributed within Oregon's pocket beach littoral cells (Komar, 1986; 1998). During a typical year, winter storm waves reach the coast from a predominately west to southwesterly direction, which produces a net seasonal transport of sand northward. Conversely, summer waves tend to approach from the northwest and the sand migrates back southward. Hence, during typical years, this seasonal exchange of sand movement within the pocket beaches tends to be balanced, with no net sediment movement. Periodically, the Oregon coast is affected by major El Nino climate

events, that disrupts the normal seasonal movement of sand. In an El Nino, ocean water levels along the Oregon coast become significantly elevated above the normal seasonal cycle of ocean water levels (Komar, 1998; Allan and Komar, 2002; Komar et al., 2011). This occurs due to the measured tides being much higher than normal, a function of enhanced warming of ocean temperatures along the coast, the geostrophic effects of northward flowing currents, and sea level "waves" that originate from the tropics. During normal years, these processes are not as strong so that the mean water levels remain close to normal. Because of the super-elevation of water levels combined with above average wave heights during an El Nino winter, the beaches and bluffs of Oregon are subject to higher swash runup and hence increased erosion potential. In addition to these processes, the tracks of extratropical storms that impact the coast are shifted further south towards California, which results in larger storm waves arriving at the coast from strongly oblique angles. This produces a stronger net northward transport of beach sand to the north that builds up immediately south of the headlands (Komar, 1998; Allan and Komar, 2002; Anderson et al., 2018).

The ocean wave climate offshore the Oregon coast is one of the most dynamic in the world. Monthly mean significant wave heights are highest during the winter months, which span the months of October to March, and lowest during the summer. Monthly mean significant wave heights tend to be highest in December and January, respectively averaging 3.9 m and 3.7 m, and lowest in July and August, where they average 1.6 and 1.7 m respectively (Ruggiero et al., 2010). Nevertheless, winter storms in the PNW can be particularly severe where typically one storm per year generates deep water significant wave heights of 10 m, with the strongest storms having generated wave heights of 14 to 15 m (Allan and Komar, 2002, 2006). The PNW is also frequently hit by extratropical storms that travel across the North Pacific Ocean, where winds sometimes reach hurricane speeds.

Significant erosion problems have been observed along the cliff-backed shorelines in Lincoln County on the central Oregon Coast (Komar, 1997; Priest 1999 Allan et al., 2015a). The geology of this region consists predominantly of moderately resistant Tertiary mudstones and siltstones (Schlicker et al., 1973), overlain by more erosive Pleistocene marine terrace sandstones (raised ancient beach and dune sands) and more recent Holocene dune sands that drape the landscape (Peterson et al., 2007). Formation of the terraces can be attributed to the uplift of the Coast Range due to the subduction of the Juan de Fuca and Gorda plates beneath the North American plate in concert with varying sea level during the Pleistocene (Orr et al., 1992). Dune sand is draped over the marine terraces in central Oregon as a result of advancing dune sheets during the sea level rise since 8,000 years ago (Peterson et al., 2007). Thus, a typical sea cliff sequence consists of Tertiary rocks at its base that may be somewhat resistant to wave attack and sub-aerial processes, capped by a layer of Pleistocene terrace sandstone or recent Holocene dune sands (Komar, 2004). Because of the dramatic ocean vistas provided atop the nearly level terraces, many homes and condominiums are now situated along the edge of eroding terraces. Servicing these communities is U.S. Highway 101, which is the main north-south transportation corridor, and in many places is located immediately adjacent to the eroding cliffs.

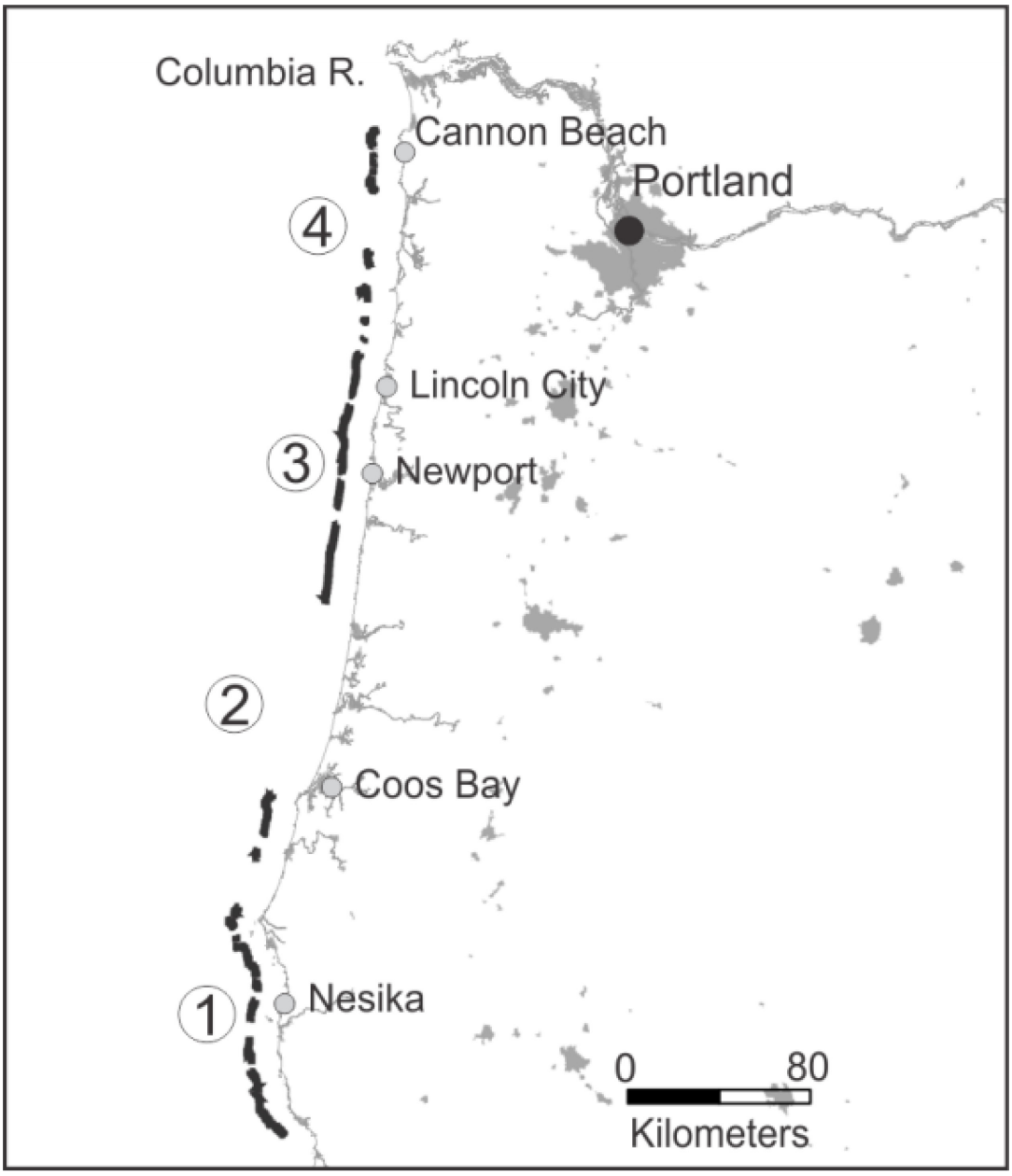

Figure 2.1: The coastal geomorphology of Oregon. Bold black lines denote the locations of sea cliffs and rocky shores. Numbers indicate regional geomorphic coastal features: plunging sea cliffs (1 & 4), rocky shorelines and shore platforms (1 & 3), wide and narrow sandy beaches backed by dunes (2 & 4) and sea cliffs (3 & 4), gravel and cobble beaches backed by sea cliffs (1 & 4), barrier spits (2 & 4), and estuaries (1-4) (from Hapke et al., 2014).

Figure 2.2: Sea cliff erosion located at Gleneden Beach, Lincoln County. The Photograph shows the presence of terrace sands that are rapidly eroding in response to cliff toe erosion. An emergency riprap structure is being constructed to mitigate the problem (Photo courtesy of J. Allan, DOGAMI, 2013).

Figure 2.3: Coastal sea cliffs located at Beverly Beach, Oregon adjacent to Highway 101 (near MP134, August 2016).

Figure 2.4: Sea cliff erosion occurring at Beverly Beach, OR. where Highway 101 runs parallel to the sea cliffs. In some cases, coastal landsliding and localized retrogression has resulted in relocation of the highway. The former location of a concrete curb is shown with the yellow, dashed line (near MP134, August 2016).

The northern Oregon coast, which includes Tillamook and Clatsop Counties, is dominated by broad sand beaches backed by prominent foredunes bounded by resistant basalt headlands (Allan et al., 2015c, 2015d, Allan 2020). The exception to this is the southern half of Clatsop County, where the beaches are backed by marine terraces (Astoria Formation, Angora sandstone), overlaid with Pleistocene terrace deposits (Witter et al., 2009). In most cases, homes and critical infrastructure are either built on stabilized foredunes or atop marine terraces. Unlike the central Oregon coast, U.S. Highway 101 is generally located further landward away from the eroding coast. Hence, when compared with the central Oregon coast, Highway 101 is much less exposed to erosion risk on the northern Oregon coast. The exception to this are several low lying areas in the vicinity of Barview, Twin Rocks and Rockaway Beach, where Highway 101 is located close to the beach and is periodically affected by coastal flooding during extreme tide events coupled with large winter storms. Periodic compound flooding is also an issue in the community of Nehalem, where extreme tides combined with high river runup result in annual flooding of the main street (Highway 101) in Nehalem.

The southern Oregon coast is dominated by prominent coastal cliffs and rocky shorelines. The geology of this region broadly reflects extensive folding and faulting, regional tectonic uplift, large-scale landsliding, and the accretion of oceanic marine sediments (Mesozoic) against the

North American continent through subduction (McClaughry et al., *in press*). The coast consists of a narrow sequence of coastal marine terraces, that transitions abruptly into the southern part of the Oregon coast range and Klamath Mountains (Burgette et al., 2023). This portion of the coast is strongly affected by ongoing rock and surface uplift associated with the Cascadia Subduction Zone (CSZ) and Mendocino triple junction deformation (Burgette et al., 2023). Sandy beaches are confined to a few areas, such as Gold Beach or the Port Orford littoral cell. South of Port Orford, Highway 101 tracks close to the coastline and is subject to coastal erosion risk along a few discrete sections of the coastline (e.g., between Port Orford and Humbug Mountain; north of Nesika Beach), with coastal landsliding being a major hazard along much of this coastline.

The Oregon Coast faces significant erosion from both ocean (large waves, high tides, and nearshore currents) and sub-aerial processes (e.g. high intensity precipitation events, wetting and drying processes, and wind). These processes will be described in Section 2.2 in more detail.

2.1.1 Coastal landslides

Landslides are a persistent problem along the entire Oregon coast given the prevalence of weak, weathered soils and climatic conditions (e.g. Allan and Hart, 2009; Witter et al., 2009; McClaughry et al., *in press*). Highway 101 traverses across many landslides, requiring routine maintenance by ODOT (Figure 1.1). North and Byrne (1965) estimated that landsliding is active along approximately 113 of the 240 km of northern coastline of Oregon (Columbia River to Florence). For example, within Lincoln County, Oregon, there are several large translational landslides moving through Tertiary (6–63 million years old) sedimentary rocks with coastal sea cliffs typically ranging from 20–60 m high (Priest et al., 2011). Priest and Allan (2004) describe these landslides from the Miocene age as thick to thin bedded, very fine to medium grained, micaceous and carbonaceous arkosic sandstone, and massive silty sandstone. They are commonly observed to be single block failures exceeding 100 m in width.

Landslides are often triggered by seismic sources, such as the CSZ, which extends under the Oregon coast range where the North American tectonic plate overrides the Juan de Fuca plate, approximately 60–120 km west of the Oregon coast (Mitchell et al., 1994). Schulz et al. (2012) utilized limit equilibrium analyses in conjunction with in-situ data to determine slip rates for landslides on the Oregon Coast (Johnson Creek, Carmel Knoll, and Devils Punchbowl). The authors concluded that these landslides were likely initiated as a result of the CSZ event and have continued to creep after their initial failure.

2.1.1.1 The Johnson Creek Landslide

One of the most extensively researched landslides along the Oregon coast is the Johnson Creek Landslide (JCL), located about 2 km south of Otter Rock and 11 km north of Newport (Priest et al., 2006; Schulz and Ellis, 2007; Priest et al., 2011; Schulz et al., 2012). The primary extents of the landslide measures approximately 360 m wide, 200 m long (Schulz and Ellis, 2007).

Highway 101 runs across the landslide and requires frequent maintenance to repair the damages resulting from the slide movement. JCL is a translational, seaward-dipping landslide displacing through a coastal sea cliff consisting of Miocene siltstone and sandstone (Astoria Formation) overlain by Quaternary marine terrace deposits (Priest et al., 2011). The basal slide plane

generally runs parallel to the dip of the Miocene rocks at approximately a 15° angle; however, the slide plane slopes inward near the toe block which tilts backwards.

Unfortunately, many efforts (Landslide Technology, 2004; Priest et al., 2008; Schulz and Ellis, 2007) of monitoring JCL have faced significant hurdles. Erosion pins installed to monitor changes on the sea cliff face were lost over the first winter season, resulting in the inability to accurately determine the total amount of erosion that took place. Inclinometer casings failed because movement was too excessive. As a result, manual extensometers of wire rope were installed to obtain subsequent measurements of movement and were used for several years to observe landslide movement. Landslide Technology (2004) and Priest et al. (2008) performed slope stability analyses to evaluate the influence of groundwater conditions, geotechnical parameters, and toe erosion on the amount of landslide movement. An important conclusion of this work was that the increase in pore water pressures was a key contributor to landslide movement; hence, efforts to minimize pore water pressure were expected to help reduce movements. The slope stability analyses determined the landslide is least stable in the southern portion of the landslide and increases in stability moving northward. This finding from the stability analysis also correlates well with measured displacements. Priest et al. (2008), Olsen et al. (2012), Conner and Olsen (2014), and Olsen (2015) used Terrestrial Laser Scanning (TLS) to capture the erosion of the sea cliff face as well as quantify landslide movement. Olsen et al. (2012) estimated landslide movement by manual extraction and comparison of features (houses, trees, and stairwells) along the crest of the coastal sea cliff face of the landslide, concluding that areas of increased landslide movement also experienced more erosion. Notably, Conner and Olsen (2014) developed a technique to analyze landslide movement from terrestrial lidar scans based on the displacements near the base of tree trunks with time as they move with the landslide.

2.1.2 Coastal erosion studies and hazard mapping

Over the past decade, DOGAMI has generated coastal erosion hazard maps for both dune- and sea cliff-backed shorelines for multiple sections of the coast in order to assist coastal resource managers with hazard delineation. Pertinent to this study are analyses of coastal change derived from several sections of the coast including Sisters Rock to North Gold Beach (Priest et al., 2004), Cascade Head to Seal Rock (Priest and Allan, 2004), Seal Rock to Cape Perpetua (Witter, Allan, and Priest, 2007) and southern Clatsop County (Witter et al., 2009). For these studies, erosion rates were estimated from aerial photographs spanning a range of lithologic units (e.g. highly resistant basalt to Tertiary rocks comprised of mudstones to sandstones, to weakly cemented sea cliffs formed in Pleistocene dune sands), clearly demonstrating highly variable rates and patterns of coastal change. In some cases these data were supplemented with precision measurements of cliff changes determined from Differential GPS. The hazard maps produced delineated areas of active erosion in addition to areas of projected high, moderate, and low risk zones of future erosion. However, a major limitation of these initial studies is the fact that the erosion rates were determined for discrete points along the shore where identifiable ground control points could be analyzed in successive photo overlays. This contrasts, with the spatially dense datasets (sampling resolutions of ~1-5 cm on the sea cliff face) that are possible from high-resolution ground-based lidar mapping. Finally, in addition to the density of the data, the DOGAMI reports also discuss the high level of uncertainty associated with the use of aerial

photographs to derive long-term erosion rates, a problem that is well–documented in the scientific literature.

Allan and Hart (2005) present a detailed study and GIS dataset of beach morphodynamics derived from analyses of 1997, 1998, and 2002 lidar datasets obtained from NOAA's Coastal Service Center. The study had two objectives: 1) To compare a variety of common gridding techniques, and 2) to develop a detailed assessment of coastal change by analyzing geo-spatial transects (100 m spacing) along the central to northern Oregon coast. These data have subsequently been reanalyzed (25 m spacing) and updated (Allan and Harris, 2012) to include high resolution, multi-return lidar (8 points/m2) flown in 2008/09 by DOGAMI, which allow for the development of bare earth Digital Elevation Models (DEMs). Analyses of these data provide important insights into the spatial and temporal variability of the coast over the past 16 years, particularly on the beach face where good lidar returns are possible. However, aside from the 2008/09 lidar, these early datasets do not lend themselves to accurate delineation of features (e.g. the sea cliff top and face) in complex terrain, especially where vegetation may be dense. Furthermore, similar to the descriptions provided above, such an approach is limited to discrete points along the shore as opposed to the spatially dense types of datasets offered by ground-based lidar. The authors recommended additional lidar beach analysis.

In 2004, DOGAMI implemented a pilot beach and shoreline monitoring network on the northern Oregon coast along the Rockaway littoral cell in Tillamook County (Allan and Hart, 2007; Allan and Hart, 2008). The purpose behind this initial effort was to begin to document the seasonal to interannual changes taking place at discrete locations on the Oregon Coast. The approach involved the use of RTK-DGPS technology to measure repeat changes at multiple sites on the Oregon coast, covering both dune-backed and sea cliff-backed beaches. Although the focus was initially in the Rockaway cell, similar monitoring efforts have since been expanded to other locations on the Oregon coast, including Neskowin (Allan and Hart, 2007), Clatsop Plains (Allan and Hart, 2008), Rocky Point near Port Orford (Allan and Hart 2009), Gold Beach, Nesika and the Netarts Littoral cell (Allan and Stimely, 2013), and in the Cannon Beach littoral cell (Allan et al., 2018). Although coastal sea cliffs are being monitored at select sites on the central Oregon coast, similar problems for extrapolating meaningful trends occur, due to the paucity of sites that can be effectively observed using this approach.

As part of the extensive National Shoreline Assessment by the USGS, Ruggiero et al. (2012) analyzed shoreline change along the Pacific Northwest coast. Most littoral cells were observed to show deficits of natural sediment supplies with the exception of the Columbia River Littoral Cell. Additional shoreline analyses are also described and documented for the entire Oregon coast in a series of reports for Clatsop (Allan et al., 2015c), Tillamook (Allan et al., 2015d), Lincoln (Allan et al., 2015a), Curry Counties (Allan et al., 2015b), and Lane and Douglas Counties (Allan et al., 2017).

Recently, Burgette et al (2023) provided updated estimates of coastwide shoreline changes derived from airborne lidar. However, unlike Ruggiero et al (2013) who focus on shoreline changes at mean high water (MHW), Burgette et al (2023) examined changes occurring at the back of the beach near the bluff or dune toe. The decision to focus on the latter reflects the simple fact that changes at the dune or bluff toe is more indicative of the effects of extreme storms (waves coupled with high tides) producing a significantly smoother signal. This contrasts

with measurements made at MHW that yields a noisy signal, strongly influenced by seasonal variability in tides and waves (Allan et al., 2003; Olsen et al., 2023). Burgette et al (2023) used the 6 m contour to approximate the dune or bluff toe and analyzed lidar data collected from 1997 to 2016; the 6 m contour was found to be a reasonable proxy for the 'toe' based on assessment of previous lidar dune/bluff toe positions undertaken by Allan et al (2012; 2015a; 2015b; 2015c; 2015d; 2017). The contours were then visually inspected, cleaned and eventually processed using the Digital Shoreline Analysis System (DSAS) tool developed by the U.S. Geological Survey (Himmelstoss and others, 2018). The processing was done by casting transects spaced 10 m apart, along the entire coast. Having processed the individual transect change rates, discrete shore reaches were identified in GIS and compiled in an Excel worksheet. The individual change rates were then smoothed using a 50 m smoothing function in Matlab to reduce the noise in the change data. Each reach was defined based on a combination of the dominant coastal geomorphology (e.g., dune- and bluff-backed beaches, cobble shorelines, rock coast, etc.) and the identified change rates. The final processed data are summarized in a series of figures (Figure 4-11 to 4-16 in Burgette et al., 2023). An example of the output results for Lincoln County is included here in Figure 2.5.

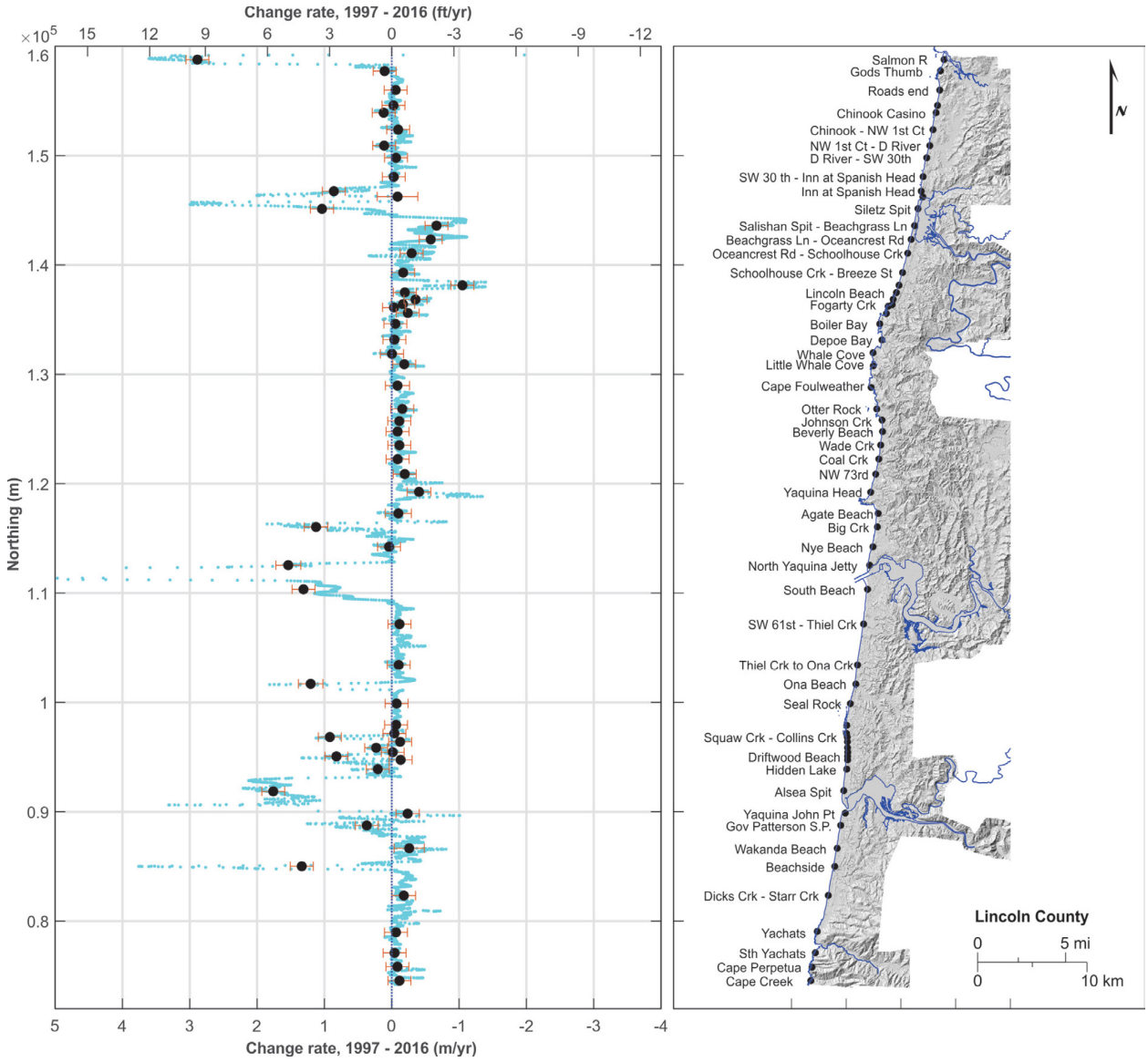

Figure 2.5. Coastal change rates (m/year) and patterns for the period 1997 to 2016 for Lincoln County. Cyan line reflects a 50 m smoothing of the individual transects, while the solid circles with uncertainty depicts the mean change for the identified study reach. Negative values indicate erosion, while positive values denote accretion (from Burgette et al., 2023).

2.2 COASTAL LANDSLIDES AND EROSION

The coastal zone is a complex, dynamic system, which regularly experiences significant morphological change, thereby affecting coastal communities, infrastructure, and public resources. Understanding the processes and rates of coastal change is critical for proper management and planning.

2.2.1 Landslides

Landslides are a natural hazard that have major societal, economic, and environmental impacts, realizing over four billion dollars of damage every year and up to 7,000 worldwide casualties per year (Schuster, 2001; Petley, 2012). These numbers are likely an underestimate due to the incorporation of landslide casualties into larger causative events, such as earthquakes, wildfire, increased erosion and heavy rainfall (Petley, 2012). These deleterious effects may be exaggerated due to a lack of social or engineering awareness of surrounding landslide activity (Burns, 2014). The impacts are not limited to the tragedy of lost lives or financial hardship. Infrastructure, including roads, rail, and utilities are frequently impacted at major economic cost and a reduced quality of life, and in the worst cases, preventing aid and access to victims of natural disasters (Schulz et al., 2012; Aruperes, 2016). These occurrences can also contaminate drinking water and harm ecosystems due to deposition of large quantities of debris and sediment (Schuster and Highland, 2001). A more detailed review of landsliding mechanisms and mechanics can be found in the ODOT SPR-740 report.

2.2.2 Geomorphological Processes

The geomorphological processes (Figure 2.6) that govern sea cliff erosion also influence the behavior of creeping, progressive coastal landslides. Erosion and destabilization of these cliffs are credited to a combination of marine and subaerial mechanisms (Trenhaile, 1987; Sunamura, 1992; Benumof et al., 2000; Hampton and Griggs, 2004; Wolters and Muller, 2008; Prasad and Kumar, 2014), which work in concert (Figure 2.7). Young et al. (2009) studied the interdependence and contributions of both waves and precipitation in eroding sea cliffs in southern California using airborne lidar data surveys acquired at 6-month intervals. Earthquakes also cause dynamic accelerations that can result in cliff failure. Nevertheless, sea cliff erosion rates are largely a function of both the resistance of the material (Benumof and Griggs, 1999) and the physical assailing processes (Benumof et al., 2000). Dong and Guzzetti (2005) determined that sea cliff erosion rates tend to slow after larger failures and discussed the need for more high-resolution data to compare the contribution of large and small events to sediment budgets.

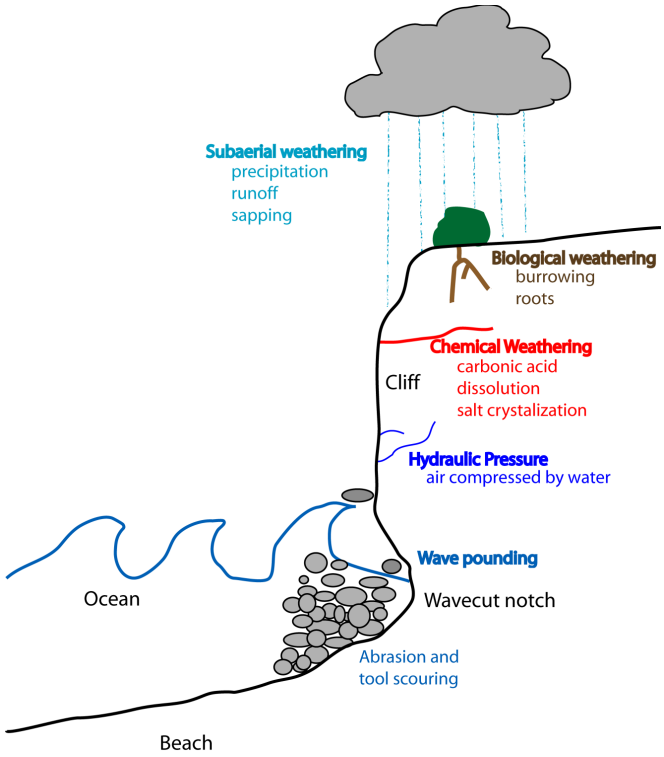

Figure 2.6: Schematic illustrating processes contributing to sea cliff erosion (from Olsen, 2009).

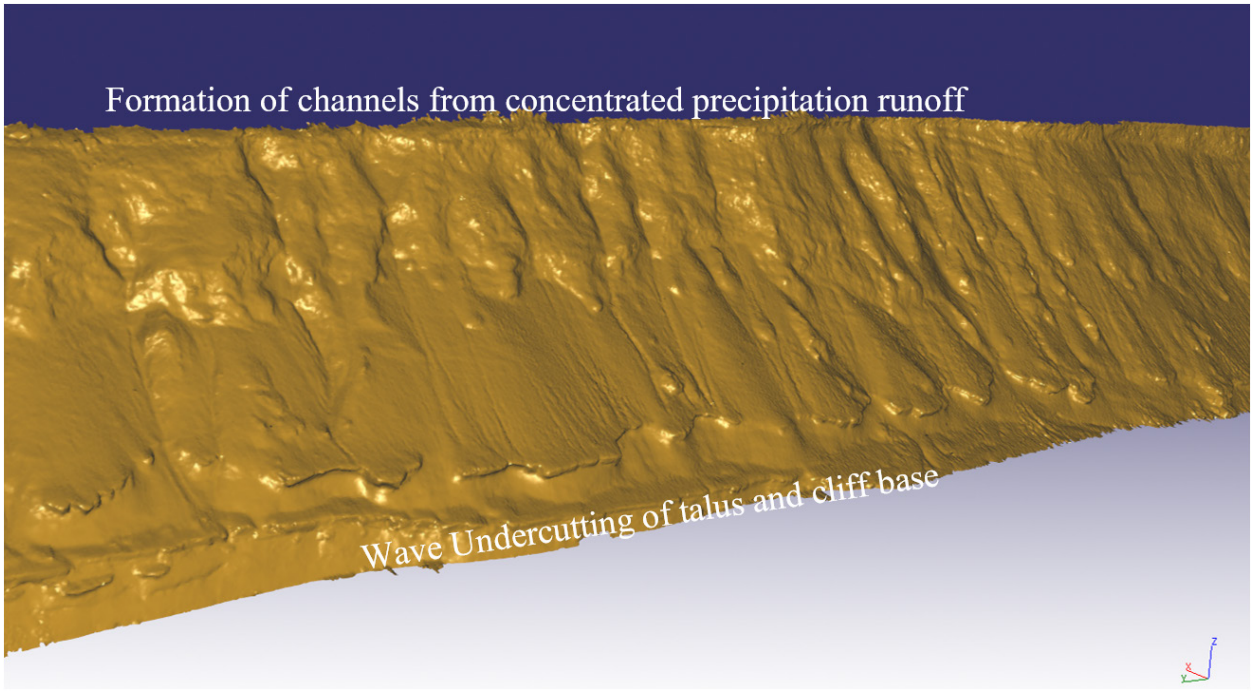

Figure 2.7: 3D surface model at Beverly Beach, OR highlighting the combination of wave-based erosion of the cliff base and talus deposits with subaerial erosion resulting from precipitation runoff incising channels into the cliff face.

While sea cliff erosion threatens development and infrastructure built on the coastline (Griggs et al., 2005), this necessary and natural process can provide vital sediment to the beach sediment budget (Haas, 2005; Young and Ashford, 2006) in locales with sandstone sea cliffs. Clay, silts, or very fine sand released from the mudstone cliffs (present along large sections of Oregon's coastline) are removed offshore and do not contribute to beach building. Sediment transport along coastlines are typically viewed as a littoral cell, defined as a segment of a shoreline that may be bounded by prominent headlands or other physical barriers. Thus, the littoral cell reflects a region in which the transport of sediments may be constrained between on-offshore sand movement, as well as alongshore sediment transport, with the net long-term change (erosion or accretion) being dependent on the balance between sand inputs and losses. In some regions (particularly in California), the beach sand budget has been shown to be in deficit, the product of damming of coastal rivers (Flick, 1994; Inman and Masters, 1991), as well as due to the construction of jetties and riverine control (Kaminsky et al., 2010), and as a result, some regions are becoming starved of sediment. This, in turn, has accelerated cliff erosion because beaches serve as a buffer zone, dissipating the incident wave energy, and ultimately play an important role in protecting sea cliffs. Nevertheless, the role and magnitude of many of these effects have not yet been determined for the Oregon Coast and need further evaluation.

Sea level rise can result in a redistribution of sediment with increased erosion of the shoreface and removal of those sediments offshore as ocean levels transgress. In contrast, when the ocean regresses, sediment is accreted onto the shore. These processes can be readily observed at prominent marine terraces located throughout the western coast of the U.S. created by sea level fluctuations.

2.2.3 Marine Erosion Processes

Marine mechanisms concentrate primarily at the toe (base) of slopes through wave action. The erosion rates are affected by the intensity, frequency, and overall duration (contact-hours) of the wave runup (Ruggiero et al., 1996), while larger storms can generate waves of sufficient height that will result in overtopping of smaller sea cliffs (Katz and Mushkin, 2013; Earlie et al., 2015). These processes are further controlled and may be enhanced in response to higher tide levels (Komar et al., 2011), or in response to the occurrence of storm surges (Allan et al., 2011). As wave energy runs up the beach and impacts the cliffs, notches and sea caves initially develop (Figure 2.8) through undercutting processes, resulting in steeper-near vertical cliff surfaces as failures propagate upward to the top of the cliff (Olsen et al., 2016). A spatially, more linear form of sea cliff retreat is observed compared with subaerial processes, which tend to be more concentrated.

Figure 2.8: Notches in sea cliffs at Fletcher's Cove, Solana Beach, CA created through wave-based erosion (from Olsen, 2009).

The impact of these waves are typically more dramatic during the winter when the waves break closer to shore and less energy is dissipated by the beach, combined with higher mean sea levels that typically occur in the Pacific Northwest. Waves also may entrain sands and gravel particles, which work similar to sandpaper as they grind against the cliff, resulting in abrasion. During high-energy storms, the waves can thrust cobbles against the base of the cliff. After a substantial amount of erosion occurs, gravity failures can occur from the notches and sea caves that develop, creating a steep cliff face. The stability of such cantilevered sections was analyzed in Young and Ashford (2008). Prior researchers have utilized parameterized wave runup modeling combined with knowledge of the tides to assess the duration of the total water levels impacting beaches (Allan et al., 2012; Stockdon et al., 2006), which can be used to analyze sea cliff erosion.

Continued erosion and undercutting from waves creates notches at the cliff toe, resulting in cantilevered, steep, vertical faces that subsequently fail (Young and Ashford, 2008; Olsen et al., 2016). Sea cliffs experiencing frequent wave attacks can erode five times faster than sea cliffs subject to only subaerial processes such as rain (Young et al., 2009). Both mechanisms drive erosion, but the underlying geologic conditions control resistance and sea cliff failure type (Young et al., 2009). This progressive behavior has been characterized as a three-stage cycle (Trenhaile, 1987; Everts, 1990; Sunamura, 1992; Hampton and Griggs, 2004) consisting of erosion, collapse, and protection. Stage one of this cycle consists of waves eroding the toe of the cliffs, causing an eventual loss in stability. Stage two is the onset of collapse, triggered by subaerial mechanisms and the loss of stability from stage one, resulting in the deposit of talus at the toe of the slope, in turn protecting the cliff from further wave erosion (Pierre and Lahousse,

2006). In the third stage, the talus is eroded away, enabling the onset of more aggressive wave attack and a re-initiation of the erosive cycle.

2.2.4 Subaerial processes

In contrast to erosion caused by wave swash processes, subaerial weathering processes erode the entire cliff face (Emery and Kuhn, 1982) and tend to relax or diminish the slope (Weissel and Driscoll, 1998). These processes tend to flatten the cliff. Runoff from precipitation erodes from the top of the cliff downward as concentrations of water forms gullies and canyons incising into the cliff. Figure 2.9 shows this process in combination with groundwater seepage at the contact between permeable rock and the more impermeable rock layers in the cliffs. Groundwater transport through the highly permeable sandstone accelerates erosion by mixing with calcium carbonate cement present in the soil to form carbonic acid. This chemical weathering caused by carbonic and humic acids dissolves the weakly cemented sandstone, which further increases surface roughness and irregularities in the cliffs. Groundwater sapping can be observed at many locales on the Oregon Coast. Additionally, the formation of tension cracks permits water to rapidly flow into the cliff, not only accelerating erosion and weathering processes, but also adding additional weight to the soil. The resulting hydrostatic pressures further widen the cracks until failure ultimately occurs.

Biological weathering occurs when plants growing in cracks break down weak sediment and push material apart (Figure 2-10). Vegetation growth on the sea cliff can also add additional weight, leading to instability. Piping can occur as plants draws water out of the soil and removes soil around the roots. Lastly, burrowing animals and insects can loosen the soil, create channels for concentrated water flow, and expose more surface area to water.

Figure 2.9. Top-down cliff erosion from subaerial processes of precipitation and groundwater sapping in Beverly Beach, OR. Note the significant presence of talus deposits at the base of the cliff (near MP 134, August 2016).

Figure 2.10. Biological erosion of Torrey Sandstone at Torrey Pines Reserve with close-up on right (from Olsen, 2009).

2.2.5 Anthropogenic contributions

Human development has dramatically contributed to the erosion of sea cliffs (Kuhn and Shepard, 1980; Moore et al., 1999). For example, irrigation and drainage pipes placed in or on the cliff eventually fail or break, contributing to an increase in water flows into the rock resulting in concentrated erosion and potentially block or sea– cliff failures (Figure 2.10). Storm drainage systems for roads and developments also can concentrate water in specific locations thereby accelerating erosion (Figure 2.11). Grading operations close to the edge of the slope can also initiate slope failures (Robinson, 1988) by removing an erosion resistant cap that protects the weaker sediment below from erosion Because the overlying terrace deposits typically consist of weakly cemented sands (Kennedy, 1975), once these top layers are removed, the sea cliffs become more permeable, increasing their potential to erode.

Figure 2.11: Recent sea cliff collapse at Beverly Beach near a broken drain pipe (near MP134, August 2016).

2.2.6 Climate Change Impacts

Over the past 50 years, observed changes in global climate patterns are affecting social and environmental norms, particularly at the interface with the built environment. In the context of impacts to infrastructure located adjacent to the coast, major environmental threats include: rising sea levels stemming from melting polar ice, increased frequency and intensity of precipitation events, increasingly severe droughts and wildfire (IPCC, 2014), and changes in storm frequency and intensity (NRC, 2012). For coastal environments, rising sea levels and increased storm intensity are primary threats towards the retreat of coastlines worldwide (Trenhaile, 2010), which may result in increased flooding, loss of beach sediment, leading to the erosion of sea cliffs, and the onset of mass movement, primarily occurring in the form of coastal landslides (Barton, 2015). Prioritization of the arrest of these erosive processes is paramount to the mitigation of these slope failures (Leshchinsky et al., 2017).

Erosion of the coastline is considered to be one of the significant threats associated with sea level rise in the United States (Dickson et al., 2007). Historically, global mean sea level increased by 0.17 between 1900 and 2009 (Church and White, 2011) and is presently rising at a srate of 3.6 mm/year based on satellite altimetry measurements[2]. By 2100, mean sea level is expected to rise from 0.18 m28m to 0.6 m (IPCC, 2007; 2023) under the low-end emission scenarios, increasing to much as 2 m under high-end emission scenarios (Sweet et al., 2022). Previous studies on the effects of wave attack on sea cliff failure have already demonstrated the influence of scour on sea cliff stability (Young and Ashford, 2006; 2008), Collins and Sitar, 2008; Young et al., 2010), resulting in slumps, collapse, and sometimes landslides. These impacts will become more

[2] https://www.aviso.altimetry.fr/en/data/products/ocean-indicators-products/mean-sea-level/data-acces.html

prevalent in the future, particularly on the Pacific Coast of North and South America due to changes in the frequency of storms, incidence of El Niño events (Storlazzi and Griggs, 2000; Allan and Komar, 2006; Barnard et al., 2015; Barnard et al., 2017), and regional increases in sea level over the remainder of this century. In particular, changes in El Niño patterns is expected to result in more frequent, intense precipitation events, changes in wave patterns and increased impact of storm events stemming from a rise in mean sea level (Barnard et al., 2015; Barnard et al., 2017). The increased erosive influences and saturation of weathering sea cliffs will only expedite the rate of retrogression (Utili and Crosta, 2011) already observed on the weakly-cemented sea cliffs common to Oregon (Hapke et al., 2006; Ruggiero, 2012). The NRC (2012) states that the natural shoreline provides partial protection; however, coastal sea cliffs, beaches, and dunes will bear the brunt of the increased erosion from storms.

In a recent study, Shadrick et al. (2022) postulate that sea level rise will likely accelerate sea cliff erosion rates based on a topographic evolution model extrapolating back 8,000 years and forecasting into the next century. They develop a relationship between sea lever rise and erosion rates based on numerical modeling, cosmogenic radionuclides, and topographic data (elevation profiles). They estimate a staggering order of magnitude increase in cliff retreat rates by 2100 from present rates. However, Dickson et al. (2023) caution in over-reliance of the Shadrick model as it oversimplifies the complex morphologic dynamics associated with erosional processes based on the findings of several process-based studies. Dickson et al. (2023) contend that erosion rates and coastal response from sea level rise will continue to be highly variable at the decadal time scales.

2.3 MONITORING TECHNOLOGIES AND PROGRAMS

Because of the economic importance of coastal zones, changes in shoreline dynamics (position over time) and the rate at which the coast may be eroding (or accreting) are of considerable interest to researchers. Hapke (2004) discusses several methods used to perform coastal cliff and sea cliff retreat measurements, which are summarized in Table 2.1. Crowell et al. (2009) discuss similar methods used in shoreline erosion mapping.

Several methods for analysis of sea cliff retreat such as digital photogrammetry (e.g., Moore et al., 1999; Hapke and Richmond, 2000), aerial (lidar) (e.g., Young and Ashford, 2006; Young et al., 2009), and oblique helicopter lidar (Rosser et al., 2008) have yielded important results, yet they have limitations for repeated coastal cliff surveys due to logistics, mobilization expense, lower spatial and temporal resolution, and/or the ability to capture the cliff face topography (including complex sea caves) in sufficient detail (Young et al., 2010). In order to document the morphological processes of interest, the corresponding data must be regularly obtained at finer temporal scales before being overprinted by other events. Lidar (specifically terrestrial or ground-based) was chosen for this study due to its high degree of accuracy as well as its ability to measure changes at high resolution for relatively short-term (i.e., less than a decade) studies. Nevertheless, other technologies such as photogrammetry are necessary for longer term studies.

Table 2.1. Advantages and disadvantages of measurement techniques for sea cliff erosion studies (modified from Hapke, 2004 and Olsen, 2009)

Technique	Advantages	Disadvantages
1. Traditional ground surveys	• Very accurate • Repeatable techniques	• Poor temporal and spatial coverage • Time consuming/expensive
2. Historical maps	• Inexpensive • Widely available • Very long temporal coverage (1850s – 1979s) • Good spatial coverage	• Low and variable accuracy/resolution • Ambiguous cliff/sea cliff edge position
3. Aerial photographs		
Unrectified	• Inexpensive • Widely available • Good temporal coverage (1920s – present) • Good spatial coverage	• Low accuracy/resolution • Ambiguous cliff/sea cliff position in 2D
Partially rectified	• Widely available • Good temporal coverage (1920s – present) • Good spatial coverage • Improved accuracy over 3a	• Ambiguous cliff/sea cliff position in 2D • Hardware/software for processing may be expensive
Fully Rectified	• Widely available • Good temporal coverage (1920s – present) • Good spatial coverage • High accuracy • Cliff/sea cliff edge digitized in 3D	• Time consuming processing • Required software expensive
4. Lidar		
Aerial lidar	• Good spatial coverage • Higher resolution and accuracy than aerial photographs • Rapid Acquisition	• Very expensive • Typically no datasets prior to 1990s • Poor coverage of cliff face
Oblique Helicopter lidar	• Higher resolution and accuracy than aerial photographs • Captures overhangs • Rapid Acquisition	• Very expensive • Typically no datasets prior to the year 2000
Terrestrial Laser Scanning	• Very high accuracy • Very high resolution • Captures overhangs and caves • Less expensive than 4a&b	• Difficult spatial coverage • Typically no datasets prior to the year 2000 • Time consuming/expensive
Combined lidar techniques	• Complete 3D model of sea cliffs • Substantial amount of data	• Expensive and logistically challenging • Poor temporal coverage • Surveys must be completed nearly simultaneously
5. SFM		
Handheld	• High Accuracy • Portable and Flexible	• Limited visibility on upper sections of cliffs • Requires survey control for accurate results • Significant overlap (80-90% required)
Unmanned Aircraft System	• High Accuracy • Flexible views of the entire cliff	• Safety and operation logistics • Requires survey control for accurate results • Significant overlap (80-90% required)

With respect to measuring sea cliff erosion, Young et al. (2009) provide a comparison of common methods for determining sea cliff retreat and observed that significant differences in values can be obtained whether measuring retreat at the toe, crest of the cliff, or by averaging across the cliff face. Overall, they found it difficult to reliably extract changes along the cliff top given obstructions due to vegetation and the resolution of historic datasets. Young et al. (2010) also compare the capabilities of airborne and terrestrial lidar for analyzing erosion of relatively shallow (~45°) sea cliffs.

2.3.1 Ground-based lidar coastal monitoring

Although the advance and retreat of these sea cliffs has traditionally been difficult to measure, advanced spatial technologies – namely terrestrial light detection and ranging or lidar data collection, have made this information attainable. TLS captures topological characteristics at high resolution, producing a detailed point cloud containing X, Y, Z coordinates, R, G, B color, and return signal intensity information. Figure 2.12 shows an example of a photographic colored point cloud obtained using ground-based lidar on a mobile platform (Figure 2.13). Figure 2.14 provides an example of change analysis and erosion quantification that can be performed using time-series, modeled lidar data. This information can then be used to create advanced spatial and temporal statistical analysis techniques to simultaneously study large- and small-scale coastal processes and trends.

Lidar technology has reliably captured geomorphic changes in sea cliffs throughout California (e.g., Collins and Sitar, 2004; Collins et al., 2007; Young and Ashford, 2007; Young, 2009; Olsen et al., 2016; Johnstone et al., 2016), Oregon (Ruggiero et al., 2013; Olsen et al., 2012; Conner and Olsen, 2014), and worldwide (e.g., Lim et al., 2005, 2011; Rosser et al., 2005; Katz and Mushkin, 2013; Earlie et al., 2015; and Whadcoat, 2017). This high-resolution topographic data enables improved characterization of not only sea cliff undercutting but also helps identify its effects on creeping landslide movements (Collins et al., 2007; Olsen et al., 2012; Conner et al., 2014; Young et al., 2015). In combination with stratigraphic mapping, analysis of sedimentological records, and interpretation of mineralogical conditions, lidar is also important to determine failure volumes and sediment yields from the cliffs (e.g., Young and Ashford, (2006, 2007, 2008); and Young et al., 2010). Data and findings from those efforts were used by the city of Solana Beach, CA to charge a “sediment fee” as part of the sea-wall permitting process because of the potential sediment loss of beach material from cliff erosion.

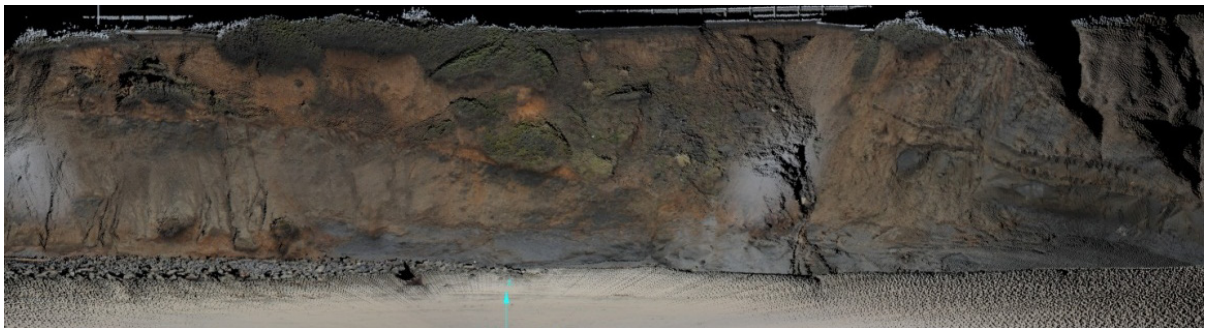

Figure 2.12: Sample lidar scan/point cloud for Beverly Beach, Oregon (February 2010).

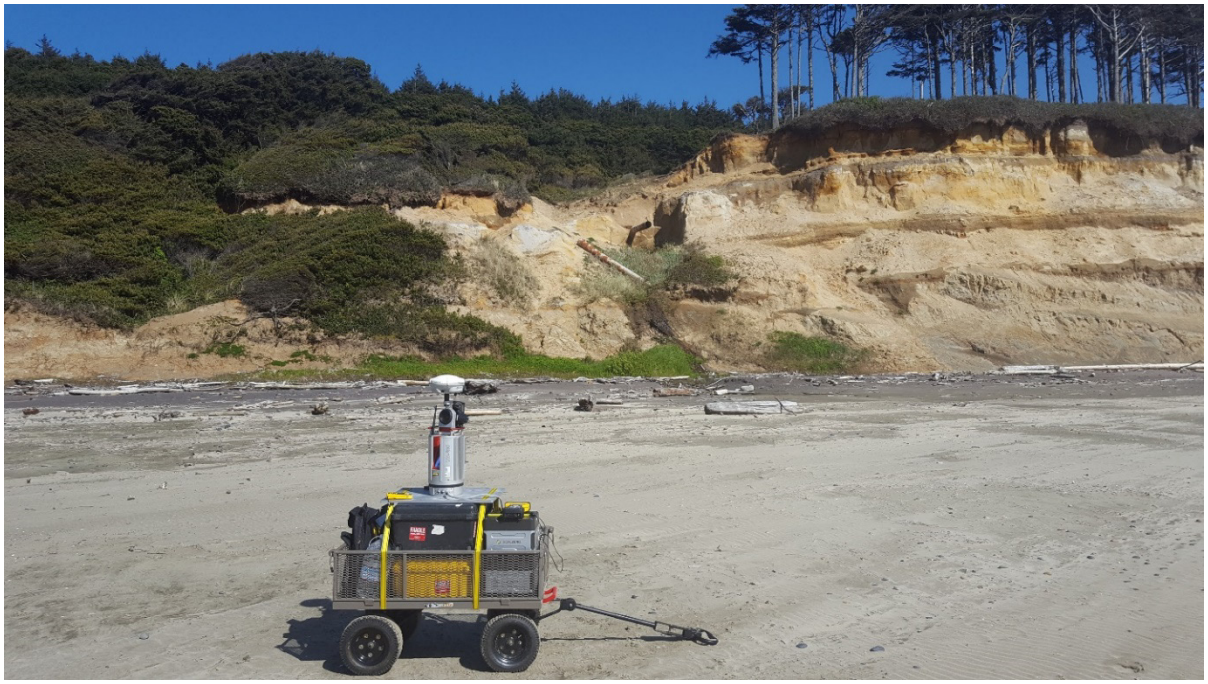

Figure 2.13: Sample Ground-based lidar setup mounted to a wagon for efficiency (Beverly Beach, May 2017).

Multiple scans are registered together in order to produce a continuous topographic model of sea cliffs for a locale of interest. Young and Ashford (2007) and Olsen et al. (2009, 2011) provide a methodology for acquiring TLS (stop and go) of long coastal cliff sections as well as a parametric analysis to determine scan acquisition parameters such as scan spacing, distance from objects, and resolution to balance efficiency with data quality. A challenge of working with TLS along coastal sections is the necessity to time the ocean tides to prevent equipment and users from being submerged. Recently, Olsen et al. (2013, 2015) have developed advanced modeling techniques to enable efficient change detection and analysis of the cliff.

Lidar has also proven to be an effective tool for landslide analysis ranging from detection and characterization of mass movement and monitoring at the regional scale with airborne laser scanning (ALS) to terrestrial laser scanning (TLS) providing site specific details at improved resolutions (cm level) (Jaboyedoff et al., 2012). TLS has been successfully implemented for geological characterization and assessment of landslides (Collins and Sitar, 2008; Collins and Stock, 2012; Dunning et al., 2010), resulting in improved understanding of the processes and mechanisms contributing to landslide movement. For a detailed review of the use of both terrestrial and airborne lidar for landslide assessments refer to Jaboyedoff et al. (2012). Young et al. (2010) performed a comparison between TLS and ALS for sea cliff erosion analysis and concluded that ALS has superior coverage capturing the cliff-top and crest, which is useful for detecting large or deep seated landslides but may not detect surficial landslides, erosion hotspots, or detailed change that can be picked up by a TLS.

Considerable work has also been undertaken in recent years to document the patterns of landslides and mechanisms for failure. For example, Burns and Madin (2010) demonstrated a methodology to use airborne lidar to map landslides in northwest Oregon, ultimately creating

landslide hazard maps that could be used by local government for planning purposes. Similarly, Schulz (2005) discussed landslide susceptibility estimation from airborne lidar data. Leshchinsky et al. (2015) developed an automated landslide mapping method, the Contour Connection Method, which was further developed SPR-786 (Leshchinksy et al., 2018).

TLS provides many advantages over traditional methods of monitoring erosion. These advantages come primarily from the density of data points collected on cliff faces. This allows for in-depth monitoring of accretion and erosion along the cliffs, as well as monitoring of large land mass movements. Figure 2.14 shows an example of such change analyses using surface models derived from lidar data.

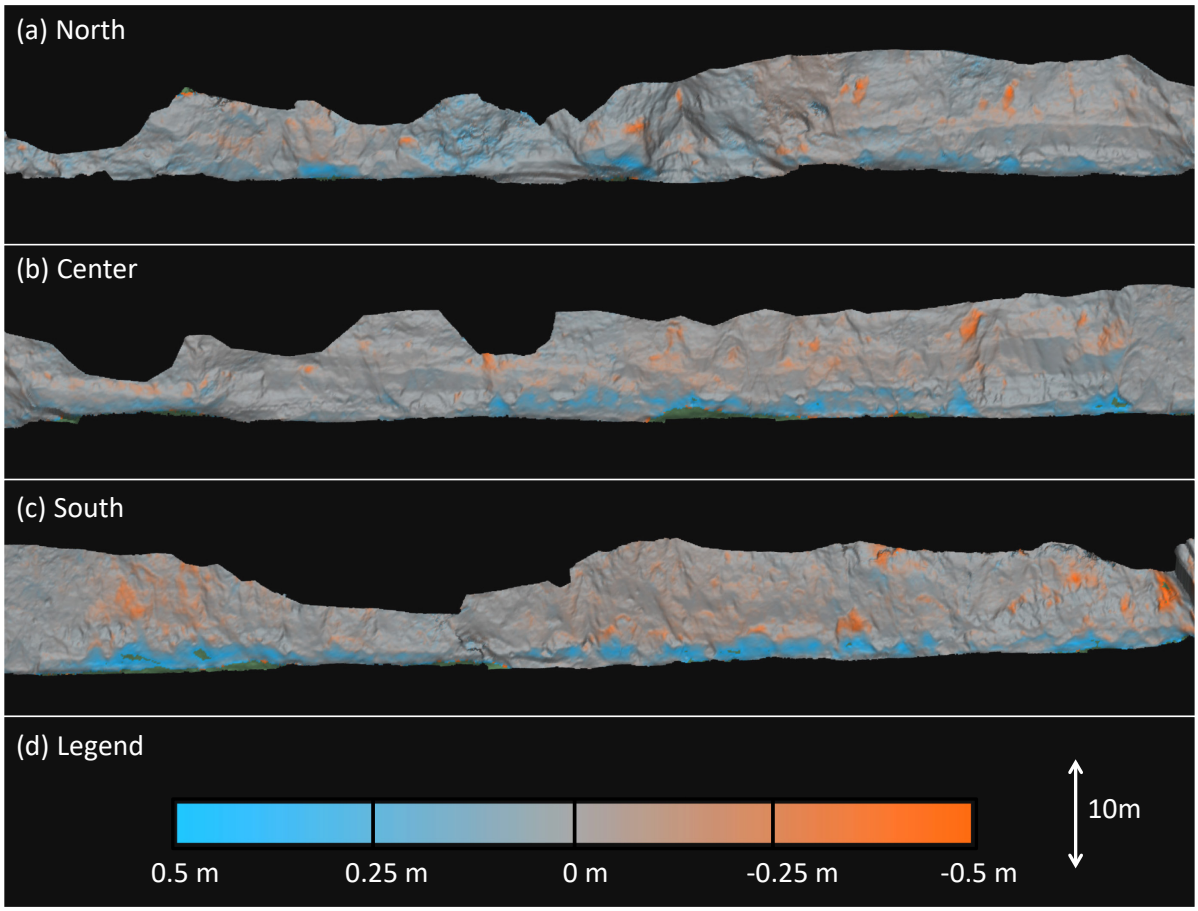

Figure 2.14: Change analysis between lidar surveys showing advance and retreat of the cliff face at the coastal Johnson Creek Landslide between May and August 2012 (courtesy of Jeremy Conner, OSU Geomatics).

Much coastal research has been concerned with the volume of material released from the cliff and overall rates of erosion (e.g., Moore et al., 1999; Hapke and Richmond, 2000), focusing on a large extent of coastline and relatively long temporal scales. In contrast, Olsen et al. (2016) document and analyze erosional processes at a finer temporal and spatial scale such as determining the rates at which material is reworked from the cliff to the beach (or other locales) The fine temporal and spatial resolution of the lidar dataset collected by Olsen et al. (2016)

provides insights on the sequencing of failures across the cliff face and illustrates how liberated material is quickly reworked by wave action, even during low energy periods such as the summer. They also documented feedback mechanisms where failed material served as a temporary stabilization to the base of the cliff against, preserving talus deposits adding transitory protection against wave erosion.

2.3.2 Other Landslide monitoring technologies

One important means of assessing the activity of landslides is through geotechnical monitoring efforts consisting of subsurface investigation, instrumentation, and in some cases, response of moving slopes to remediation efforts. Conventional landslide monitoring consists of data collection at rather low temporal resolution – that is, data are collected at relatively long intervals (Dasenbrock et al., 2012). Conventionally, critical data on pore water pressure is collected through use of piezometers, flumes, and flowmeters. Movements are often monitored through use of tensiometers, titlmeters, Global Positioning System (GPS)/Global Navigation Satellite System (GNSS), Structure from Motion(SfM)/Multi-view Stereopsis (MVS) photogrammetry, and primarily, inclinometers (Gili et al., 2000). Other technologies include Micro-Electrical-Mechanical-Systems (MEMs) Arrays, Interferometric Synthetic Aperture Radar (InSAR), and Light Detection and Ranging (lidar). These techniques each have positive and negative attributions for landslide monitoring dependent on landslide characteristics. This section will discuss these techniques, with the exception of lidar, which was discussed in detail in Section 2.3.1.

2.3.2.1 Inclinometers

Inclinometers (e.g., Wieczorek and Snyder, 2009) monitor tilt and infer movement at discrete locations within a drilled cased boring in a given landslide. This is accomplished by measuring the inclination (both in X-Y directions) at predefined locations, periodically monitoring the variation of the original inclination of the tube. Inclinometers can be configured in place and electronically record readings or manually inserted and removed from the tube to obtain readings at discrete times; the former is referred to as an in-place inclinometer (IPI) system. Although inclinometers may provide subsurface deformations within a landslide that other techniques cannot capture, such as shear planes and discontinuities, they have poor spatial and temporal resolution. Manual inclinometer measurements can often result in reading error and large intervals between reading, providing limited insight into real time landslide movements and velocities. However, in-place inclinometer systems, may provide more continuous temporal resolution for movements (Cornforth, 2005; Stark and Choi, 2008), but are often limited by depth resolution and their ability to capture three-dimensional deformations. Furthermore, they do not work when moderate to excessive movement occurs, due to deformation of the casing preventing inclination measurement. (This was a common problem experienced by Schulz and Ellis (2012) in monitoring the JCL). Lastly, the manual nature of reading conventional inclinometer systems may result in reading errors.

2.3.2.2 MEMS Array

Newer technologies such as in-place inclinometers that utilize MEMS have provided an ability to provide high-resolution subsurface data in both time and three-dimensional space (Dasenbrock et al., 2011; Dasenbrock et al., 2012; Barendse and Machan, 2012). The ability for these systems to characterize three-dimensional movements at a high frequency are critical to coordinating the real-time-response of factors that drive slope instability (i.e., erosion, rainfall) and the movements that result from these driving forces.

2.3.2.3 GPS/GNSS Technology

GPS receivers can be permanently mounted at discrete locations on landslides to monitor movement by comparing the positional changes of the GPS units compared to other stable units in the GPS network. Wang (2011) reported the ability to resolve landslide movements as fine as 2 mm horizontally and 6 mm vertically using four-hour observations at sites with an open view of the sky. Unfortunately, the cost of survey-grade GPS units necessary for this level of detection often only enables a few receivers to be installed on a single slide, limiting the spatial resolution as well as the number of landslides that can be monitored. This technique is best suited for landslides near high population areas where it can be utilized to provide early warning.

2.3.2.4 SAR remote Sensing

Interferometric Synthetic Aperture Radar (InSAR) determines fine displacements by analyzing the phase change between radar images. InSAR can be difficult to apply in forested environments (Rosen et al., 2000). Vegetation canopies result in mixed elevations between the ground and canopy top as well as reduce correlation between images because of volumetric scattering. InSAR provides increased spatial coverage compared with traditional techniques but can be limited in temporal coverage by repeat passes.

2.3.2.1 Structure from Motion(SfM)/Multi-view Stereopsis (MVS) photogrammetry

Additional technologies can provide an alternative to lidar data and still provide high resolution compared to airborne or satellite platforms. These include kite aerial photography (Bryson et al., 2013) and Uncrewed Aircraft Systems (UAS) technology (Mancini et al., 2013). Structure from motion, multi-view stereopsis photogrammetric procedures (Fonstad et al. 2013) can produce point clouds useful for change analysis, provided adequate survey control or kinematic positioning technologies (e.g., RTK-GNSS) are utilized. Key challenges in utilizing kite or UAS technology for coastal erosion studies include difficulties such as: (1) piloting during moderate and strong windy conditions, common in coastal environments, (2) precipitation or other adverse weather, (3) maintaining line of sight in the rugged, vegetated terrain, (4) safely operating above the ocean waves, and (5) potential disruptions to birds and other wildlife. These require careful planning for field data collection. Nevertheless, these technologies can perform efficient surveys and capture details in areas that are otherwise inaccessible.

2.3.2.2 NASA EOS program

In April 2016, NASA's Earth Observation System (EOS) program established the CEOS Disaster Working Group Landslide Pilot. This working group is focused on demonstrating the utility of satellite observation throughout landslide disaster risk management, including preparedness, response, and recovery at global, regional, and local scales. The international program has a distinct, multi-hazard focus on cascading impacts and risks. The SPR-807 team has been active in this working group and has submitted the Arizona Inn site as a candidate for monitoring in this pilot program.

2.4 SLOPE STABILITY ANALYSIS TECHNIQUES

Landslides are a worldwide hazard that have major economic, social, and environmental impacts. Landslides, defined as a downslope movement of rock, soil and debris (Cruden, 1991), occur in various forms, often induced by external disturbances, including heavy rainfall, seismic events, and progressive destabilization from external processes such as consistent ocean wave or river erosion of the toe. These slope failures may occur rapidly, sometimes exhibiting high mobility and potentially devastating consequences. More often, however, they exhibit seasonal, progressive displacements from destabilizing influences. In either scenario, the relative stability of the slope prior to movement is typically assessed using a comparison of internal shear stresses to available shear strength, commonly referred to as a slope stability analysis (Abramson, 2002). Slope stability analyses require assumptions about material properties (e.g. unit weight, shear strength, stratigraphy and weathering, etc.) and hydrogeological conditions and a potential surface of rupture, often constrained to a singular moment in time. However, many actual slope failures experience highly time-dependent stability patterns, influenced by changes in hydrology, mobilization of shear strength (e.g. peak, fully-softened, residual friction, cohesive/brittle strength, etc.), erosive processes such as undercutting, and movement. This study couples geotechnical slope stability tools with the resulting changes in slope morphology and hydrology.

Creeping landslides, also known as slow earthflows, exhibit progressive movements that stem from metastable conditions and changes in porewater pressure that may cause seasonal instability (Highland and Bobrowsky, 2008; Bjerrum, 1967). These failures may be imperceptible until it has compromised sensitive linear infrastructure, such as buried utilities or roads. Albeit slow, the movements can gradually accelerate with destabilizing effects, either from anthropogenic or natural influences. Anthropogenic influences include excavations and embankment construction in vulnerable locations and adverse alteration of site hydrology (Ohlmacher and Davis, 2003). Natural destabilizing processes include heavy rainfall, seismic loading, or toe undercutting from the erosive power of rivers or waves (Highland and Bobrowsky, 2008). In addition to the aforementioned destabilizing mechanisms, these slides often occur due to adverse geologic conditions, such as bedding planes, weak seams, and in-place weathering, which will often govern the rate and types of movements realized (Willetts, 2000). These potentially large landslides are of particular relevance to Coastal Oregon, which can be generally characterized by highly-bedded, weak geology in between more resistant basalt headlands, all of which are subject to intense winter storms associated with heavy precipitation and intensive sea cliff erosion (Schulz et al., 2012).

Despite the deleterious effects associated with creeping landslides, there is limited means of assessing these slope movements with time. Most research has focused on field reconnaissance and instrumented observations about creeping landslides (Van Asch and Van Steijn, 1991; Furuya et al., 1999; Iten et al., 2008). Research assessing time-dependent landslide susceptibility has concentrated primarily on the effects of precipitation and changes in partial saturation (Lu et al., 2012; Yoo and Jung, 2006; Chen et al., 2017); however, these approaches only considered the relative stability of slopes and do not consider changes in stability that result from movement. Other studies have employed complex continuum analyses to assess the coupled movement of progressive landslides under rainfall (Eberhardt et al., 2007a; Leshchinsky et al., 2015), but employed complex constitutive models that require expertise in appropriate usage. Semi-empirical and analytical approaches have been proposed that correlate creep velocities with s (Van Asch, 1984; Van Genuchten and DeRijke, 1989; Van Asch and Van Genuchten, 1990; Puzrin and Schmid, 2011); nevertheless, these approaches do not account for the time-dependent processes associated with toe undercutting stemming from fluvial or marine erosion processes.

The connection between undercutting processes and creeping slope stability are well-documented qualitatively, but poorly constrained quantitatively. This challenge stems from the difficulty in measuring erosive processes and coupling these measurements with geomechanics-based stability analyses. Often, slope stability analyses based on limit equilibrium (LE) or limit analysis (LA) methods are used to assess the relative stability of a potential slope failure. These methods employ assumptions that may constrain applicability, including the following assumptions: (1) that the landslide components are rigid, (2) the kinematics are known (i.e., the surface of rupture associated with failure), and (3) the hypothetical statics assumed are appropriate (Duncan and Wright, 1980). For generalized failure surfaces that are complex, yet realistic, rigorous slope stability methods that satisfy both moment and force equilibrium, such as the Spencer (1967), Morgenstern-Price (1965), or Janbu (1975) methods should be employed, which often discretized with vertical slices that capture the failure geometry. These methods evaluate stability only for conditions at a given moment of time and do not assess changes in stability from movements. Furthermore, the assumption that the landslide body is rigid can be an unrealistic assumption for slope failures that mobilize shear strength unevenly along the surface of rupture (Duncan et al., 2014). However, for creeping landslides that demonstrate competent blocks or masses that move, such an analysis would be appropriate.

The effects of undercutting on progressive slope stability in consideration of time-dependent undercutting processes have seldom been quantified. Midgley et al. (2012) established a Bank Stability and Toe Erosion Model (BSTEM) that focuses on streambank stability, creating a time-dependent model that incorporates a simplified limit equilibrium module that assesses the stability of horizontal layers, vertical slices, or cantilever shear failure. The toe erosion module estimates bank undercutting through fluvial erosion utilizing an excess shear stress equation (Partheniades, 1965; Simon et al., 2000). This stability model eventually exhibits instability and collapse but does not assess movements explicitly. The application of such models to coastal sea cliff undercutting is limited and none have been directly applied towards a coupled interaction with creeping landslides.

2.5 SHORELINE ANALYSIS TECHNIQUES

Several GIS tools have been created to determine coastal change rates. This section will describe some common tools used to analyze sea cliff erosion.

Duffy and Dickson (1995) developed SHOREGRID using ArcInfo® Macro Language (AML) to calculate shoreline erosion rates from digitized 2-D shorelines (from DEMs or aerial photographs, etc.) between two epochs. SHOREGRID has been successfully implemented to investigate sea cliff retreat (Moore et al., 1999; Moore and Griggs, 2002). In this program, digitized shorelines are converted to grids with a value of "1" in each grid cell that intersects the shoreline. SHOREGRID then calculates the shoreline erosion rate by dividing the shortest distance between two shoreline grids by the time difference. SHOREGRID also predicts future shorelines based on a linear projection of the calculated erosion rates.

One of the most prevalent tools for shoreline analysis is the Digital Shoreline Analysis System (DSAS, Himmelstoss et al., 2014; previous versions: Himmelstoss et al., 2018, Thieler et al., 2005; DSMS/DSAS, Danforth and Thieler, 1992). DSAS inputs shorelines from several epochs digitized in GIS. It then creates transects for the area of interest from the original shoreline. At each transect, it implements regression techniques to calculate the linear rates of change from the multiple digitized shorelines. The DSAS tool has been applied successfully to evaluate sea cliff top retreat (Hapke and Reid, 2007) and various beach shoreline proxies (Esteves et al., 2006; Morton et al., 2005; Harris et al., 2005; Himmelstoss et al., 2006; Pendleton et al., 2004; Hapke et al., 2010).

It is worth noting that the SHOREGRID and DSAS tools are primarily aimed at analyzing 2D shoreline data; however, recent advances in coastal remote sensing now provide high-resolution, 3D topographical data, which is particularly important for sea cliff studies.

Bossak et al. (2005) developed the Coastal Impact Assessment Tool (CIAT) to predict coastal storm impacts using beach slopes derived from topographic datasets such as lidar. The tool utilizes 3-D visualization features in GIS for scenario evaluation. The tool also calculates estimated water run-ups during storms, which provides useful information to identify potential coastal damage during storm events.

The Topographical Compartment Analysis Tool (TopCAT), developed by Olsen et al. (2012) was developed in Visual Basic for Applications (VBA) for Geographic Information Systems (GIS). TopCAT divides the study region into discrete "compartments" from which alongshore topographic and volumetric change may be quantified (Figure 2.15). Young and Ashford (2006b; 2007) initially implemented this approach in a manual GIS environment. Portions of TopCAT and the general topographic change compartment methodology have been successfully implemented in several recent coastal cliff geomorphic studies in Southern California (e.g. Young et al., 2009a, 2009b, 2010, 2011). Although TopCAT was specifically designed for the morphological analysis of sea cliffs and beaches but may be applied to other elongated features experiencing topographical change, such as stream beds, riverbanks, coastal dunes, and so forth.

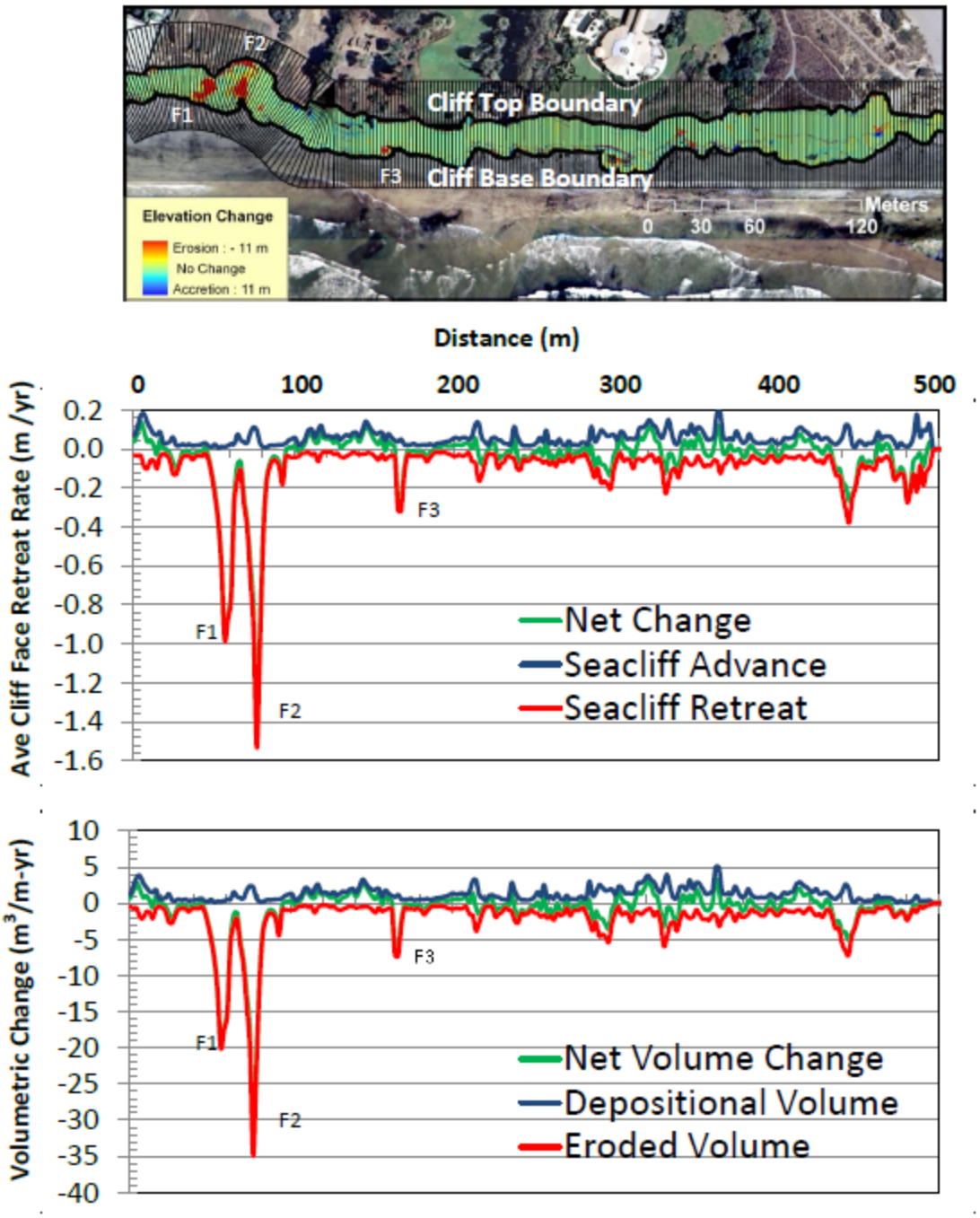

Figure 2.15: Volumetric and topographic change analysis completed for Dog Beach, CA using the GIS-based tool TopCAT (Olsen et al., 2012).

TopCAT offers several advantages to performing coastal erosion studies: (1) TopCAT is not limited to transects, but instead works with the entire data grid thereby accounting for the data between transects, (2) TopCAT can also account for bends in the shoreline; transects at close intervals can overlap in these locations, forcing a larger sampling interval, which could limit the ability of the user to study localized phenomena, (3), Vectorized approaches require the analyst

to select the top, base, or other consistent location of the cliff for comparative analysis. Young et al. (2009a) discuss how estimates of cliff retreat vary depending on whether the cliff top, base, or face is used for comparison. TopCAT, in contrast, uses 3-D data of the entire cliff face to estimate mean cliff face retreat, and (4), TopCAT allows for continuous volumetric analysis, which provides valuable information for sediment budget analysis.

Nevertheless, because TopCAT operates within ArcGIS and implements spatial analyst tools, it inherits many processing limitations (e.g. size of dataset) that the user would experience in ArcGIS implementing those tools manually. Generally, this is most significant when generating DEM datasets for sections of large (> 50 km) extents with small cell sizes (< 1 m). While TopCAT was not utilized directly in this research due to deprecation of VBA by ArcGIS, some of its core functionality for computing alongshore erosion rates and volumes has been integrated into the Rambo software used in this research.

2.6 MACHINE LEARNING

Scripp's Institution of Oceanography at UCSD has performed extensive analysis using lidar data for sea cliff erosion assessments (e.g., Young et al., 2018; Swirad et al., 2021). They perform regular mobile lidar surveys of several sea cliff regions along the southern California Coast. Recently, Swirad and Young (2021) explored the use of machine learning to perform erosion evaluation of sea cliffs, particularly to separate erosion and deposition as well as identify areas of vegetation growth. In this study, they quantified erosion for 866 km of sea cliffs along the California coastline using airborne lidar datasets obtained from 2009-2011 compared with 2016. The analysis was supplemented with NDVI information to help identify vegetated areas of the slope. In their study, they found that the highest 1% of erosion volumes (> 3243 m^3) dominated the total eroded volume of material (67%).

2.7 EROSION FORECASTING

Several models have been proposed to forecast erosion based on historical trends and modeling. Examples include:

- Time series forecasting algorithms (Calkoen et al., 2021).
- Machine Learning (Beuzen et al., 2019; Montaño et al., 2020; Calkoen et al., 2021).
- Ordinary Least Squares (Calkoen et al., 2021).
- Artificial Neural Networks in a GIS Environment (Peponi et al., 2019) which considers anthropogenic activities.
- Multimodel ensemble (Limber et al., 2018).
- Multiple Linear Regression models (Abushandi et al., 2020).
- Evolutionary Polynomial Regression (Bruno et al., 2018) with both simple linear and multilinear regression.

3.0 OVERVIEW OF STUDY SITES

Five sites (Figure 3.1, Table 3.1) were selected for this research. From North to South, these sites are: Silver Point, Arch Cape, Spencer Creek (Beverly Beach), Arizona Inn, and Hooskanaden. These sites represent a range of geologic processes and conditions across the Oregon Coast including different levels of activity and magnitude of anticipated failure.

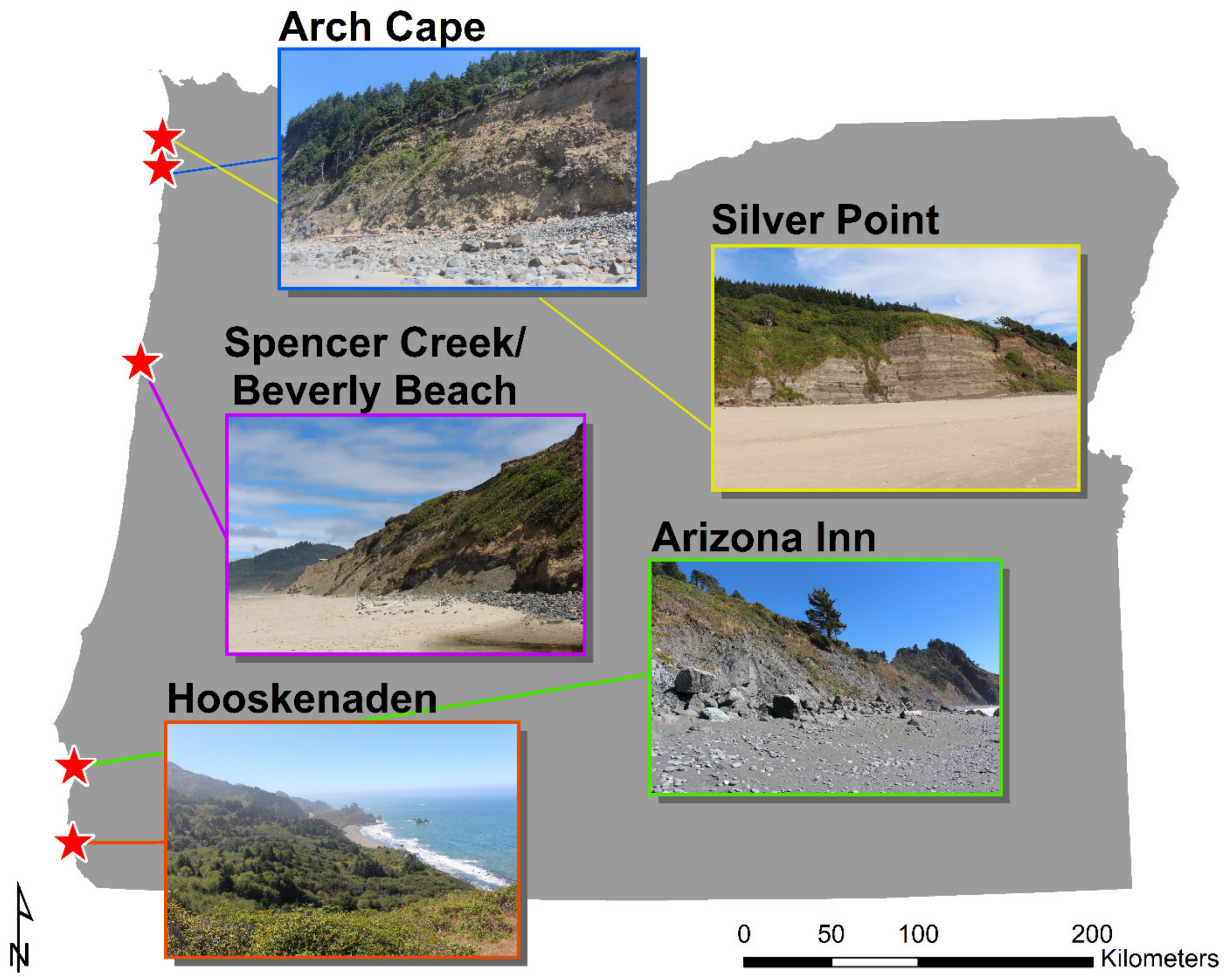

Figure 3.1: Map of study site locations.

Table 3.1: Summary of study site locations.

Site	Highway 101 MP	County	Latitude	Longitude
Silver Point	31.8	Clatsop	45.855458	-123.963799
Arch Cape	35.95	Clatsop	45.797884	-123.967618
Beverly Beach	134	Lincoln	44.729558	-124.059009
Arizona Inn	312.5	Curry	42.623975	-124.398966
Hooskanaden	344.1	Curry	42.219946	-124.373157

3.1 SILVER POINT

The Silver Point site is located south of Cannon Beach, around 700 m south of west Sitka Street on Highway 101 between mileposts 31 & 32. At this point, Highway 101 runs parallel to the coast and is separated by a small sea cliff and gently inclined slope. Figure 3.5 shows the sea cliff at the most seaward point. The study area extends from around 120 m north of the westernmost point to around 150 m south of the point. Moving landward, this site changes from a wide sandy beach to a steep coastal sea cliff that varies from approximately 5 to 30 m in height that shows well-defined seaward dipping bedding planes in places (Figure 3.6). For the most part, the sea cliff is void of vegetation. On top of the sea cliff there is a heavily vegetated gentle slope extending upward to Highway 101. The geology of this varies from late Pleistocene to Holocene landslide deposits mixed with Grande Ronde basalt from the mid-Miocene in the north and middle sections (Witter et al., 2009). The south section is principally comprised of Angola Peak sandstone (Witter et al., 2009) light brown to grey in color, interbedded with siltstone (Schlicker et al., 1972) from the Astoria Formation deposited during the Miocene. This unit consists of arkosic and lithic sandstone containing cross bedding and laminations interbedded with carbonaceous and mica rich siltstones (Niem, 1975). This unit is well exposed in much of the coastal sea cliff as shown in Figure 3.6 where well defined beds 10-50 cm thick can be seen. Geologic maps published by Schlicker et al. (1972) state this area as dipping gently to the southeast at approximately 5 to 10˚.

Study of this site is important as previous large-scale landslides have occurred here such as the 1974 Silver Point landslide, which displaced over 2 million cubic yards (1.5 million m^3) of material, moved Highway 101 35 ft (~11 m), and cost over $1 million to repair (Witter et al., 2009). With most geologic maps classifying this area as active landslide (Schilicker et al., 1972; Niem et al., 1985), this site is at risk of future mass movement especially during periods of high precipitation such as storm events during the winter months (which was interpreted to be the cause of the 1974 landslide (Squier, 1974)) with block failure up to 250 ft (~76 m) in width possible (Allan & Priest, 2001).

Figure 3.2: The coastal sea cliff at the most westerly point of Silver Point (facing east) (near MP32, August 2016).

Figure 3.3: Showing coastal sea cliff at Silver Point study site, containing well defined beds from the Astoria Formation, taken facing south east (near MP32, August 2016).

3.2 ARCH CAPE

The Arch Cape site is located on U.S Highway 101 (Highway 101) at Milepost 36 immediately south of the Arch Cape tunnel and approximately 1 mile south of the town of Arch Cape, Clatsop County, OR. At this site, Highway 101 runs roughly parallel to the shoreline and is separated by a steep coastal landslide deposit experiencing rapid eroding. Figure 3.2 shows the section of road above the site, whilst Figure 3.3 shows the steep drop from the road to the shoreline.

The primary area of study extends seaward from the tunnel about 50 m south. The shoreline at this location (moving landward) changes from a small section of sandy beach to a steep cobble/boulder berm around 10 to 25 m wide that is flush against the sea cliff (Figure 3.4). The cobble berm has a crest elevation of approximately 7 m with a mean grain size of approximately 70 mm (Allan et al., 2005). The cobbles are smooth and well-sorted throughout the berm, increasing in angularity and size, with more abundant presence of boulders towards the north. The coastal sea cliff itself is a landslide deposit around 35 m in height with a gradient of roughly 45˚ and contains sparse vegetation at its base up until around 10 m where vegetation increases. Highway 101 sits upon this sea cliff and trees also appear around the elevation of the Highway.

Arch Cape lies within the Astoria Formation and is mainly composed of sandstone with some siltstone from the Miocene (Schilicker et al., 1972). Just north of the study area this formation is bounded by extrusive basalt from the Grande Ronde basalt formation (Ruggiero et al., 2013). The beginning of this unit is visible in the topography as the elevation sharply rises due to the increase hardness of the basalt and corresponds roughly with the start of the Arch Cape tunnel. This Grande Ronde basalt provides many of the cobbles and boulders that form the berm at the base of the sea cliff in the study area.

Figure 3.4: US Highway 101 facing north just before the Arch Cape tunnel (near MP36, August 2016).

Figure 3.5: Facing west (towards to ocean) from Highway 101, showing the steep coastal sea cliff rapidly descending to the beach (near MP36, August 2016).

Figure 3.6: The coastal sea cliff and cobble/boulder berm along the toe of the Arch Cape site (facing southeast) (near MP36, August 2016).

Data from ODOT's unstable slope database shows this site as requiring repair once every five years with heavy precipitation cited as the primary cause of movement. Currently, temporary retaining walls and pavement patches are used to protect the highway at this location (Crook & Mohney, 2014); however, they are required to be replaced every 12-15 years (Crook & Mohney, 2014). No work (aside from the current work for SPR-807) has yet been done to determine the

extent of sea cliff erosion at this site (Crook & Mohney, 2014), which is another factor that may have large implications for the highway moving forward.

3.3 SPENCER CREEK

The Spencer Creek site is located approximately 1 km north from the corner of NE Avery St and NE 115th St, Beverly Beach, just north of milepost 134 on Highway 101. Figure 3.7 shows Highway 101 running parallel to the coastline separated by a coastal sea cliff. The study area extends about 400 m south of the Highway 101 bridge crossing Spencer Creek to about 400 m north of the bridge. Moving landward the area changes from a wide sandy beach to a steep coastal sea cliff around 20 m in height with a gradient of about 30˚ and varying amounts of vegetation. Typical sea cliffs are shown in Figures 3.7 & 3.9. The typical front face of these sea cliffs is shown in Figure 3.9, while Highway 101 sitting on top of this sea cliff is separated by a 5 to 10 ft (1.5 to 3.0 m) wide shoulder as shown in Figure 3.8.

The geology of this area consists primarily consists of siltstone and sandstone from the Astoria Formation, which dips around 20˚ to the east. This is overlain by interbedded estuary deposits consisting of layers of loose silt and sand interbedded with soft clayey silt and organics. The estuary deposits vary from around 90 ft (~27 m) thick (around Spencer Creek) down to 10 ft (~3 m) thick on the lateral edges of the site (Shannon & Wilson, Inc., 2015).

Figure 3.7: Photograph of the Spencer Creek site, facing south, with Highway 101 on the left separated from ocean by the crumbling coastal sea cliff (Near MP 134, August 2016).

Previous studies by Priest (1999) estimates erosion rates in the sea cliffs surrounding Spencer Creek to be 0.2 to 1.5 ft (0.06 to 0.46 m) per year. This combined with local mass movement events (Figure 3.8) causes problems for Highway 101 along this stretch requiring frequent repaving of the highway. So, whilst large failure events are unlikely, small cumulative events

slowly build up causing damage to the road and infrastructure, including Spencer Creek bridge, which was recently constructed in 2008 costing $20.2 million US. Note that in winter 2024, emergency repairs were necessary due to slumping failures that occurred at this site.

Figure 3.8: Mass movement and infrastructure damage along Highway 101 at Spencer Creek, (facing south, near MP 134, August 2016).

Figure 3.9: Example coastal sea cliff failure at Spencer Creek (facing east, near MP 134, August 2016).

3.4 ARIZONA INN

The Arizona Inn landslide is located approximately 14.5 miles north of Gold Beach between Highway 101 MP 315 and 316. Figure 3.10 is taken from the landslide, looking down on the highway running parallel to the coastline, separated by a steep sea cliff.

The study area extends south from lookout rock about 650 m and extends landward around 350 m from Highway 101 to cover the Arizona Inn landslide. Moving landward, the site extends from a narrow sandy beach to a cobble/boulder beach about 10 m wide before reaching the sea cliff (Figure 3.11). The sea cliff at this site is around 50 m in height, sparsely vegetated at its base and more heavily vegetated towards the top where Highway 101 sits. East of Highway101, there is a large landslide around 120 m in height, and about 600 m wide.

Figure 3.10: Photograph showing Highway 101 running through Arizona Inn (facing south from the upper section of the landslide deposit). Note the freshly paved section as a repair to the creeping landslide movement (August 2016).

Figure 3.11: Photograph showing beach and coastal sea cliff at Arizona Inn (facing south, August 2017).

Arizona Inn's geology consists of the Humbug Mountain Conglomerate from the Elk Subterrane of the Western Klamath terrane that was deposited during the Lower Cretaceous and dips approximately 45˚southwest (McClaughry et al., 2013). Towards the coast this deposit is overlain by landslide deposits, which includes quaternary deposits and surficial anthropogenic materials (compacted fill, asphalt) that have been dislocated from prior landslide movements. . Below the Humbug Mountain Conglomerate there is Colebrooke Schist from the Pickett Peak terrane from the Upper Jurassic. At this location Elk subterrane has been thrust on top of the Pickett Peak terrane. This is evident from the thrust sheet window present at higher elevations to the east (McClaughry et al., 2013), as well as core logging conducted along the landslide. The southern extent of the landslide is bounded by a planar shear surface that forms the north face of a large rock mass that forms the headland in the south, which also bounds the landslide below the ground (Squier et al., 1994).

Arizona Inn failed catastrophically in 1993, closing Highway 101 for 2 weeks (Squier et al., 1994). Aside from catastrophic failures, Arizona Inn exhibits creep style mass movement that results in small but cumulative damage that builds up over time. Large Catastrophic failures generally correlate with large rainfall events similar to much of Oregon (Squier et al., 1994). Additionally, a large failure occurred in January 2023, resulting in a closure of nearly a week at this site. Section 12.0 provides more information on this failure and analysis of the monitoring data.

3.5 HOOSKANADEN

Hooskanaden is the southernmost site and is located approximately 13 miles SSE of Gold Beach, just north of milepost 344 on Highway 101. Figure 3.12 shows an overview of the site with Highway 101 running parallel to the coastline. The study area at this location extends from the intersection of Hooskanaden Creek and Highway 101 NNW around 850 m and from Highway 101 around 450 m E-SE to the coast. Moving landward, the study area extends from a wide pebble/cobble beach (Figure 3.13) to a coastal sea cliff around 10 m high in sections. On top of the sea cliff, a heavily vegitated landslide extends landward around 400 m W-NW horizontally and 60 m vertically before intersecting Highway 101.

The geology of Hooskanaden is composed of Marine Sedimentary rocks from the late Cretaceous period. This includes the Cape Sebastian sandstone as well as the Hunter Cove Formation (which includes sandstone, shale, and conglomerate) (Ramp et al., 1977). The south side of the landslide is loosely bounded by a SE-NW trending fault that cuts along the ridgeline extending NW from the Hooskanaden Creek-Highway 101 intersection (Ramp et al., 1977). Within the landslide the Marine Sedimentary rocks previously mentioned have been heavily displaced and intermixed from various fault and shear zones existing in the area (Mohney & Raker, 2004).

Figure 3.12: Overview photograph of the Hooskanaden site (facing south, August 2016).

Figure 3.13: Picture showing beach and coastal sea cliff at Hooskanaden, taken facing north (August 2016).

The Hooskanaden slide has always challenged Highway 101. Despite poor quality fill soil availability on the southern Oregon Coast, constructors recognized the site as unstable and built an embankment, rather than a bridge, over the adjacent Hooskanaden Creek. While Carpenterville Road, unsigned Oregon Route 255, presents some sense of an alternate route to Highway 101 during road closures at the Hooskanaden slide, the road routinely suffers from landslides causing single lane or entire road closures during the winter season. Even in other seasons, the road is steep, narrow, and has sharp curves, meaning that travel is slow and not feasible for some highway traffic.

A large surge event occurred in February 2019 at Hooskanaden, resulting in an extended closure and reduced capacity for a substantial period of time. This event is described in Section 11.0 of the report with analyses from the monitoring data.

4.0 SURVEY DATA COLLECTION

This chapter summarizes the data collected as part of this research project. Additional details of the methodology are described in Appendix A.

4.1 PLANNING

Execution of surveys required substantial planning to work around environmental challenges (e.g., precipitation, wind, and tides). Surveys were completed twice a year: a Spring survey in May/June and a fall survey in September/October to help capture winter and summer erosion trends. Initial plans were developed months ahead of the survey to ensure adequate staffing; however, those plans often required adaptation given the current environmental conditions.

4.2 DATA COLLECTION

As set out in the research methodology (Appendix A), bi-annual lidar surveys were conducted at all five sites during the fall and spring seasons in order to capture data relating to changes over the summer (expected accretion) and winter (expected erosion) months. These data collection procedures were based on those developed by Olsen et al. (2009, 2011). Generally, the field work for each site generally consisted of the following:

1. Perform safety briefing on site to discuss potential hazards and ensure all team members are aware of emergency protocols.

2. Set up safety signs when working near the roadway.

3. Setup of a GNSS base station on an established control point for each site. The GNSS base was set to log data at a 1-second epoch rate.

4. Capture of 360-degree scans spaced approximately 30 m apart along the cliff face, roadway, or atop the slide. A scanner with high accuracy level compensators or inclination sensors was used.

5. A GNSS rover was mounted above the scanner with a calibrated offset to capture X, Y, Z coordinates for the scanner location to support the geo-referencing.

6. Additionally, a total station was deployed at some sites for higher accuracy monitoring. The total station was not used at Spencer Creek due to safety issues given then the high traffic, narrow shoulders, and steep drop-off. At the south coast sites, total station surveys could not be continued due to loss of monitoring pins during maintenance operations.

Table 4.1 through Table 4.5 summarize the survey work conducted at each site. Data processing included backup, georeferencing, exporting to standard pointcloud formats (.las or .e57), and cropping to the area of interest. Given the volatile environment surveyed in this project, there are some small gaps/missing data at some of the sites, especially in the beginning of the project when some of the methods and field plan were still being refined. This information, along with

survey dates and types are summarized in the tables below as well as outlined in the following sections.

In order to maintain consistent data collection throughout the seven-year project, at the onset of the project, site plan posters summarizing the specific data collection to take place at each site were created. These plan posters contain useful information such as: scan position locations, GNSS base station setup positions, total station setup positions, total station survey markers, current and new MEMs sensor positions, and other useful logistical information about each site. These posters can be found in Figure 4.2 through Figure 4.6 for the sites studied.

Note that equipment utilized changed throughout the project given its duration. Several scanners and drone systems were employed. Note that while there are some differences in these systems, care was taken in the planning and implementation to ensure that the resulting point clouds and imagery products were consistent between the epochs.

The scanners utilized include:

- Riegl VZ-400. A long range (600 m), efficient scanner (125,000 points per second). The scanner could be mounted to a wagon and only approximate (within a few degrees) leveling is needed. The scanner utilizes an external camera. The scanner was damaged during one of the surveys at Arch Cape. It was repaired a few times; however, it ultimately was no longer economical to repair and was retired during the project. The scanner has a calibrated GNSS mount.

- Leica P40/P50. The Leica P40 (maximum range: 270 m) was upgraded to a Leica P50 (maximum range 1 km) during the project. The scanning process is very efficient (1 million points per second); however, photographic images were not acquired as those take substantial time to capture (~8 minutes per scan). The scanner has a calibrated GNSS mount (Figure 4.1).

- Leica BLK360. This scanner is a very small, portable scanner, which is advantageous in coastal environments with wet, slippery terrain. However, the range is limited to 65 m. It was used on a few surveys to fill in gaps between the longer-range scans. The scanner does not have a calibrated GNSS mount so it required additional processing to manually estimate its position and orientation relative to the other scans. Given the narrow range of the scanner, this was sometimes a challenging task.

- Leica RTC360. This close-range scanner (65 m at high resolution, 130 m at medium resolution) is relatively compact, easy to transport, and extremely efficient (2 million points per second). It can capture a full 360-degree scan and photograph within 3 minutes. A custom GNSS mount was designed and utilized so that the scanner could be employed with the same efficient workflow.

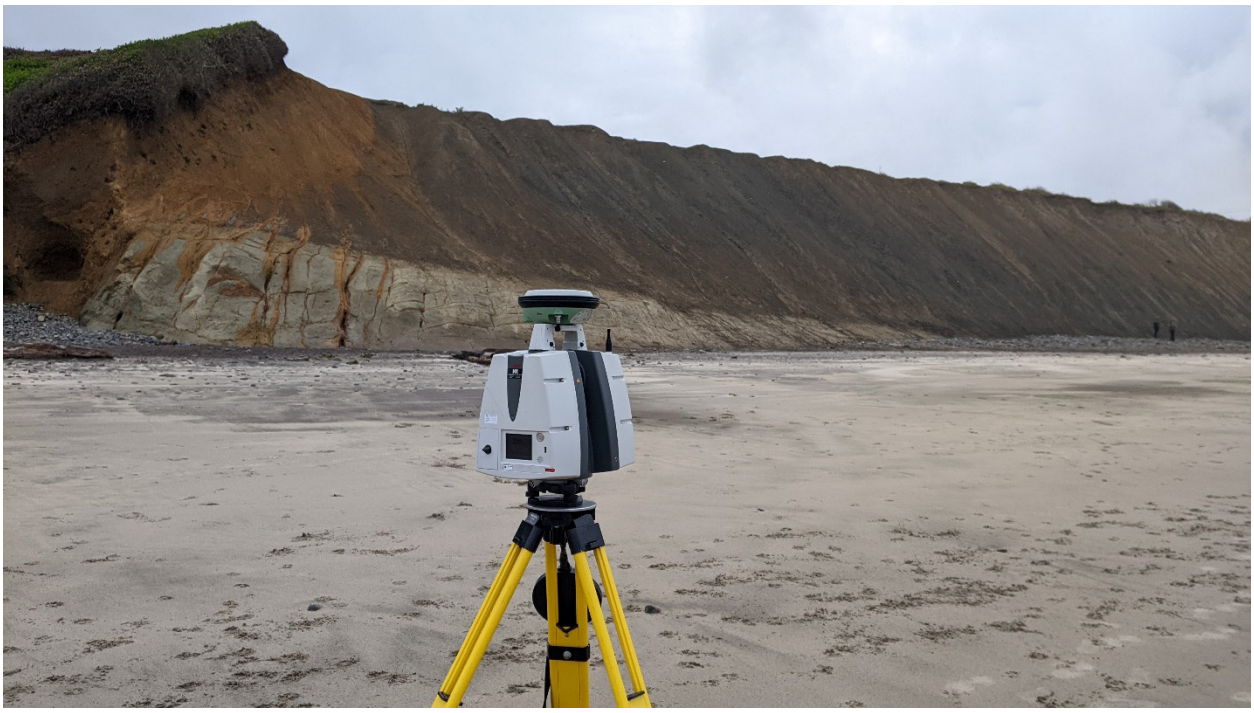

Figure 4.1: Example terrestrial laser scan setup with GNSS sensor for georeferencing.

The following UAS systems were deployed for some of the surveys, particularly for the larger south coast sites. Note that the use of UAS technology evolved substantially over the course of the project, particularly with the introduction of RTK systems. (UAS technology was in its infancy when the project started). Prior to the RTK systems, a substantial amount of ground control points was necessary, which require a substantial amount of field effort to place and obtain coordinates.

- Sensefly Alibris. This unit was deployed as a proof of concept to capture data on the sea cliffs at Arizona Inn. However, it was a challenge to fly this system at this site given the difficulty in estimating its height above water when capturing the cliff given the steep dropoff.

- Phoenix MiniRanger UAS lidar system. This unit was deployed by the NSF NHERI RAPID Facility at the University of Washington several times at the south coast landslide sites of Hooskanaden and Arizona Inn to improve spatial coverage and resolution.

- DJI Phantom 4 Pro RTK. The DJI P4P RTK unit was deployed at most south coast surveys starting in June 2020. This system substantially reduced the number of control points required, resulting in efficient surveys, particularly for those acquired during the Hooskanaden surge event. Notably, given some software errors, this system had issues logging photographic or GNSS data for some flights performed. The data were checked in the field to the extent possible to minimize data loss.

4.2.1 Silver Point

Table 4.1: Summary of data collected and processed at Silver Point.

		Silver Point		
Survey Epoch	**Survey Date**	**Scanner Used**	**Total Station**	**Comment**
2016 Fall	09/07/2016	VZ-400		
2017 Spring	06/01/2017	VZ-400	X	
2017 Fall	10/09/2017	VZ-400	X	SP12 missing GNSS coordinates.
2018 Spring	05/17/2018	VZ-400, BLK360		Total station malfunction
2018 Fall	10/09/2018	VZ-400	X	
2019 Spring	05/09/2019	VZ-400	X	No RGB in scans due to camera malfunction.
2019 Fall	9/28/2019 10/14/2019	VZ-400	X	Only scans and total station data were captured for the 09/28/2019 survey (i.e., no GNSS base station data, no GNSS mount for VZ-400 data). Scans with GNSS were conducted on 10/14/2019 to correct the issues with missing data.
2020 Spring	06/03/2020	VZ-400	X	
2020 Fall	10/01/2020	VZ-400		
2021 Spring	06/21/2021	VZ-400	X	
2021 Fall	09/27/2021	VZ-400		
2022 Spring	05/27/2022	P50	X	No RGB in scans
2022 Fall	09/27/2022	P50	X	No RGB in scans
2023 Spring	06/21/2023	P50, RTC360	X	No RGB in P50 scans. Prototype GNSS mount for RTC360 used.

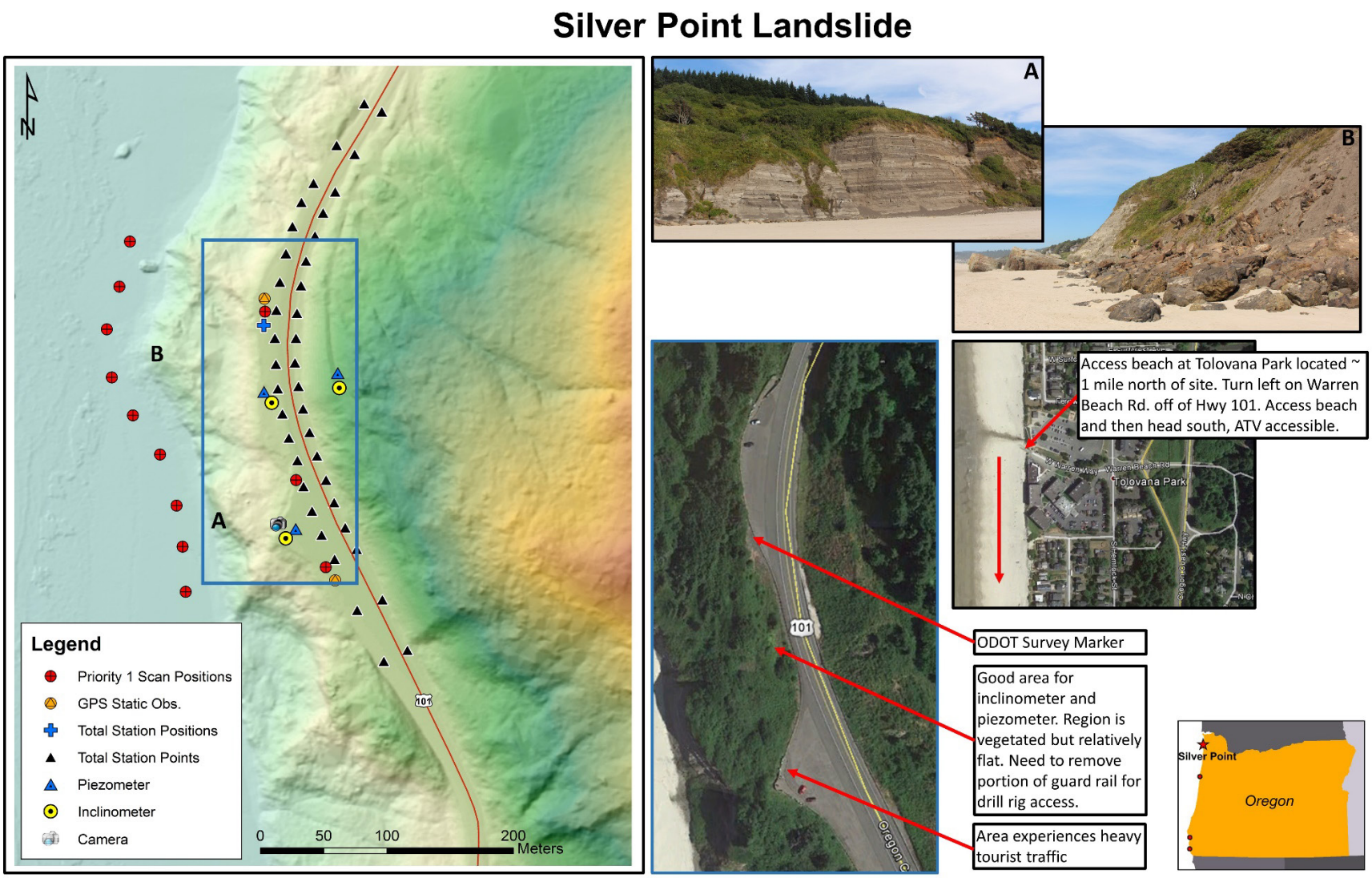

Figure 4.2: Site poster of Silver Point created displaying: Scan positions, GNSS base setup positions, total station setups and other useful information about the site.

4.2.2 Arch Cape

Table 4.2: Summary of data collected and processed at Arch Cape.

Arch Cape				
Survey Epoch	**Survey Date**	**Scanner Used**	**Total Station**	**Comment**
2016 Fall	09/07/2016	VZ-400	-	
2017 Spring	06/02/2017	VZ-400	X	Only five scans collected due to damage of the scanner during survey work.
2017 Fall	10/09/2017	VZ-400	X	Only one scan was collected due to damage of the battery during survey work.
2018 Spring	05/18/2018	VZ-400, BLK360	-	Total Station malfunction.
2018 Fall	10/09/2018	VZ-400, BLK360	X	
2019 Spring	05/09/2019	VZ-400	X	No RGB in scans due to camera failure.
2019 Fall	09/29/2019, 10/15/2019	VZ-400	X	Only scans and total station data were captured for the 09/29/2019 survey (i.e., no GNSS base station data, no GNSS mount for VZ-400 data). Scans with GNSS were conducted on 10/15/2019 to correct the issues with missing data.
2020 Spring	06/03/2020	VZ-400	X	
2020 Fall	10/01/2020	VZ-400		
2021 Spring	06/22/2021	VZ-400	X	Too few pins were recoverable with the total station.
2021 Fall	09/27/2021	VZ-400		
2022 Spring	05/27/2022	P50		No RGB in scans
2022 Fall	09/26/2022	P50		No RGB in scans
2023 Spring	06/22/2023	P50, RTC360		No RGB in P50 scans. An initial prototype GNSS mount for the RTC360 was tested.

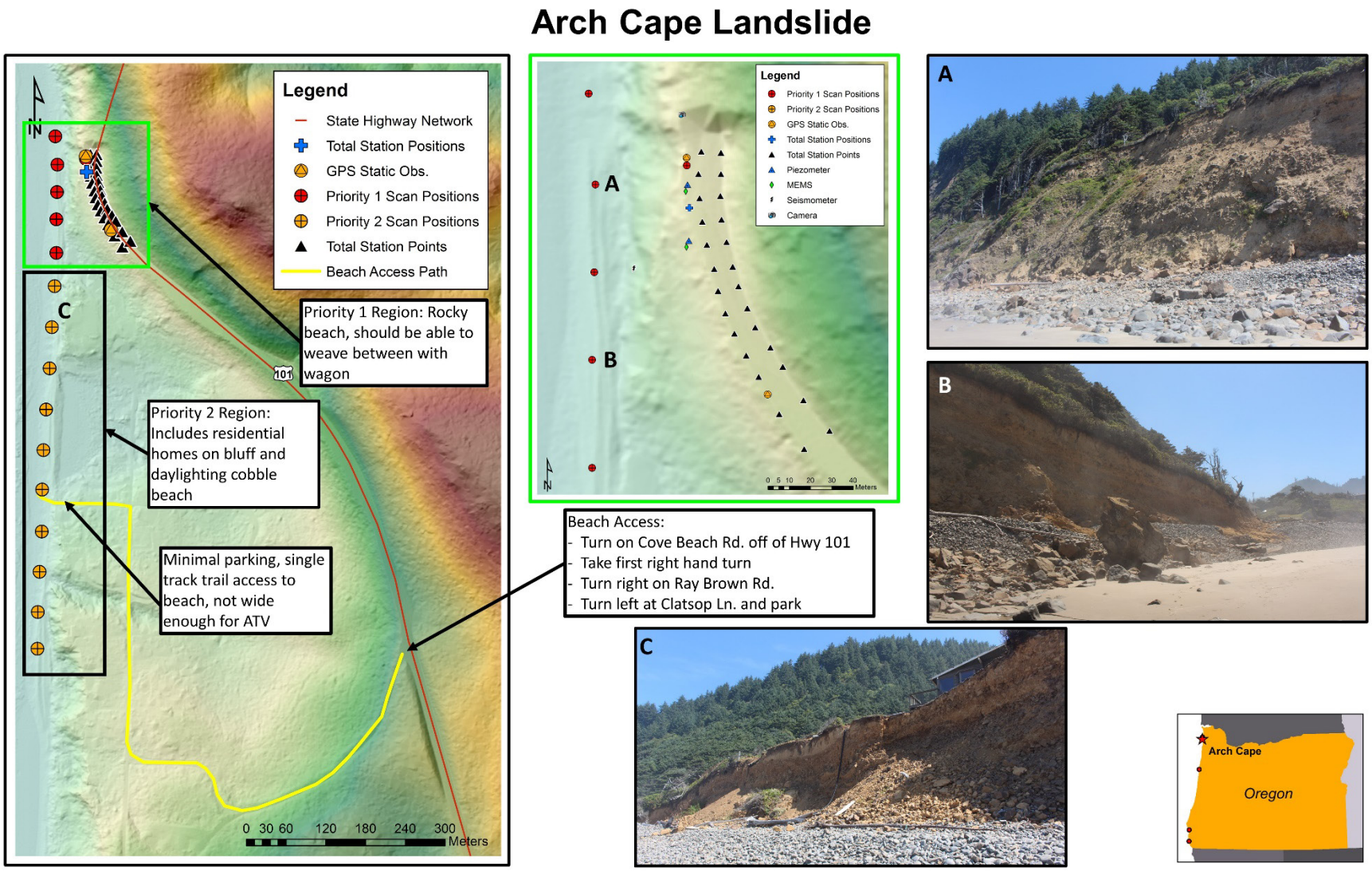

Figure 4.3: Site poster of Arch Cape created displaying: Scan positions, GNSS base setup positions, total station setups and other useful information about the site.

4.2.3 Spencer Creek

Table 4.3: Summary of data collected and processed at Spencer Creek.

Spencer Creek			
Survey Epoch	**Survey Date**	**Scanner Used**	**Comment**
2016 Fall	09/22/2016	VZ-400	
2017 Spring	05/08/2017	VZ-400	
2017 Fall	10/03/2017	VZ-400	
2018 Spring	05/16/2018	VZ-400	
2018 Fall	11/08/2018	VZ-400	
2019 Spring	05/31/2019	VZ-400	No RGB in scans
2019 Fall	10/10/2019	VZ-400	
2020 Spring	06/11/2020	VZ-400	
2020 Fall	09/16/2020	VZ-400	
2021 Spring	06/24/2021	VZ-400	
2021 Fall	09/29/2021	VZ-400	
2022 Spring	06/11/2022	P50	No RGB in scans
2022 Fall	10/14/2022	P50	No RGB in scans
2023 Spring	06/02/2023	RTC360	A prototype GNSS mount for the RTC360 was used.

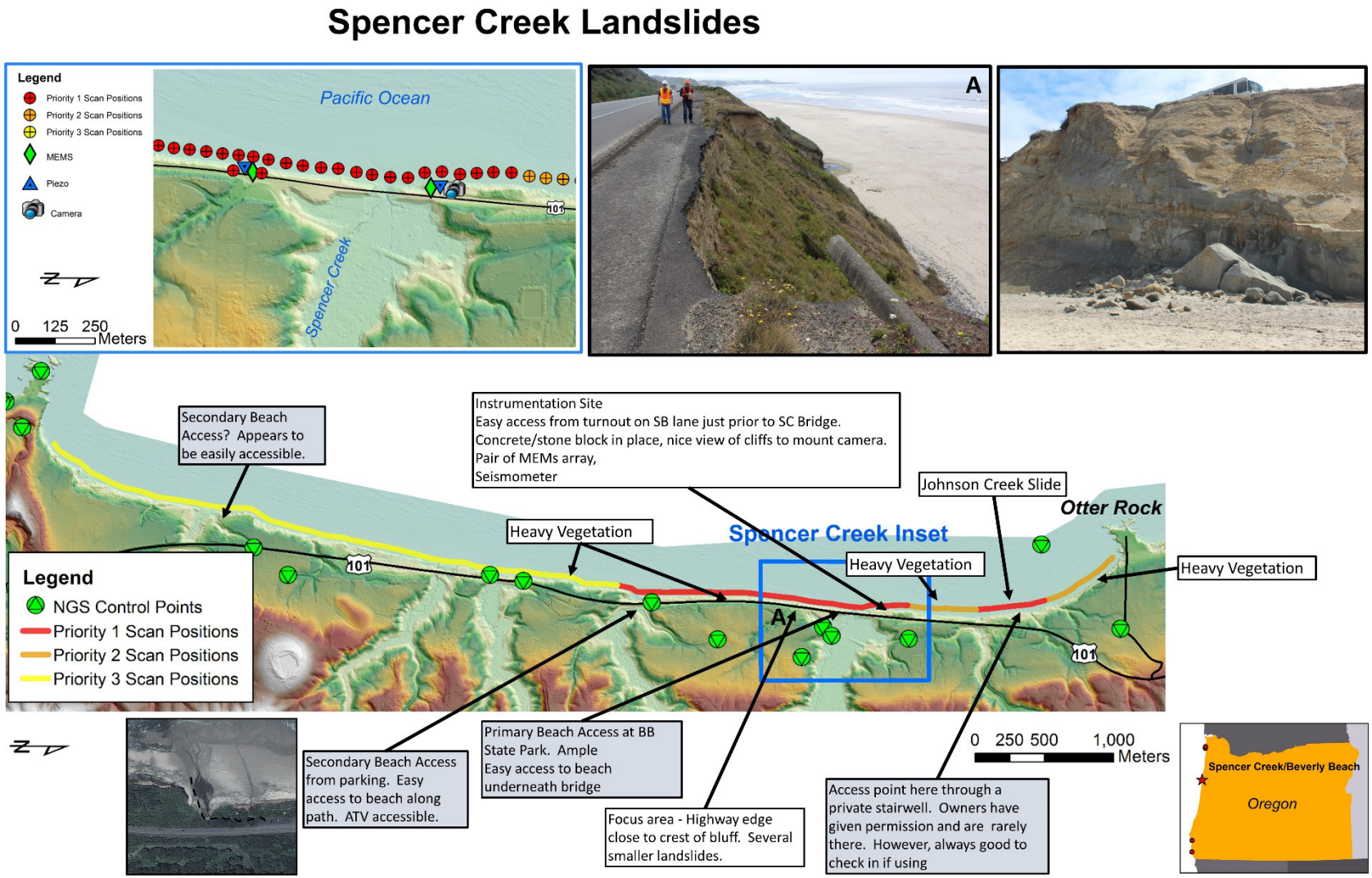

Figure 4.4: Site poster of Spencer Creek created displaying: Scan positions, MEM's positions and other useful information about the site.

4.2.4 Arizona Inn

Table 4.4: Summary of data collected and processed at Arizona Inn.

Arizona Inn				
Survey Epoch	**Survey Date**	**Sensors Used**	**Total Station**	**Comment**
2016 Fall	10/19/2016	VZ-400, Exom Alibris		
2017 Spring	06/14/2017	VZ-400	X	
2017 Fall	11/27/2017	VZ-400		
2018 Spring	06/18/2018	VZ-400	X	
2018 Fall	10/15/2018	VZ-400		
2019 Spring	06/24/2019	VZ-400, MiniRanger		No RGB in scans
2019 Fall	10/03/2019	VZ-400, DJI P4P		
2020 Spring	06/22/2020	VZ-400, DJI P4P		
2020 Fall	09/21/2020	VZ-400, MiniRanger		
2021 Spring	02/17/2021	DJI P4P		
	05/11/2021	MiniRanger		
	06/14/2021	P50, DJI P4P		No RGB in scans
2021 Fall	09/30/2021	P50, DJI P4P		No RGB in scans
2022 Spring	05/30/2022	P50, DJI P4P		No RGB in scans
2022 Fall	09/28/2022	P50, DJI P4P		No RGB in scans
2023 Spring	01/21/2023	DJI P4P		Special survey to capture the large landslide movements and fix RTK GNSS units installed on site.
	06/07/2023	P50, RTC360, DJI P4P MiniRanger		No RGB in P50 scans. Several P50 scans did not capture a full 360-degree field of view due to an improper setting on the scanner.

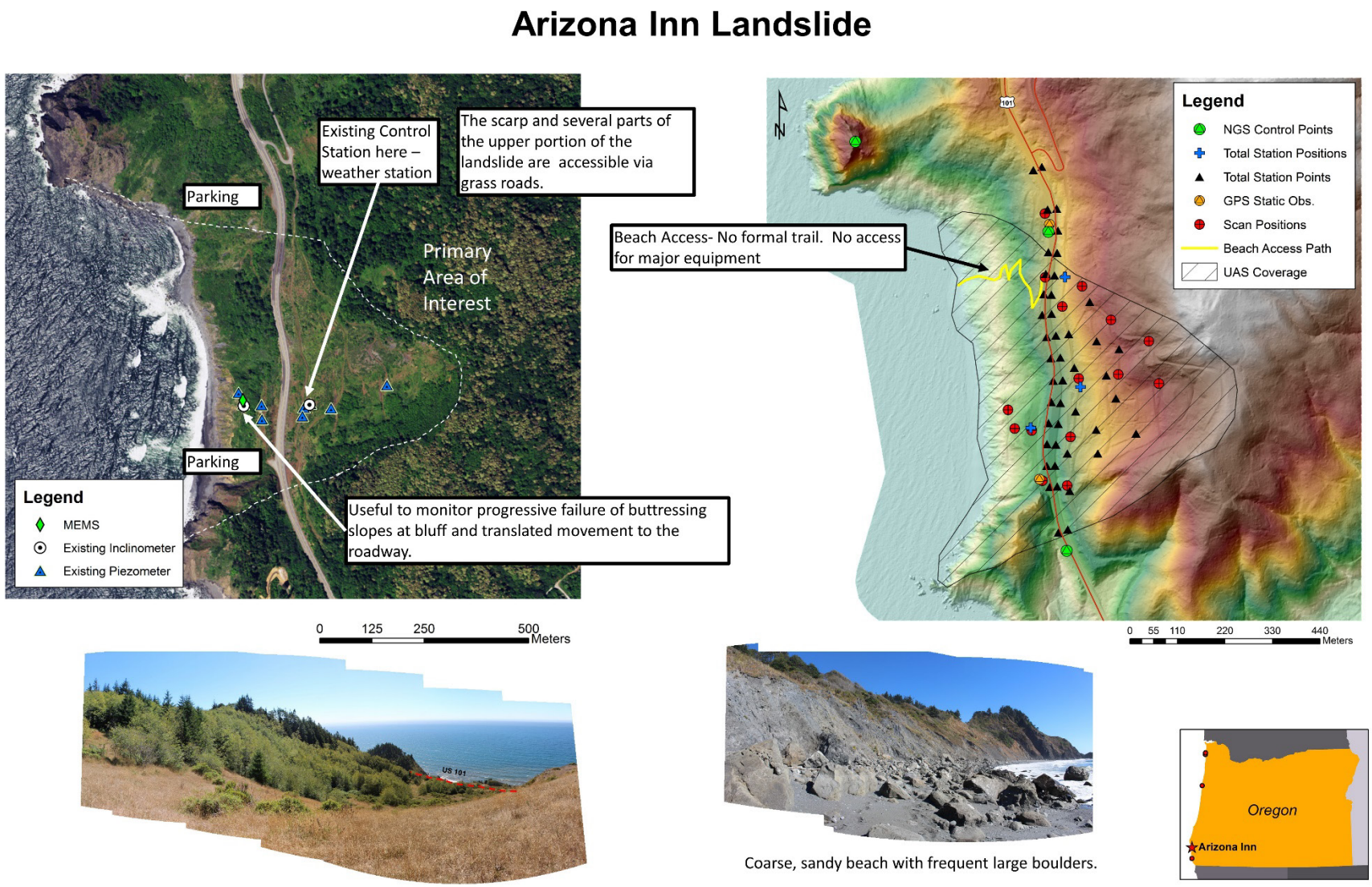

Figure 4.5: Site poster of Arizona Inn created displaying: Scan positions, GNSS base setup positions, total station setups and other useful information about the site.

4.2.5 Hooskanaden

Table 4.5: Summary of data collected and processed at Hooskanaden.

Hooskanaden				
Survey Epoch	**Survey Date**	**Scanner Used**	**Total Station**	**Comments**
2016 Fall	10/18/2016	VZ-400		
2017 Spring	06/12/2017	P40	X	
2017 Fall	11/28/2017	VZ-400	X	No Beach Scans
2018 Spring	06/19/2018	VZ-400	X	
2018 Fall	10/16/2018	VZ-400		
2019 Spring	03/02/2019	VZ-400, DJI P4P		No RGB in scans, No Beach Scans
	03/15/2019	VZ-400, MiniRanger		No RGB in scans
	06/24/2019	VZ-400, MiniRanger, DJI P4P		No RGB in scans
2019 Fall	10/04/2019	VZ-400, DJI P4P		
2020 Spring	06/23/2020	VZ-400, DJI P4P		
2020 Fall	09/22/2020	VZ-400, DJI P4P, MiniRanger		
2021 Spring	05/12/2021	MiniRanger		
	06/16/2021	VZ-400, DJI P4P		
2021 Fall	10/02/2021	P50, DJI P4P		No RGB in scans
2022 Spring	05/31/2022	P50, DJI P4P		No RGB in scans
2022 Fall	09/30/2022	P50, DJI P4P		No RGB in scans
2023 Spring	06/08/2023	P50, RTC360, DJI P4P		Several P50 scans did not capture a full 360 degree field of view due to an improper setting on the scanner. P50 scans were not captured with RGB.

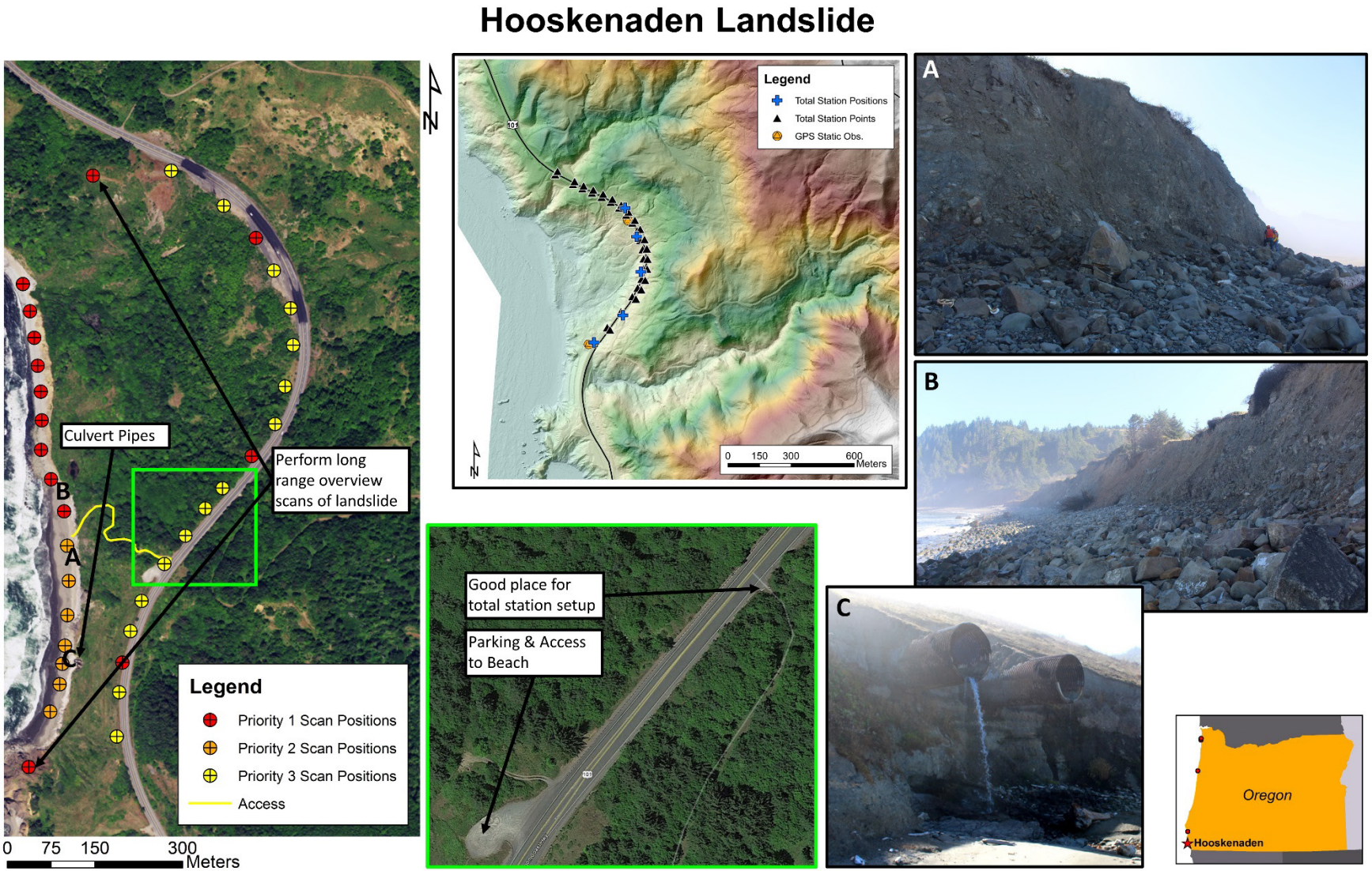

Figure 4.6: Site poster of Hooskanaden created displaying: Scan positions, GNSS base setup positions, total station setups and other useful information about the site.

4.3 ISSUES ENCOUNTERED

As mentioned above, several issues have periodically impeded field data collection during some surveys. Some of these issues have resulted in an adaptation and change to the original fieldwork plan outlined in the previously submitted methodology. Those are highlighted in section 4.4 below.

- In spring of 2017 there was an incident with carrying the Riegl VZ-400 at the Arch Cape site across slick rocks during the field survey which resulted in only five TLS scans being collected at this site, and the P40 TLS having to be used at other sites for this epoch.

- In fall of 2017 a sneaker wave damaged the battery being used to power the Riegl VZ-400 at the Arch Cape site during the field survey and as a result no beach scans were collected. Also a large swell occurred during the Hooskanaden survey, rendering the beach inaccessible to the survey crew.

- In spring of 2018 a malfunction occurred with the total station during the north coast surveys (Arch Cape and Silver Point); hence, no total station measurements were obtained.

- In spring of 2019, the camera connection port for the Riegl VZ-400 malfunctioned, and as a result none of the scans surveyed in the spring 2019 epoch contain RGB values. In summer of 2019 the Riegl VZ-400 and camera were sent to the manufacturer for repair, maintenance, and re-calibration. Full operation was restored for the Fall 2019 surveys.

- Total station observations were discontinued at the faster moving landslide sites (Arizona Inn and Hooskanaden) after Spring 2018. Given the frequent repairs and maintenance at the site, the hubs used for monitoring were frequently lost. However, many objects such as telephone poles and guardrails serve as similar reference points and movements can be extracted from the TLS data.

- In the Spring 2023 surveys, an operator error resulted in the Leica P50 scans only capturing a 180-degree field of view instead of the full 360-degree field of view. The registration process was adapted to include the UAS SfM/MVS derived point clouds to compensate for the inconsistent overlap between scans.

4.4 MODIFICATIONS TO THE FIELD COLLECTION PLAN

During the course of the 7-year monitoring project, several factors necessitated modification to the initial field collection plan. These factors include: (1) evolution of technology, including faster, more accurate scanners with a smaller form to facilitate efficient data capture, as well as software improvements (2) substantial advancements to UAS and SfM/MvS photogrammetric technologies, enabling efficient coverage over large areas, (3) loss of survey pins during maintenance activities, and (4) damages to equipment during field work as a result of operation on the precarious terrain.

4.4.1 Scanner modifications

As a result of the narrow beach issues encountered at the Arch Cape and Hooskanaden, the BLK360 TLS was utilized for some surveys at these sites to collect data in conjunction with the Riegl VZ-400 when the tide results in a narrow beach during field work (Figure 4.7). The BLK provided the following benefits (1): fewer scans are required with the bulkier, more expensive VZ-400 which reduces the operation time in the hazardous tidal zone; (2), scans can be conducted at closer spacing and closer the sea cliff and farther from the waves without dramatically increasing the survey duration; and (3) light weight and simple setup of the BLK (no external batteries) allows it to be easily removed from harm's way in the event of a sneaker wave or other situation.

The BLK360 scans are registered to the Riegl VZ-400 scans (which are constrained to RTK GNSS positions) during processing using a cloud-to-cloud registration algorithm in order to georeferenced the scans. This process has been outlined in depth in an updated version of the methodology. Note that while the BLK scanner was easy to operate in the field, the registration process of combining the BLK scans with the longer-range scans was somewhat challenging given the limited range and field of view. Hence, subsequent surveys continued with using the longer-range scanner at the original spacing intervals.

Several years into the project, the Riegl VZ-400 scanner required frequent maintenance and repair given that its age and amount of use. Hence, the Leica P40/P50 was utilized to continue the field work. At the conclusion of the project, the Leica RTC360 laser scanner with a custom GNSS mount was introduced for highly efficient surveys of the coastline.

4.4.2 Introduction of UAS technology

At the two south coast sites (Arizona Inn and Hooskanaden) problems have been encountered with the envisioned total station – road alignment survey strategy. While this part of the project was not outlined in the original workplan, plans were made to conduct these measurements at the south coast (Arizona Inn and Hooskanaden) and north coast (Arch Cape and Silver Point) sites in order to track any movements in the road at a more precise level than TLS scans as well as provide validation of movements observed in the TLS data. Given the rapid movement of the south coast landslides, the road surfaces are continually repaved, resulting in frequent removal of PK nail control points that were set to monitor the road. As a result, most of these markers are lost before they can be resurveyed. Any replacement PK nails are also quickly removed. However, given the large changes taking place at these sites and the overall success of the TLS surveys, the decision was made to remove this part of the survey from the south coast sites and spend more time conducting extra TLS scans. Additional scans are now performed on the upper portion of the Hooskanaden landslide and the Arizona Inn landslide. Lastly, to further supplement the data collection at these active sites, in later surveys, additional UAS SfM/MVS photogrammetric data were collected at the south coastal sites, predominately with a DJI Phantom 4 Pro (P4P) UAS system. The UAS system enabled the capture of high resolution orthomosaics across the entire slide as well as the capability to generate SfM/MVS photogrammetric point clouds that can be combined with the TLS data to model the site.

Figure 4.7: Photograph of the BLK360 TLS (terrestrial laser scanner) being used to survey the sea cliff at the Hooskanaden beach during the bi-annual field survey on October 4, 2019.

4.5 UAS LIDAR AND SFM/MVS SURVEYS

After the destructive Hooskanaden landslide event in February 2019, we quickly mobilized to the site and conducted repeat TLS scans (Figure 4.8) and UAS SfM/MVS photogrammetric flights on the actively moving landslide on the weekend of March 2, 2019. Several weeks later the OSU team collaborated with the NSF Natural Hazards Research Infrastructure (NHERI) RAPID Facility team at the University of Washington to conduct UAS lidar surveys at Hooskanaden using their Phoenix miniRanger UAS lidar system (Figure 4.9) as well as collect additional TLS scans to serve as validation. This survey was conducted on the weekend of March 15, 2019. These surveys were conducted as bonus surveys to provide data associated with the Hooskanaden landslide event (Figure 4.10). An additional UAS lidar survey was performed later during the regular spring survey (week of June 24, 2019). This was also performed in collaboration with the RAPID Facility with flights conducted at both the Arizona Inn and Hooskanaden sites. Additional UAS SfM/MVS photogrammetric flights were conducted using the DJI Phantom 4 pro as well as the regular TLS survey. Analysis from data associated with the Hooskanaden landslide event as well as UAS lidar data is described in Section 11.0.

Figure 4.8: Photograph of Riegl VZ-400 TLS setup to conduct high resolution repeat scans of the actively moving Hooskanaden landslide on March 2, 2019.

Figure 4.9: Photograph capturing the RAPID Facility's phoenix lidar miniRanger UAS lidar system being operated at the Hooskanaden landslide on March 15, 2019. Photo Credit: Nick Mathews (OSU).

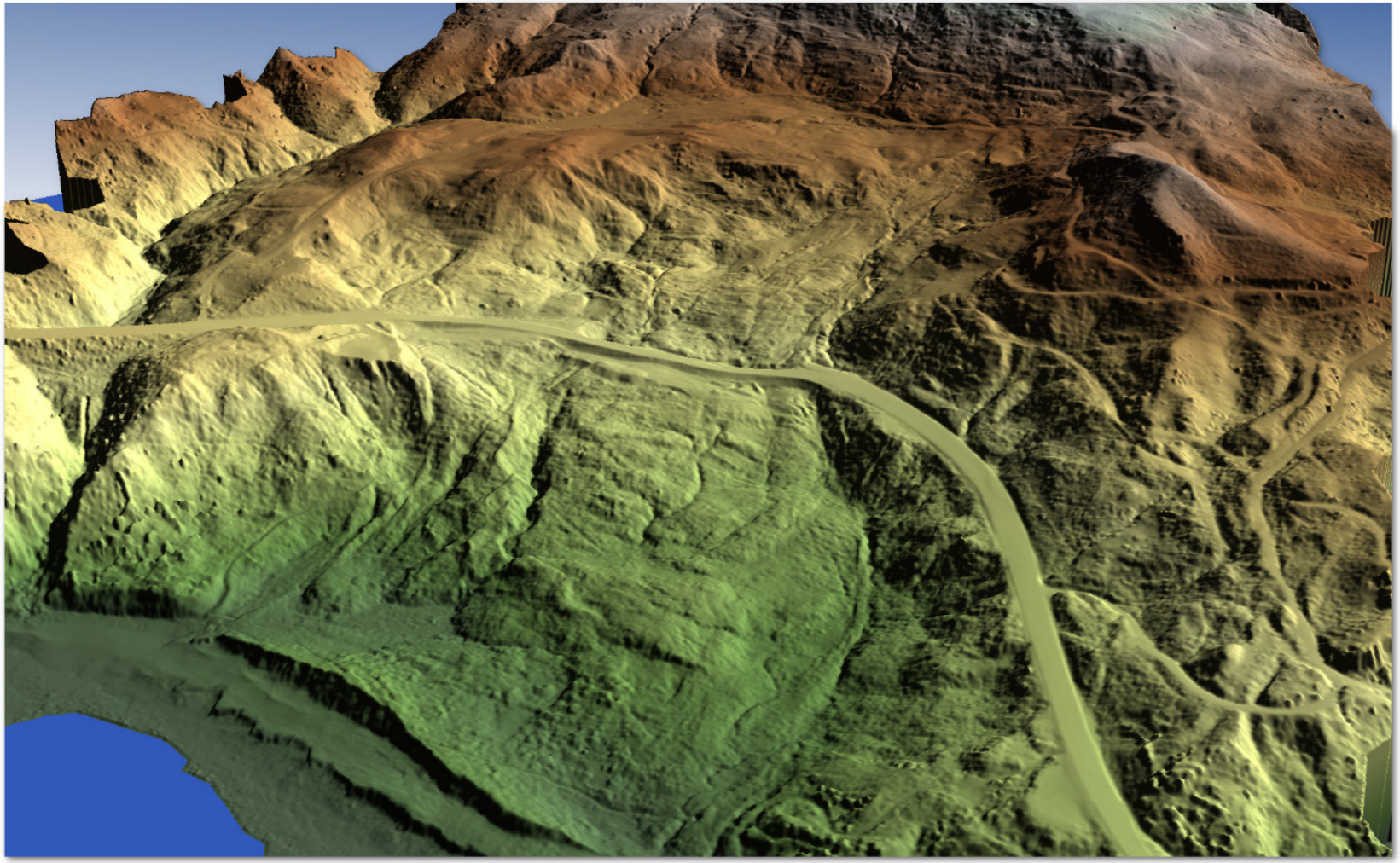

Figure 4.10: Example 3D view of the final 0.5m DEM created from data collected by the UAS lidar survey conducted at the Hooskanaden landslide from March 15, 2019. (Image Credit: Benjamin Babbel (OSU)).

5.0 SURVEY DATA PROCESSING

This section provides a brief summary of data processing procedures. The reader is referred to Appendix A for more specific details of the workflow.

5.1 GEOREFERENCING

Data collected in the field were georeferenced into the OCRS Coastal Zone NAD83(2011) Epoch 2010.00 with elevations referenced to Geoid12B. The raw data from the GNSS base station were processed using the NGS Online User Positioning Service (OPUS). Leica infinity software was then used to process the GNSS data collected at the GNSS rover at the scan locations. These data were then used as constraints in the software registration.

Depending on the scanners utilized two similar workflows were executed:

- For surveys completed with the Riegl VZ-400 scanner, Riegl Riscan Pro software was used to perform a coarse registration of the software. Then PointReg (Olsen et al., 2009, 2011, 2013) was used to refine the azimuth of the scanner as well as the elevation of the scanner in a least squares adjustment. The X and Y position of the scanner remained fixed to the GNSS coordinates. The leveling also remained fixed to the scanner inclination sensor readings.

- For surveys completed with the Leica P40/P50 or Leica RTC360, the registration was performed in Lecia Cyclone software with the GNSS coordinates used as constraints in conjunction with cloud-to-cloud surface matching. The scans were constrained to be level based on the level compensation performed during the scan.

For UAS surveys, data processing was completed in Agisoft Metashape or Bentley Context Capture software. Point clouds, orthophotos, and digital surface models were created.

5.2 CLIFF EXTRACTION

Once scans were georeferenced, each scan was filtered based on a polygon outlining the cliff face using either CloudCompare, Leica Cyclone, or Maptek PointStudio software. The scans were then cleaned to remove extraneous noise from moisture. The Rambo software (Olsen et al., 2021) was used to remove vegetation from the cliff face.

5.3 EROSION ANALYSIS

This section describes the change analysis to evaluate erosional trends. A more detailed description of the change analysis is provided in Senogles (2023). Section 11.0 outlines the analysis methods for evaluating landslide displacements over time.

Erosional change analysis was primarily completed in the Rambo software (Olsen et al., 2021) for erosion analysis and SlideSim\LADI for landslide analysis. Multiple data epochs could be

analyzed in a single session. The resulting output files could then be used for the visualizations and statistical analysis (e.g., Section 8.0).

Change analyses were carried out on an intersurvey and interannual (using the Fall surveys) basis to compute both the seasonal (winter/spring) and annual erosion rates. Each point cloud was mapped to a 0.1 m grid using the best-fit plane and grid structure of the first survey epoch at each site. Change was computed by differencing each subsequent epoch of data across this grid (Olsen et al., 2015). A significant change threshold of 0.05 m was used at each site to reduce the effect of georeferencing errors on the final results based on average RMS values derived during registration.

Additionally, the total volume loss (cumulative volume change of all cells that experienced significant erosion) was computed for each intersurvey (period between subsequent survey epochs) and each subsection of sea cliff to further distill overall erosion. When applicable, the volume loss was normalized by time between survey epochs and by surface area of the cliff/subsection to allow for a more direct comparison across site morphologies and scopes. For each change period, erosional clusters were mapped using a connected components algorithm (Olsen et al., 2015) to allow for calculating the distribution of failure magnitudes for each change epoch.

To relate the measured cliff response to different processes, an erosion zone classification system was developed. In this classification system, conceptually, the cliff is classified into three erosional zones that enable contrasting controls on erosion to be evaluated, including: scour, transition, and subaerial zones for each change epoch. The scour zone encompasses all parts of the cliff that were directly impacted by wave scour for a given change period, defined as the region at or beneath the elevation of the maximum TWL (See Section 7.0 for calculation methods). The transition zone covers those parts of the sea cliff directly above the scour zone that are indirectly impacted by wave scour – i.e. experience cliff retreat due to undercutting, slumping, or other mechanisms driven by toe instability caused by wave scour. The subaerial zone encompasses areas of the cliff directly above the transition zone that experience retreat predominantly due to subaerial weathering processes.

This erosion zone classification system was implemented as outlined in Figure 5.1 to classify the change grid point clouds. Firstly, using the calculated TWLs (Section 7.1) for each site, points equal to or below the maximum TWL for the given change epoch were classified as part of the scour zone, since it is assumed that these points were subject to wave scour during the intersurvey period. The connected components algorithm was used to cluster significant change cells that were connected either horizontally, or vertically. The clusters were mapped back to the original pre-change point cloud, where points above the maximum TWL that belonged to the same cluster as one or more points at, or below the maximum TWL were classified as part of the transition zone. Additionally, any point directly below another point in the transition zone was also classified as part of the transition zone. This results in the top of the transition zone for a given subsection of sea cliff being defined as the top of a change cluster that is bisected by the maximum TWL. Any remaining points above the transition zone were assigned to the subaerial weathering zone.

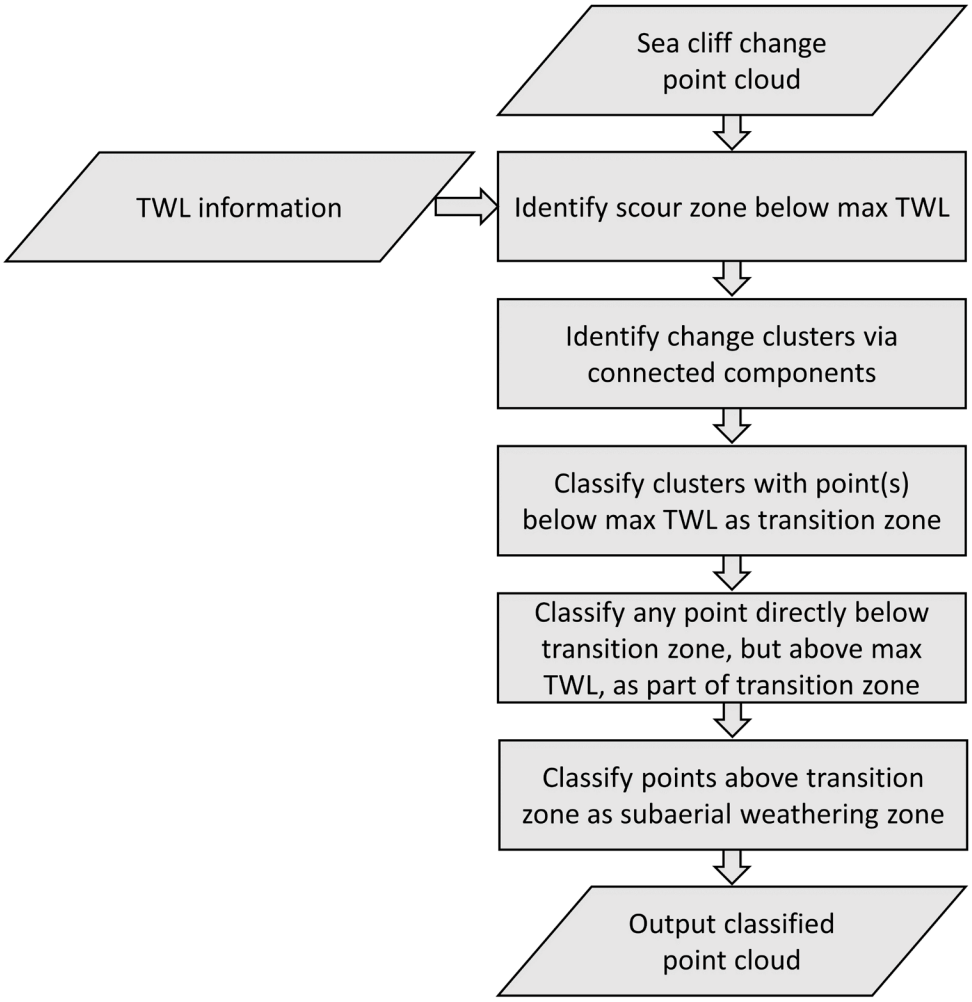

Figure 5.1: Flow chart detailing the erosion zone classification scheme used to spatially classify the point cloud for each change epoch.

To assess the correlation between driving factors (wave energy, precipitation) and volume losses for each of the erosional zones, Kendall's correlation coefficient (τ) (Kendall, 1938) was used. Kendall's correlation coefficient was chosen since it is non-parametric, and evaluates correlation based on a monotonic relationship. Unlike Spearman's correlation coefficient, Kendall's τ is more interpretable (based on the probabilities of observing concordant and discordant pairs), and is generally considered more robust, less sensitive to error, and with more accurate p-values for smaller datasets (Gilpin, 1993; Newson, 2002; Xu et al., 2013). P-values were computed to test the null hypothesis for each corresponding pair of driving factors and volume loss, a p-value of 0.05 was used as the threshold for statistical significance.

6.0 ENVIRONMENTAL FACTORS STATISTICAL ANALYSIS

6.1 METHODOLOGY

Hourly deep-water wave heights, and peak periods were retrieved from nearby buoys. For Spencer Creek, the Stonewall Bank NDBC (national data buoy center) buoy was used, which is approximately 38 km WSW of Spencer Creek. The Astoria Canyon CDIP (coastal data information program) was used for Silver Point and Arch Cape, which is approximately 61 km and 64 km NW of each site respectively. Note that the Astoria Canyon buoy experienced a 44-day outage in 2019, for this period, the nearby Columbia River NDBC (~12 km east of the Astoria Canyon buoy) buoy was used to infill missing data.

Tidal data were retrieved from nearby tide gauges. For Spencer Creek, the South Beach tide gauge was used, which is approximately 23 km south of Spencer Creek. The Astoria tidal gauge was used for Silver Point and Arch Cape, which is approximately 42 km and 48km north of each site respectively. An average beach slope was computed for each epoch for each site using a gradient approximation method (Zevenbergen & Thorne, 1987) applied across a 5x5 m window of a DEM created with RAMBO from the TLS point cloud data of the beach.

From these datasets, the height of the 2% exceedance value of wave runups ($R_{2\%}$) were calculated using the deepwater wave height (H_O), peak period (L_O), and beach slope (θ_B) measurements and the empirically derived constant as shown in Equation 6-1 (Stockdon et al., 2006):

$$\boldsymbol{R_{2\%} = 1.1\left(0.35\tan\beta\,(H_oL_o)^{\frac{1}{2}} + \frac{[H_oL_o(0.563\tan\beta^2 + 0.004)]^{\frac{1}{2}}}{2}\right)} \quad \textbf{(6-1)}$$

$R_{2\%}$ was then combined with the tidal elevation measured from the tidal data to yield the hourly TWL (total water level) at each site. Using the TWL, various metrics were computed between subsequent survey epochs. Wave contact hours (WCH) were computed as the summation of the total number of hours that the TWL exceeded the elevation of the sea cliff toe for the given change period. The elevation of the sea cliff toe (H_{Toe}) was computed for each site by computing the mean elevation of toe points spaced 0.1 m apart laterally across the sea cliff (Table 6.1). Hourly wave energy densities (E_d) were then computed as shown in Equation 6-2 (Splinter et al., 2014):

$$\boldsymbol{E_d = \frac{1}{8}\rho g {H_s}^2} \quad \textbf{(6-2)}$$

where ρ is density of seawater, and g is gravity. The wave energy density was then used to compute the total wave energy (E) that impacted the sea cliff between each epoch as shown in Equation 6-3:

$$f(E_d, TWL) = \begin{cases} E_d(TWL - H_{Toe}), & TWL > H_{Toe} \\ 0, & TWL \leq H_{Toe} \end{cases} \quad \textbf{(6-3)}$$

$$E = \sum_{i=0}^{N} f(E_{di}, TWL_i) \quad \textbf{(6-4)}$$

Equation 6-4 yields the total wave energy in contact with the sea cliff for each change period.

Table 6.1: Summary of site morphology for each of the four sites. LC = length of sea cliff, HC = height of sea cliff, θC = slope of sea cliff, AC = aspect of sea cliff, HToe = height of sea cliff toe, and θB = slope of beach.

Site	L_C (m)	H_C (m)	θ_C (deg)	A_C (deg)	H_{Toe} (m)	θ_B (deg)	Beach material	Geologic summary
Arch Cape	140	3 - 35	50 - 75	267	7.2	11.3	Cobble/boulder berm	weakly-lithified landslide deposits
Silver Point	250	5 - 25	45 - 75	261	5.2	3.0	Sand with loose cobble/boulders in sections	Landslide deposits mixed with basalt, and sandstone in south
Spencer Creek North	350	8 - 30	35 - 50	270	5.2	2.2	Sand	Estuarine deposits and siltstone/sandstone from the Astoria formation
Spencer Creek South	550	10 - 17	40 - 60	275	4.5	2.3	Sand	Estuarine deposits and siltstone/sandstone from the Astoria formation

Spatially-modelled daily precipitation data for each site were retrieved from PRISM (*PRISM Climate Group*) for the period from August 1, 2016 through July 31, 2022. Using these data, several metrics were computed between subsequent survey epochs: cumulative, maximum 48-hour, weekly, and monthly precipitation. These metrics enabled correlations to be drawn between both the total precipitation experienced, as well as a variety of proxies for precipitation intensity and its control on overall sea cliff erosion trends observed.

To robustly evaluate the correlation between driving factors (wave energy, precipitation) and volume loss both overall, and for each of the erosional zone, Kendall's correlation coefficient (τ) (Kendall, 1938) was used. Kendall's correlation coefficient was chosen because it is non-parametric, and evaluates correlation based on a monotonic relationship. Unlike Spearman's correlation coefficient, Kendall's τ is more interpretable (based on the probabilities of observing concordant and discordant pairs), and is generally considered more robust, less sensitive to error, and with more accurate p-values for smaller datasets (Gilpin, 1993; Newson, 2002; Xu et al.,

2013). P-values were computed to test the null hypothesis for each corresponding pair of driving factors and volume loss, a p-value of 0.05 was used as the threshold for statistical significance.

6.2 PRECIPITATION AND WAVE DATA RESULTS

Table 6.2 contains the maximum weekly precipitation (mm) between each survey epoch at each site over the study period. The maximum weekly precipitation was 315 mm around October 3, 2022 at Arch Cape, 285 mm around October 20, 2017 at Silver Point, and 235 mm around February 7 2017 at Spencer Creek.

Table 6.3 contains the cumulative wave energy (MegaJoules, MJ) between each survey epoch at each site over the study period. At Arch Cape the maximum cumulative wave energy over the study period was 7.75 MJ and occurred between the fall 2016 and winter 2017 surveys. At Silver Point the maximum cumulative wave energy was 1.45 MJ and occurred between fall 2020 and spring 2021. While at Spencer Creek, the maximum cumulative wave energy was 0.98 and 3.10 MJ for the north and south sections, respectively, and occurred between fall 2021 and spring 2022.

Table 6.2: Maximum weekly precipitation (mm) in between each of the survey epochs at each of the sites over the study period.

	Arch Cape	Silver Point	Spencer Creek North	Spencer Creek South
F2016 to S2017	295	252	235	235
S2017 to F2017	310	77		87
F2017 to S2018		285	135	136
S2018 to F2018	77	70	109	109
F2018 to S2019	190	160	145	145
S2019 to F2019	97	78		80
F2019 to S2020	205	166	130	130
S2020 to F2020	139	104	23	23
F2020 to S2021	200	165	175	175
S2021 to F2021	86	78	48	48
F2021 to S2022	277	245	186	186
S2022 to F2022	101	101	46	46
F2022 to S2023	315	241	182	182

Table 6.3: Cumulative wave energy (MJ) in between each of the survey epochs at each of the sites over the study period.

	Arch Cape	Silver Point	Spencer Creek North	Spencer Creek South
F2016 to S2017	7.75	0.71	0.04	0.66
S2017 to F2017	3.95	0.02		0.02
F2017 to S2018		0.94	0.53	1.13
S2018 to F2018	0.00	0.00	0.00	0.00
F2018 to S2019	3.07	0.15	0.10	0.74
S2019 to F2019	0.00	0.00		0.00
F2019 to S2020	5.79	0.64	0.32	0.98
S2020 to F2020	0.00	0.00	0.00	0.00
F2020 to S2021	5.22	1.46	0.35	1.73
S2021 to F2021	0.00	0.00	0.00	0.03
F2021 to S2022	3.10	1.38	0.98	3.10
S2022 to F2022	0.00	0.00	0.00	0.00
F2022 to S2023	4.05	0.16	0.36	1.73

7.0 TERRESTRIAL LIDAR EROSIONAL ANALYSIS

This section describes the analyses performed on the terrestrial lidar data collected during this study. These analyses focused on quantifying sea cliff erosion across each study site both wholistically (i.e., across the whole cliff/study period), as well as at a hyperspatial/temporal scale (i.e., specific sections of the cliff over smaller periods of time within the study). A wide variety of analyses was selected in order to gain a more comprehensive insight into the controls and forcing factors driving sea cliff erosion at each of the sites.

The following section presents both the results and discussion from the TLS analysis. The results are presented according to each study area since each site is impacted and governed by different processes in order to make the results and subsequent discussion/analysis easier to follow. For each site, the overall volume change for the entire cliff, and for each erosion zone are presented, including their seasonal variance. Metrics that capture the forcing factors (wave energy and precipitation intensity) are also presented as well as their correlation with the volume losses in each erosion zone. Maximum weekly precipitation was found to have the strongest correlation with subaerial volume loss and is included in the results section.

7.1 SILVER POINT

The overall time series of volume loss, wave energy, and precipitation at Silver Point for the study duration is shown in Figure 7.1. During the time period, the sea cliff at Silver Point lost approximately 1734 m^3 overall, with 14% (251 m^3), 51% (878 m^3), and 35% (605 m^3) of volume loss occurring in the scour, transition, and subaerial zones respectively. Change maps between survey epochs and the three erosion classification zones for each change epoch are shown in Figure 7.1 and Figure 7.2 respectively. Seasonally, the volume loss varied across the scour, transition, and subaerial zones from a range of 0.0 m^3 – 0.0 m^3 (no detectable loss), 0.0 m^3 – 1.2 m^3, and 21 m^3 – 68 m^3 in the summer, to 23 m^3 – 51 m^3, 37 m^3 – 324 m^3, and 38 m^3 – 83 m^3 in the winter, respectively (Table 7.1). Inter-survey epoch cumulative wave energy varied from an average of 0.003 MJ (σ = 0.007 MJ) in the summer, up to an average of 0.78 MJ (σ = 0.52 MJ) in the winter.

The maximum cumulative wave energy (1.45 MJ) occurred between fall 2020 and spring 2021 and corresponds with the largest volume loss in the wave scour zone (51 m^3). Maximum weekly precipitation between survey epochs varied from an average of 81 mm (σ = 13 mm) in the summer to an average of 212 mm (σ = 55 mm) in the winter. When compared to the historical maximum weekly precipitation between 1981 and 2021 (77 mm and 229 mm for summer and winter periods respectively) this is fairly representative of recent history. The maximum weekly precipitation over the study period (285 mm) occurred between October 17, and October 23, 2017. Over the study period, positive correlations between cumulative wave energy and both the scour zone and cliff as whole were observed, $\tau = 0.80$, $p < 0.001$ and $\tau = 0.52$, $p = 0.02$ respectively. Similar positive correlations between maximum weekly precipitation and both the subaerial and cliff as a whole were observed, $\tau = 0.55$, $p = 0.008$.

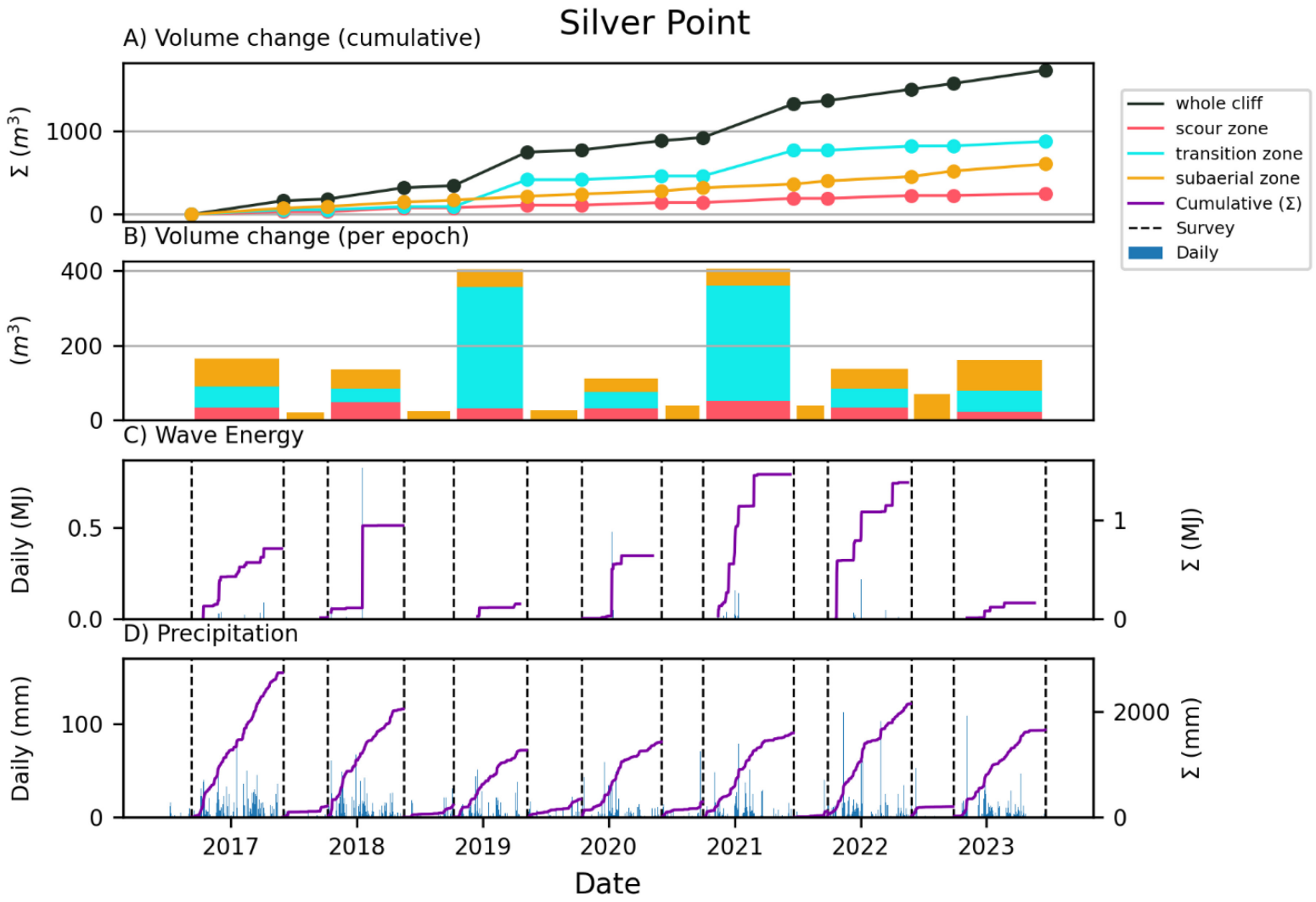

Figure 7.1: Erosion and environmental data over the study period at Silver Point. A) The cumulative volume loss overall and for each erosional zone, dashed line indicates average over the period. B) The volume loss per epoch for each erosional zone. C) The daily wave energy over the period and the cumulative wave energy between each survey. D) The daily precipitation over the period and the cumulative precipitation between each survey.

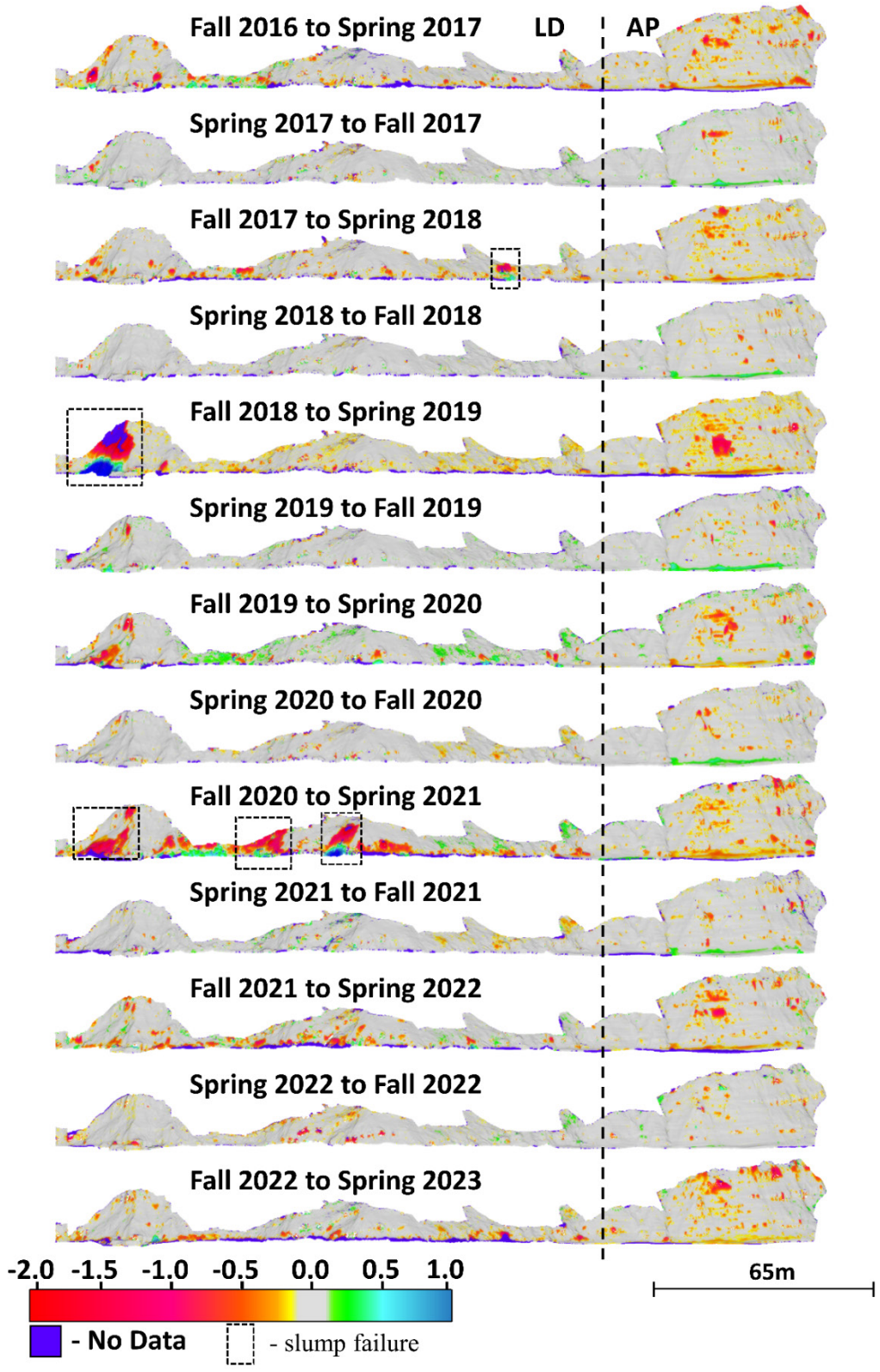

Figure 7.2: Erosion across the sea cliff for Silver Point for each epoch with annotations for each distinct section. LD = Landslide Deposits, AP = Angola Peak sandstone. Rectangle annotations show example slump failures.

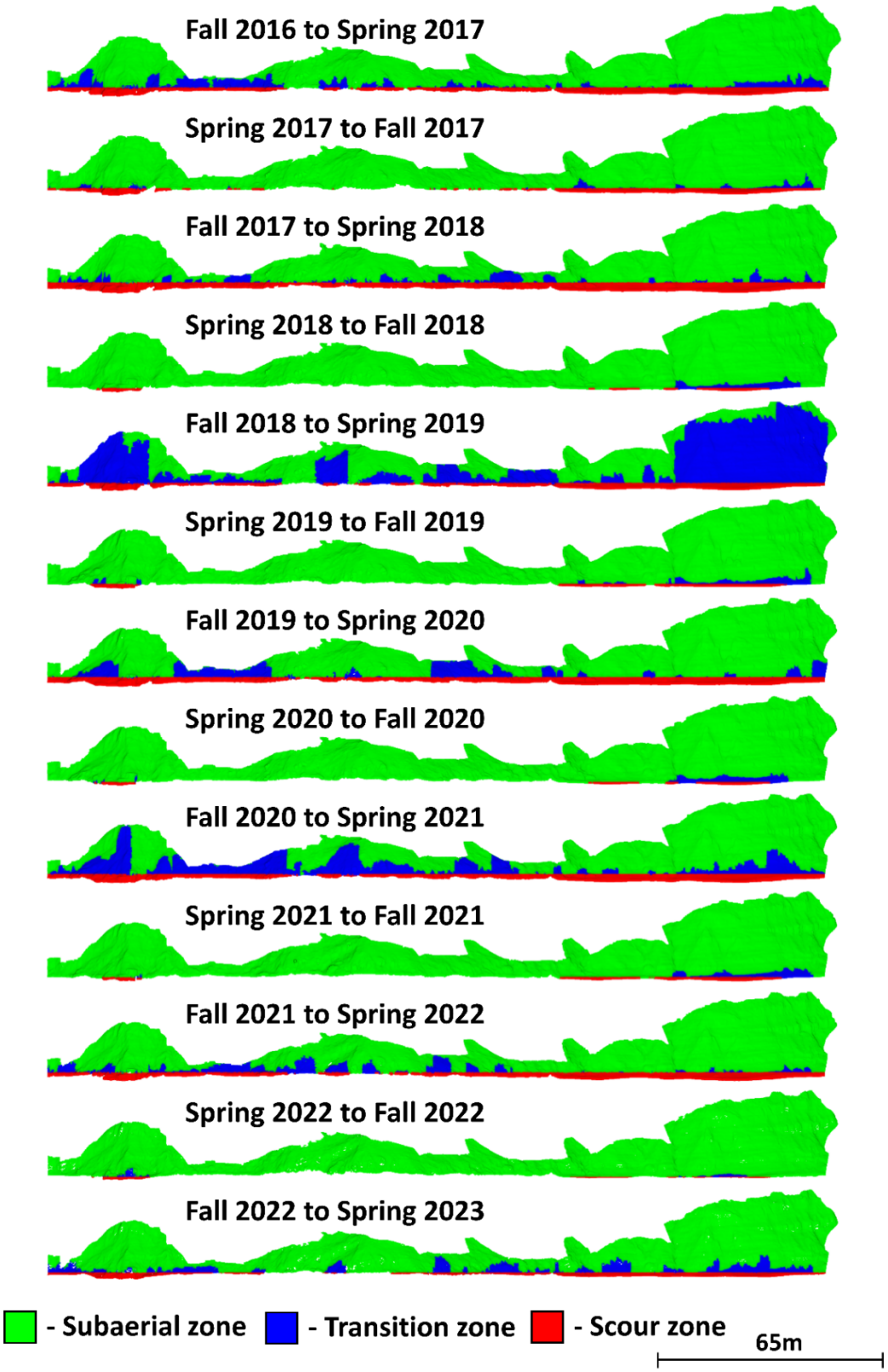

Figure 7.3: Erosion zone classification across the sea cliff at Silver Point for each change epoch.

Table 7.1: Seasonal volume loss (m^3) per zone per epoch at Silver Point. Summary statistics, maximum, minimum, mean, median, and standard deviation, are included at the bottom of the table.

	Scour zone		Transition zone		Subaerial zone		Whole sea cliff	
	Summer	**Winter**	**Summer**	**Winter**	**Summer**	**Winter**	**Summer**	**Winter**
2016	N/A	32.8	N/A	56.3	N/A	75.4	N/A	164.5
2017	0.0	47.5	0.0	36.6	20.7	51.5	20.8	135.6
2018	0.0	31.3	0.1	324.1	24.5	47.2	24.6	402.6
2019	0.0	30.9	0.4	43.9	25.2	37.5	25.6	112.3
2020	0.0	50.9	0.1	308.4	38.0	44.9	38.1	404.2
2021	0.0	34.0	0.2	50.9	38.0	51.9	38.2	136.9
2022	0.4	22.7	1.2	55.6	67.8	82.8	69.4	161.1
Min	0.0	30.9	0.0	36.6	20.7	37.5	20.8	112.3
Max	0.4	50.9	1.2	324.1	67.8	82.8	69.4	404.2
Mean	0.1	36.0	0.4	137.4	37.8	56.8	38.3	226.0
Median	0.0	33.4	0.2	55.9	37.8	51.7	38.1	162.8
Std. Dev.	0.1	10.0	0.5	124.4	17.4	16.6	17.9	121.8

Erosion at Silver Point can be geographically separated into two distinct zones. Erosion in the southern portion of the site is more consistently active as the sandstone unit is eroded along its toe during the winter, resulting in medium to large rockfalls occurring scattered throughout the cliff (Figure 7.2). These rockfalls continued to occur in the ensuing summer months but became smaller and less frequent. The north and middle sections (composed primarily of landslide deposits) in comparison experienced relatively fewer rockfalls and instead volume loss into the transition was primarily in the form of slumping failures driven by toe instability due to winter wave scour. The magnitude of these slump failures varied annually with large slump failures occurring between fall 2018 and spring 2019 and fall 2020 and spring 2021 surveys (Figure 7.2). The north and middle section experienced relatively little erosion during the summer months. Volume loss in the subaerial zone was well correlated with maximum weekly precipitation (τ = 0.55, p = 0.008 indicating that ground water seepage likely plays a role in driving subaerial erosion at Silver Point.

7.2 ARCH CAPE

Time series data of sea cliff volume loss, wave energy, and precipitation at Arch Cape is shown in Figure 7.4. Overall, the cliff at Arch Cape lost approximately 1156 m^3 of material over the seven-year time period. Of this, approximately 23% (315 m^3) was from the scour zone, 58% (804 m^3) was from the transition zone, and 19% (266 m^3) was from the subaerial zone. Figure 7.5 shows the change maps between each survey epoch, while Figure 7.6 shows the erosion responses within the three classification zones for each intersurvey epoch. Volume loss in the scour, transition, and subaerial zones varied from a range of 0.0 m^3 - 0.6 m^3, 0.0 – 2.5 m^3, and 7 m^3 – 43 m^3 respectively in the summer periods, to a range of 9 m^3 – 74 m^3, 30 m^3 – 306 m^3, and 7 m^3 – 36 m^3 in the winter periods (Table 7.2).

Cumulative wave energy varied from 0 MJ in the summer months up to an average of 4.71 MJ in the winter months. The maximum cumulative wave energy between surveys (7.75 MJ) occurred over the winter period between the fall 2016 and spring 2017 surveys (Figure 7-4). Maximum weekly precipitation between survey epochs varied from 77 mm around September 13, 2018 up to 310 mm around October 20, 2017 (Figure 7-4). For historical perspective, the average maximum weekly precipitation between the years 1981 and 2021 was 292 mm and 94 mm over the winter and summer months, respectively. Overall, volume loss in both the scour and transition zone were positively correlated with wave energy across each of the epochs ($\tau = 0.56$, $p = 0.02$ (Figure 7.13B)). Unlike Silver Point, no relationship between volume loss and maximum weekly precipitation in the subaerial zone was found ($\tau = 0.03$, $p = 0.95$ (Figure 7-13B)).

At Arch Cape, overall volume loss was primarily driven by wave scour erosion at the sea cliff base over the winter months. Given the extremely narrow sand beach, coupled with the steep cobble berm that produces a high wave runup, this is expected. Instability caused by this toe erosion led to larger cliff collapse/toppling failure in the transition zone. The amount of cliff collapse/toppling failure varied year to year, driven by erosion at the toe and over steepening of the cliff face. This process played out gradually, increasing the elevation of the transition zone (Figure 7.6) over a period of several years eventually leading to over steepening and large cliff collapse, which resets the process. This pattern is most easily observed at the south end of the sea cliff (right side of Figure 7.5). During the summer months, volume loss was significantly lower due to no wave energy impacting the cliff toe and thus volume loss was primarily composed of subaerial weathering, including delayed loss of loosened material partially scoured from the previous winter.

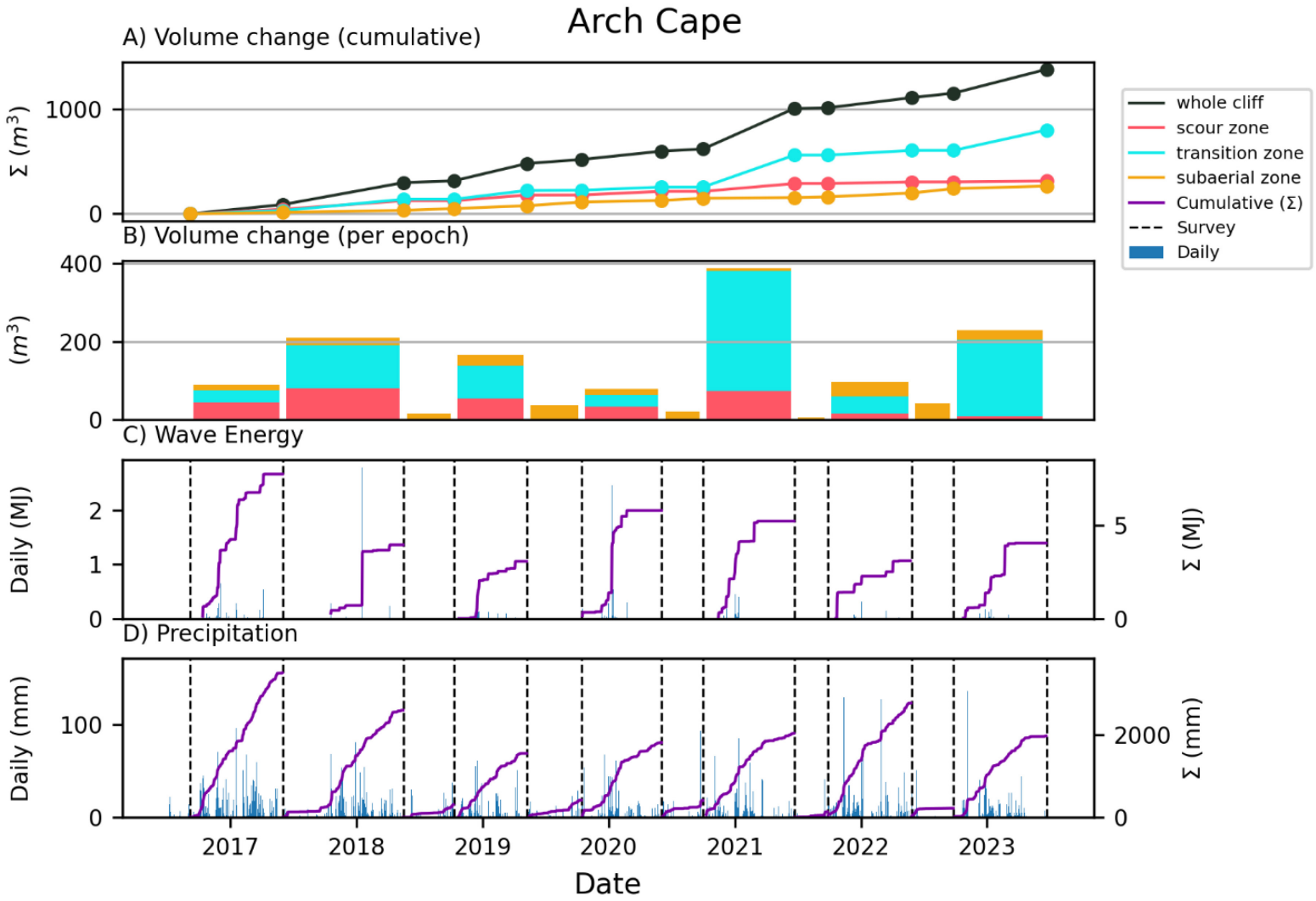

Figure 7.4: Erosion and environmental data over the study period at Arch Cape. A) The cumulative volume loss overall and for each erosional zone, dashed line indicates average over the period. B) The volume loss per epoch for each erosional zone. C) The daily wave energy over the period and the cumulative wave energy between each survey. D) The daily precipitation over the period and the cumulative precipitation between each survey.

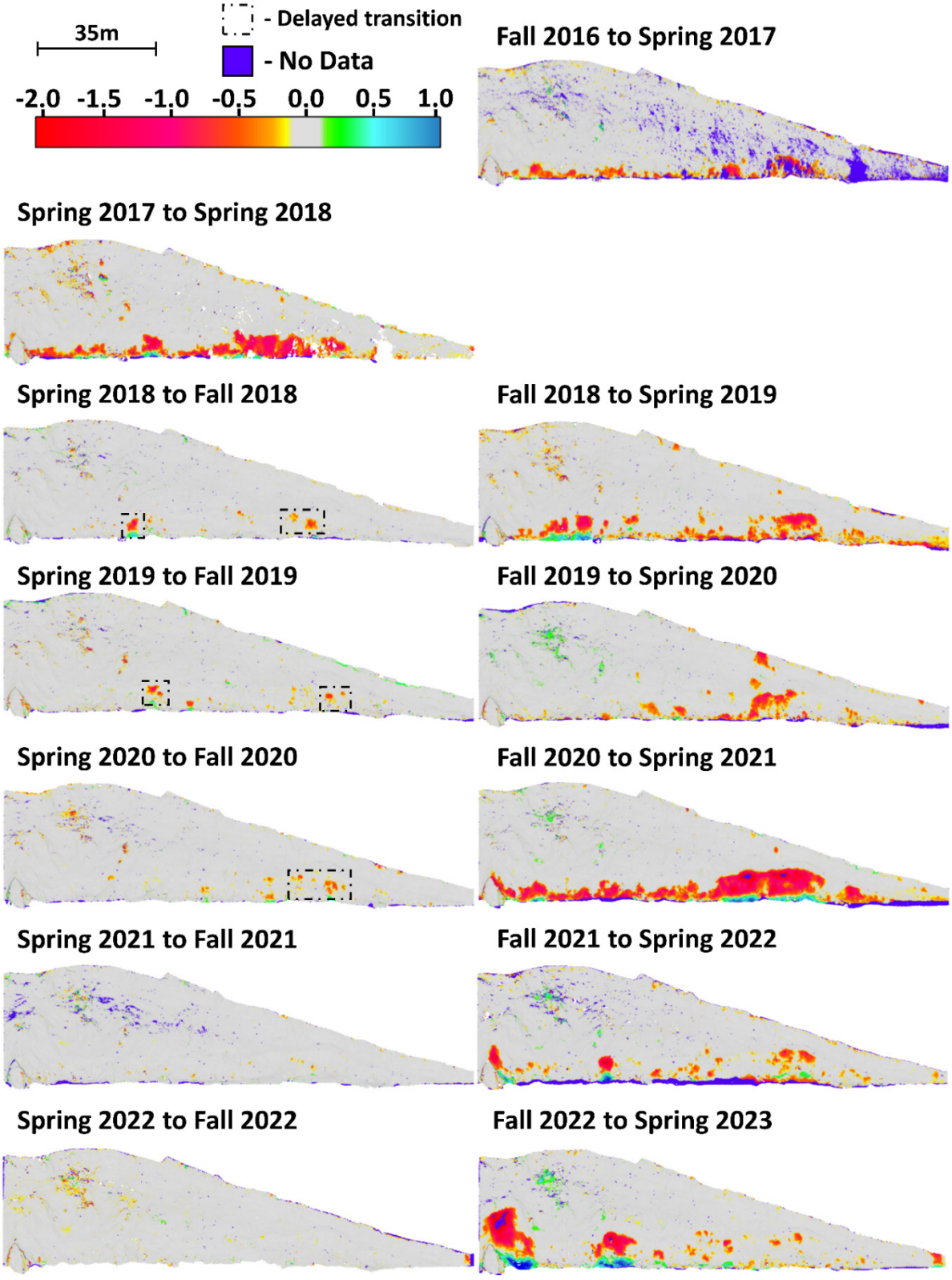

Figure 7.5: Erosion across the sea cliff at Arch Cape for each epoch. Note missing survey in Fall 2017. Rectangle annotations show examples of failures in the subaerial zone that occurred during the summer, a product of the previous winters scour/transition zone.

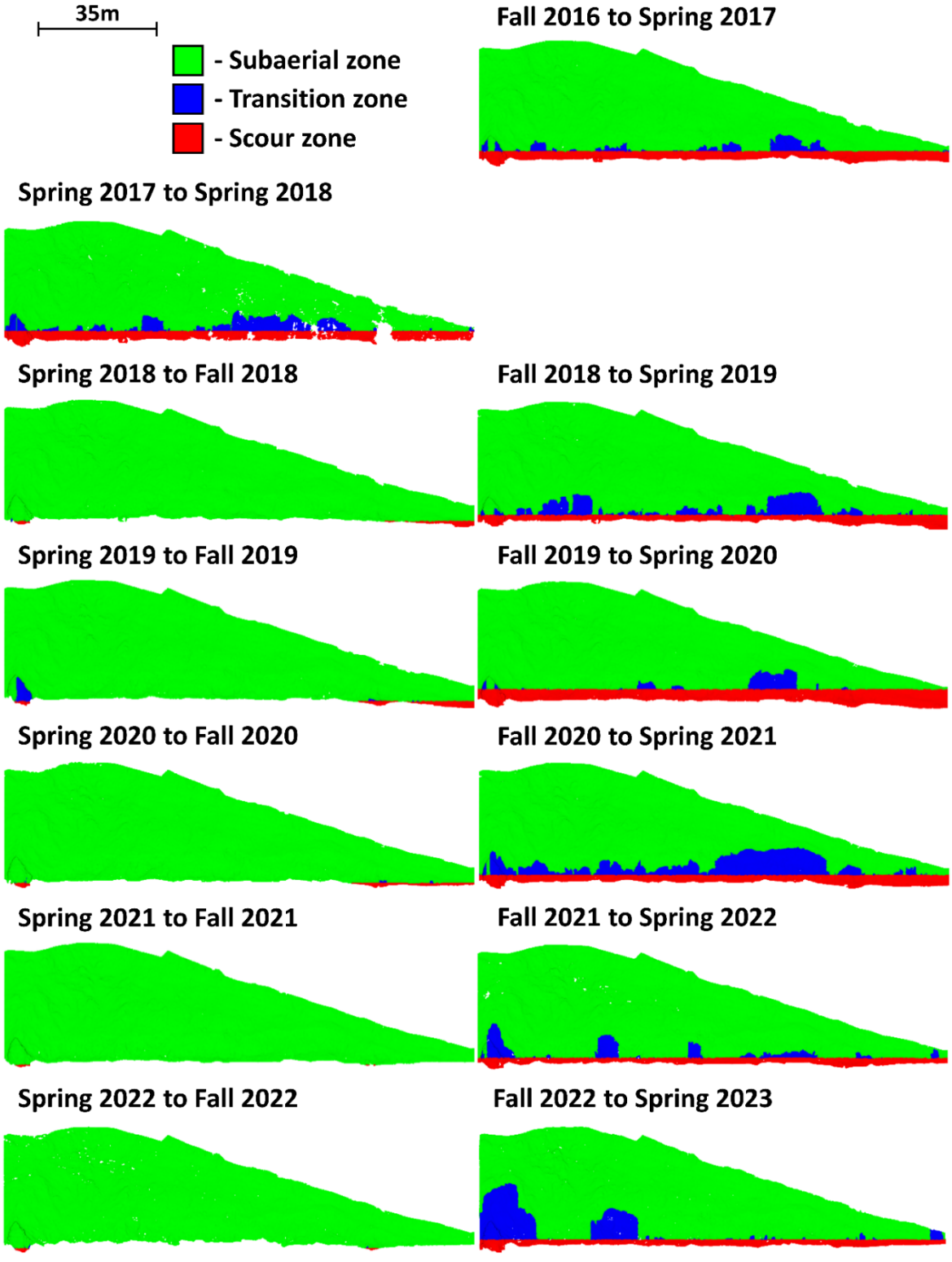

Figure 7.6: Erosion zone classification across the sea cliff at Arch Cape for each epoch. Note missing survey in fall 2017.

Table 7.2: Seasonal volume loss (m^3) per zone per epoch at Arch Cape. * = spring to spring measurement rather than fall to spring. Summary statistics, maximum, minimum, mean, median, and standard deviation, are included at the bottom of the table.

	Scour zone		Transition zone		Subaerial zone		Whole sea cliff	
	summer	winter	summer	winter	summer	winter	summer	winter
2016	N/A	44.3	N/A	31.0	N/A	13.9	N/A	89.2
2017	N/A	81.6*	N/A	108.7*	N/A	19.7*	N/A	210*
2018	0.1	54.4	0.0	84.5	17.0	27.3	17.1	166.2
2019	0.6	34.5	2.5	29.8	35.0	15.8	38.1	80.1
2020	0.1	74.6	0.1	306.2	20.9	6.8	21.0	387.6
2021	0.0	15.8	0.0	44.9	6.7	36.4	6.7	97.1
2022	0.2	8.8	0.1	195.8	42.6	24	42.8	228.6
Min	0.0	15.8	0.0	29.8	6.7	6.8	6.7	80.1
Max	0.6	81.6	2.5	306.2	42.6	36.4	42.8	387.6
Mean	0.2	44.9	0.7	126.3	24.5	20.8	25.0	191.8
Median	0.1	44.6	0.1	96.6	22.7	20.3	23.0	179.0
Std. Dev.	0.2	26.9	1.1	103.3	13.6	10.0	14.0	111.2

7.3 SPENCER CREEK

For analyses at Spencer Creek, the site was divided into two sections (north and south of Spencer Creek) due to the different cliff morphology and geology as well as beach profile between the two sections. Volume loss, wave energy, and precipitation data as time series for Spencer Creek North and South are shown in Figure 7.7 and Figure 7.8, respectively. Over the study period, the sea cliffs at Spencer Creek North lost ~1969 m^3 of sea cliff material, with ~21% (421 m^3), 41% (806 m^3) and 38% (742 m^3) of volume loss having occurred in the scour, transition, and subaerial zones respectively (Table 7.3). While the Spencer Creek South section lost approximately 5,052 m^3 of material with approximately 20% (999 m^3), 58% (2949 m^3), and 22% (1104 m^3) of volume loss occurred in the scour, transition, and subaerial zones respectively (Table 7.4).

At Spencer Creek North, the average volume loss in the scour, transition, and subaerial zones varied seasonally, ranging from 0 m^3 – 0 m^3, 0 m^3 – 0 m^3, and 18 m^3 – 158 m^3 in the summer and ranging from 1 m^3 – 116 m^3, 28 m^3 – 363 m^3, and 22 m^3 – 161 m^3 in the winter, respectively Table 7-3_. While at Spencer Creek South, the volume losses varied seasonally for the three zones (scour, transition, and subaerial) between 0 m^3 – 0.4 m^3, 0 m^3 – 0.3 m^3, and 27 m^3 – 185 m^3 in the summer, to ~ 79 m^3 – 290 m^3, 165 m^3 – 778 m^3, and 45 m^3 – 185 m^3 in the winter respectively. Change maps between survey epochs for Spencer Creek North and South are shown in Figure 7.9 and Figure 7.10, while the erosion classification zones are shown in Figure 7.11 & Figure 7.12. At Spencer Creek North, cumulative wave energy was positively correlated with volume loss in the scour zone ($\tau = 0.80$, $p = 0.001$), while at Spencer Creek South, cumulative wave energy was positively correlated with volume loss in both the scour and transition zones ($\tau = 0.41$, $p = 0.06$ and $\tau = 0.64$, $p = 0.002$ respectively). Positive correlation was also noted between maximum weekly precipitation and both the subaerial zone and cliff as a whole at

Spencer Creek North ($\tau = 0.49$, $p = 0.04$ and $\tau = 0.60$, $p = 0.01$ respectively) and Spencer Creek South ($\tau = 0.44$, $p = 0.04$ and $\tau = 0.62$, $p = 0.003$ respectively) (Table 7.5).

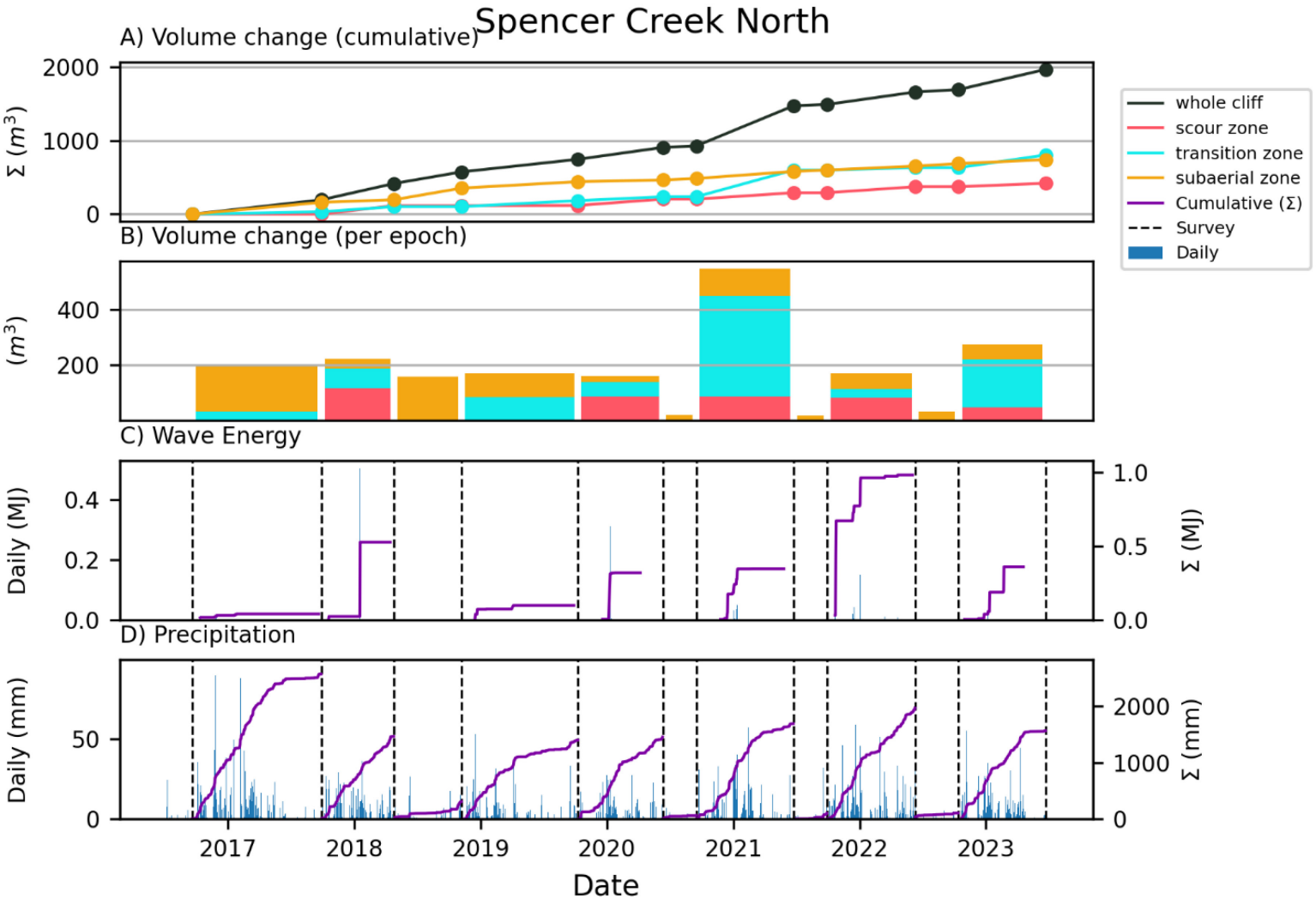

Figure 7.7: Erosion and environmental data over the study period at Spencer Creek North. A) The cumulative volume loss overall and for each erosional zone, dashed line indicates average over the period. B) The volume loss per epoch for each erosional zone. C) The daily wave energy over the period and the cumulative wave energy between each survey. D) The daily precipitation over the period and the cumulative precipitation between each survey.

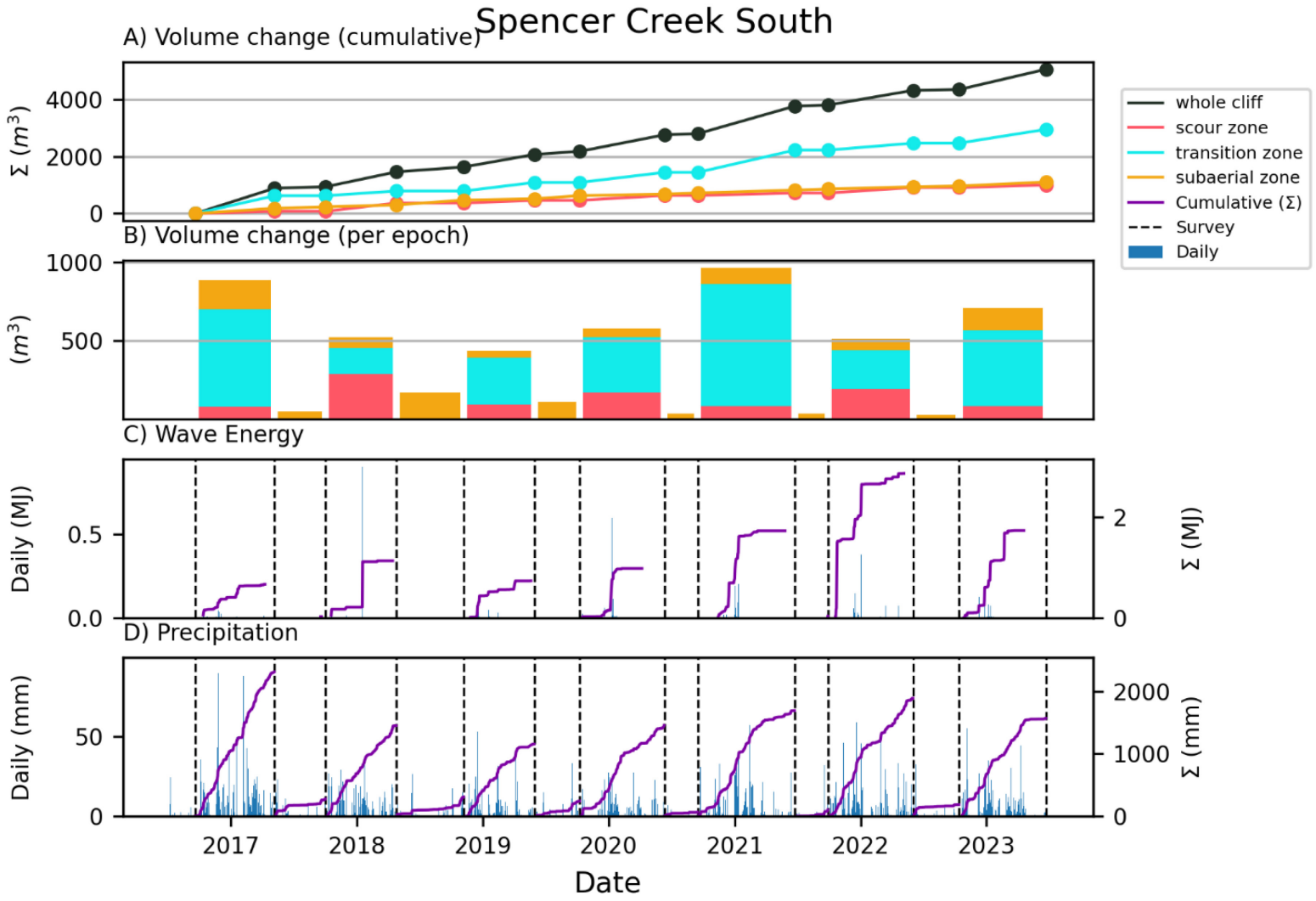

Figure 7.8: Erosion and environmental data over the study period at Spencer Creek South. A) The cumulative volume loss overall and for each erosional zone, dashed line indicates average over the period. B) The volume loss per epoch for each erosional zone. C) The daily wave energy over the period and the cumulative wave energy between each survey. D) The daily precipitation over the period and the cumulative precipitation between each survey.

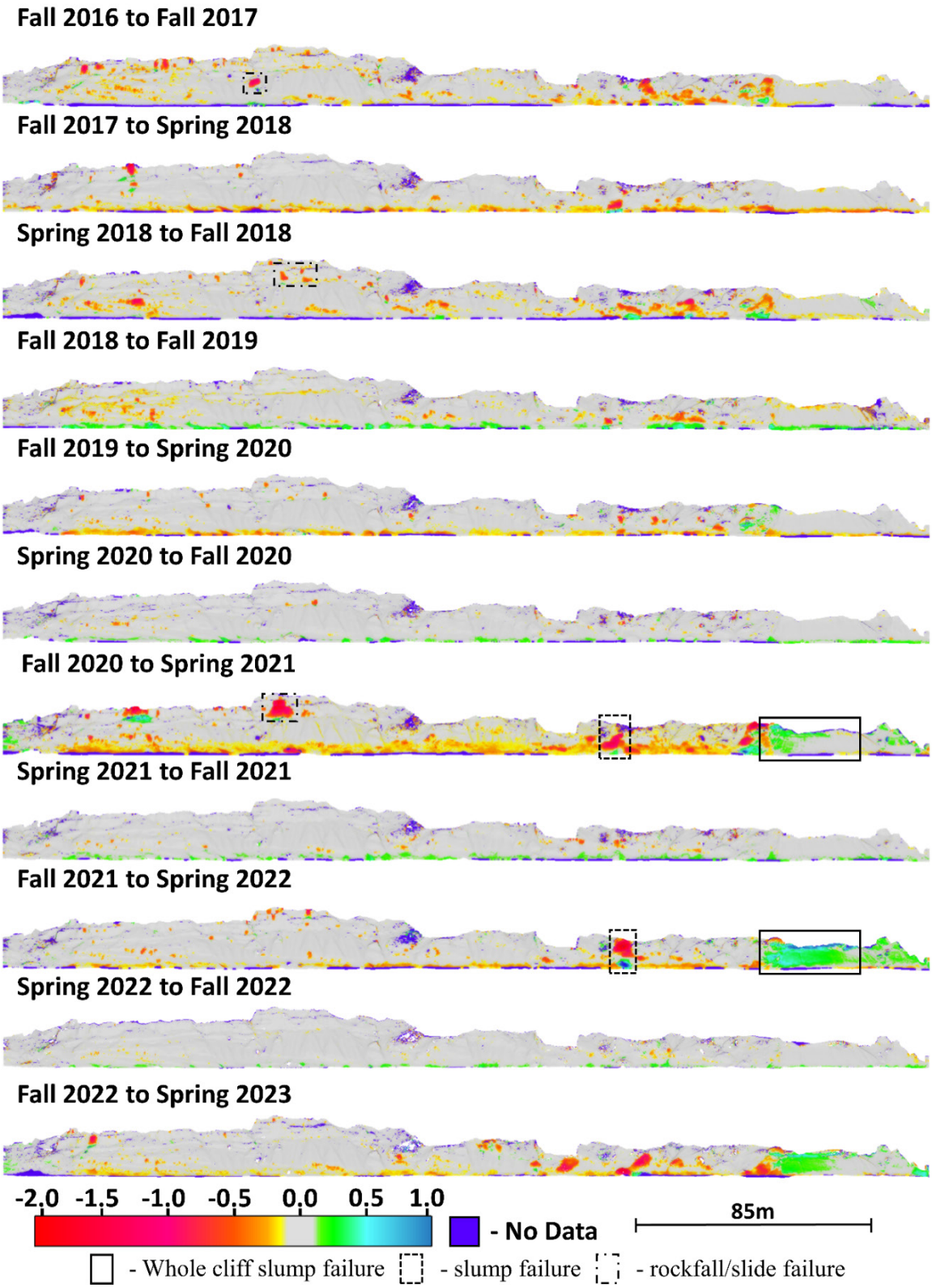

Figure 7.9: Erosion across the sea cliff at Spencer Creek North for each epoch with annotations showing example failure types. Note the missing surveys in spring 2017 and spring 2019 due to poor GNSS conditions during the time of survey.

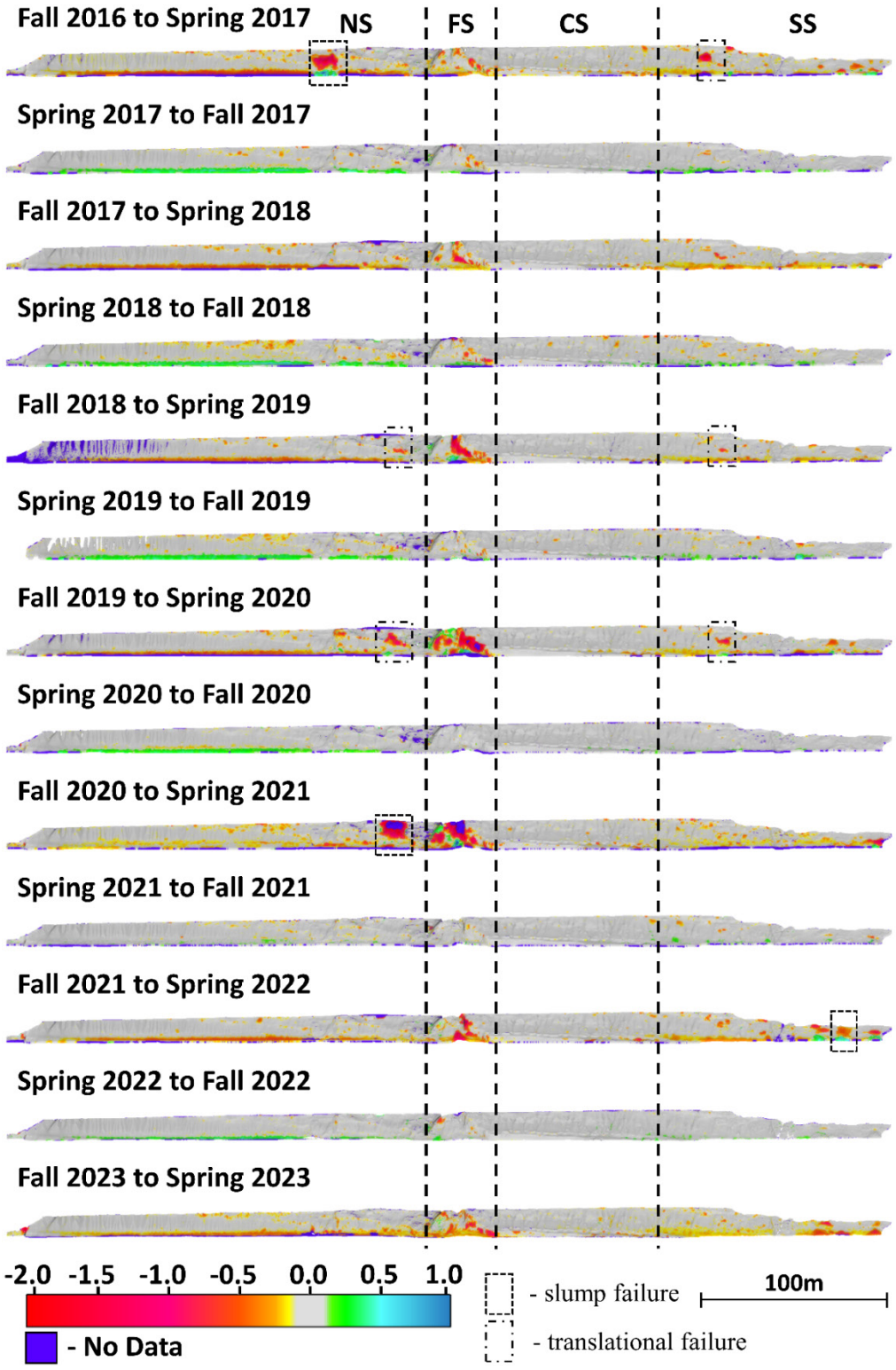

Figure 7.10: Erosion across the sea cliff for Spencer Creek South for each epoch with annotations for each distinct section. NS = North Section, FS = Fault Section, CS = Center Section, SS = South Section. Rectangle annotations show example slump/translational failures.

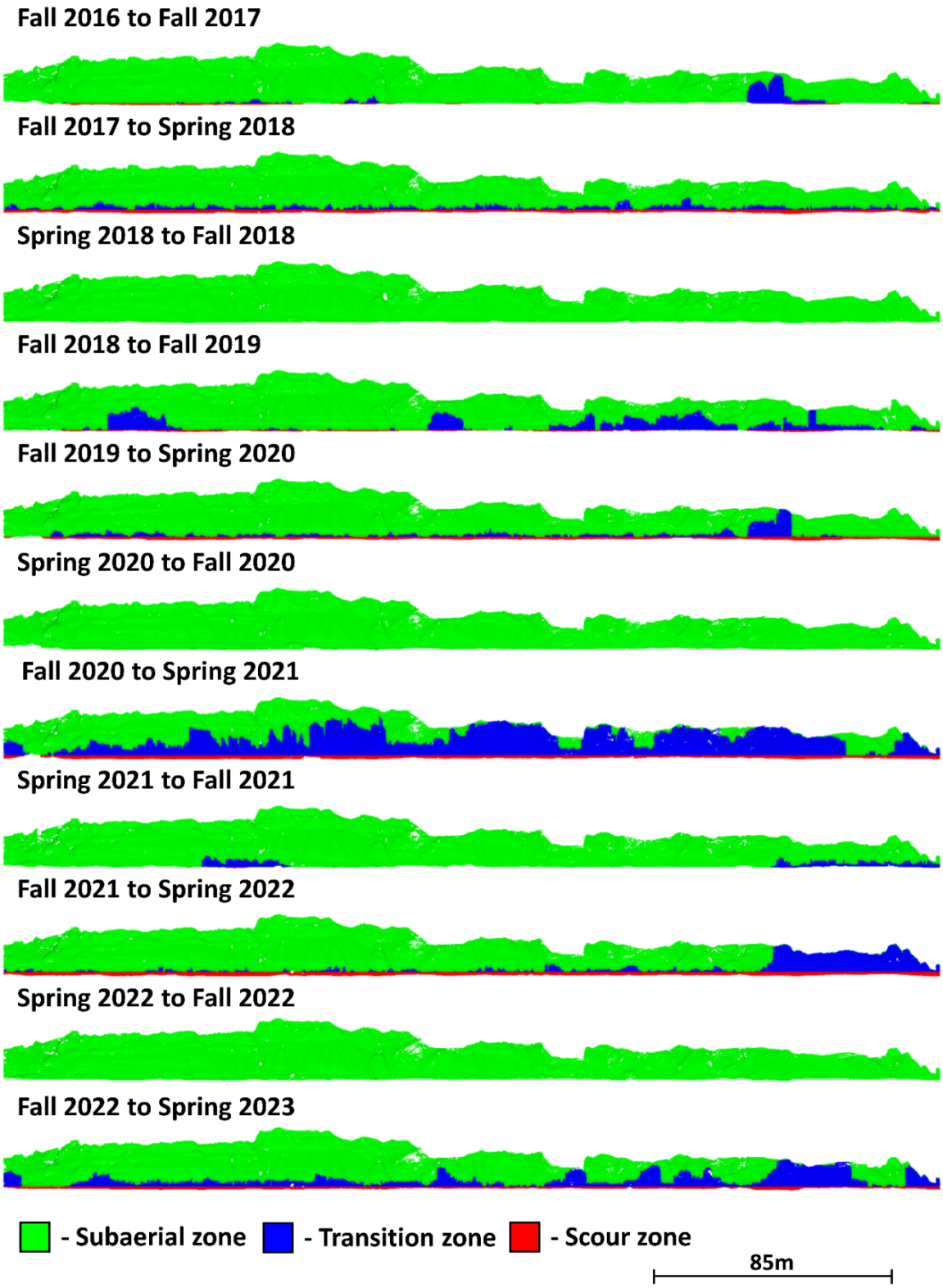

Figure 7.11: Erosion zone classification across the sea cliff at Spencer Creek North for each change epoch. Note the missing surveys in spring 2017 and spring 2019.

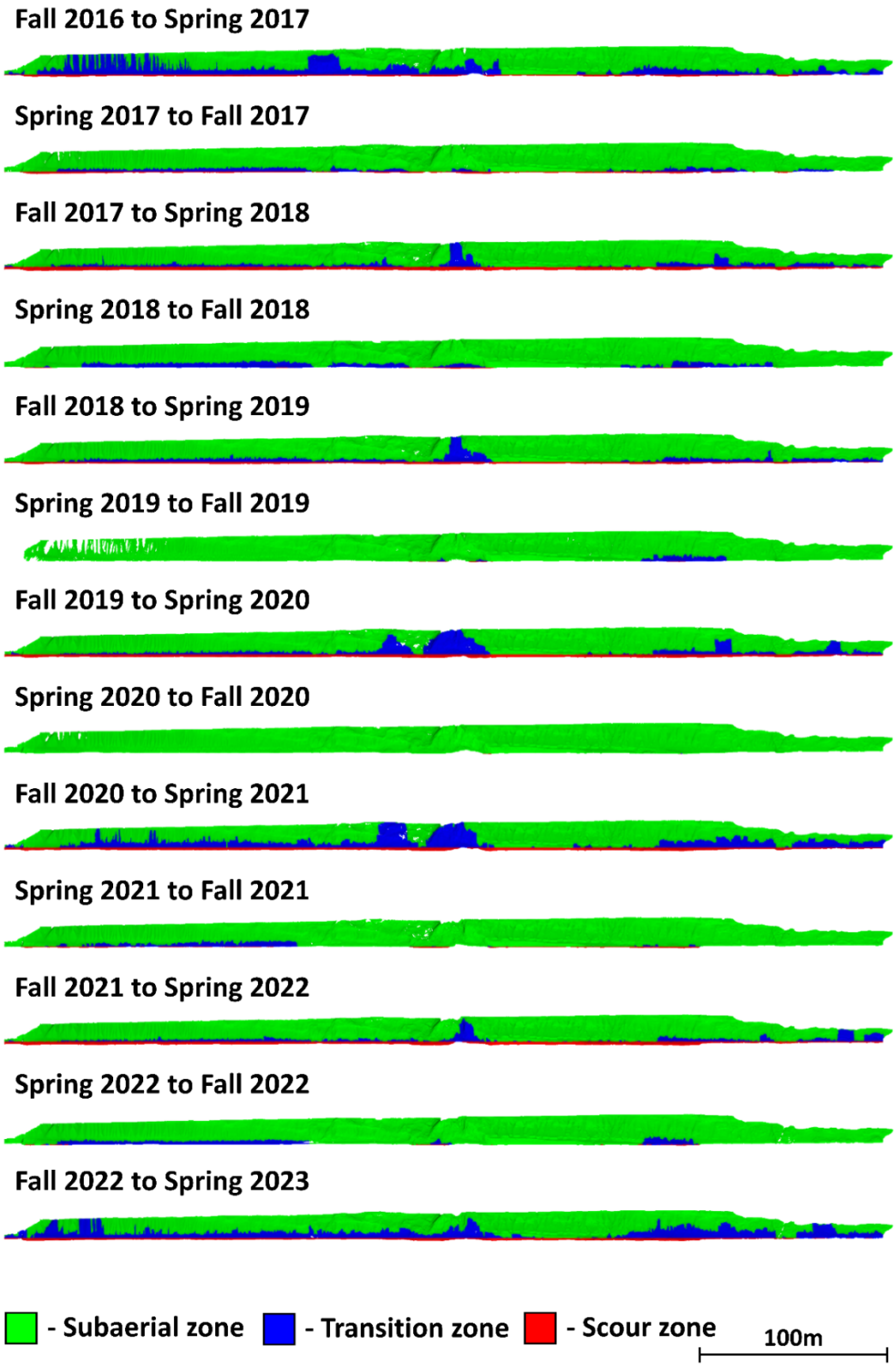

Figure 7.12: Erosion zone classification across the sea cliff at Spencer Creek South for each change epoch.

Table 7.3: Seasonal volume loss (m^3) per zone per epoch at Spencer Creek North, ** = fall to fall measurement rather than fall to spring. Summary statistics, maximum, minimum, mean, median, and standard deviation, are included at the bottom of the table.

	Scour zone		Transition zone		Subaerial zone		Whole sea cliff	
	summer	winter	summer	winter	summer	winter	summer	winter
2016	N/A	1.0**	N/A	32.8**	N/A	161.3**	N/A	195.1**
2017	N/A	116.2	N/A	70.4	N/A	35.5	N/A	222.2
2018	0.0	2.1	0.0	81.5**	158.5	87.3**	158.5	170.8**
2019	N/A	86.3	N/A	52.9	N/A	22.5	N/A	161.6
2020	0.0	86.5	0.0	362.7	20.7	96.0	20.7	545.2
2021	0.0	86.8	0.0	27.7	18.4	54.6	18.4	169.2
2022	0.0	46.8	0.0	173.0	32.9	54.7	32.9	274.5
Min	0.0	1.0	0.0	27.7	18.4	22.5	18.4	161.6
Max	0.0	116.2	0.0	362.7	158.5	161.3	158.5	545.2
Mean	0.0	59.8	0.0	133.5	67.9	77.3	67.9	271.7
Median	0.0	70.8	0.0	76.0	32.9	66.0	32.9	208.6
Std. Dev.	0.0	43.3	0.0	123.8	60.8	48.4	60.8	143.7

Table 7.4: Seasonal volume loss (m^3) per zone per epoch at Spencer Creek South. Summary statistics, maximum, minimum, mean, median, and standard deviation, are included at the bottom of the table.

	Scour zone		Transition zone		Subaerial zone		Whole sea cliff	
	summer	winter	summer	winter	summer	winter	summer	winter
2016	N/A	79.4	N/A	623.6	N/A	184.7	N/A	887.8
2017	0.1	289.7	0.3	164.5	49.4	67.3	49.8	521.6
2018	0.0	93.5	0.0	300.0	170.9	45.0	171.0	438.5
2019	0.0	171.6	0.0	353.2	109.0	53.7	109.1	578.5
2020	0.0	83.7	0.0	778.4	38.4	103	38.4	965.1
2021	0.4	212.0	0.2	228.1	37.4	76.7	38.0	516.8
2022	0.0	79.4	0.0	483.0	27.2	141.3	27.3	710.2
Min	0.0	79.4	0.0	164.5	27.2	45.0	27.3	438.5
Max	0.4	289.7	0.3	778.4	170.9	184.7	171.0	965.1
Mean	0.1	152.0	0.1	432.3	78.8	100.2	79.0	669.1
Median	0.1	122.7	0.1	392.8	49.4	88.5	49.8	623.8
Std. Dev.	0.2	79.9	0.1	219.6	56.0	51.0	55.9	196.5

At Spencer Creek North erosion at the base of the sea cliff was more intermittent than the other sites with some winters (fall 2016 to fall 2017 and fall 2018 to fall 2019) seeing relatively little wave energy impacting the cliff (Figure 7.7) and correspondingly relatively little erosion at the base/scour zone (Figure 7.7 and Figure 7.9). This is in part due to both the relatively high cliff toe (H_{Toe} = 5.2 m) and the broad sand beach that offer some protection, combined with the presence of a basalt dike (Otter Rock) ~1 km due west of the sea cliff. Spencer Creek North experienced the highest proportional volume loss (38%) in the subaerial zone of all of the sites in this study (Table 7.3). The toe of the sea cliff at Spencer Creek North sits approximately 0.7 m higher than the cliff toe at Spencer Creek South, which may account for differences in the erosional patterns despite their similar geology. Erosion at Spencer Creek North appears to be driven by groundwater seepage over epochs with relatively little wave energy. This is also seen in the relatively better correlation between volume loss across the whole site and maximum weekly precipitation ($\tau = 0.60$, $p = 0.01$) compared to cumulative wave energy ($\tau = 0.52$, $p = 0.03$). Epochs with low wave energy experienced sporadic rockfalls/slides concentrated in the steep Astoria siltstone/sandstone sections with relatively fewer events over the summer periods (Figure 7.9). Winter epochs with higher wave energy experienced significant volume loss at the toe, as well as the rockfall/slides described above. Additionally, slumping failures are present during high wave energy epochs in the gentler sloping estuarine deposits, driven by instability due to removal of cliff toe material. Over the fall 2020 – spring 2021 and fall 2021 – spring 2022 epochs, a large section of cliff approximately 35 m wide slumped forward approximately 0.5 m (shown as accretion in Figure 7.9). This may lead to a significant erosion in the coming years.

Erosion at Spencer Creek South was laterally variable along the sea cliff. The north section composed of estuary deposits throughout, experienced significant ocean driven toe erosion in the scour zone during the winter months with small translational slides and occasional large slump events occurring into the transition zone (Figure 7.10). Given the high correlation between the transition zone and both the cumulative wave energy ($\tau = 0.61$, $p = 0.004$) and maximum weekly precipitation ($\tau = 0.64$, $p = 0.002$), and the presence of rills, it is reasonable to conclude that these slump events exhibit strong wave and precipitation driven controls. The center of the sea cliff at the fault zone experienced rapid erosion over the study period, with large block toppling failures occurring in most winters resulting from ocean driven toe instability. Immediately south of the fault zone there was relatively little toe erosion in the scour zone, and relatively little erosion overall. The toe at this section is composed of sandstone from the Astoria formation and appears significantly less erodible than the estuarine deposits present at other parts of the cliff. This section may experience more significant erosion in the future during large storm events that exceed the elevation of the sandstone layers, especially given projected sea level rise. South of this section, the sandstone layer dips below the beach exposing only the estuarine deposits, thus experiencing very similar erosional patterns to those within the north section. Small amounts of erosion occur during the summer periods primarily located around areas that failed over the previous winter.

7.4 ALL SITES

Overall, the average annual erosion rate across the entire sea cliff over the full study period was 0.13 m/yr, 0.08 m/yr, 0.05 m/yr, and 0.07 m/yr for Arch Cape, Silver Point, Spencer Creek North, and Spencer Creek South, respectively. Long-term erosion rates were derived using the digital shoreline analysis system (DSAS) (Himmelstoss et al., 2018) with 10 m spaced transects from orthorectified imagery collected in 1967 and 2018. These rates were determined to be 0.13 m/yr, 0.13 m/yr, 0.09 m/yr, and 0.12 m/yr for Arch Cape, Silver Point, Spencer Creek North, and Spencer Creek South, respectively. This indicates that with the exception of Arch Cape, the erosion observed during this study is representative of a lower than average erosion rate compared to the long-term data recorded since 1967.

Correlations between volume loss and precipitation proxies are shown in Table 7.5. Figure 7.13 shows correlations of volumetric change with wave energy and precipitation for all sites. Each site exhibited a strong seasonal variance in volume loss across the sea cliff between the summer and winter months. This was especially evident in the scour and transition zones, with volume losses near zero in the summer. These results are entirely consistent with periods when little/no wave energy is directly impacting the toe of the sea cliffs (Figure 7.4, Figure 7.1, Figure 7.7, Figure 7.8, and Table 6.3). Hence, the TLS confirms that there is generally very little volume loss caused either directly, or indirectly by ocean forcing factors during the summer. The subaerial zone on the other hand continued to experience volume loss over the summer. Further, our measurements indicated that the average summer volume loss was ~16% lower compared with the average winter volume loss across all sites.

Of the volume loss that occurred in the subaerial zone over the summer months, a significant amount occurred within the geographic extents of the scour/transition zone from the previous winter. Most of this volume loss is likely delayed failure and removal of weakened material due to instabilities caused by wave scour over the winter period (see annotations in Figure 7.5 as an example). A separate sub-classification was added to the erosion zone classifier for change epochs encompassing the summer months in order to determine the contribution of this delayed response to summer subaerial volume loss. This sub-zone was created from the points in the subaerial zone during the summer that were part of, or connected to, the scour or transition zone during the previous winter period. This new sub-classification zone (named the delayed transition zone) contributed 4 – 7% of total volume loss over the study period across each of the sites and made up 44 – 55% of the total volume loss that occurred in the subaerial zone over the summer months. Normalized by area, the cumulative volume change was 3.7, 1.3, 2.2, and 2.7 times higher in the delayed transition zone compared to the rest of the subaerial zone for Arch Cape, Silver Point, Spencer Creek North, and Spencer Creek South, respectively. This demonstrates the presence of an erosional lag following wave scour induced erosional events that persists at least into the summer months. This may be similar to the observation of spatio-temporal clustering of rockfalls (Whadcoat, 2017) or a localized equivalent of observed decay in failure following weakening and/or removal of unstable, dilated rock (Massey et al., 2022).

Table 7.5: Kendall's τ between driving forces and volume loss per zone. Red = p > 0.05, yellow = 0.01 <= p <= 0.05, green = p < 0.01.

	Arch Cape (n = 10)				Silver Point (n = 11)				Spencer Creek North (n = 9)				Spencer Creek South (n = 11)			
Zone	**WE**		**PREC**		**WE**		**PREC**		**WE**		**PREC**		**WE**		**PREC**	
	τ	**p**	**τ**	**p**	**τ**	**p**	**τ**	**p**	**τ**	**p**	**τ**	**p**	**τ**	**p**	**τ**	**p**
Scour	0.48	0.03	0.56	0.02	0.61	0.00	0.80	0.00	0.37	0.13	0.80	0.00	0.41	0.06	0.77	0.00
Transition	0.61	0.01	0.56	0.02	0.48	0.02	0.47	0.03	0.52	0.03	0.53	0.03	0.64	0.00	0.61	0.00
Subaerial	0.03	0.95	-0.30	0.20	0.55	0.01	0.27	0.21	0.49	0.04	0.10	0.69	0.44	0.04	0.27	0.21
Overall	0.64	0.00	0.56	0.02	0.55	0.01	0.52	0.02	0.60	0.01	0.52	0.03	0.62	0.00	0.51	0.02

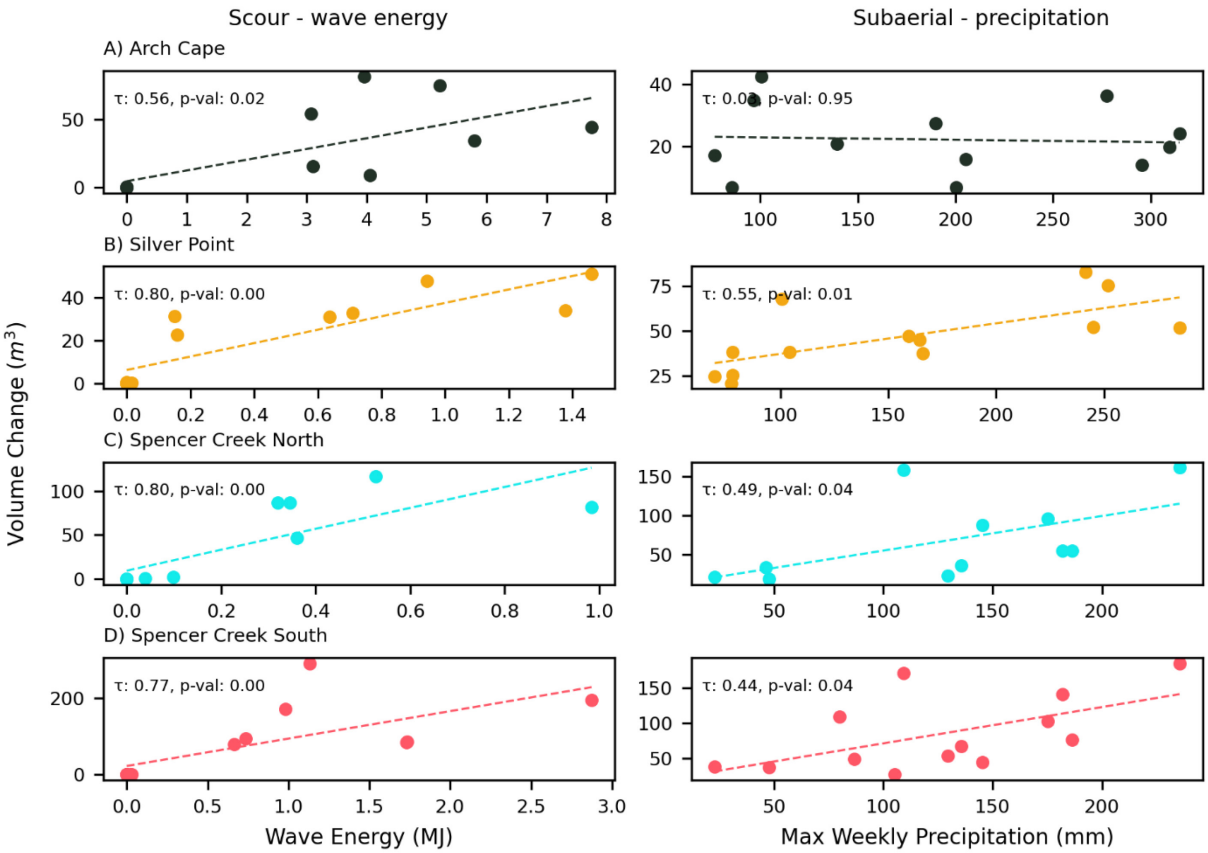

Figure 7.13: Statistical correlations between volume loss in the scour zone and cumulative wave energy (left column), and volume loss in the subaerial zone and maximum weekly precipitation (right column) for each study site.

7.4.1 Magnitude Frequency

Previous studies have identified that the magnitude-frequency distributions of various slope failures are fat-tailed and can be summarized with a power-law fit (Barlow et al., 2012; Dussauge et al., 2003; Graber & Santi, 2022; Malamud et al., 2004; Massey et al., 2022). Power-law scaling exponents *(β)* indicate the volume loss contribution of small magnitude events compared to large magnitude events with $\beta < 1$ indicating that larger magnitude events contribute more to overall volume loss. The power-law scaling exponent (β) varies across the literature, depending on: hazard type, geologic material, environmental conditions, seismic conditions, and data collection frequency. Volume-frequency data from each erosion zone were fit using a power-law for each study site in order to observe how these results fit into the broader research. Volume bins were chosen by visual inspection of data between a minimum of $3x10^{-3}$ m^3 and maximum of 30 m^3 to prevent the "rollover" influencing the fit. The occurrences (frequency) in each volume bin were normalized by both time between survey, and surface area of the erosion zone to yield the number of events per day per m^2. The scaling coefficient (a) and exponent (β) describing the power-law model were then computed via least-squares regression. R^2 values were computed to access the quality of fit of each power-law distribution. The volume-frequency fits for each erosion zone and each site are shown in Figure 7.14.

A meta-analysis by Graber & Santi (2022) compared power-law fits from 46 rock fall inventories, and the scaling exponent for the cumulative distribution function varied from -0.20 to -1.40 (mean = -0.71, $\sigma = 0.28$). This puts the average magnitude-frequency β observed in the subaerial zones of this study (mean = -0.87, $\sigma = 0.05$) close to the mean of other rock fall inventories in the literature. The average β observed in volume - frequency (Figure 7.14) in the scour, and transition zone of this study (mean = -0.37, $\sigma = 0.10$, and mean = -0.33, $\sigma = 0.04$, respectively) are significantly lower than the subaerial zone, and towards the bottom range of what is observed in other rockfall inventories in the literature. This indicates the proportionally higher contribution of large events to overall volume loss in the scour and transition zones compared to both the subaerial zone and other rock fall inventories. This is expected given that overall volume loss in these zones is driven in a large part by large infrequent external forces (wave energy) and scour is likely merged into large regions of erosion owing to limited survey frequency in winter months where the sites are inaccessible. Similarly low β values have been observed following stormy periods at other sea cliffs (Gilham et al., 2019; Westoby et al., 2020). Overall, the trends of β values are similar across each of the sites in the scour and transition zones suggests that wave energy negates the difference in geology. It is worth noting, however, that β values observed in the data may be slightly lower than the real β values due to superimposition of failures given the frequency intervals of surveys in this study (Williams et al., 2019).

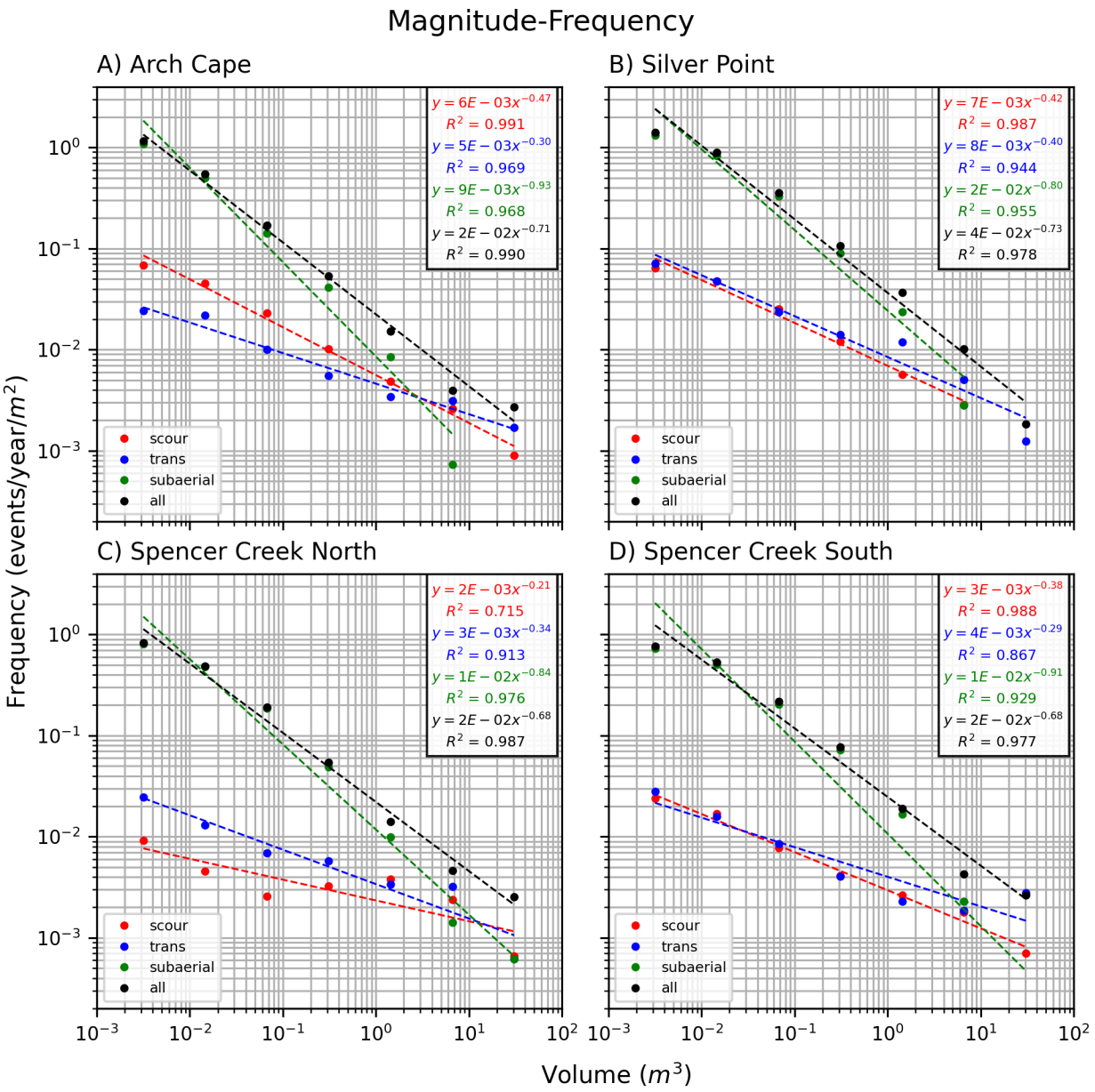

Figure 7.14: Volume-frequency curves plotted on log – log scale for each erosional zone at: A) Arch Cape, B) Silver Point, C) Spencer Creek North, and D) Spencer Creek South, where frequency is the number of failure events in each volume bin normalized by time and surface area to events/year/m^2. Power-law equations and R^2 values are provided for each fit. The lower magnitude of the scaling exponent (β) in the scour and transition zones indicate the relatively higher contribution of large volume failures to the overall volume loss, compared to the subaerial zone.

8.0 IN-SITU SENSOR INSTALLATION

This chapter contains information about instrumentation installed at each site, including the type of instrumentation and the duration of service.

8.1 INSTALLATION OF MEMS

After the selection of the sites, visits to the sites were conducted to verify the proposed locations for drilling boreholes to install the instrumentation. MEMs (consisting of Measurand Shape Accel Array (SAA) systems) and piezometer sensors were installed in the drilled boreholes at Arch Cape, Arizona Inn, Silver Point, and Spencer Creek during the winter of 2016/2017. The same system was then installed at Hooskanaden in late November 2017. Figure 8.1 shows the drill rig utilized for the drilling for this project, whilst Figure 8.2 shows an example of the borehole cores recovered from drilling providing additional information about each of the landslides. After drilling was complete to the planned depth, SAA MEMs and piezometer sensors were installed into the hole. Accelerometers are spaced every meter on the SAA MEMs. Two piezometers were installed at each site below the water table at different elevations. The housing for the electrical components (Figure 8.3) was then installed at the site with concrete and a steel post as shown in Figure 8.4.

Figure 8.1: Drill rig actively drilling borehole for SAA MEM's installation at Arch Cape on January 20, 2017. Photograph Credit: Dr Michael Bunn.

Figure 8.2: Example borehole cores recovered from Arizona Inn during drilling on February 2, 2017. Photograph Credit: Dr Michael Bunn.

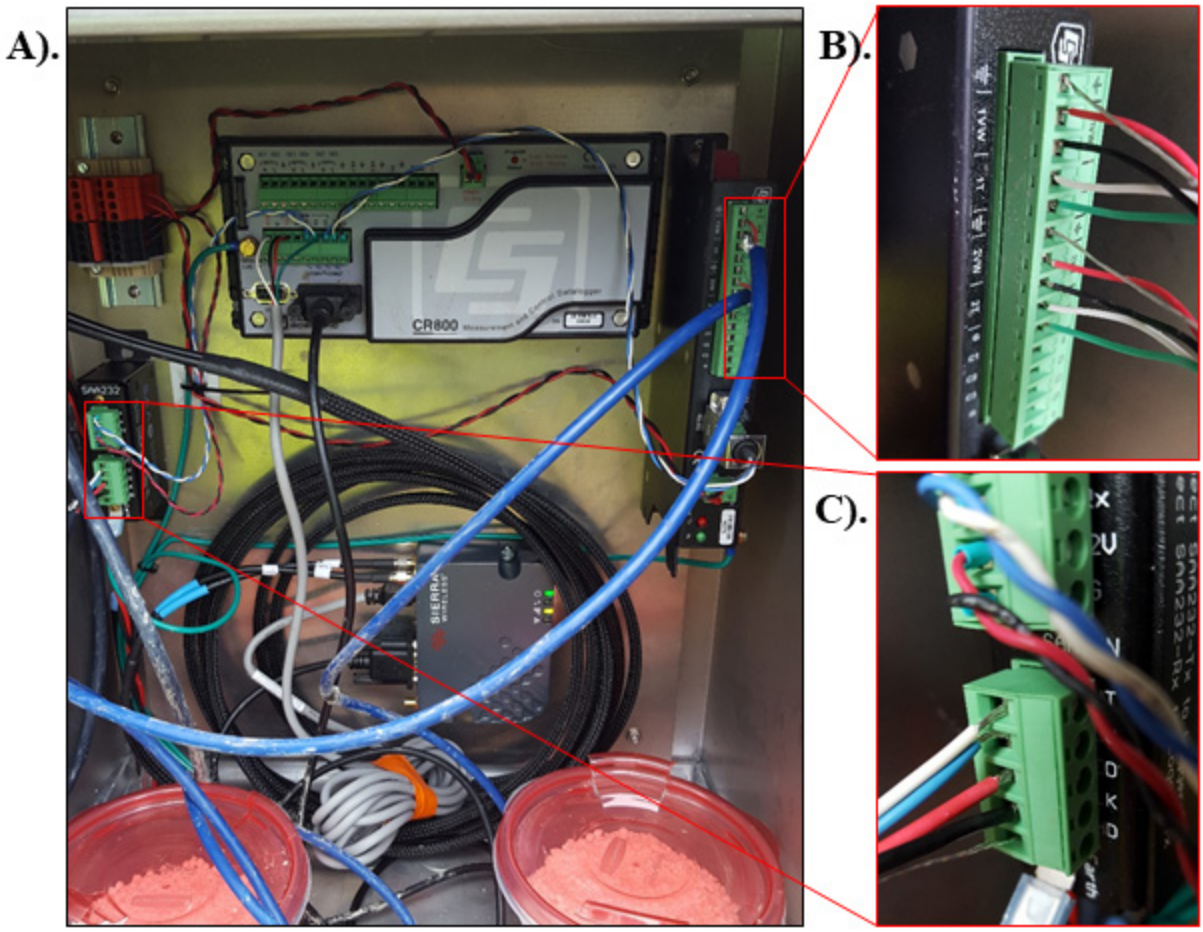

Figure 8.3: Electronics used to operate the SAA sensor. A). Overview of electronic components contained in the weatherproof casing including data logger and wireless modem. B). Pore pressure transducer multiplexer. C). SAA multiplexer. Photograph Credit: Dr Michael Bunn.

The SAA installed at Hooskanaden stopped reporting data after it sheared in January 2018, after approximately 150 mm of movement in the two months the system was installed (approximately 3 mm/day). The SAA at Arizona Inn stopped reporting data after it sheared in March 2019, with a cumulative total of 80 mm of movement. The instruments at Silver Point stopped functioning on October 1, 2020, after the wiring and solar charging was compromised by vandals – there was approximately 4 cm of surface movement in the system, a majority of which appeared to occur during an event on May 10, 2018. The SAA systems at Arch Cape lasted until February 6, 2023, with modest toppling kinematics and surface movements of approximately. The SAA system at Beverly Beach South lasted until October 31, 2023, with approximately 70 cm of surface displacements, primarily of which appeared to occur from an event in January 2024. The SAA system at Beverly Beach North lasted until February 12, 2021, when it was sheared by movement (> 27 cm) of a slump within the adjacent sea cliff. Movements recorded were limited to the upper meter of the inclinometer as it was near the headscarp of the failure.

Figure 8.4: Final SAA MEM's sensor setup at Spencer Creek on January 27, 2017. Composed of solar panel for power supply, SAA electrical components (top box), SAA battery (bottom box), and SAA sensor (in borehole). Photograph Credit: Dr Michael Bunn.

8.2 INSTALLATION OF RTK GNSS SENSORS

On-site instrumentation is essential to understand the kinematics of landslides. However, subsurface instrumentation will no longer perform once sheared by a moving slide. Arizona Inn and Hooskanaden Landslides were instrumented as part of ODOT Research SPR-807 and SPR-808 (Leshchinsky, 2018), representing active landslides that threaten much of the southern sections of Highway 101 in Oregon. These landslides move yearly as a result of rainfall and significant coastal erosion. Just recently, Hooskanaden began its most remarkable failure in decades, moving over 150 ft (~ 46 m) since the onset of failure on February 25, 2019 after almost 0.3 m of rain occurred in 24 hours, and the slide continued to move substantially several weeks after the main event. The rapid movement as well as the failure of this magnitude has resulted in shearing of the installed subsurface instrumentation and closure of Highway 101 with no effective means of quantitatively monitoring its movements through traditional geotechnical instrumentation. A quick-hit research and STIP supplemental funding to SPR-807 piloted recent advances in low-cost surface geospatial monitoring technologies (Global Navigation Satellite System Real Time kinematic, GNSS RTK) to monitor landslide movement for both Hooskanaden and Arizona Inn under conditions where subsurface investigation and monitoring is no longer ideal. Appendix C describes these systems in more detail and provides sample datasets. SPR-878 will build upon these results and deploy upgraded versions of these systems at additional sites.

As described in Section 8.1, both the Arizona Inn and Hooskanaden landslides were instrumented with state-of-the-art geotechnical monitoring systems– including both MEMS inclinometers, conventional piezometers and dataloggers– sending data back to OSU every half hour for analysis and interpretation. For both landslides, the shear zone has now been identified, a critical step in understanding the mechanics of a landslide. However, owing to the large internal deformations of these landslides, this instrumentation failed. Hooskanaden's monitoring system (installed in 2017 for SPR-808 (Leshchinsky, 2018)) sheared within 2.5 months due to its significant movement even prior to its recent dramatic failure. Arizona Inn's system (installed in 2016) saw progressive seasonal movements for its first two years until a sea cliff collapse in January 2019, after which it advanced relatively quickly. Owing to heavy rainfall, the same day that Hooskanaden began to fail catastrophically, the Arizona Inn landslide moved so much that its instruments have now also sheared and failed. This landslide, previously fixed in 1996, showed renewed signs of distress and instability as a potential upcoming threat to mobility on Highway 101 during the SPR-807 monitoring. Fortunately, GNSS sensors were installed prior to the major failure in January 2023. The current challenge of collecting long-term landslide monitoring data within large earthflows that traverse Highway 101 on the South Coast of Oregon is the physical limitation (breakage) of subsurface instruments during high landslide activity.

Based on the work to date on SPR-807 and prior efforts by ODOT, long-term geotechnical monitoring of these two highly active landslides is neither practical nor safe. However, by using rapidly deployable systems of small, inexpensive RTK GNSS units, ODOT may leverage real-time data to monitor slide movements without the concern of losing instrumentation under significant ground distress. Such a system has been employed successfully in numerous slides (e.g. Gili et al., 2000; Squarzoni et al., 2005; Benoit et al., 2015, etc.), and would enable high temporal resolution for landslide velocities with increased spatial resolution by deploying several nodes throughout the landslide mass. Supplemented with change detection using high-resolution lidar and photogrammetric techniques, which are already ongoing, we may increase spatial resolution of change. Thus, we may corroborate slide movement vectors between GNSS units, which have better survey control in both horizontal and vertical directions. Change detection has been demonstrated to be a reasonable means of estimating landslide distress, demonstrated by the project team for the Spangler landslide in 2018-2019 (Babbel et al., 2019); however, challenges such as vegetation and survey control may limit its accuracy. These monitoring efforts are also limited in terms of temporal resolution. RTK GNSS enables more continuous tracking of landslide movements than repeat UAS or TLS lidar surveys. Examples of their use to support change detection are provided in Sections 10.0 to 12.0.

8.2.1 Research tasks

In the pilot investigation of GNSS landslide monitoring technology, the research team completed the following tasks during SPR-807:

1. Designed, fabricated, and employed rapidly deployable RTK GNSS units. Pilot systems were installed at the Hooskanaden and Arizona Inn landslides (e.g., Figure 4.15). The team worked with ODOT Geometronics for survey control, coordination, and implementation recommendations. Additionally, several pilot tests were conducted during the design process. The sensor design was also upgraded to be more robust against strong winds on the coast.

2. Leveraged past monitoring of slope failures and erosion from SPR-807 and SPR-808 to corroborate RTK GNSS and lidar change detection measurements. Knowledge of the slide plane observed from the in-situ monitoring described in Section 8.1 supplemented observed surface movements and enabled interpretation of slide kinematics.

3. Created a framework and guidance for reconstructing slide dynamics and plausible slide planes based on surface movement trajectories (Section 13.0).

4. Corroborated relationships between ongoing monitoring of rainfall and coastal erosion with landslide movements, relevant to both SPR-807 and SPR-808 (Section 11.0 and 12.0).

5. Provided recommended guidance for GNSS RTK rapid deployment for future landslides impacting ODOT infrastructure (Appendix C and ongoing work in SPR-878).

Figure 8.5. Example RTK GNSS rover system installed at the Arizona Inn site.

8.2.2 Implementation and significance

Deployment of a GNSS RTK system provided long-term, continual landslide monitoring data critical to SPR-807, SPR-808, and Region 3, and also showcased a potential technology transfer that may enable ODOT to have significant cost-savings through augmenting the cost of extensive drilling and geotechnical monitoring. In lieu of subsurface instrumentation lost to these two active slides, this research supported the monitoring needs that are a part of ODOT Research Projects SPR-807 and SPR-808, as well as provided guidance for and proof-of-concept of these

supplementary surface monitoring techniques for ODOT. In the case of landslides that exhibit significant seasonal movements – e.g. many of the landslides on Oregon's South Coast – GNSS RTK may be the only viable means of long-term monitoring of landslide kinematics. Understanding landslide kinematics assists ODOT with planning for mitigation to avoid or at least preparation for the next slide closure of our highway systems. SPR-878 will continue to build upon these efforts and deploy these sensors to additional sites.

9.0 IN-SITU SENSOR DATA ANALYSIS

9.1 FIELD INSTUMENTATION DATA ANALYSIS

This section describes the current analysis results from the instrumentation installed at the sites.

9.1.1 Silver Point

Silver Point has shown some activity around May 2018, primarily as an expression of toppling (Figure 9.2) behind the major slump that daylights at the sea cliff. This suggests recent, but intermittent activity of a sea cliff failure at the site. Movement occurred during elevated levels of groundwater. However, groundwater levels have progressively increased at the site since monitoring without always being associated with ground movements. This likely suggests localized activity downslope of the boring may be driving the observed toppling response and extension upslope. Unfortunately, this site became irreparable from vandals in April 2020.

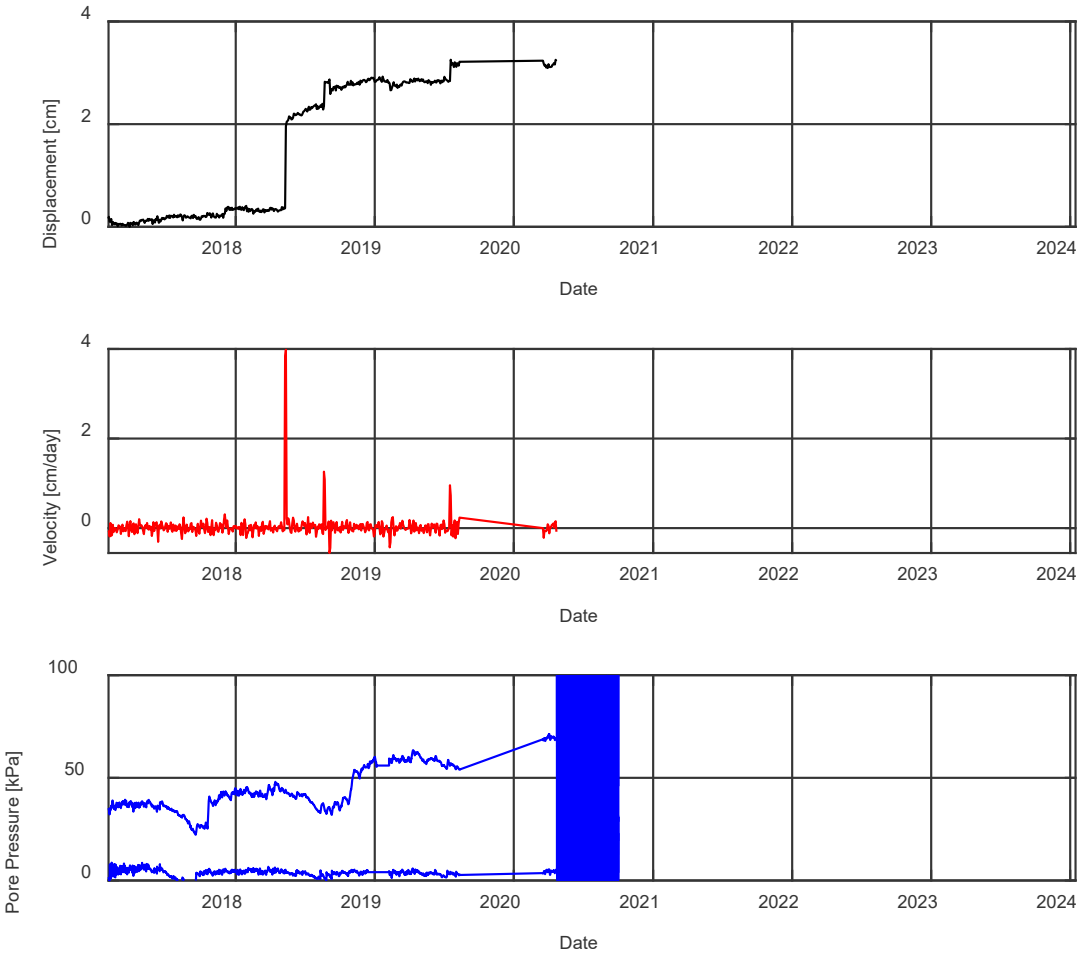

Figure 9.1: Monitoring data from Silver Point site. One displacement event occurred on May 10-12, 2018. The site lost functionality owing to vandalism in April 2020.

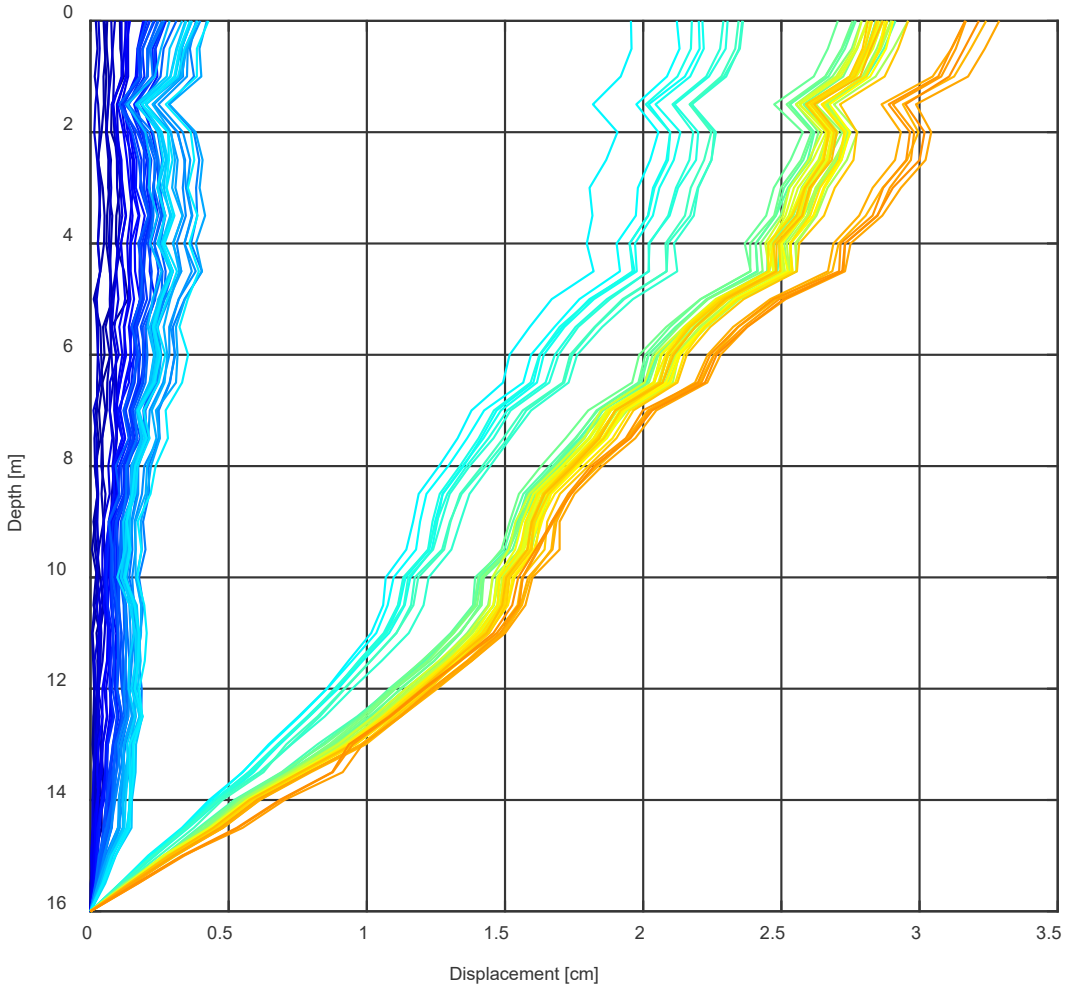

Figure 9.2: Measured shear profile at Silver Point site, demonstrating toppling behaviour that occurred between May 10-12, 2018.

9.1.2 Arch Cape

Arch Cape has been the third most active site, with notable topping occurring within the monitored inclinometer system. This corresponds to an expression of toppling relating to the slump in front of the boring. Overall extension has been almost 50 mm since installation (Figure 9.3 and Figure 9.4), over 40 mm of which may be attributed to ground movements, suggesting movement of the slope failure on the leeward side towards the ocean. However, the movement appears to have slowed over the past few years, making it difficult to discern whether movements owe to settlement of grout or equilibration of the ground. This site is by far the most constrained, where progression of slumps from coastal erosion on the narrow beach below may leave limited right-of-way to enter the tunnel just meters north of the site. Interestingly, the piezometric response of the site constantly follows tidal changes (Figure 9.5) with a slight lag, suggesting a level of connectivity between the sea cliff and the ocean tides. This may result from voids in the cliff (e.g., sea caves) that were infilled with beach sand and then subsequently closed off by landslide deposits from failure of the upper portion of the slope. The system lost functionality in February 2023.

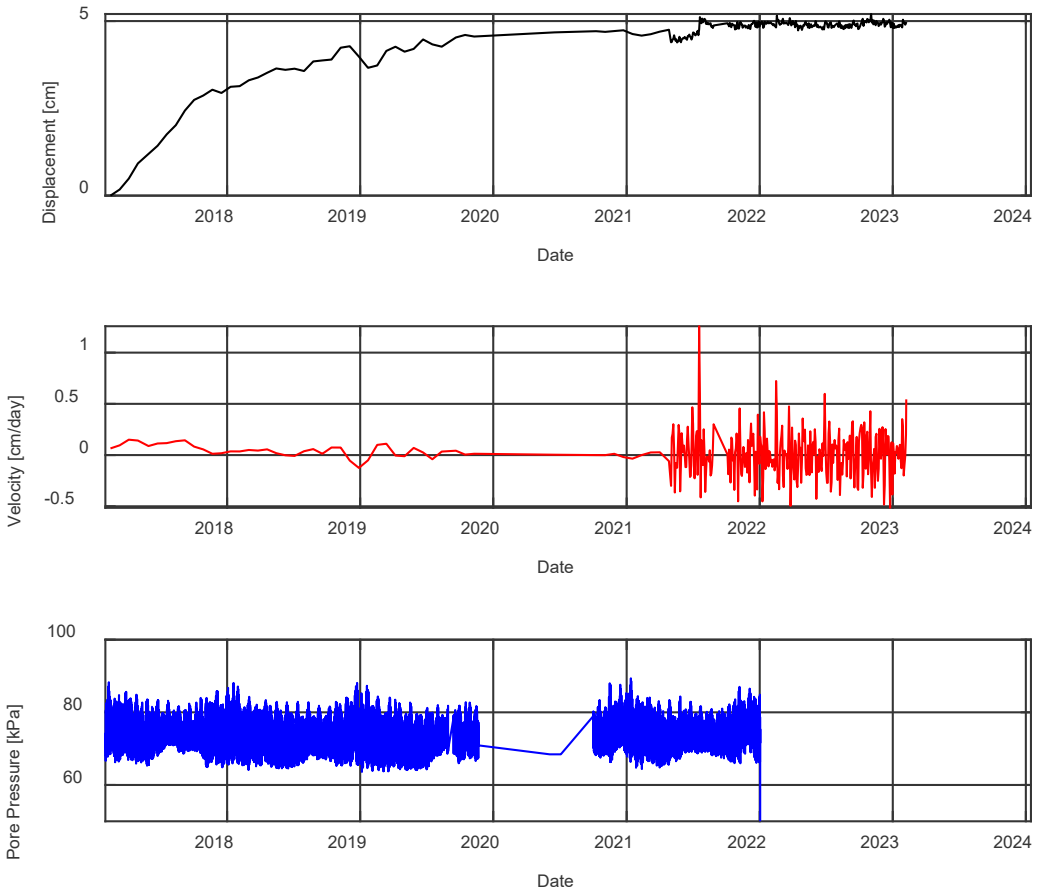

Figure 9.3: Monitored velocities and pore water pressures in the Arch Cape site. The transition in velocity and displacement resolution owes to processing very large datasets and changes in intervals owing to data processing. A data gap exists from 2019-2020.

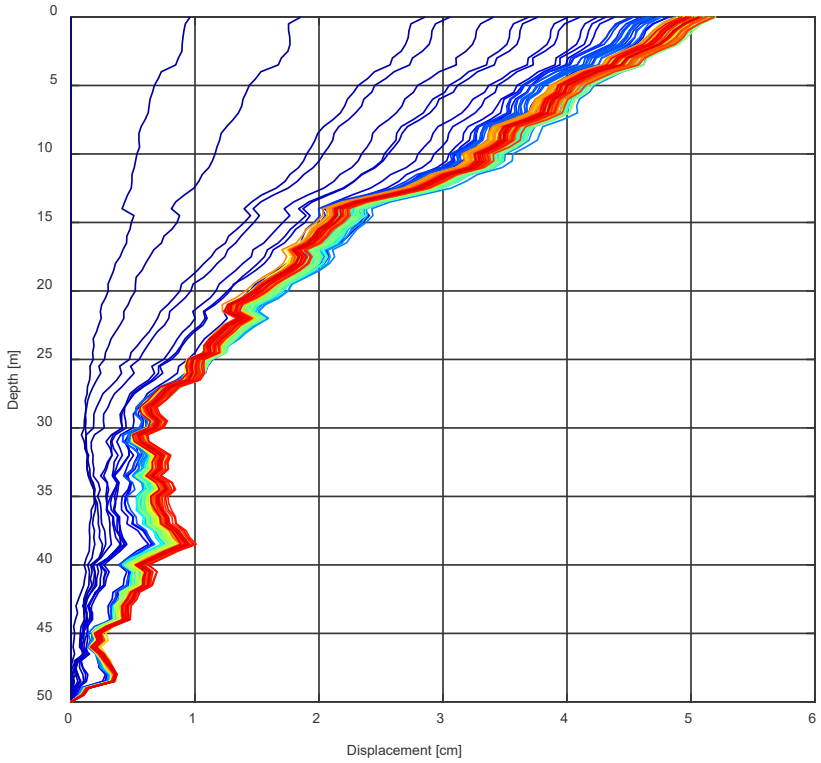

Figure 9.4: Monitored shear profile at the Arch Cape site. The initial discontinuity with time likely reflects settlement of the grout used in installation.

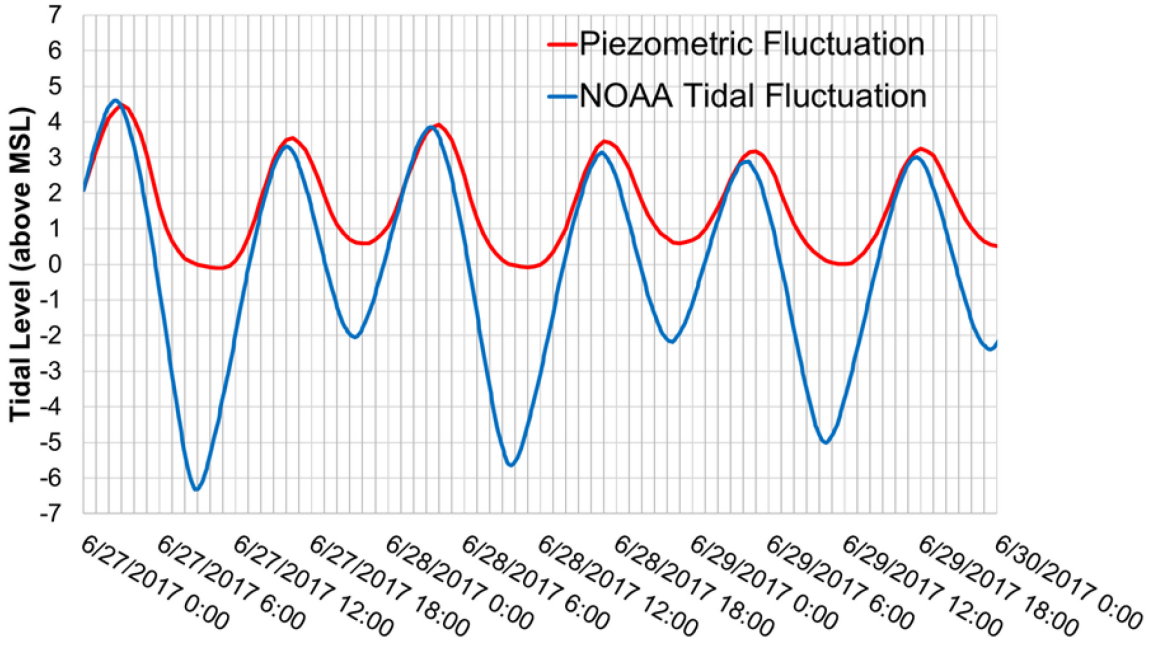

Figure 9.5: Piezometric profile of lower piezometer in comparison to tidal fluctuations.

9.1.1 Spencer Creek North

Spencer Creek North has shown limited deformation since the installation of borings in early 2017, but eventually was part of a failure that occurred from February 3-5, 2021. It has also provided interesting insight into the rate of change in groundwater within the cemented sea cliffs that comprise much of Oregon's Central Coast (Figure 9.6). Groundwater levels change rapidly after storm events at this site, likely owing to the geologic structure of the sea cliffs in comparison to those just south of the site (which are less weathered). During the failure, the inclinometer was just within the headscarp; consequently, the recorded depth of failure was 2 m, but the actual maximum depth was likely between 8 and 15 m in thickness. Throughout the wintertime, groundwater levels tend to stay elevated, eventually reaching steady state levels in the relatively dry summer and fall months. Figure 9.8 shows the instrumentation and tension cracking observed at the site resulting from the failure.

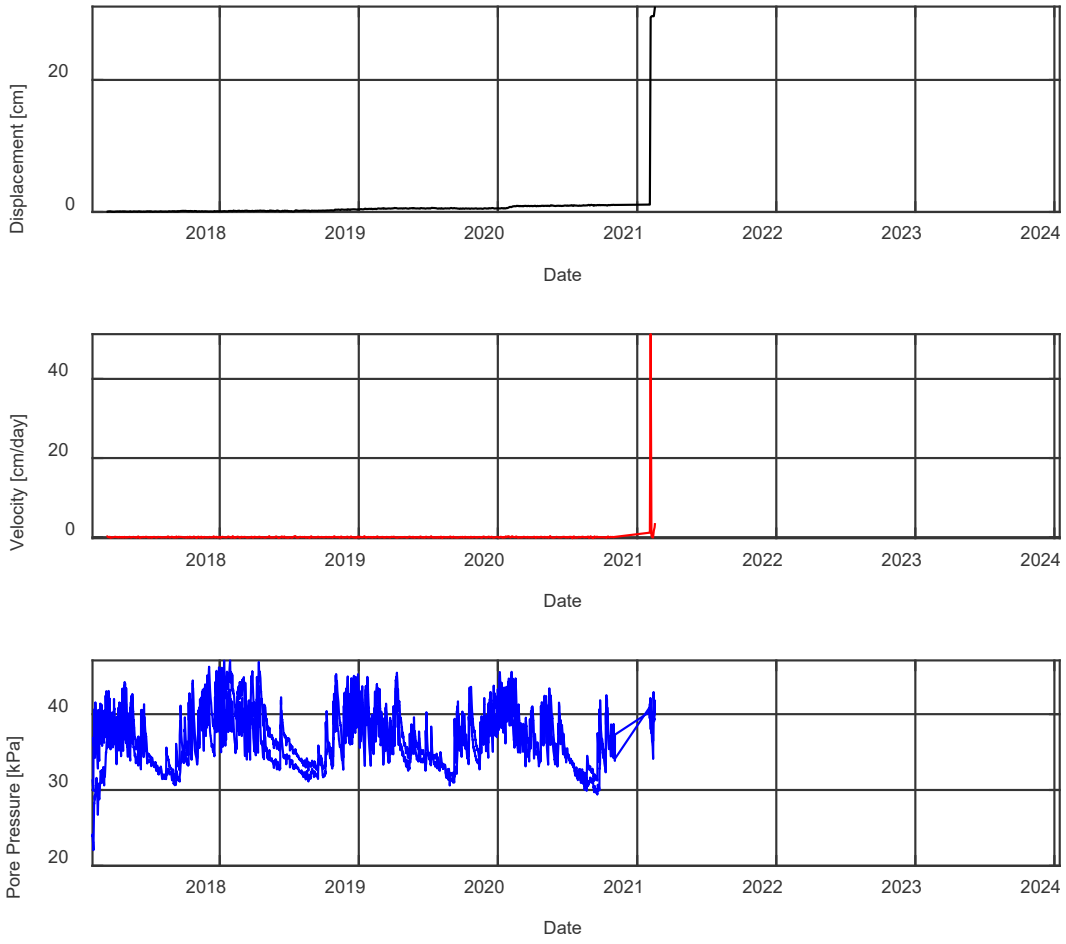

Figure 9.6: Monitored velocities and pore water pressures in the Spencer Creek North site.

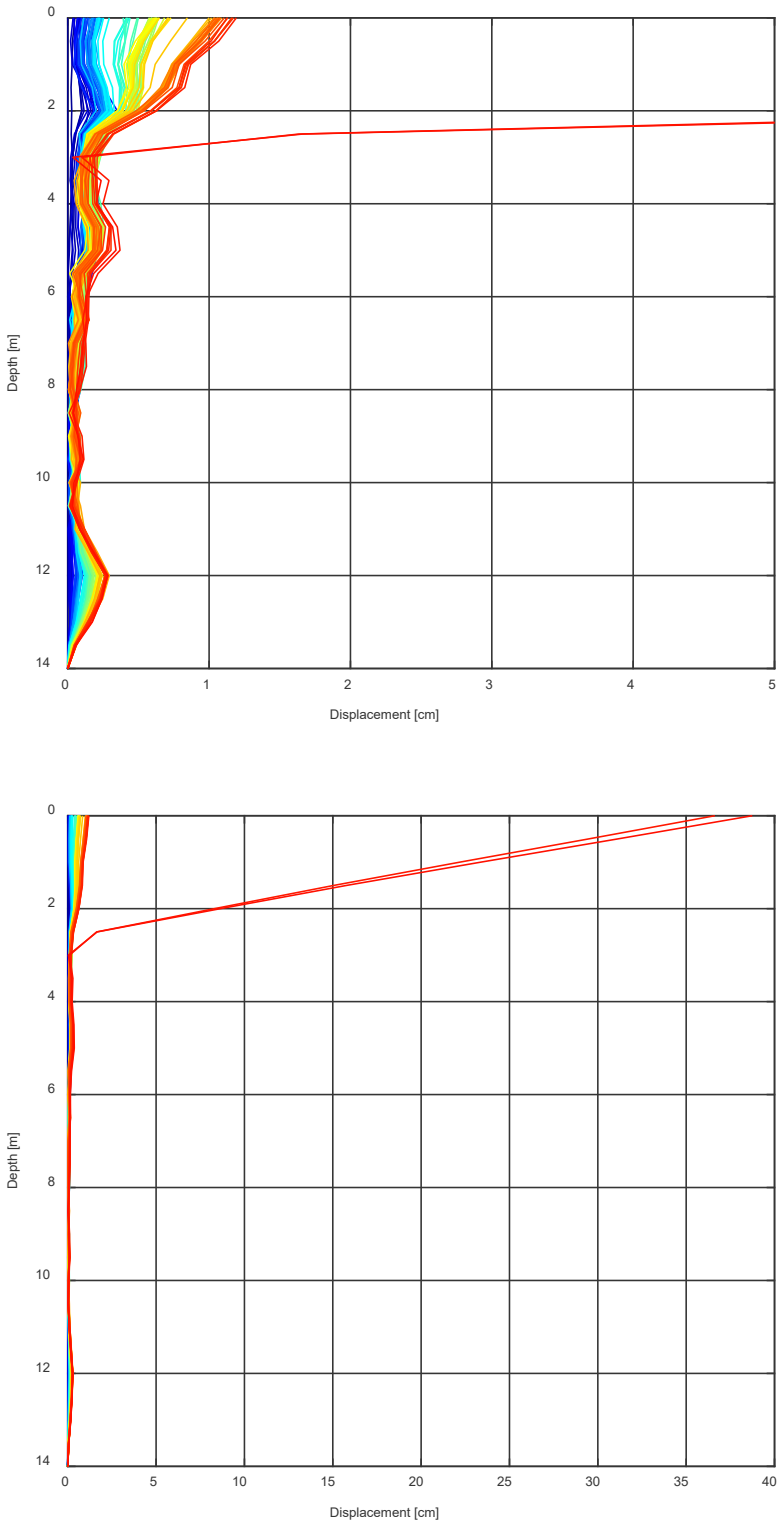

Figure 9.7. Inclinometer data before (left) and after (right) the 2021 failure event.

(a)

Figure 9.8(a): Instrumentation and tension cracks from slump failure occurring in 2021 at the Spencer Creek North Site. (a) close-up view in 2021, (b) larger view in 2021, and (c) larger view in 2022 showing continued slumping at the site.

(b)

(c)

Figure 9.9(b-c). Instrumentation and tension cracks from slump failure occurring in 2021 at the Spencer Creek North Site. (a) close-up view in 2021, (b) larger view in 2021, and (c) larger view in 2022 showing continued slumping at the site.

9.1.1 Spencer Creek South

Spencer Creek South has shown limited deformation since installation of borings in early 2017 until an event that occurred from January 22-26, 2022. Nonetheless, it has provided interesting insight into the rate of change in groundwater within the cemented sea cliffs that comprise much of Oregon's Central Coast (Figure 9.9). Groundwater levels change rapidly after storm events, gradually dropping to steady state levels after period of modest rainfall. Throughout the wintertime, groundwater levels tend to stay elevated, eventually reaching steady state levels in the relatively dry summer and fall months. The failure event demonstrates a distinct shear zone at 12 m below the ground surface, which demonstrates the relative rapidity and intermittency of these failure events.

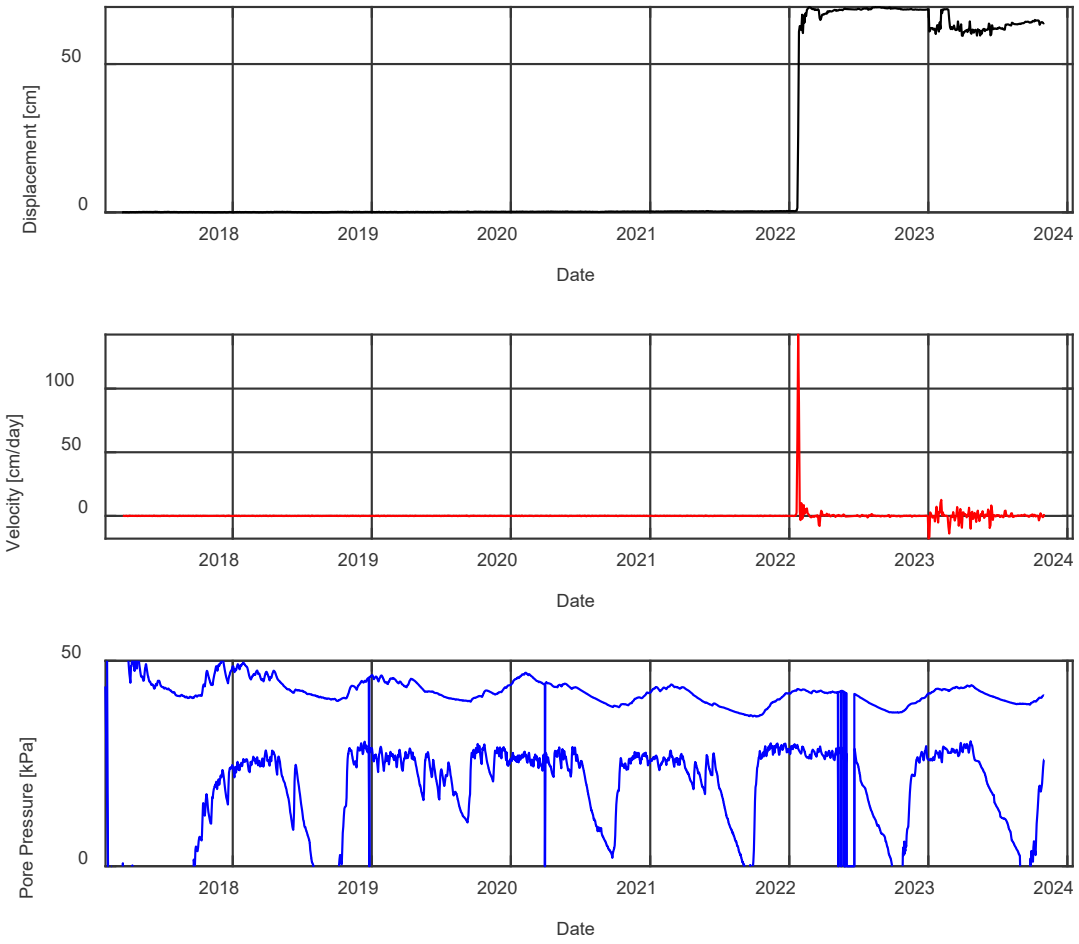

Figure 9.10: Monitored velocities and pore water pressures in the Spencer Creek South site. The discontinuity (January 22-26, 2022) likely reflects ground movements nearby the inclinometer, which occurred during high groundwater conditions.

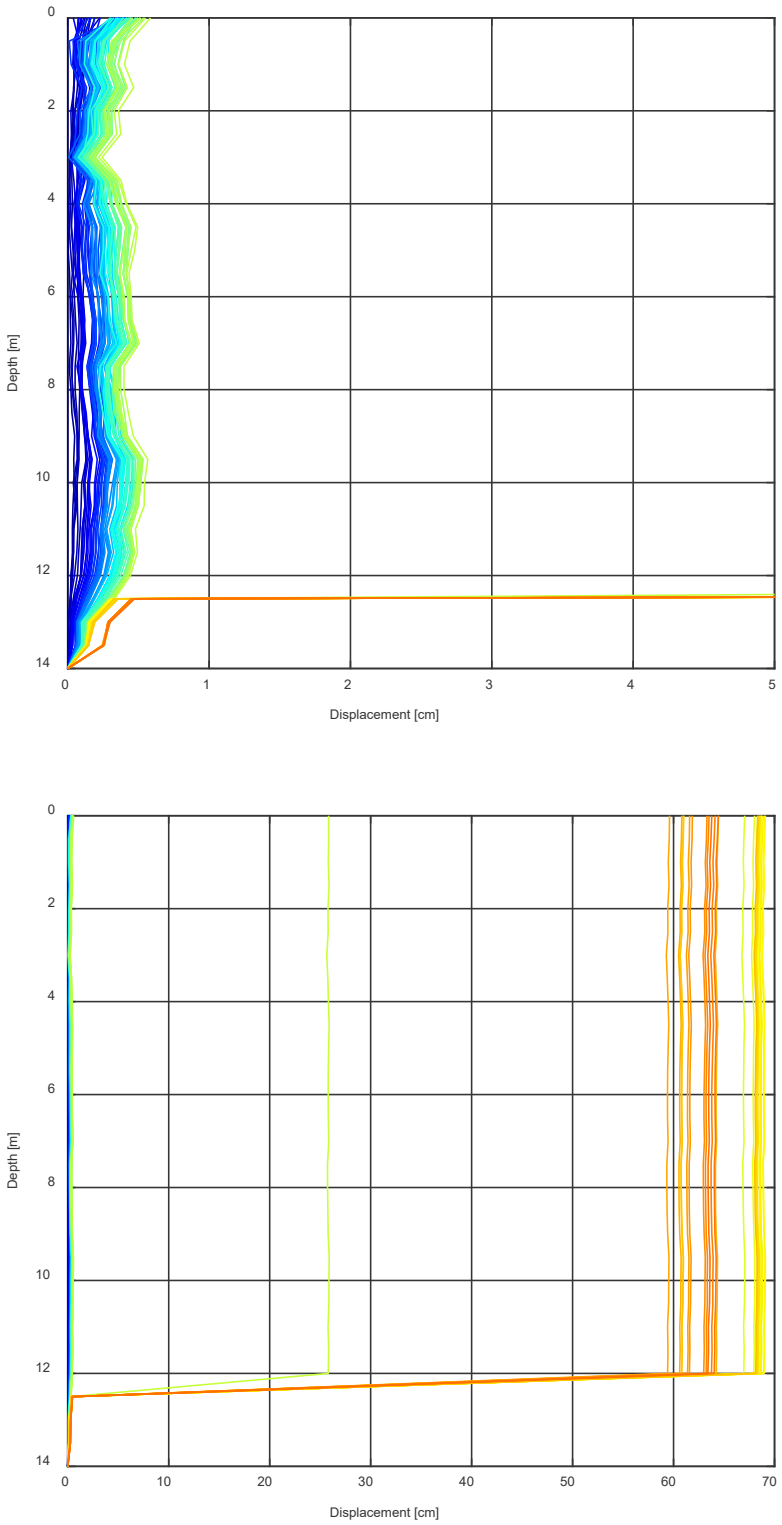

Figure 9.11: Inclinometer Movements at Spencer Creek South. A distinct event occurred in January 2022, with a clear shear zone at approximately 12m b.g.l. This is associated with a nearby complex of sea cliff slumps.

9.1.1 Arizona Inn

Arizona Inn has been the second most active landslide of the six instrumented sites. It has shown progressive movements since the installation of inclinometers and piezometers. A large sea cliff collapse at the toe has been observed since installation and has progressed significantly. During the winter of 2019, there was significant rainfall, resulting in the onset of significant acceleration (almost 10 mm in an hour, Figure 9.11 and Figure 9.12). After an early march storm that caused Hooskanaden to fail, the inclinometer system at Arizona Inn also failed. The data on landslide movements and depth of the shear zone was transferred to ODOT Region 3 for use in potential planning for mitigation in the coming biennium, a direct transfer of relevant data. Interestingly, after movement, piezometric levels dropped in the landslide, owing to significant movement of the lower sea cliff collapse. The coupled real-time monitoring of groundwater and a shear profile shown below exhibits the utility of such a coupled system.

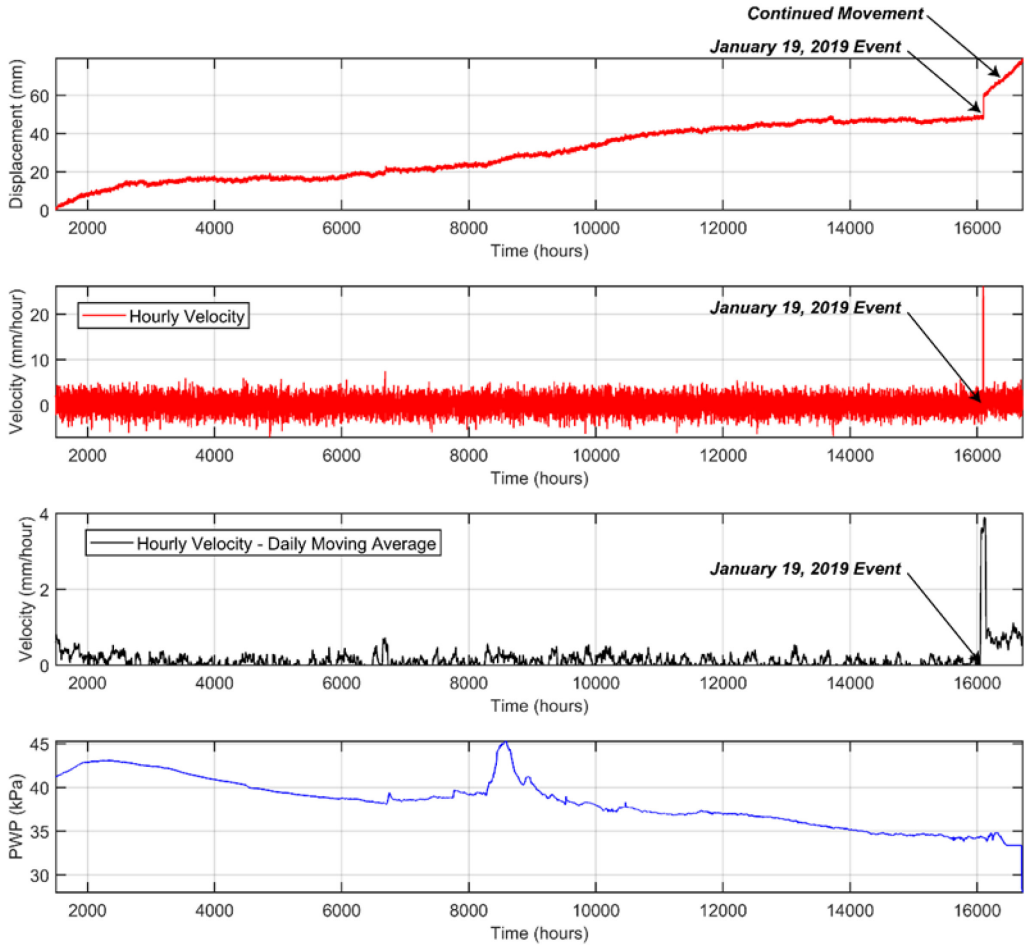

Figure 9.12: Monitored landslide velocities and pore water pressures in the Arizona Inn landslide.

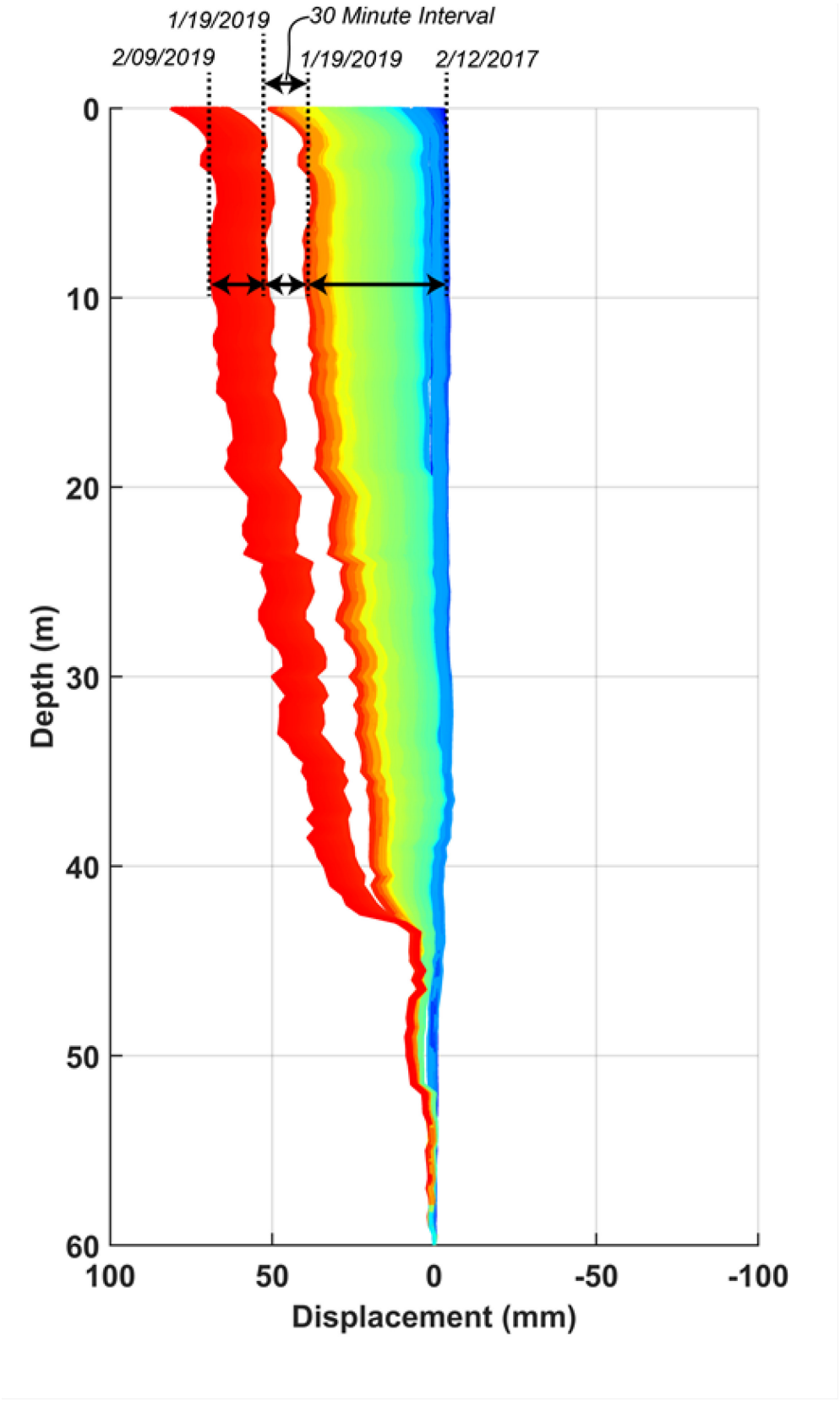

Figure 9.13: Monitored shear profile at the Arizona Inn landslide.

9.1.2 Hooskanaden

Hooskanaden has been the most active landslide of the six instrumented sites. An inclinometer was installed in November 2017, and soon thereafter sheared along with piezometers by January of 2018 with over 150 mm of displacement (Figure 9.13). The shear plane was measured at 35 m, and the shear profile was used by ODOT R3 engineers after the significant movement that occurred in 2019. No borings or monitoring had been installed in the landslide to date, thus this data was invaluable for repair efforts of Highway 101 after failure. At the time of installation, Hooskanaden exhibited a relatively constant velocity of 3 mm/day. This is commensurate with yearly velocities of 1-2 m per year (under progressive, but not catastrophic failure conditions). Piezometric levels did not change significantly after the grout within the borehole had set but are suggestive of elevated pore pressures that are greater than hydrostatic levels (i.e., 55 m of head as compared to 35 m of depth). The short lifespan of ground instruments at Hooskanaden has prompted further surface monitoring, including several flights of UAS lidar and installation of a series of GNSS rovers throughout the slide mass. The SAA at Hooskanaden was not operation during the 2019 surge event described in Section 11.0.

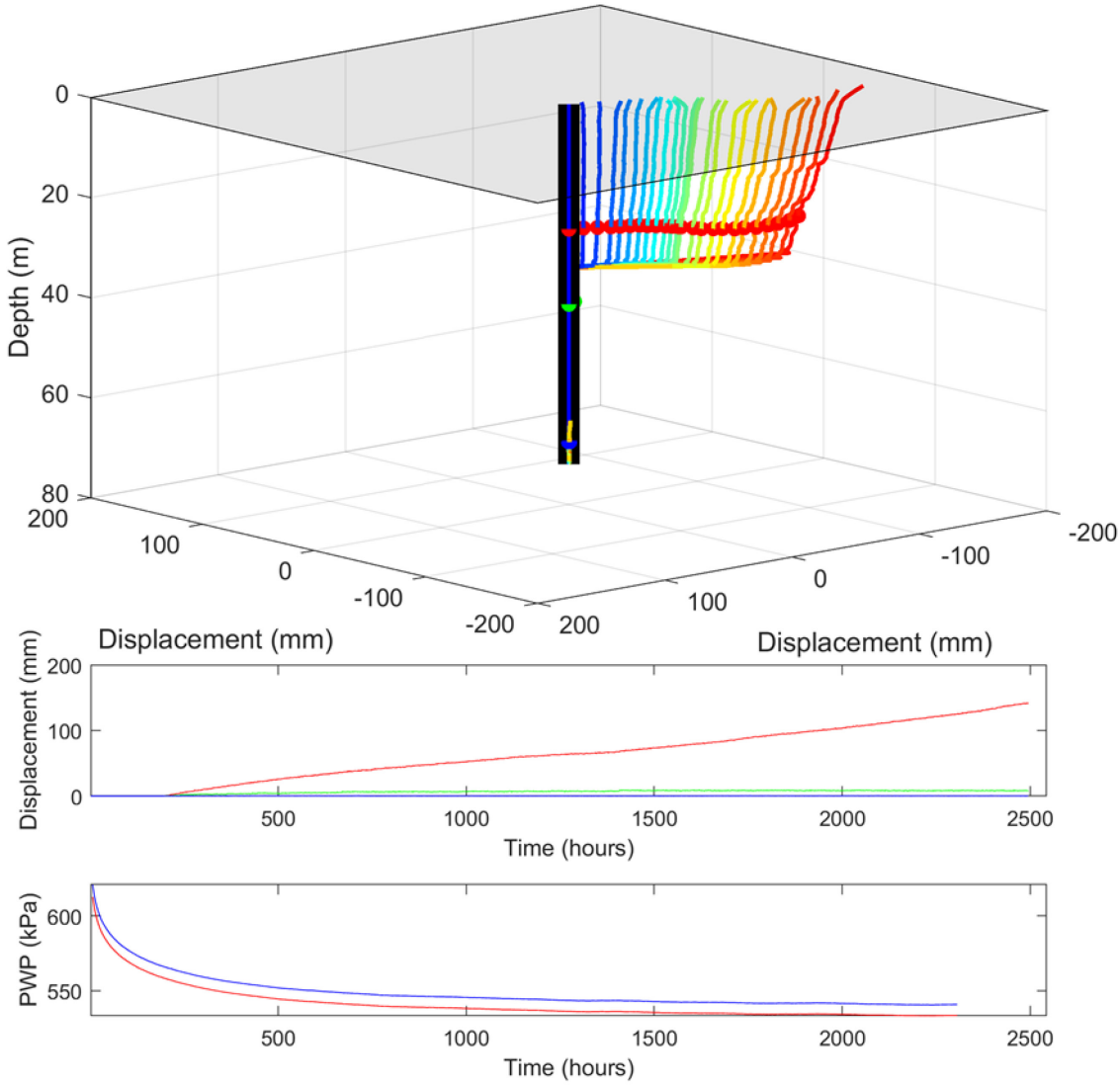

Figure 9.14: Displacements, pore pressures, and inclinometer profile from Hooskanaden monitoring site.

10.0 LANDSLIDE DATA ANALYSIS METHODS

This section describes the new methods developed to perform analyses with the landslide associated data collected during this study. These analyses focused on quantifying landslide displacement rates (both spatially and temporally) across Arizona Inn and Hooskanaden. The implementation of these tools are presented in Section 11.0 for Hooskanaden and Section 12.0 for Arizona Inn.

Landslide data collected in this study included geospatial survey data consisting of terrestrial lidar, UAS SfM, and UAS lidar data. Additionally, near real-time displacement measurement data was obtained using RTK-GNSS rovers installed at Arizona Inn and Hooskanaden mid-way through the study as outlined in Appendix C. In order to analyze these data two unique, novel landslide analysis tools were developed, *SlideSim*, and *LADI*. A summary of the methodology of each method is outlined below.

10.1 SLIDESIM

SlideSim accurately extracts dense 3D vectors of landslide displacement between sequential, high resolution geospatial survey data in the form of DEMs (Digital Elevation Models). A complete description of the creation, methodology, and application of *SlideSim* can be found in Senogles et al. (2022). The following contains a short summary as it pertains to this study.

SlideSim produces an optimal flow predictor that outputs dense 3D landslide displacement vectors between sequential DEM rasters by using a physics-based simulation approach to enable self-supervised learning of the network. *SlideSim* consists of three primary steps:

1. Generation and simulation of synthetic training data through deterministic modeling of the landslide surface using a conservation of mass (COM) approach for many different input scenarios;

2. End-to-end training of an optical flow predictor network using RAFT (Recurrent All-Pairs Field Transforms) (Teed & Deng, 2020) architecture and transfer learning followed by training on the simulated dataset;

3. Inference and calculation of the 3D landslide displacement vector map by first feeding sequential DEM rasters through the trained model to generate 2D horizontal displacement vectors followed by deterministic computation of the vertical component of displacement.

A synthetic dataset of labeled displaced landslide DEM rasters is generated to train the optical flow predictor using a self-supervised learning process, where the supervisory signal used in training is generated in an automated process. Synthetic data enable a sufficient amount of training data, which are impractical to collect and hand label from sets of pre and post-movement DEMs of actual landslide movements. To generate synthetic data, a physics-based, conservation of mass (COM) approach similar is used. The principle of COM states that the mass of a closed system must remain constant over time. Using this principle and assuming incompressible

behavior and rigid basal motion, the change in elevation across the landslide can be computed such that the mass of the landslide remains constant for a given set of boundary conditions (landslide boundary and slip surface) and a given velocity field. This approach allows a synthetic DEM raster representing the displaced landslide to be generated over N movement epochs using finite grids representing unique landslide boundary grids, landslide slip surface elevations (SSEM), and horizontal velocity rates. Figure 10.1 shows realistic approximations of these finite grid approximations.

The landslide boundary raster serves as a Boolean mask where cells contain values of 0 and 1 outside and within the landslide boundaries, respectively. These were drawn to represent possible landslide boundaries and did not necessarily represent the precise, real-world landslide boundary. The slip surface elevation model (SSEM) is generated for each landslide boundary by fitting a 3D hybrid-spline surface to the landslide boundary (Bunn et al., 2020), which provides a first order estimate of the 3D landslide slip surface based on surface expressions of landslide features. Two-dimensional (2D) horizontal velocity grids are generated using a randomly initialized spline procedure to generate complex velocity grids representing a wide range of possible landslide displacement scenarios.

After training of the optical flow predictor network using the above augmented data and simulation procedure, displacements between two DEMs can be computed by performing inference on the trained model. Visual representations of the DEMs should be computed and fed into the model along with the optimized weight parameters computed during the training process, which will output a “flow” raster where each cell contains the predicted horizontal (u) and vertical (v) velocities between the two DEMs in image coordinates. The actual vertical component of displacement can then be calculated by computing the per cell difference of the DEMs using a remapping procedure to correct for the horizontal displacement prior to vertical differencing.

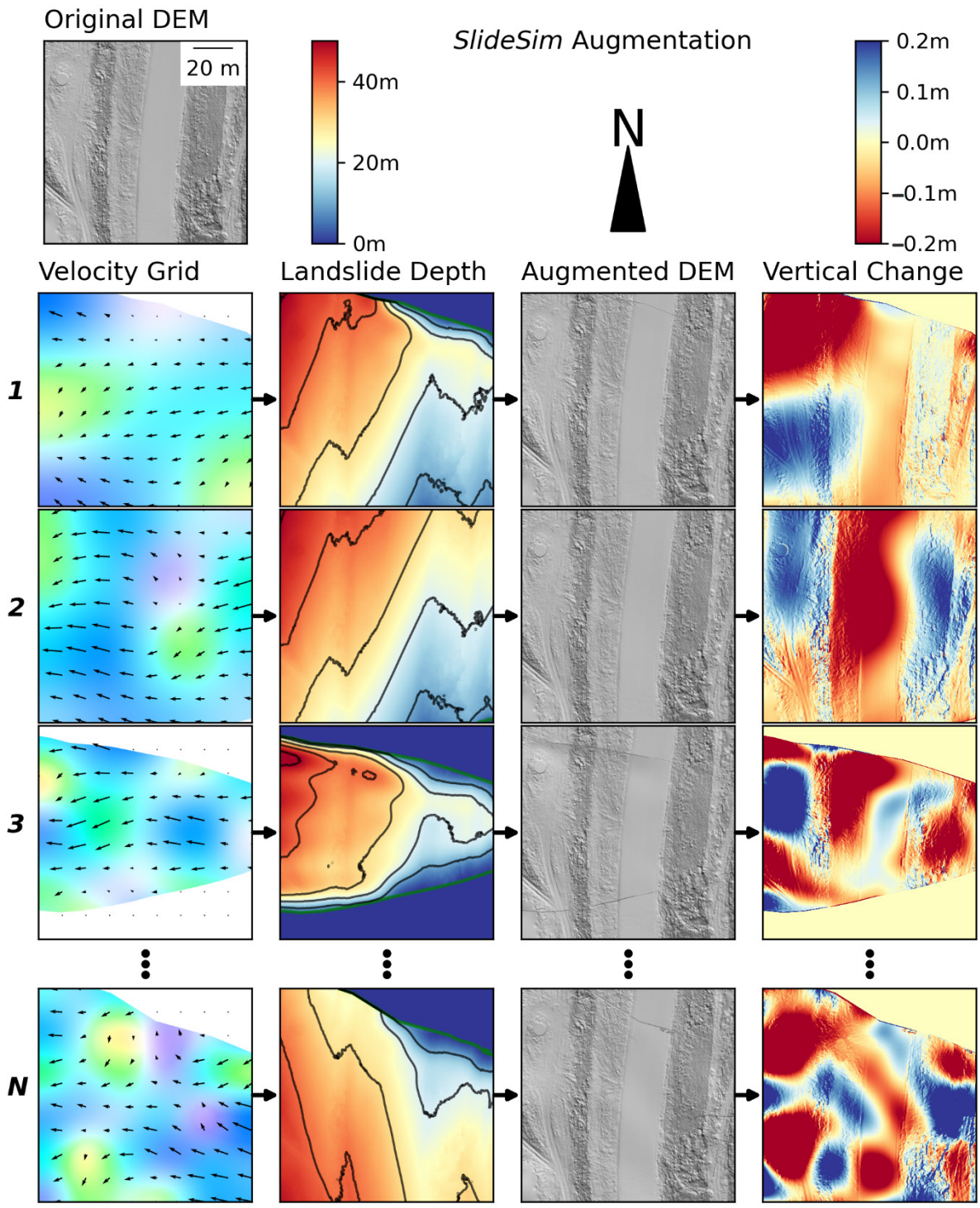

Figure 10.1: Examples of *SlideSim* augmentation, showing the augmentation of the original DEM for several velocity grid, landslide boundary, and slip surface combinations. The numbers of coarse grid points used to generate each of the velocity grids are 9, 16, 25, and 36 for rows 1, 2, 3, and N, respectively. Velocity vector magnitude/direction is indicated by quiver arrows (scaled 20×) as well as background color (blue= substantial movement, green/yellow = intermediate, purple = small).

10.2 LADI

LADI (Landslide Displacement Interpolation) was developed to enable high spatial, high temporal resolution interpolation of landslide surface displacement by combining high spatial resolution, remotely-sensed observation data with high temporal resolution in-situ sensor data. A complete description of the motivation, creation, methodology, and application of *LADI* can be found in Senogles et al. (2023).). The following section contains a short summary of the *LADI* methodology as it pertains to this study. An implementation of *LADI* in the Python programming language is available at https://github.com/asenogles/ladi/ in conjunction with this report.

LADI assumes that the spatial pattern of landslide displacement remains relatively constant over short time intervals between sequential spatial surveys. This assumption is applicable to slow-moving, non-evacuative, deep-seated, landslides but may not be applied to other landslide hazards, such as catastrophic events like debris flows or rockfalls that typically occur at timescales precluding direct observation. To perform interpolation, LADI utilizes a Kalman filter inspired approach for both the spatial and temporal components of interpolation. Kalman filters are a set of model-based filters that combine measurements and their modeled uncertainties with a predicted state based on physical modelling of the previous state to produce an estimate of the current state. A common application of Kalman filters is for dynamic positioning and trajectory estimation for kinematic surveying applications, where measurement data from multiple sensors, such as GNSS and IMU and their uncertainties are combined recursively to estimate the current position.

LADI separates the design of the spatial interpolation (referred to as the spatial filter, or SF) from temporal interpolation (referred to as the temporal filter, or TF), allowing interpolation across each domain to be ran independently or combined (Figure 10.2). Computationally, landslide displacement for a given time interval can be spatially approximated using a 2D numerical discrete grid (referred to as the dense displacement grid, or DDG), where each cell contains the 2D or 3D vector of displacement that occurred at that cell location. To operate, *LADI* requires at least one DDG (computed from two spatial surveys), referred to as the calibration data, and at least one displacement measurement taken at the time where the spatial interpolation is desired. Using these data, *LADI* first computes and subsequently normalizes the spatial displacement gradient across the landslide using the calibration DDG data in the pre-processing stage. A sparse displacement grid (SDG), which is a grid with missing data with the same dimensions as the DDG is then created and seeded with the displacement measurement(s). The SDG along with the normalized gradients are then used to compute the interpolated DDG using the SF component of *LADI*. This SF is composed of an adapted spatial Kalman filter that follows the regular Kalman filter convention of computing a forward and backward pass and combining the passes with a smoothing filter. If additional data epochs are present, the TF can be used to further smooth the data along the time axis of each spatial cell using a temporal Kalman filter. A full description of each part of *LADI* including the mathematical derivations can be found in Senogles et al. (2023).

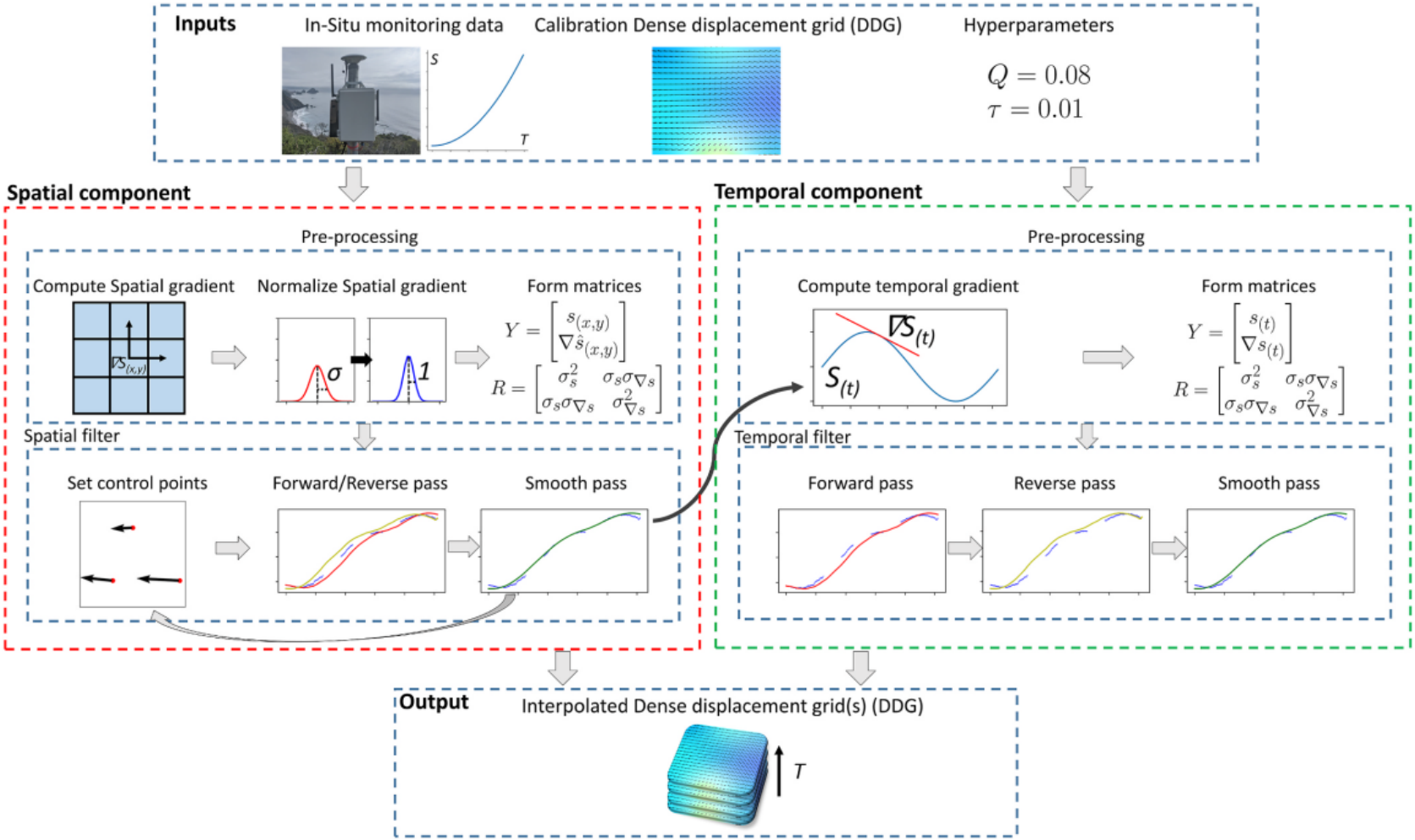

Figure 10.2: Outline of the *LADI* methodology, including inputs, pre-processing steps, spatial and temporal filters, and output.

11.0 HOOSKANADEN LANDSLIDE SURGE EVENT

This section summarizes key highlights from the detailed analysis conducted by Alberti et al. (2020). Readers are referred to Alberti et al. (2020) for more thorough documentation of the event.

In 2019, the Hooskanaden landslide displayed a vertical surface displacement exceeding 12 m and a lateral displacement of over 40 m, primarily concentrated near US101 (Alberti et al., 2020). These measurements were derived from manual feature tracking between two lidar epochs collected on November 21, 2018 (terrestrial lidar) and March 15, 2019 (UAS lidar). While the landslide has been historically active with several large movements in the past several decades, this represents the first major event in over 20 years. The majority of this movement occurred within a three-day period defining the associated surge event. The maximum surface displacement rate at the highway grade reached approximately 60 cm/h during the surge, placing it within the range observed in other earthflow surge events. Due to the earthflow's relatively regular activity, subsurface knowledge of the landslide shear surface before the surge is limited.

A comparison of TLS and UAS data enabled digitization of 3D vectors representing the kinematics of the failure. These vectors were created by selecting similar features (i.e., utility poles, trees, stumps) in Potree visualization (Data are available at: http://research.engr.oregonstate.edu/geomatics/projects/OregonCoast/Hooskanaden/Feb2019/lidar/), and represent the epoch between October 2018 and March 2019 (Figure 11.1). The vectors of movement highlight that the greatest mass movements occurred in the central part of the earthflow that traverses Highway 101, corresponding to the steepest topography at the site. Movements in the central portion of the earthflow ranged from 15 to 40 m of 3D displacement, generally oriented in the downslope direction of the topography. More modest movements (2-5 m) were observed upslope in (1) the major contributing area that nears Carpenterville Highway, and (2) on the northern flanks of the landslide. These significant, but more modest movements are an expression of extension, which is corroborated by numerous tension cracks observed throughout in this portion of the earthflow (Figure 11.2D). Downslope of the most active portion of the earthflow is a relatively gentle bench, which exhibited moderate displacements, ranging from 5-10 m. This portion of the earthflow begins at the base of the most active landslide zone and ends the Pacific Ocean. The lower displacements with respect to the central portion of the slide mass are and expression of compression, which is corroborated by notable heave on the order of 3-5 m near the ocean, most notably observed as a fault gouge that daylighted within the narrow beach at the base of the earthflow (Figure 11.2A).

A particle image velocimetry (PIV) analysis (Figure 11.3) was completed to evaluate the horizontal movement occurring at the site. Two composite orthophotos from surveys approximately 24 hours apart on March 2, 2019 and March 3, 2019 were compared. From this analysis compression is observed near the toe of the slide where the horizontal displacement vectors become shorter and shorter. Additionally, it appears to consist of two distinct flows between the northern and southern portion of the slide. Example detail images of the orthophoto collected on March 3, 2019 survey are shown in Figure 11.4.

The only recent subsurface data, obtained through borehole drilling and sampling in the winter of 2017-2018 west of Highway 101, revealed a distinct shear surface at a depth of approximately 30 m below grade. The borehole, equipped with a MEMS inclinometer and two Vibrating Wire Transducer (VWT) piezometers, recorded about 15 cm of horizontal movement between November 21, 2018, and January 9, 2019. A perched water table was noted at around 5 m in depth during drilling, but it disappeared the next day, likely due to ponded water on the eastern side of the highway alignment. A piezometer at the base of the boring indicated a groundwater depth of 15 m below grade; however, substantial uncertainty exists with this estimate as the piezometer sheared within 48 days of installation, and it is possible that the grout surrounding the piezometer had not entirely cured or enable natural hydrological pathways yet.

The main mass of the landslide varies in depth from at least 30 to over 45 m, with the shear surface depth at the highway alignment estimated at approximately 33 m. A time lag of approximately 1 week between correlated peak daily rainfall and landslide acceleration suggests modulated rainwater infiltration to the active shear zone at the slide base, where infiltrating groundwater must pass through mixed geologic materials or highly-sheared claystone, sandstone and claystone boulders, and a matrix of fine-grained material.

Based on known geologic conditions and limited subsurface data, the Hooskanaden Slide is speculated to consist of several compounded zones of movement rather than a single mass failing along a single sliding surface. These compartmentalized masses align with the regional structure of the Otter Point Formation, with individual movements contributing to the overall mass movement. The surge behavior of the active zone traversing Highway 101 had led to notable tension cracks in the upper portion of the landslide and significant lateral displacements in the lower bench near the Pacific Ocean shoreline.

Additionally, uplifting of the toe of the landslide was observed, reaching over 6 m in some locations. This uplift resulted in the formation of a secondary "sea cliff" on the gravel beach approximately 20 to 40 m westward from the existing coastal sea cliff. The greatest uplift occurred in the southern part of the toe, corresponding to larger horizontal displacements further upslope. This uplifting demonstrates rotation at the Hooskanaden landslide toe, likely due to significant compressive stress in its relatively gentle topography.

The upper portion of the landslide exhibited expressions of unloading with numerous tension cracks and limited surface displacements. The lower portion of the landslide, which is adjacent to the Pacific Ocean, exhibited notable lateral surface displacements in response to added vertical and lateral compression from the most active surge zone. This resulted in notable lateral displacements throughout the lower bench and significant uplift at the landslide toe, which daylights at a gravel beach.

The Hooskanaden landslide exhibits regular, but slow activity most years. Its surge behavior does not correspond to exceptionally wet years, but does exhibit periodicity, having realized surges in 1977, 1995, and 2019. The observations herein are presented to provide insight towards the most recent surge event. Additional observations from other temporal monitoring (e.g., InSAR or satellite optical imagery) may provide added insight on the kinematics and precursors associated with the Hooskanaden landslide, and other similar earthflows along the Southern Oregon Coast.

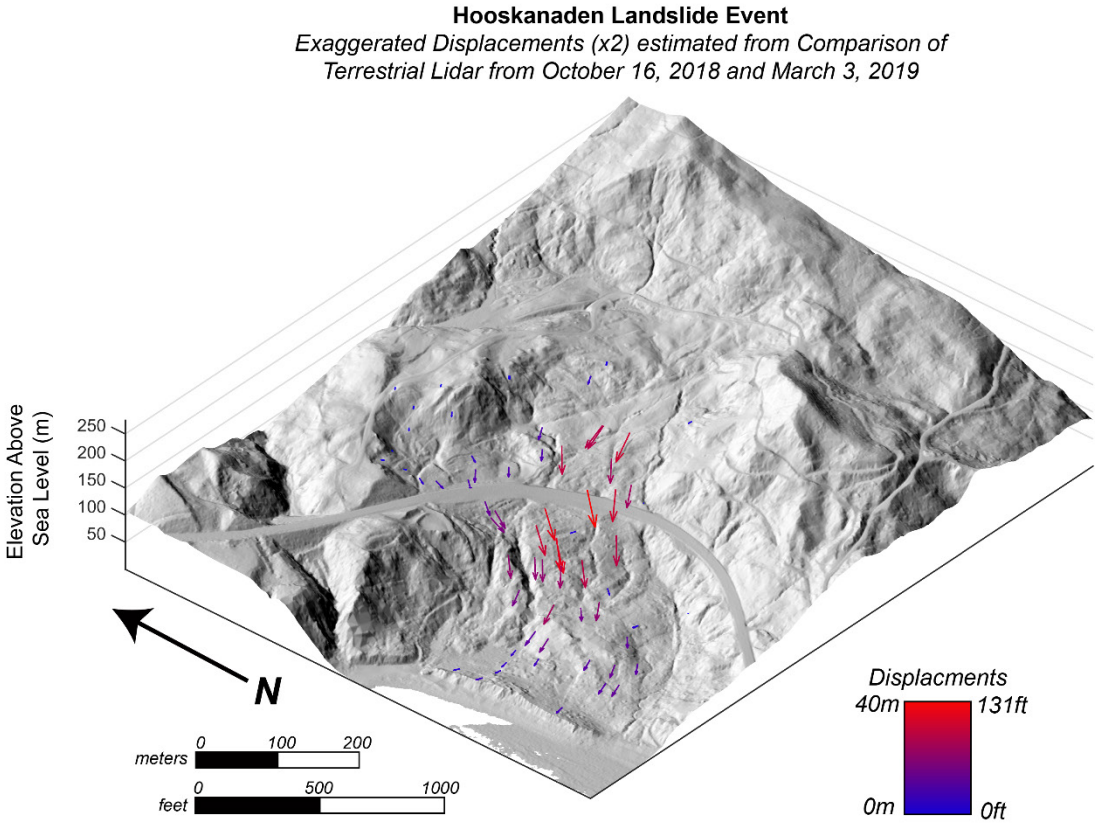

Figure 11.1: 3D movement vectors across the Hooskanaden landslide from the 2019 surge event. These vectors were created by extracting similar features (e.g., utility poles, trees, stumps) from TLS derived pointclouds, representing a time period between October 16, 2018 and March 3, 2019.

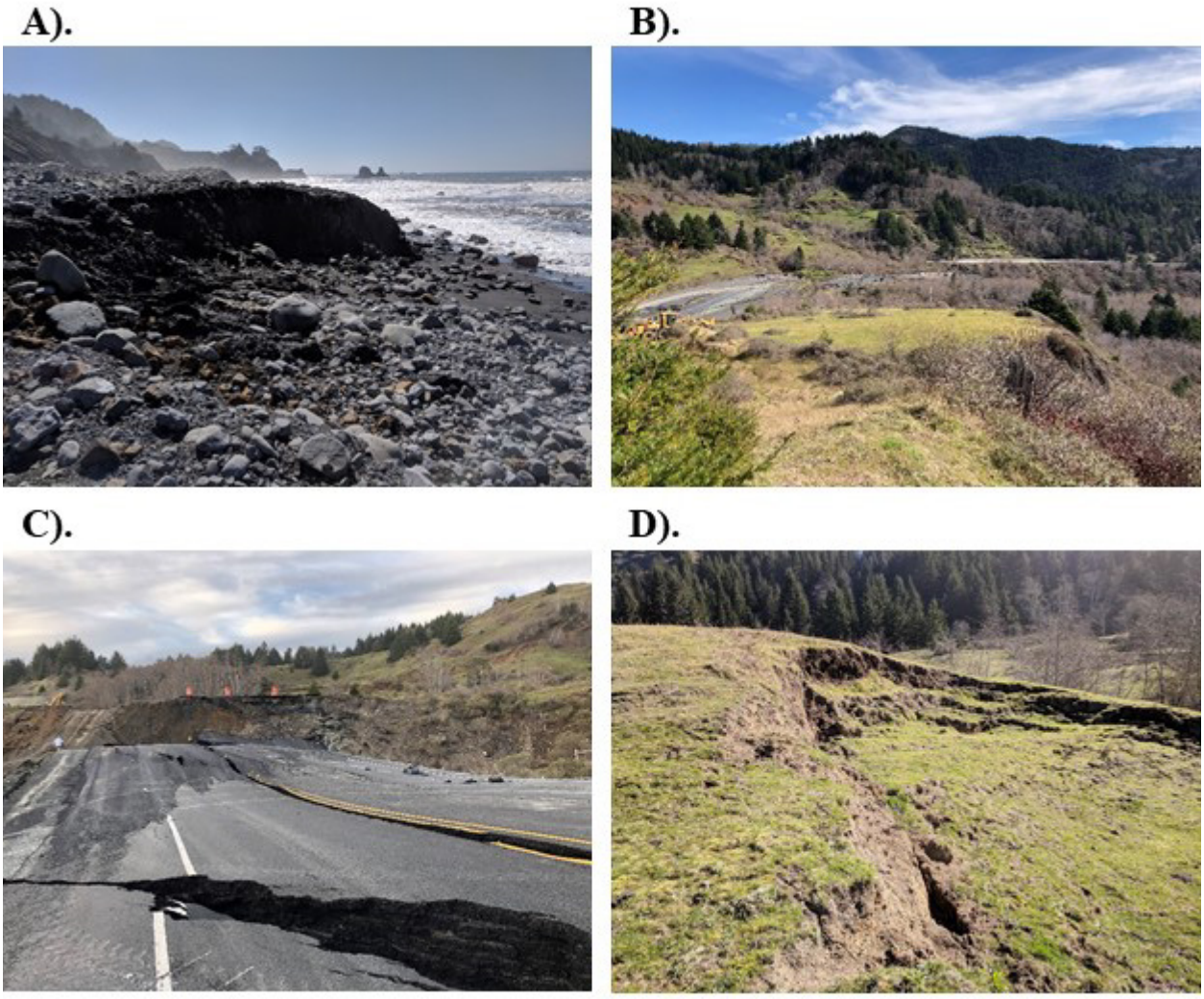

Figure 11.2: Photographs aquired in early March 2019 shortly after the Hooskanaden landslide event. A). Uplift of the beach at the toe of the landslide. B). Overview of the damage caused to Highway 101. C). Close up damage caused to the road by the landslide. D). An example tension crack/scarp from the upper portion of the landslide (above the road).

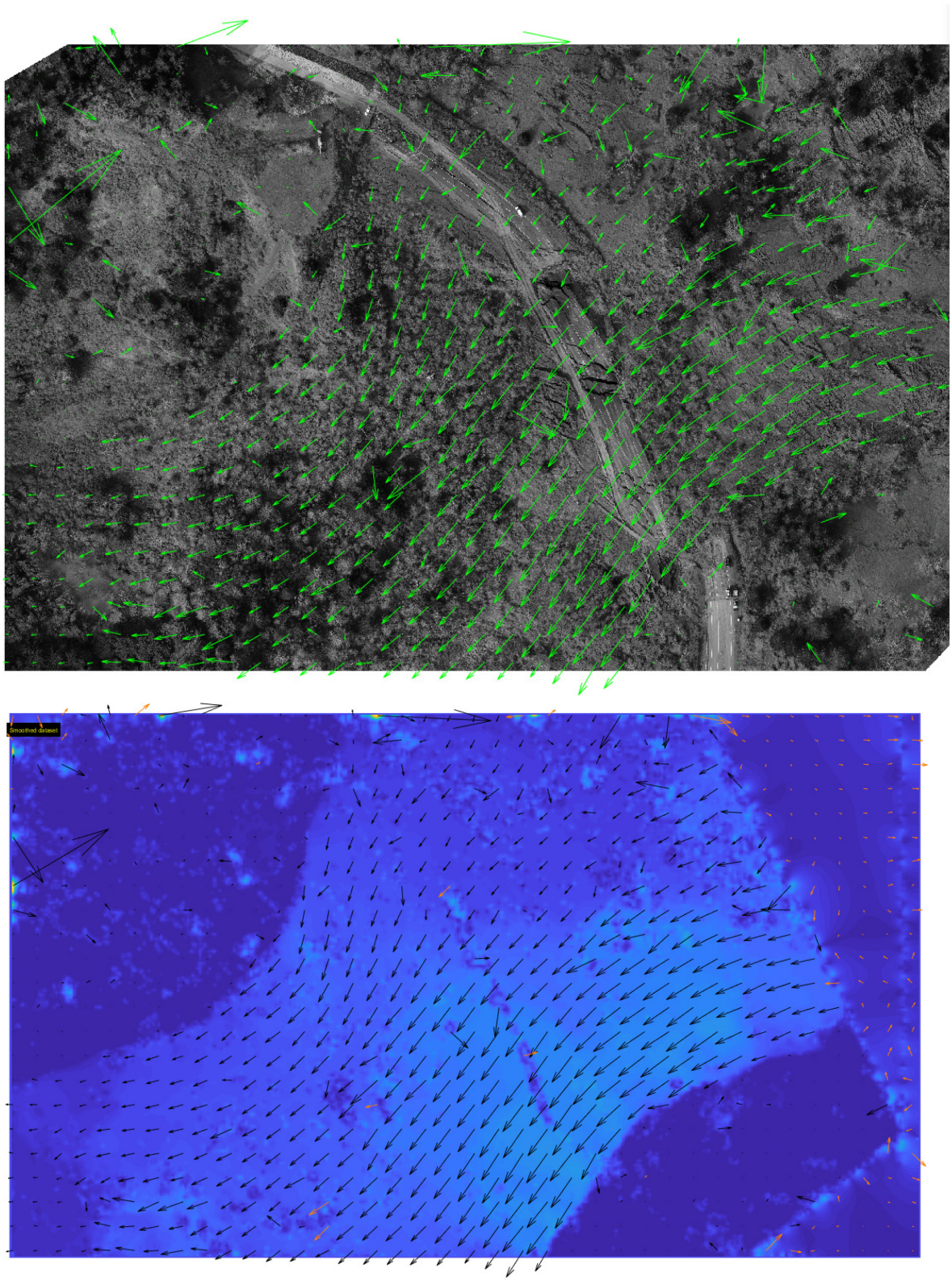

Figure 11.3: Particle image velocimetry (PIV) analysis of the two UAS photogrammetric surveys completed of the slide in late February 2019. The surveys were approximately 1 day apart when the landslide was moving at a rate of approximately 0.3 m per hour.

Figure 11.4: Detailed orthophotos acquired for the site on March 3, 2019. The orthophoto and SfM/MVS derived DSM can be explored at: https://research.engr.oregonstate.edu/geomatics/projects/OregonCoast/Hooskanaden/Feb2019/uas/ortho/

12.0 ARIZONA INN

12.1 ARIZONA INN MULTI-EPOCH ANALYSIS

As described in Section 4.0, terrestrial lidar data were collected along Highway 101 at Arizona Inn throughout the duration of the study. Bare earth DEMs were created with the data collected from each survey using RAMBO (Olsen et al., 2021) to first ground filter the data and then subsequently create the DEM. An optical flow predictor was trained with these DEMs along with augmented data using *SlideSim* (Senogles et al., 2022) as summarized in section 10.1. This predictor was then used to compute annual dense displacement grids representing the measured displacement across the survey area for each year. The annual dense displacement grids are shown in A) through G) in Figure 12.1. Overall, an increasing trend was noted throughout the study period, with landslide displacement at the site slowly increasing year over year culminating in the large failure event observed in January 2023. Subplot H) in Figure 12.1 shows a graph of measured displacements at the Arizona Inn cistern over the study. Annual displacement at the cistern was approximately 0.16 m in 2017, and 2018, increasing to approximately 0.21 – 0.24 m in 2019 – 2021. A larger increase in annual displacement to 0.5 m occurred in 2022, before the maximum annual displacement over the study of approximately 6.3 m in 2023.

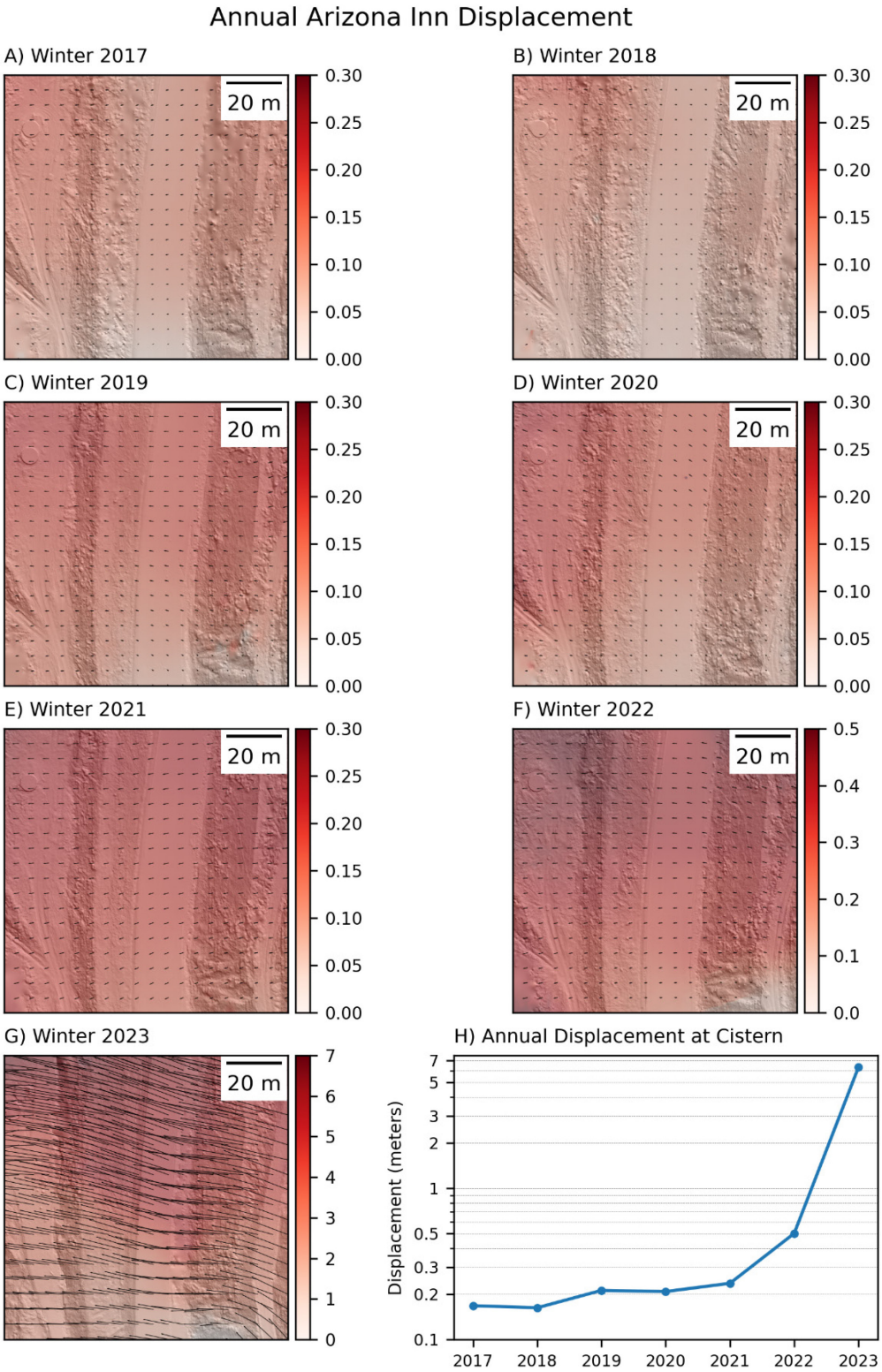

Figure 12.1: Timeseries of annual landslide displacements along the Southern portion of Highway 101 at Arizona Inn using the TLS surveys and *SlideSim*. A) through G) show visualization of displacements. H) shows the annual displacement measured at the cistern. Vector arrows are scaled 10x.

12.2 ARIZONA INN 2023 FAILURE

The Arizona Inn landslide experienced significant displacements towards the end of the study period from January 8 to 10, 2023 which resulted in a complete closure of this section of US Highway 101 for 6 days. Prior to this event, total displacements during the winter season averaged less than 0.5 m around the main cistern over the course of this study. The RTK-GNSS system installed at Arizona Inn during this study enabled near real time measurements during this event, and over the course of 48 hours reported 6.1 m and 3.6 m of displacement at rovers 1 and 2, respectively. Total landslide displacement across Arizona Inn was derived using SlideSim with UAS SfM data collected as part of this study from the previous (May 30, 2022) and following Spring (June 7, 2023). A visualization of this displacement is shown in Figure 12.2. Combining the displacement measurements made by the RTK-GNSS rovers with data from UAS SfM/UAS lidar enabled rapid characterization and a high spatial, high temporal resolution reconstruction of the displacement event using LADI and SlideSim as shown in Figure 12.3. Figure 12.4 and Figure 12.5 show example photographs of cracking observed at several locations across the slide as well as damages to the highway.

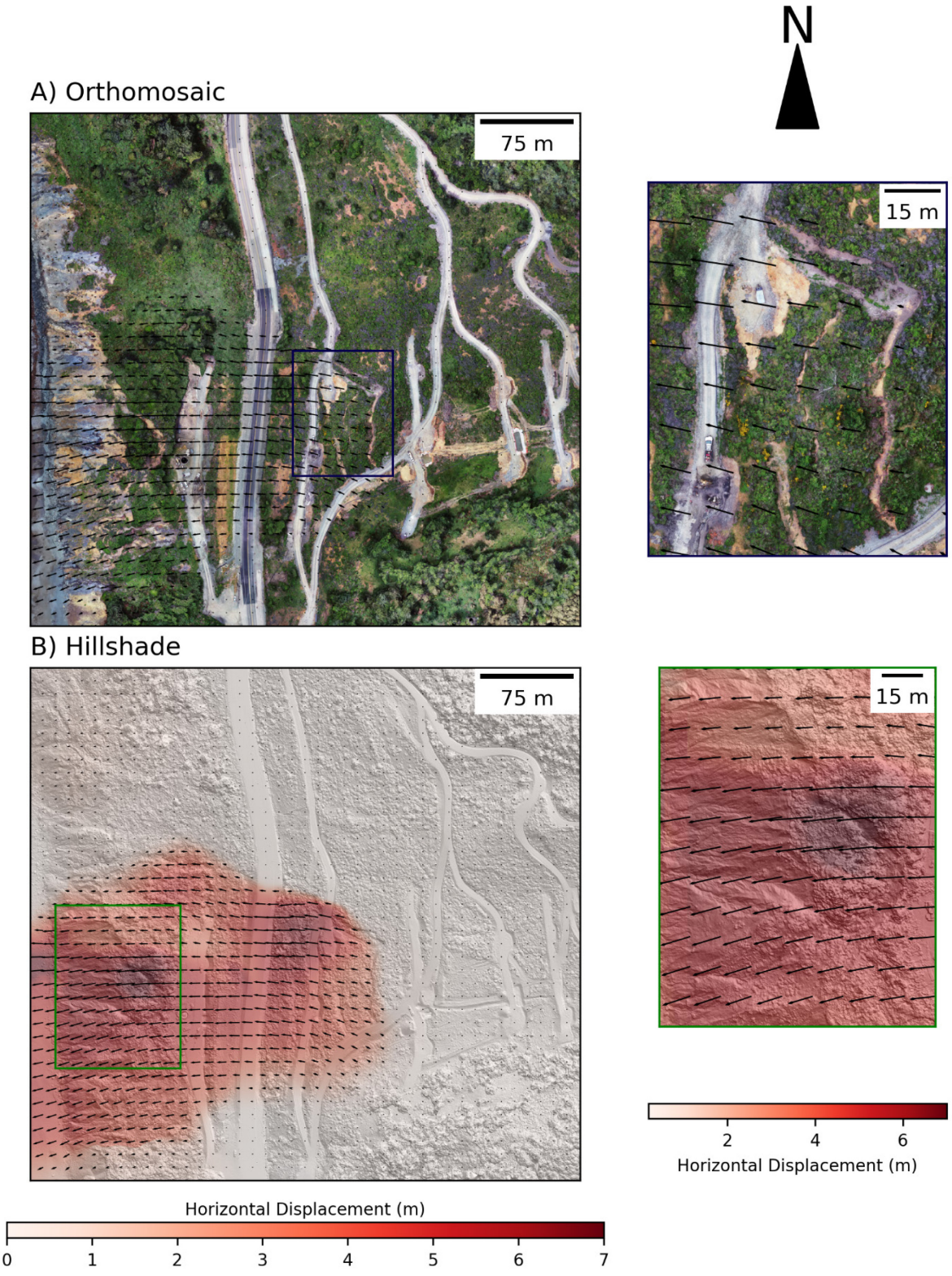

Figure 12.2: Landslide Displacement at Arizona Inn computed using *SlideSim* with UAS SfM data collected on May 30, 2022 and June 7, 2023 (before and after the January 2023 failure event. Vectors are scaled 2x.

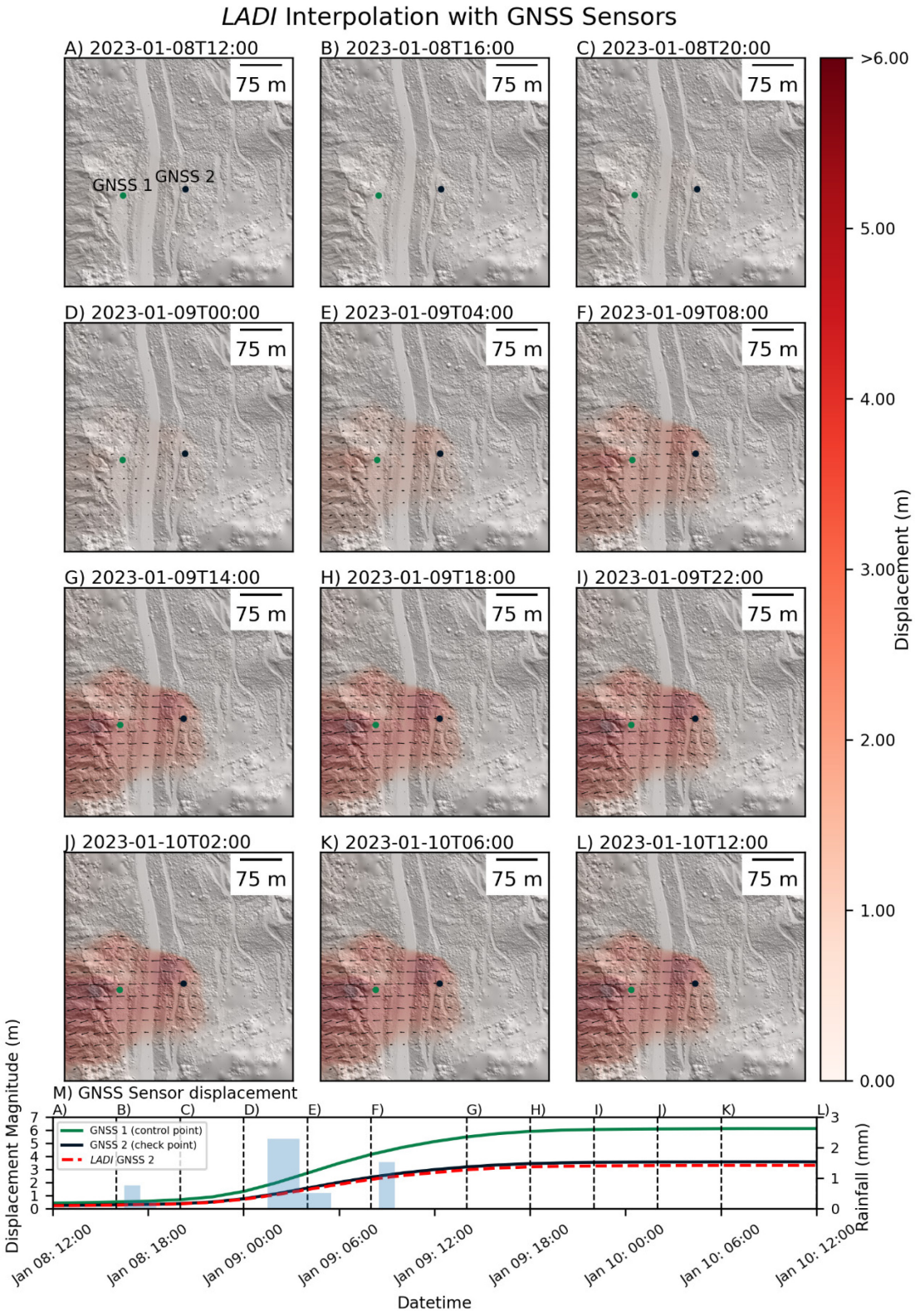

Figure 12.3: *LADI* interpolation of the surge event at the Arizona Inn Landslide between January 8 to 10, 2023 using the RTK-GNSS rover 1 as the single control point.

Figure 12.4: Examples of tension cracks (a) near Rover 1 and the cistern and (b) on the upper slopes above the highway. (January 20, 2023)

Figure 12.5: Examples of damage to highway 101 and temporary one-lane access road (a) adjacent to highway, (b) view from above the highway, and (c) additional distress observed in the northern section. (January 20, 2023)

13.0 PROGRESSIVE FAILURE MODELING WITH CLIMATE VARIABLES

In SPR-807 (this project and report) and SPR-843 (Olsen et al., 2024), we have developed two primary frameworks to assess the influence of coastal erosion impacts on (1) progressive landslide movements, and (2) sea cliff retreat. Elements of the former work has been published in Leshchinsky et al. (2019) and Alberti et al. (2022), and some of its components and key findings described herein. The latter work is also described herein.

13.1 PROGRESSIVE LANDSLIDE MOVEMENTS

In the published study (Leshchinsky et al., 2019), a framework is presented that captures the coupled relationship between undercutting, pore pressure change, and progressive landslide movement. This model captures the evolution of landslide geometry (Figure 13.1) and undercutting rate and how these factors may influence observed landslide movements. Three of the test sites observed in this project were used as a basis for creating this model (Figure 13.2), including both Beverly Beach sites and the Arizona Inn landslide. Historical data regarding pore pressures and movements were used for geotechnical modeling (Figure 13.3), while reasonable rates of undercutting were estimated from repeat TLS capture at sites. Model outputs demonstrate that progressive landslides that have a smaller length to depth ratio are more sensitive to undercutting, particularly with increased erosion from wave attack (Figure 13.4). That is, with increased undercutting, landslides with small length to width ratios may realize a nonlinear increase in yearly movements with amplified erosion. Landslides with large length to width ratios demonstrate an increase in yearly movements with erosion but are much less sensitive. All landslides exhibited notable decreases with yearly movements if erosion was decreased or completely arrested. However, the primary driver of landslide movements, as expected, stemmed from increases in pore pressures associated with groundwater changes in wet months.

We expand upon this study with idealized, three-dimensional slope stability analysis of the same landslides (Alberti et al., 2022). Through this, we develop simple relationships between landslide slope, coastal retreat, and landslide advance (Figure 13.5). These relationships are also presented for various planform aspect ratios of coastal landslides (Figure 13.6). General findings include:

- As the volume of a coastal landslide increases, there is a noticeable reduction in its forward movement for a given rate of eroded landslide volume. This suggests that erosion plays a particularly significant role in smaller landslide failures.

- Landslides with smaller aspect ratios (coastline parallel width greater than coastline orthogonal width) are more susceptible to wave scour, leading to proportional erosion and heightened potential for advancement.

- Steeper landslides experience greater advancement for a given level of erosion and retreat.

- Analyzing the comparison between theoretical advance and retreat relationships and actual observed movements of coastal landslides allows for the identification of the relative importance of erosion as a driving force. In the absence of other destabilizing conditions, retreat tends to surpass landslide advance under typical landslide conditions.

These studies demonstrate that armoring or prevention of undercutting in progressive coastal landslides of modest size may significantly decrease yearly movements, especially when instability is driven by erosion as a primary control. Further, increased erosion may greatly exacerbate the activity of these landslides. Management of groundwater is critical for arresting all movements in these slope failures.

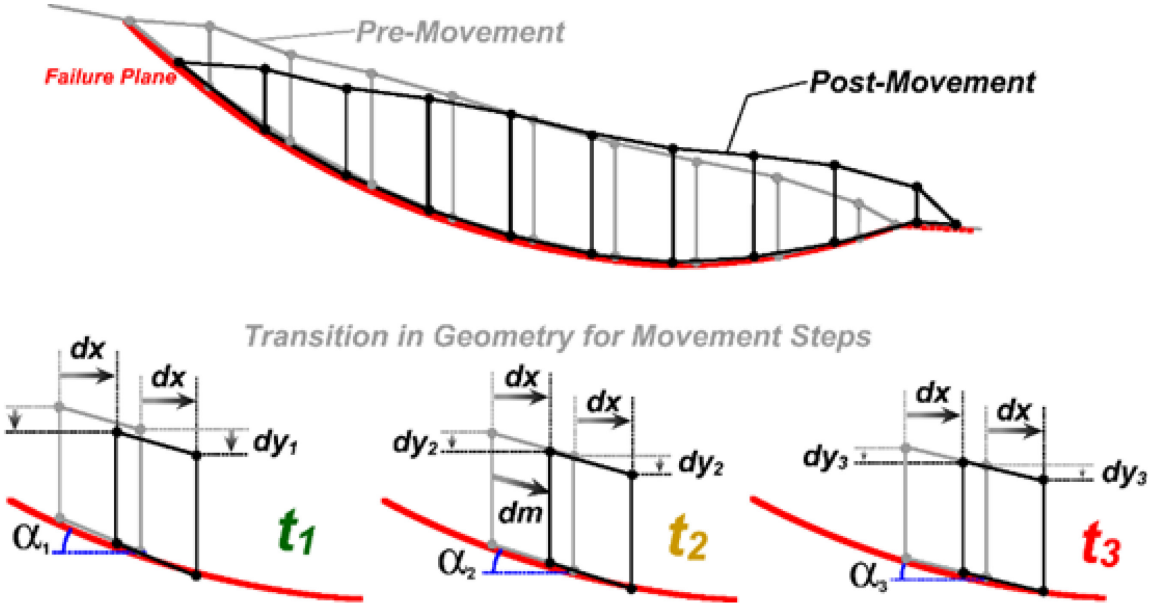

Figure 13.1: After Leshchinsky et al. (2019). Schematic of movement steps and notation.

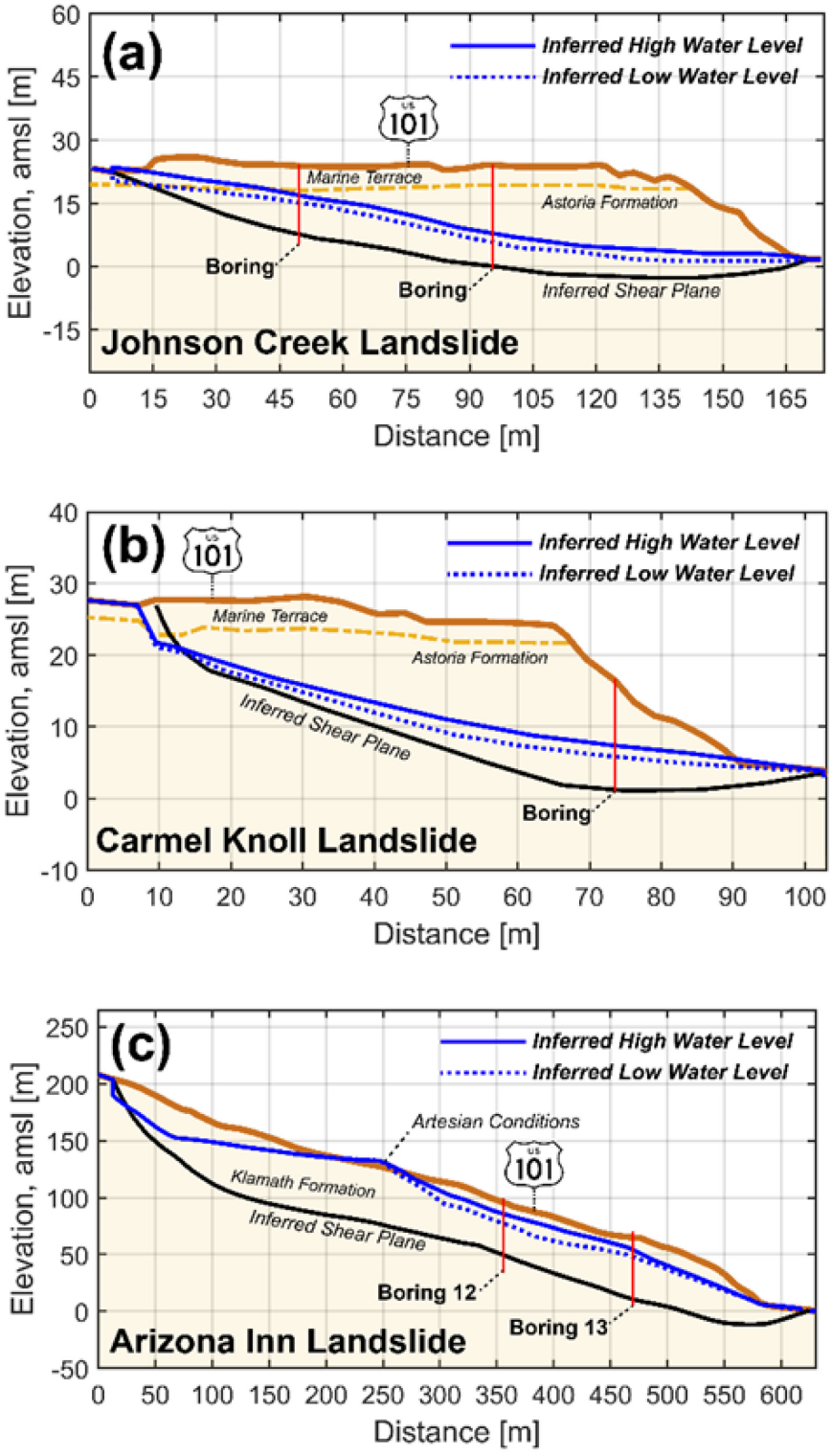

Figure 13.2: After Leshchinsky et al. (2019). Landslide and phreatic surface geometry for (a) Johnson Creek (after Schulz and Wang 2014); (b) Carmel Knoll (after Schulz and Wang 2014); and, (c) Arizona Inn landslides (after ODOT, 1995).

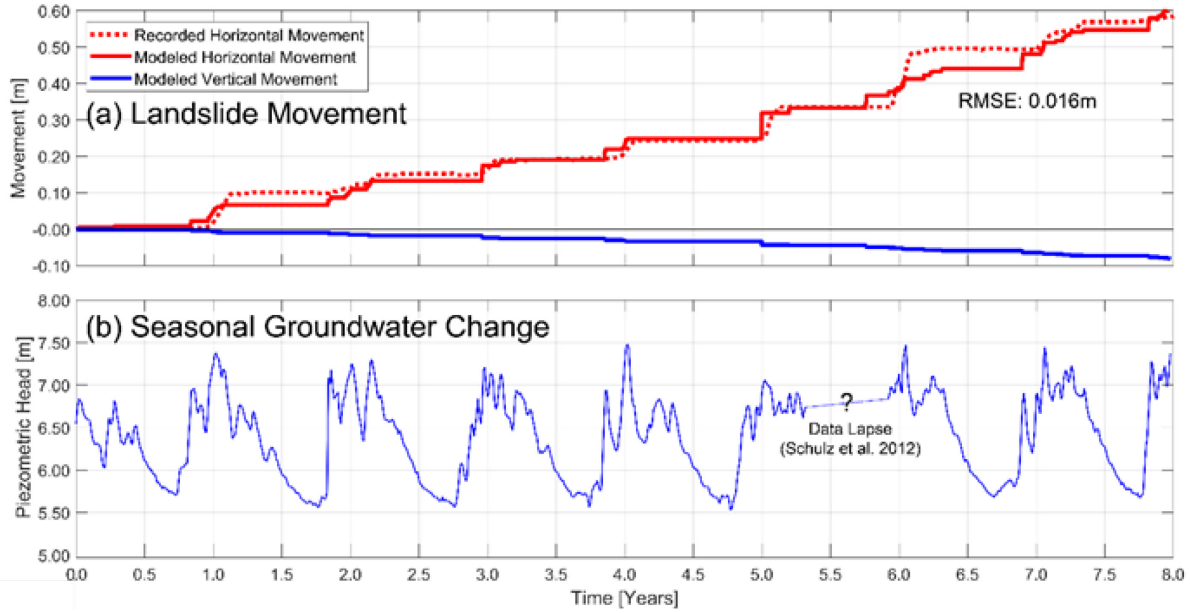

Figure 13.3: From Leshchinsky et al. (2019). (a) Modelled and measured landslide movement for the Johnson Creek Landslide and (b) measured piezometric head from January 2005 to January 2013 (after Schulz et al. 2014).

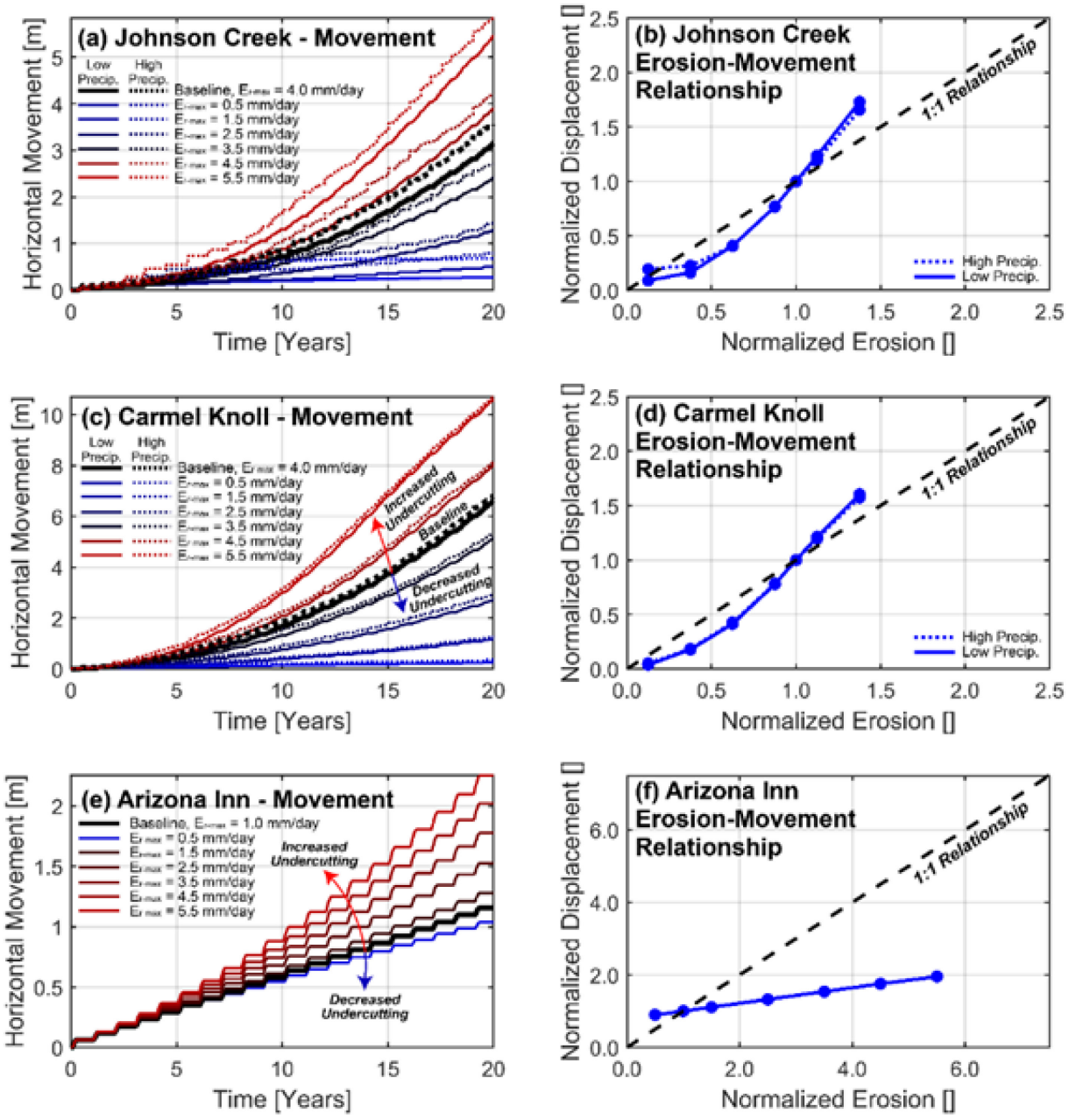

Figure 13.4: After Leshchinsky et al. (2019). Modelled landslide movements for select landslides over 20 years considering high and low precipitation conditions (dashed and solid lines, respectively) and various erosion rates (a) Johnson Creek; (c) Carmel Knoll; and (e) Arizona Inn. Inferred relationship between landslide movement and increased or decreased erosion after 20 years for select landslides (b) Johnson Creek; (d) Carmel Knoll; and (e) Arizona Inn.

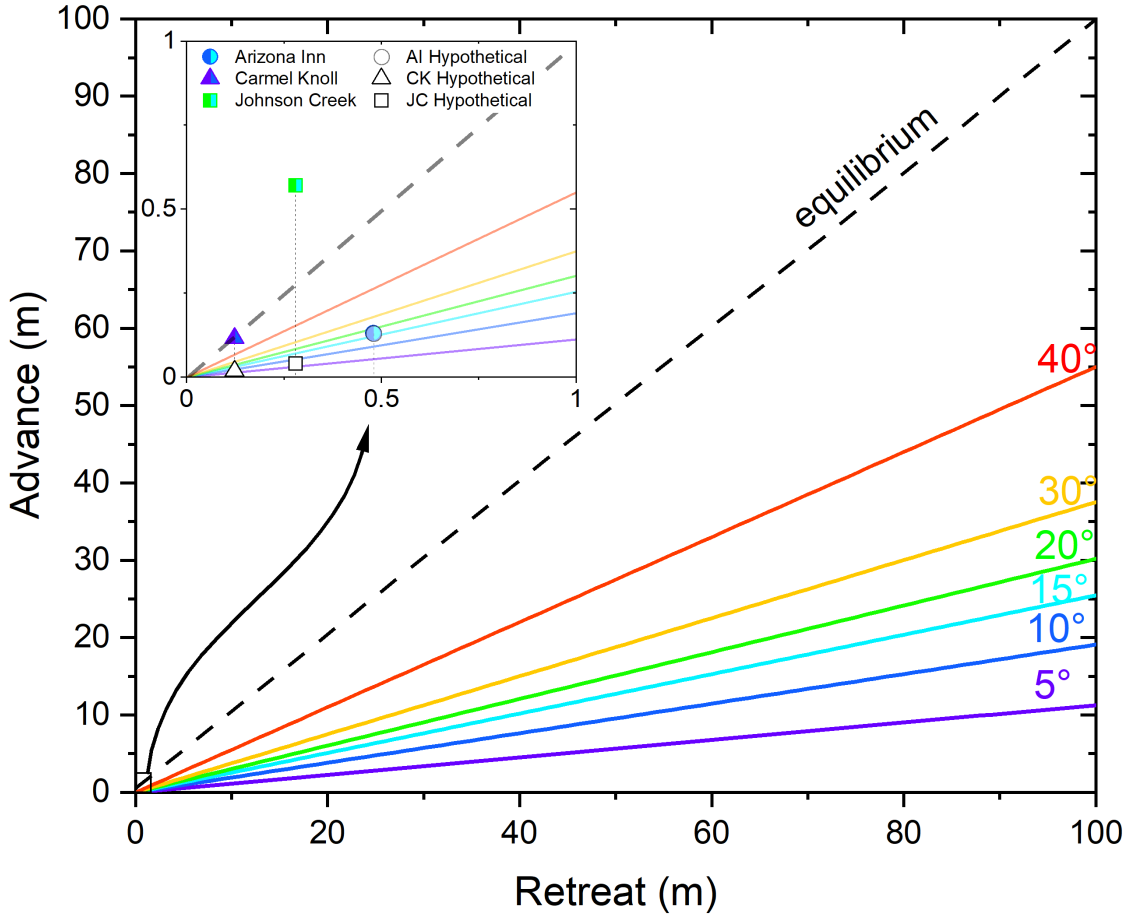

Figure 13.5: After Alberti et al. (2022)– Relationships between landslide advance and retreat for various landslide angles. Below the equilibrium line (black dashed line) the erosion is dominant, above, groundwater forcing is dominant, shown for various coastal landslides in Oregon. The correspondence of Arizona Inn with its representative geometric line suggests that erosion is a dominant control on landslide advance.

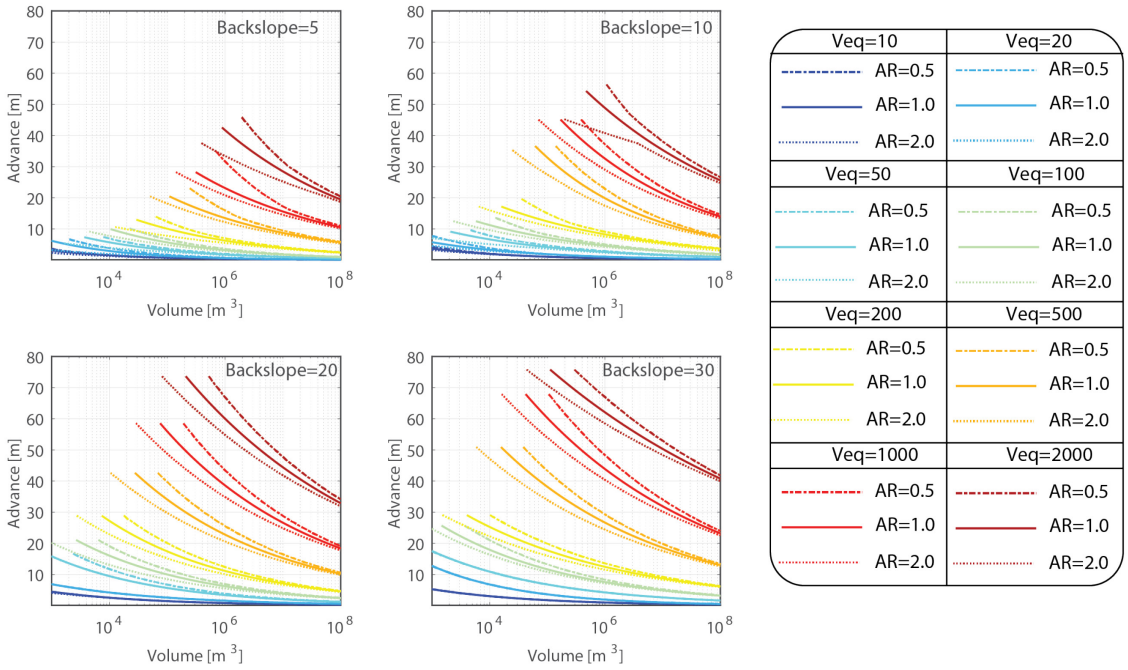

Figure 13.6: After Alberti et al. (2022). Sensitivity of landslide advance to aspect ratio (0.5 – 1 – 2) and erosion rates.

13.2 SEA CLIFF RETREAT FROM COLLAPSE AND OVERHANG FAILURE

While wave undercutting amplifies the mass movements of large coastal landslides, it may significantly exacerbate the retreat of cemented coastal sea cliffs, many of which have limited clearance from existing ODOT right-of-way. Through both SPR-807 and SPR-843 (Olsen et al., 2024), a framework has been created that imparts undercutting and assesses both (1) overhang failures, and (2) catastrophic slope failures (Figure 13.7). Each of these failures provides temporary self-armoring of a given sea cliff, which eventually erodes away. This feedback captures the general processes that dictate sea cliff retreat and is easily generalized to the sites monitored in this project. Inputs from repeat TLS collection (i.e. undercutting rates, erosion of failed material) may be directly used as inputs for this model. Undercutting rates and armor erosion rates may be amplified to appropriately capture potential effects of sea level rise and wave runup. Geotechnical parameters were determined from forensic analysis of ongoing sea cliff failures in the vicinity.

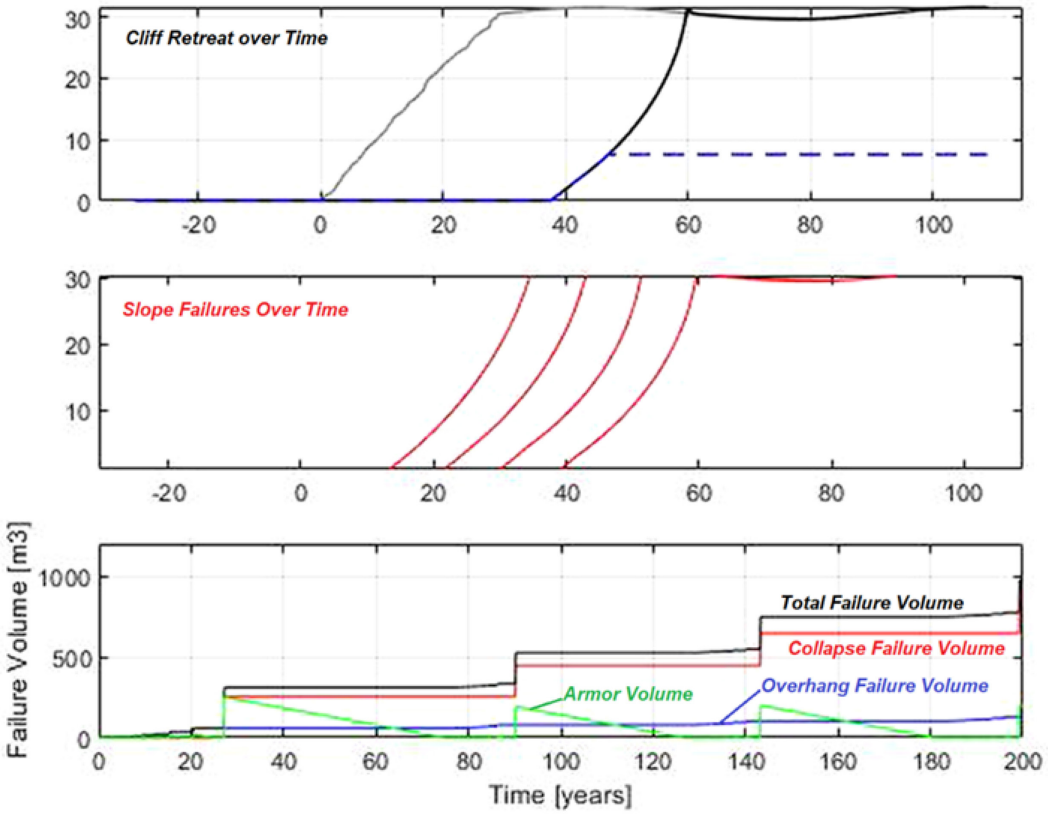

Figure 13.7: Model of sea cliff retreat considering overhang failures, collapse failures, and self-armouring. The retreat of the sea cliff over 200 years is shown in the top figure, with the grey line representing initial conditions and the black line representing final conditions. Retreat over this time period and soil conditions is approximately 35 m.

13.3 EROSION RATE FLUCTUATIONS

Both models can account for potential increases in erosion stemming from sea level rise and increased wave attack. The normalized relationships proposed in Figure 13.4 are generalized so relative changes in erosion may be used to directly assess how changes in sea cliff erosion rates influence landslide movements. These results may be interpolated to assess relative changes in landslide movements for progressive failures along the Oregon Coast. Ongoing assessment of erosion behavior from repeat TLS collection informs existing erosion rates in comparison to normalized relationships presented to infer sensitivity of landslide movements to sea cliff erosion. The normalized relationships between erosion and mass movement, along with a variety of length to depth ratios will provide simple, generalizable outputs to a variety of landslide conditions, just as shown in Figure 13.4 to 13.6. Ongoing monitoring will provide updated erosion rates over time, along with changes in potential movement.

Erosion rates from TLS are used to inform baseline dynamics governing sea cliff retreat. As these input parameters may be directly assessed, baseline coastal retreat can be assessed and a

retreat rate may be determined explicitly (for example, in Figure 13.7, the retreat rate is 0.18 m/year).

13.4 POTENTIAL APPLICATIONS

In SPR-843, the initial model developed in SPR-807 was expanded to analyze multiple cross sections for longer sections of coastline (Figure 13.8). The reader is referred to that report (Olsen et al., 2024) for additional information on this model and its application to precarious sites along Highway 101.

Advances to the hydrological aspects of the model were also implemented to include run up and total water levels computed from tidal data from NOAA combined with wave activity from wave buoys recording significant wave heights, wave direction, and wave period. This information was combined with the geometric data provided by lidar to compute wave contact hours and runup. In SPR-843 (Olsen et al., 2024), these output results of sea cliff crest recession were input into a geodatabase in ArcGIS software and combined with multiple other datasets for targeted risk assessment and climate change adaptation planning. These results enabled visualization of potential shoreline locations in coming decades and providing spatial context to the threat of sea cliff retreat with respect to ODOT right-of-way.

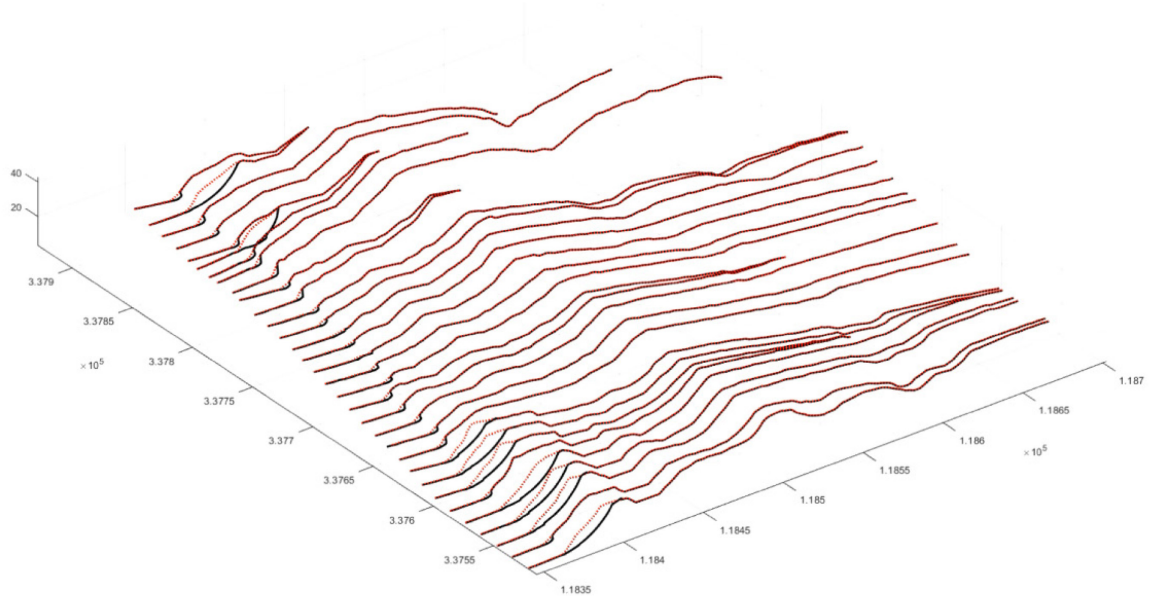

Figure 13.8: Example results of progressive collapses on multiple cross sections using the framework developed in SPR-843.

With this framework, increases in undercutting and erosion may also be directly assessed, providing a range of potential retreat rates considering a variety of erosion scenarios. Armored conditions can also be assessed to highlight the potential influence of mitigation systems on coastal retreat.

14.0 BENFITS TO ODOT AND IMPLEMENTATION

This project has both short term benefits already realized in the life span of the project as well as benefits that will continue beyond the life of the project.

14.1 SHORT TERM

Several short-term benefits have been identified since the start of the project, including:

- The data collected for Hooskanaden for this research project played an immediate role in ODOT's response to the large failure of Highway 101 at Hooskanaden. By having baseline data in place from this project, additional surveys could be rapidly conducted such that displacement vectors could be quickly obtained to show the magnitude and distribution of movement across the site. The UAS lidar data also was used by ODOT Geometronics to minimize the amount of field survey work needed in the difficult terrain, enabling designers to begin work on a new alignment much sooner after the event. The UAS orthophotos and UAS lidar data were also immediately used by Region 3 Geologists.

- The GNSS monitoring sensors at Arizona Inn were pivotal in determining the magnitude of movement and tracking additional post failure movements at the Arizona Inn to determine when it was safe and feasible to open the road, conduct construction activities, perform on site investigations, and allow inspectors into the cistern.

- The research methodology document provides guidelines to help ODOT with establishing monitoring programs for other sites in the future. The guidance and demonstrated success of utilizing new technologies such as UAS lidar, RTK UAS SFM/MVS surveys, and MEMs sensors are applicable to a wide range of monitoring projects beyond coastal erosion and landslide studies. The project team has had numerous conversations with ODOT personnel regarding these technologies and lessons learned.

- Training presentations have also been given at the Engineering ODOT Geotechnical and Geology Technology Transfer Meetings, describing the various monitoring approaches, results and benefits.

- Developed analysis code including code and scripts to process and analyze terrestrial lidar data, code for logging and transmitting sensor data from the in-situ instrumentation, and code to analyze progressive failures. These scripts are provided in the digital appendices.

14.2 LONGER TERM BENEFITS

ODOT needs a coordinated program to establish the system and tools needed to initiate, manage, and analyze data assessing coastal landslide and erosion risks along the coastal highway system, and potentially other highway systems throughout Oregon. The methodologies developed and findings from this project enable ODOT to:

- Relate to environmental factors and climate changes with site conditions, erosion rates, landslide movements to determine risk levels and strategies for adapting highway infrastructure to be more robust against chronic erosion and catastrophic events. Results from this project will also inform climate impacts to groundwater changes, their effects on landslide movement, and to differentiate these effects from those related to coastal erosion rates at the most vulnerable sites.

- Utilize advanced methods and sensors for geotechnical investigation and monitoring of landslides that can subsequently be adapted for common agency practice resulting in more accurate and efficient landslide monitoring and mitigation efforts, particularly from loss of sea cliff support due to erosion.

- Respond quicker (and possibly before) emergency events. Having a well-designed monitoring program in place with supporting long term baseline data at critical priority sites will benefit ODOT's ability to effectively manage its coastal highway. Such a system can help identify and potentially even predict when specific sites are approaching high levels of stress, enabling corrective action to be quickly implemented before an impending failure occurs, minimizing risk to the travelling public as well as ODOT personnel.

- Systematically analyze lidar and photogrammetric datasets acquired for long sections of coastline adjacent to Highway 101 using the tools developed in this research to identify priority sites and future trends. While this study and SPR-843 performed detailed analysis for several sites, continued monitoring and analysis is important to capture the variability associated with weather patterns and coastal processes (Allan et al., 2003). ODOT can also utilize this information in planning to evaluate the potential impacts of potential mitigation techniques and future scenario events. The analysis framework also allows ODOT to analyze other sections of highway facing similar hazards such as river or stream erosion, failure of cut slopes, etc. Lastly, it can help ODOT identify longer-term solutions to chronic erosion hazards by being able to better understand the unique characteristics of each site.

- Evaluate the effectiveness of mitigation techniques. ODOT could use the tools developed in this research to monitor sites with mitigation and adjacent sections of coastline. A major challenge in certain types of coastal engineering mitigation techniques used to address cliff erosion, is that they can result in unanticipated feedback that includes accelerated erosion adjacent to the engineered slope.

- Understand how coastal erosion affects the retreat of cliffs over various time scales (e.g., mid- and long-term), particularly in the context of its proximity to the location of vulnerable ODOT right-of-way. By characterizing actual evolution of sea cliff morphology with monitoring, we may project volumes of cliff collapse and retreat of sea cliffs with and without mitigation. This may guide strategic mitigation efforts.

- The GNSS sensors at Arizona Inn can be expanded to other sites. In addition, they can potentially be utilized for early warning detection once triggering thresholds are

determined and monitoring software is developed. Some of this work will be undertaken in SPR-878.

- The project also provided training and workforce development opportunities for OSU students and ODOT staff.

14.3 BROADER APPLICATIONS

This research can be used by ODOT to inform project-level risk and decision making where coastal infrastructure is threatened by landslides and erosion and mitigation efforts are required (e.g., Arizona Inn). It can also inform planning and land-use at a policy-level regarding the need for coastal engineering where critical highway infrastructure is threatened by future sea cliff retreat. Improved projections of timing for infrastructure damage or loss provides ODOT with information needed to make informed decisions regarding coastal engineering planning of public property or adaptation strategies (e.g., re-routing) at the policy-level. Further, this research could be used by the agency to justify exceptions to land use goals and other environmental restrictions when proposing construction projects to protect infrastructure. This includes exceptions to Statewide Goal 18 (Beaches and Dunes) regulated by the Department of Land Conservation and Development (DLCD) and coastal permits issued through the Oregon Parks and Recreation Department (OPRD). At the time of the writing of this report, ODOT is preparing a Goal 18 exception for Spencer Creek and looking at mitigation options, particularly given recent cliff erosion and slumping next to the highway that occurred in January 2024.

14.4 DATA VISUALIZATION

A key challenge of a project at this scale and many of the activities at ODOT is to efficiently share and utilize data that are collected. This section describes some example prototype viewers created for subsets of the data collected on the project. These visualization systems enable efficient access to the data as well as effective collaboration and communication. Two of the viewers were created to assist in the emergency response efforts following the 2019 Hooskanden surge.

A web framework for visualizing and manipulating the inclinometer data along with the point cloud in a potree view was developed (Figure 14.1). This interface, built using potree to enable efficient streaming of point cloud data, allows users to: visualize the displacement over time, exaggerate the displacement (both horizontally and vertically) for easier viewing, change the radius of the inclinometer, view a color-coded legend of the soil layers, and animate the displacing inclinometer through time. This can be viewed for the Hooskanaden site at the following web address: https://research.engr.oregonstate.edu/geomatics/projects/oregon-coast/spr807/hooskanaden/inclinometer-view.html. This framework builds on efforts of the digital-appendix from SPR-809 - https://research.engr.oregonstate.edu/geomatics/projects/rockfall/spr-809/digital-appendix/.

Given the volume of geophysical data collected in this project (and likely in future monitoring projects such as SPR-878), a streamlined process to convert files and setup repeatable and updateable html formatting to create these viewers will be important. This can be achieved by

developing scripts for generating/updating html files as more survey epochs become available to ensure the website is easily updatable in the future.

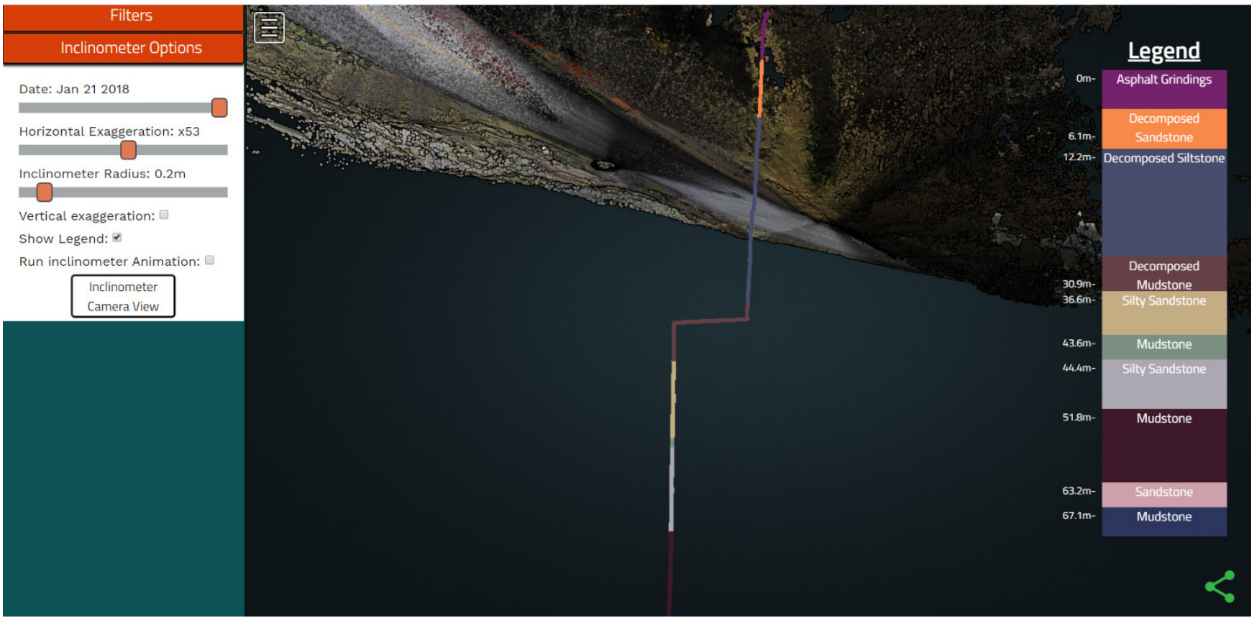

Figure 14.1: Interface of interactive inclinometer within a potree viewer. Along with options to manipulate the inclinometer (on the left) and a scale bar on the right.

Two additional prototypes were created to assist with the Hooskanden response:

- Orthophoto and Digital Surface Model viewer: https://research.engr.oregonstate.edu/geomatics/projects/OregonCoast/Hooskanaden/Feb2019/uas/ortho/ (This site contains high resolution orthophotographs collected from UAS on March 3, 2019 and June 24, 2019 showing the post-failure conditions and the reconstructed highway, respectively. It also contains a digital surface model from the March 3, 2019, UAS survey).

- Multi epoch point cloud viewer: https://research.engr.oregonstate.edu/geomatics/projects/OregonCoast/Hooskanaden/Feb2019/lidar/ (contains several epochs of point clouds captured at Hooskanaden).

These prototypes all can be adapted and built upon to expand the usage of the SPR-807 data as well as for use with future projects such as SPR-878.

Figure 14.2: Example screenshots of the interface of interactive web viewer of high resolution orthophotographs following the February 2019 Hooskanaden surge.

s

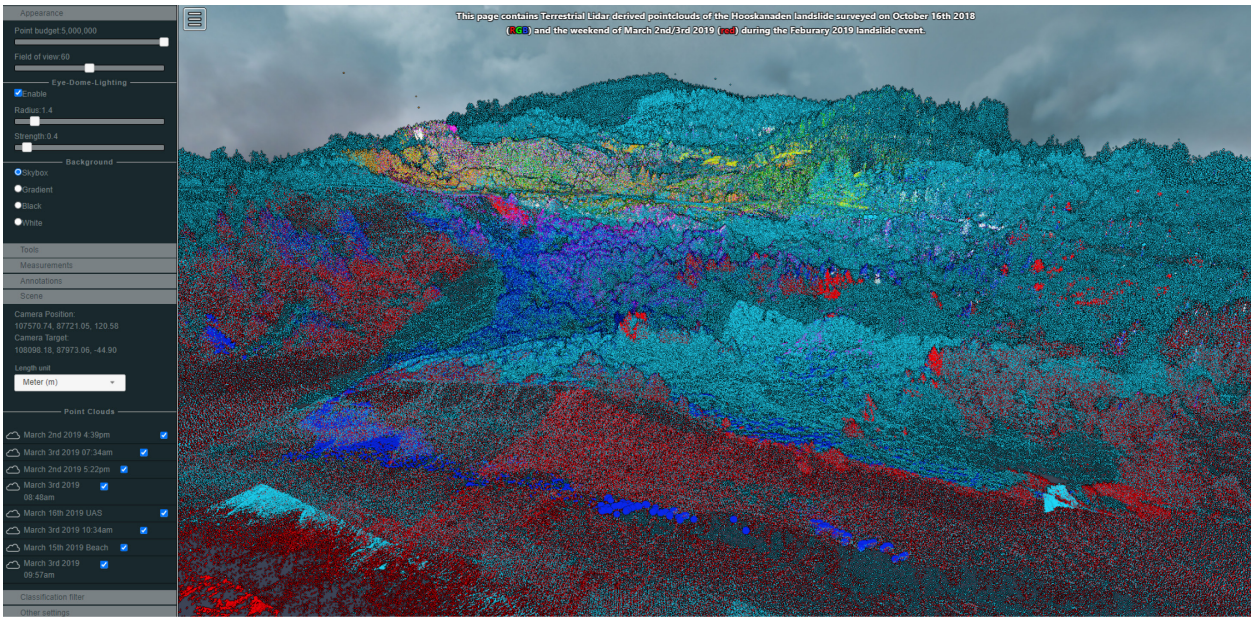

Figure 14.3: Example screenshots of the interface of interactive point cloud viewer with data collected during the February 2019 Hooskanaden surge.

15.0 CONCLUSIONS

Many important insights were gained through the course of this research. The research papers submitted with this report provide more detail as to the conclusions for each component of extensive study. Below is a summary of key findings.

15.1 MONITORING

This project demonstrates the high value and importance of investing in ongoing monitoring of active sites. It provides ODOT with considerable evidence of the value and use cases of different types and combinations of monitoring technologies including MEMS inclinometers, in-situ RTK GNSS sensors, terrestrial and UAS lidar, and UAS photogrammetry. Three of the five sites studied in this research experienced large failures resulting in highway closure and reduced access during the monitoring period. In these efforts, the monitoring data was crucial to assist ODOT with decision making and necessary rebuilding efforts at those sites. Future failures will almost certainly continue to plague these sites until ODOT can identify longer lasting solutions.

Based on these examples, it is strongly recommended that ODOT:

- Continue and expand monitoring efforts at these active sites with additional GNSS units, remote sensing surveys (e.g., UAS photogrammetry and lidar), and new sensors that become available. Extend this approach to other high priority sites. Further implementation of this work will occur in SPR-878 for Arizona Inn and Hooskanaden as well as other sites on the Oregon coast and in the Oregon coast range.

- Develop a long-term monitoring plan that prioritizes sites and monitors at a frequency relative to activity and hazard risk. This monitoring plan should include a combination of in-situ sensors and remotely sensed data. The complexity and magnitude of the monitoring effort should scale with the risk level and specific hazards associated with the site. For smaller sites, sites with localized ground movements, or sites with slower rates such as Silver Point or Arch Cape, a single sensor may be adequate. However, more complex landslides such as Arizona Inn and Hooskanaden require a much denser monitoring network and more frequent surveys to capture movements.

- Consider utilizing some of the mobile lidar dataset collected for monitoring purposes to minimize additional collection efforts. Note that the mobile lidar data will have limited view downslope adjacent to the highway and will not capture sea cliffs. However, it can capture larger movements on and adjacent to the highway to identify signs of distress before catastrophic failures occur. Fusing data both on the roadway and the sea cliffs themselves can provide a much more comprehensive picture of the relationship between the erosional processes and landslide movements (e.g., Conner and Olsen, 2012).

- Develop a data management system to archive geospatial and geotechnical data collected at the sites that enables rapid retrieval in the future should a sizeable event occur. (Particularly by the engineering geology staff). In conjunction with this, develop visualization and analysis tools to explore these data in conjunction with geotechnical information building upon the prototypes presented in this research.

15.2 CORRELATION OF ENVIRONMENTAL FACTORS AND EROSION RATES

When evaluating the erosional rates from the change detection analysis of the lidar data and correlating those with data from environmental sensors, several insights were obtained:

- Substantial erosion activity was observed at the sites during the monitoring period. The MEMS sensors, TLS data, and UAS surveys all showed movements and changes at each site. Large failures with significant damage were observed at three sites (Hooskanaden, Arizona Inn, and Spencer Creek) during periods of heavy rainfall. However, note that the instability and resulting failures at Arizona Inn and Spencer Creek was predominately driven by coastal processes eroding the toe.

- A novel erosion zone classifier was developed that uses observed erosion patterns to spatially classify the sea cliff into scour, transition, and subaerial zones.

- Each site studied showed unique relationships (or lack thereof) between erosional responses and environmental forcings (wave runup processes, energy, and rainfall), highlighting the complexity of coastal processes. Differences in correlation with wave energy and precipitation were observed between the scour, transition, and subaerial zones and between sites. For example, Arch Cape showed relatively similar correlation values for wave energy and precipitation in the scour and transition zones. However, the subaerial zone showed a stronger correlation with precipitation. Spencer Creek South showed stronger correlation with wave energy in the scour zone compared with Spencer Creek North.

- The volume loss in the scour zone is driven by wave-scour with inter-survey cumulative wave energy strongly correlated with volume loss in the scour zone across all sites (Kendall coefficients, τ, ranging from 0.41 to 0.80). These results strongly suggest that sea cliff scour zone volume loss is likely to increase as sea levels increase, since ocean water levels determine the runup elevations reached by wave processes. However, note that rising sea level rise does not necessarily translate to increased wave energy. Instead it governs the heights reached by waves. Hence, wave impact hours would be expected to increase at all levels across the profile.

- Precipitation intensity (maximum weekly precipitation), was only significantly correlated with volume loss in the subaerial zone at two of the sites (Silver Point and Spencer Creek North), indicating the complexity and site-specific constraints of this process.

- Summertime cliff erosion in the subaerial zone was shown to be 1.3 to 3.7 times higher when compared with the transition zone. Summer cliff erosion was also higher than the scour zone from the preceding winter, indicating a lag effect of over erosion and steepening in the preceding winter, followed by upper cliff failure in the ensuing summer. This observation reveals that removal of unstable, dilated rock following large storm driven erosion events can persist throughout the summer. The decay rate of this process is currently unknown, and future work using higher frequency surveys is required.

- The transition zone, where large failures propagate upward from the scour zone, has been shown to contribute the most to overall cliff volume loss.

- Volume-frequency relationships fitted via power-law across each of the zones show the scaling exponent (β) is lower in the scour and transition zones compared to other rockfall inventories, while comparable in the subaerial zone, suggesting the tendency for larger apparent failure volumes over the given data collection frequency periods in the scour and transition zones.

15.3 CONCEPTUAL KNOWLEDGE ON LANDSLIDE MECHANICS

Utilizing the data collected and the developed models, insights on landslide mechanics were obtained, including:

- Model outputs demonstrate that progressive landslides that have a smaller length to depth ratio are more sensitive to undercutting, particularly with increased erosion from wave attack. All landslides exhibited notable decreases with annual movements if erosion was decreased or completely arrested. However, the primary driver of landslide movements, as expected, stemmed from increases in pore pressures associated with groundwater changes in wet months.

- As the volume of a coastal landslide increases, there is a noticeable reduction in its forward movement for a given rate of eroded landslide volume. This suggests that erosion plays a particularly significant role in smaller landslide failures, compared with larger landslides.

- Landslides with smaller aspect ratios (coastline parallel width greater than coastline orthogonal width) are more susceptible to wave scour, leading to proportional erosion and heightened potential for advancement. Further, steeper landslides experience greater advancement for a given level of erosion and retreat.

- Analyzing the comparison between theoretical advance and retreat relationships and actual observed movements of coastal landslides allows for the identification of the relative importance of erosion as a driving force. In the absence of other destabilizing conditions, retreat tends to surpass landslide advance under typical landslide conditions.

16.0 REFERENCES

Abushandi, E. and Abualkishik, A., 2020. Shoreline Erosion Assessment Modelling for Sohar Region: Measurements, Analysis, and Scenario. *Scientific Reports,* 10, 4048. https://doi.org/10.1038/s41598-020-61033-y

Alberti, S., Olsen, M. J., Allan, J., & Leshchinsky, B. (2022). Feedback thresholds between coastal retreat and landslide activity. *Engineering Geology*, *301*, 106620.

Alberti, S., Senogles, A., Kingen, K., Booth, A., Castro, P., DeKoekkoek, J., Glover-Cutter, K., Mohney, C., Olsen, M. and Leshchinsky, B., 2020. The Hooskanaden Landslide: historic and recent surge behavior of an active earthflow on the Oregon Coast. *Landslides*, 17(11), pp.2589-2602.

Allan, J.C. (2020), Temporal and spatial changes in coastal morphology, Tillamook County, Oregon. Open-File Report O-20-04, Oregon Department of Geology and Mineral Industries, Portland, Oregon, 27 pp.

Allan, J. C., Gabel, L., and O'Brien, F., 2018, Beach and shoreline dynamics in the Cannon Beach littoral cell: Implications for dune management. *Special Paper 49*, 118 pp, Oregon Department of Geology and Mineral Industries.

Allan, J.C., Ruggiero, P., Cohn, N., O'Brien, F., Serafin, K., Roberts, J.T., Gabel, L.S., (2017). Coastal Flood Hazard Study, Lane and Douglas Counties, Oregon, O-17-05, 190pp, Oregon Department of Geology and Mineral Industries, Portland, Oregon.

Allan, J. C., Ruggiero, P., Cohn, N., Garcia, G., O'Brien, F., Serafin, K. A., Stimely, L., and Roberts, J. T., 2015a, Coastal Flood Hazard Study, Lincoln County, Oregon., *O-15-06*, 361 pp, Oregon Department of Geology and Mineral Industries, Portland, Oregon.

Allan, J. C., Ruggiero, P., Cohn, N., O'Brien, F., Serafin, K. A., Roberts, J. T., and Stimely, L., 2015b, Coastal Flood Hazard Study, Curry County, Oregon., O-15-07, 246 pp, Oregon Department of Geology and Mineral Industries.

Allan, J. C., Ruggiero, P., Garcia, G., Harris, E. L., Roberts, J. T., and Stimely, L., 2015c, Coastal Flood Hazard Study, Clatsop County, Oregon., O-15-05, 210 pp, Oregon Department of Geology and Mineral Industries.

Allan, J. C., Ruggiero, P., Garcia, G., O'Brien, F., Stimely, L., and Roberts, J. T., 2015d, Coastal Flood Hazard Study, Tillamook County, Oregon., *Special Paper 47*, 283 pp, Oregon Department of Geology and Mineral Industries.

Allan, J. C., and L. Stimely (2013), Oregon Beach Shoreline Mapping and Analysis Program: Quantifying Short to Long-term Beach and Shoreline Changes in the Gold Beach, Nesika, and Netarts Littoral Cells., *O-13-07*, 46 pp, Oregon Department of Geology and Mineral Industries, Portland, Oregon.

Allan, J. C., P. Ruggiero, and J. T. Roberts (2012), Coastal Flood Insurance Study, Coos County, Oregon, *Special Paper 44*, 132 pp, Oregon Department of Geology and Mineral Industries, Portland, Oregon.

Allan, J.C. and Harris, E.L., 2012. An "Expanded" Geospatial Database of Beach and Sea cliff Morphology Determined from LIDAR Data collected on the Northern Oregon Coast; Tillamook to Clatsop County. Open file report O-12-08, Oregon Department of Geology and Mineral Industries, Portland: 23p.

Allan, J. C., R. C. Witter, P. Ruggiero, and A. D. Hawkes (2009), Coastal geomorphology, hazards, and management issues along the Pacific Northwest coast of Oregon and Washington, in *Volcanoes to vineyards: Geologic field trips through the dynamic landscape of the Pacific Northwest: Geological Society of America Field Guide 15*, edited by J. E. O'Connor, R. J. Dorsey and I. P. Madin, pp. 495-519, The Geological Society of America.

Allan, J. C., Komar, P. D., and Ruggiero, P., (2011). Storm surge magnitude and frequencies on the central Oregon coast, in Proceedings Solutions to Coastal Disasters 2011, Anchorage, Alaska, 2011, American Society of Civil Engineers.

Allan, J. C. and R. Hart (2009). Beach and shoreline response to an artificial landslide at Rocky Point, Port Orford, on the southern Oregon Coast. Open file report O-09-01, Oregon Department of Geology and Mineral Industries, Portland: 56p.

Allan, J. C., and Hart, R., (2008), Oregon beach and shoreline mapping and analysis program: 2007-2008 beach monitoring report., O-08-15, 60 pp,Oregon Department of Geology and Mineral Industries.

Allan, J. C., and Hart, R., (2007), Assessing the temporal and spatial variability of coastal change in the Neskowin littoral cell: Developing a comprehensive monitoring program for Oregon beaches., O-07-01, 31 pp, Oregon Department of Geology and Mineral Industries.

Allan, J.C. and Komar, P.D. (2006), Climate controls on U.S. West Coast erosion processes. *Journal of Coastal Research*, 22(3): 511-529.

Allan, J.C. and Hart, R., (2005). A geographical information system (GIS) data set of beach morphodynamics derived from 1997, 1998, and 2002 LIDAR data for the central to northern Oregon coast. Open file report O-05-09, Oregon Department of Geology and Mineral Industries, Portland.

Allan, J. C., Geitgey, R. P., & Hart, R. (2005). Dynamic revetments for coastal erosion stabilization: A feasibility analysis for application on the Oregon Coast. Oregon Department of Geology and Mineral Industries.

Allan, J.C., Komar, P.D. and Priest, G.R. (2003), Shoreline variability on the high-energy Oregon coast and its usefulness in erosion-hazard assessments. In: M.R. Byrnes, M. Crowell and C. Fowler (Editors), Shoreline mapping and change analysis: Technical considerations and management implications. *Journal of Coastal Research*, pp. 83-105.

Allan, J.C. and Komar, P.D. (2002), Extreme storms on the Pacific Northwest Coast during the 1997-98 El Niño and 1998-99 La Niña. *Journal of Coastal Research*, 18(1): 175-193.

Allan, J. C., and Priest, G. R., (2001), Coastal erosion hazard zones along the Clatsop Plains, Oregon: Gearhart to Fort Stevens: Oregon Department of Geology and Mineral Industries Open-File Report O-01-04, 56 p

Anderson, D., Ruggiero, P., Antolinez, J.A., Mendez, F.J. and Allen, J. (2018), A climate index optimized for longshore sediment transport reveals interannual and multi-decadal littoral cell rotations. *Journal of Geophysical Research: Earth Surface*, 123.

Aruperes, L., Ganug, N. and A. Maryono. (2016). “Extreme weather persists, blocking access to victims.” Jakarta Post. Wed, June 22 2016. Online.

Babbel BJ, Olsen MJ, Che E, Leshchinsky BA, Simpson C, Dafni J. Evaluation of Uncrewed Aircraft Systems’ Lidar Data Quality. ISPRS International Journal of Geo-Information. 2019; 8(12):532. https://doi.org/10.3390/ijgi8120532.

Barendse, M., & Machan, G. (2012). Field Evaluations of “ShapeAccelArray” In-place MEMS Inclinometer Strings for Subsurface Deformation Monitoring (No. SPR# C-06-02).

Barnard, P. L., Hoover, D., Hubbard, D. M., Snyder, A., Ludka, B. C., Allan, J., Kaminsky, G. M., Ruggiero, P., Gallien, T. W., Gabel, L., McCandless, D., Weiner, H. M., Cohn, N., Anderson, D. L., and Serafin, K. A., 2017, Extreme oceanographic forcing and coastal response due to the 2015-16 El Niño: Nature Communications, v. 8.

Barnard, P. L., Short, A. D., Harley, M. D., Splinter, K. D., Vitousek, S., Turner, I. L., Allan, J., Banno, M., Bryan, K. R., Doria, A., Hansen, J. E., Kato, S., Kuriyama, Y., Randall-Goodwin, E., Ruggiero, P., Walker, I. J., and Heathfield, D. K., 2015, Coastal vulnerability across the Pacific dominated by El Niño/Southern Oscillation: Nature Geoscience.

Barton, M. (2015). Climate change, sea level rise and coastal landslides. In *Engineering Geology for Society and Territory-Volume 1* (pp. 415-418). Springer, Cham.

Beuzen, T., Goldstein, E.B., and Splinter, K.D., (2019). Ensemble models from Machine Learning: An example of wave runup and coastal dune erosion. *Natural Hazards and Earth System Sciences*, 19(10), 2295–2309. doi:10.5194/nhess-19-2295-2019

Benumof, B.T. and Griggs, G.B., 1999. "The dependence of sea cliff erosion rates, cliff material properties, and physical processes: San Diego County, California." Shore and Beach, 67(4), 29-41.

Benumof, B.T., Storlazzi, C.D., Seymour, R.J., and Griggs, G.B, 2000. "The relationship between incident wave energy and sea cliff erosion rates: San Diego County, California," Journal of Coastal Research, 16(4), 1162-1178.

Bruno, DE, Barca E, Goncalves RM, de Arajuo Queiroz HA, Berardi, L., and Passarella G. (2018). Linear and evolutionary polynomial regression models to forecast coastal dynamics: Comparison and reliability assessment, Geomorphology, 300, 128-140.

Bryson, M., M. Johnson-Roberson, R. J. Murphy, and D. Bongiorno (2013), Kite Aerial Photography for Low-Cost, Ultra-high Spatial Resolution Multi-Spectral Mapping of Intertidal Landscapes, *PLoS ONE*, *8*(9), 15.

Burns, S. (2014). "The Oso Landslide, Washington, March 22, 2014 Shows The Need For Susceptibility Maps And Insurance." *2014 GSA Annual Meeting in Vancouver, British Columbia*.

Burgette, R.J., Eduardo F. Guerrero, Jonathan C. Allan, Fletcher E. O'Brien, Jason D. McClaughry, Lowell H. Anthony, Robert W. Hairston-Porter, and Jon Franczyk (2023). Geologic Assessment of Potential Cable Landing Sites Along the Oregon Coast, DOGAMI Special Paper 54, 101pp.

Calkoen, F., Luijendijk, A., Rivero, C. R., Kras, E., and Baart, F., (2021). Traditional vs. machine-learning methods for forecasting Sandy shoreline evolution using historic satellite-derived shorelines. *Remote Sensing*, 13(5), 934. doi:10.3390/rs13050934

Church, J.A. and White, N.J., 2011. Sea-Level Rise from the Late 19th to the Early 21st Century. *Surveys in Geophysics*. doi: 10.1007/s10712-011-9119-1

Collins, B. D., & Sitar, N. (2008). Processes of coastal sea cliff erosion in weakly lithified sands, Pacifica, California, USA. *Geomorphology*, *97*(3), 483-501.

Collins, B., and Sitar, N. (2004). "Application of high resolution 3d laser scanning to slope stability studies." *Proc., 39th Annual Symposium on Engineering Geology and Geotechnical Eng.*, Butte, MT, 79–92.

Collins, B. D., & Stock, G. M. (2012). Lidar-based rock-fall hazard characterization of cliffs. In GeoCongress 2012: State of the Art and Practice in Geotechnical Engineering (pp. 3021-3030).

Collins, B., Kayen, R., Reiss, T., and Sitar, N. 2007. "Terrestrial LIDAR investigation of the December 2003 and January 2007 activations of the Northridge Sea cliff Landslide, Daly City, California." *U.S. Geologic Survey, Open File Report 2007-1079*, 32pg.

Cornforth, D. H. (2005). Landslides in practice. Investigation, analysis, and remedial/preventative options in soils. *John Wiley & Sons Inc. Hoboken New Jersey*, 596.

Crozier, M. J. (2010). Deciphering the effect of climate change on landslide activity: A review. *Geomorphology*, *124*(3), 260-267.

Danforth, W.W., and Thieler, E.R., 1992. "Digital Shoreline Analysis System (DSAS) User's Guide, Version 1.0," US Geological Survey Open-File Report 92-355, 42pg.

Dasenbrock, D. D., Abdoun, T., & Bennett, V. (2011). Real-time structural health monitoring of landslides and geotechnical assets with shapeaccelarrays. In *Geo-Frontiers 2011: Advances in Geotechnical Engineering* (pp. 1585-1594).

Dasenbrock, D., C. L. Levesque, and L. Danisch. "Long-term rate behavior monitoring using automated MEMS-based sensing arrays in an urban landslide environment." *Proceedings of the 11th international and 2nd north american symposium on landslides, Banff, Alberta, Canada*. 2012.

Dickson, M. E., Walkden, M. J., & Hall, J. W. (2007). Systemic impacts of climate change on an eroding coastal region over the twenty-first century. *Climatic change*, *84*(2), 141-166.

Dickson, M. E., Matsumoto, H., Stephenson, W. J., Swirad, Z. M., Thompson, C. F., & Young, A. P. (2023). Sea-level rise may not uniformly accelerate cliff erosion rates. Nature Communications, 14(1), 8485. https://doi.org/10.1038/s41467-023-44149-3

Duffy, W. and S.M. Dickson 1995. "Using Grid and Graph to Quantify and Display Shoreline Change," Proceedings of the 1995 ESRI International User Conference, p. 74.

Earlie, C. S., Young, A. P., Masselink, G. and Russell, P. E. (2015), Coastal cliff ground motions and response to extreme storm waves. Geophys. Res. Lett., 42: 847–854. http://dx.doi.org/10.1002/2014GL062534

Emery, K.O. and Kuhn, G.G., 1982. "Sea cliffs: their processes, profiles, and Classification," Geological Society of America Bulletin, 93, 644-654.

Fonstad, M. A., J. T. Dietrich, B. C. Courville, J. L. Jensen, and P. E. Carbonneau (2013), Topographic structure from motion: a new development in photogrammetric measurement, *Earth Surface Processes and Landforms*, *38*, 421-430.

Gili, J. A., Corominas, J., & Rius, J. (2000). Using Global Positioning System techniques in landslide monitoring. *Engineering geology*, *55*(3), 167-192.

Haas, J., 2005. "Grain size and mineralogical characteristics of beach sand with implications for sediment provenance in the Oceanside Littoral Cell." MS Thesis, University of California, San Diego (UCSD), San Diego, CA, 126 p.

Hampton, M. A., and G. B. Griggs (Eds.) (2004), *Formation, Evolution, and Stability of Coastal Cliffs-Status and Trends*, 123 pp., U.S Geological Survey Professional Paper 1693.

Hanna, E., Huybrechts, P., Steffen, K., Cappelen, J., Huff, R., Shuman, C., ... & Griffiths, M. (2008). Increased runoff from melt from the Greenland Ice Sheet: a response to global warming. *Journal of Climate*, *21*(2), 331-341.

Hapke, C. 2004. "The measurement and interpretation of coastal cliff and sea cliff retreat," In Formation, Evolution and Stability of Coastal Cliffs-Status and Trends, USGS Professional Paper 1963, Editors: Hampton, M.A. and Griggs, G.B., http://pubs.usgs.gov/pp/pp1693/pp1693.pdf

Hapke, C. J., P. N. Adams, J. Allan, A. Ashton, G. B. Griggs, M. A. Hampton, J. Kelly, and A. P. Young (2014), Rocky Coast Geomorphology: A Global Synthesis – The USA, in *Rock Coast Geomorphology: A Global Synthesis*, edited by D. M. Kennedy, W. J. Stephenson and L. Naylor, pp. 135-152, The Geological Society of London, Memoirs, 40, London.

Hapke, C.J., Himmelstoss, E.A., Kratzmann, M.G., List, J.H., and Thieler, E.R., 2010, National Assessment of Shoreline Change: Historical Shoreline Change along the New England and Mid-Atlantic Coasts: U.S. Geological Survey Open-File Report 2010-1118.

Hapke, C. J., & Reid, D. (2007). National assessment of shoreline change, Part 4: Historical coastal cliff retreat along the California coast (No. 2007-1133). US Geological Survey.

Hapke, C. J., Reid, D., Richmond, B. M., Ruggiero, P., & List, J. (2006). *National assessment of shoreline change Part 3: Historical shoreline change and associated coastal land loss along sandy shorelines of the California Coast* (No. 2006-1219). Geological Survey (US).

Hapke, C., and Richmond, B., 2000. "Monitoring beach morphology changes using small-format aerial photography and digital softcopy photogrammetry." Environmental Geosciences, Special Issue on Coastal Hazard Mapping Techniques, 7(1), 32-37.

Himmelstoss, E.A., Henderson, R.E., Farris, A.S., Kratzmann, M.G., Bartlett, M.K., Ergul, A., McAndrews, J., Cibaj, R., Zichichi, J.L., and Thieler, E.R., 2024, Digital Shoreline Analysis System version 6.0: U.S. Geological Survey software release, https://doi.org/10.5066/P13WIZ8M.

Himmelstoss, E.A., Henderson, R.E., Kratzmann, M.G., and Farris, A.S., 2018. Digital shoreline analysis system (DSAS) version 5.0 user guide, *US Geological Survey*, 2331-1258. https://www.usgs.gov/centers/whcmsc/science/digital-shoreline-analysis-system-dsas

Himmelstoss, E.A., FitzGerald, D.M., Rosen, P.S., and Allen, J.R. (2006). "Bluff Evolution along Coastal Drumlins: Boston Harbor Islands, Massachusetts," *Journal of Coastal Research* 2006(225), 1230-1240. https://doi.org/10.2112/06A-0005.1

Hormann, L. (2012). "ODOT's Climate Change Adaptation Strategy Report." www.oregon.gov, Apr. 2012, www.oregon.gov/ODOT/Programs/TDD%20Documents/Climate-Change-Adaptation-Strategy.pdf.

IPCC: Intergovernmental Panel On Climate Change. "Climate change 2007: The physical science basis." Agenda 6.07 (2007): 333.

IPCC: Intergovernmental Panel On Climate Change. (2014). *Climate Change 2014–Impacts, Adaptation and Vulnerability: Regional Aspects*. Cambridge University Press.

IPCC: Intergovernmental Panel On Climate Change. (2023). Summary for Policymakers. In: Climate Change 2023: Synthesis Report. Contribution of Working Groups I, II and III to the Sixth Assessment Report of the Intergovernmental Panel on Climate Change [Core Writing Team, H. Lee and J. Romero (eds.)]. IPCC, Geneva, Switzerland, pp. 1-34, doi: 10.59327/IPCC/AR6-9789291691647.001.

Jaboyedoff, M., Oppikofer, T, Abellan, A., Derron, M.H., Loye, A., Metzger, R., Pedrazzini, A. 2012."Use of LiDAR in landslide investigations: a review," Natural Hazards.

Jamieson, M., 2019. Investigation of Multi-constellation RTK GNSS Survey Productivity and Coordinate Accuracy. Masters Thesis, Oregon State University.

Kaminsky, G. M., Ruggiero, P., Buijsman, M. C., McCandless, D., and Gelfenbaum, G., 2010, Historical evolution of the Columbia River littoral cell: Marine Geology, v. 273, p. 96-126.

Katz, O., Mushkin, A., (2013) Characteristics of sea-cliff erosion induced by a strong winter storm in the eastern Mediterranean, *Quaternary Research*, 80(1) p. 20-32.

Komar, P.D., (1986). The 1982-1983 El Niño and erosion on the coast of Oregon, Shore and Beach, 54, 3-12.

Komar, P. D. (1997), The Pacific Northwest Coast: Living with the Shores of Oregon and Washington, 195 pp., Duke University Press, Durham and London.

Komar, P.D. (1998), The 1997-98 El Niño and erosion on the Oregon coast. *Shore & Beach*, 66(3): 33-41.

Komar, P. D. (2004), Oregon's coastal cliffs: Processes and erosion impacts, *Professional Paper 1693*, 123 pp, United States Government.

Komar, P. D., Allan, J. C., and Ruggiero, P., 2011, Sea Level Variations along the U.S. Pacific Northwest Coast: Tectonic and Climate Controls Journal of Coastal Research, v. 27, no. 5, p. 808-823.

Leshchinsky, B. A., Olsen, M. J., & Bunn, M. D. (2018). Enhancing landslide inventorying, LiDAR hazard assessment and asset management (No. FHWA-OR-RD-18-18). Oregon. Dept. of Transportation. Research Section.

Leshchinsky, B., Olsen, M. J., Mohney, C., Glover-Cutter, K., Crook, G., Allan, J., ... & Mathews, N. (2017). Mitigating coastal landslide damage. *Science*, *357*(6355), 981-982.

Leshchinsky, B., Olsen, M.J., Mohney, C. O'Banion, M.S., Bunn, M., Allan, J., and McClung, R. (2019). "A Framework for Quantifying Progressive Landslide Movement Stemming from Undercutting Processes and Hydrological Changes," Journal of Geophysical Research-Earth Surface, 124(2), 616-638. AGU. https://doi.org/10.1029/2018JF004833

Leshchinsky, B., Olsen, M.J., Mohney, C., Glover-Cutter, K., Crook, G., Allan, J. Bunn, M., O'Banion, M.S., and Mathews, N. (2017). Mitigating coastal landslide damage, Science, 357(6355), 981-982. DOI: 10.1126/science.aao1722

Leshchinsky, B. A., Olsen, M. J., & Tanyu, B. F. (2015). Contour Connection Method for automated identification and classification of landslide deposits. Computers & geosciences, 74, 27-38.

Lim, M., N. J. Rosser, D. N. Petley, and M. Keen (2011), Quantifying the controls and influence of tide and wave impacts on coastal rock cliff erosion, J. Coastal Res., 27(1), 46– 56.

Lim, M., Petley, D.N., Rosser, N.J., Allison, R.J., and Long, A.J., 2005. "Combined digital photogrammetry and time-of-flight laser scanning for monitoring cliff evolution," The Photogrammetric Record, 20(110), 109-129.

Limber, P.W., Barnard, P.L., Vitousek, S., and Erikson, L.H. (2018). A model ensemble for projecting multidecadal coastal cliff retreat during the 21st Century. *Journal of Geophysical Research: Earth Surface*, 123(7), 1566–1589. doi:10.1029/2017jf004401

Mancini, F., M. Dubbini, M. Gattelli, F. Stecchi, S. Fabbri, and G. Gabbianelli (2013), Using Unmanned Aerial Vehicles (UAV) for High-Resolution Reconstruction of Topography: The Structure from Motion Approach on Coastal Environments, *Remote Sensing*, *5*, 6880-6898.

McClaughry, J.D., Lina, M.A., Jones, C.B., Mickelson, K.A., Wiley, T.J., (2013), Geologic map of the southwestern Oregon coast between Crook Point and Port Orford, Curry County, Oregon, Plate 3, State of Oregon, Dept. of Geology and Mineral Industries, Open file report

McClaughry, J.D., Darin, M.H., Azzopardi, C.J.M, Anthony, L.H., Allan, J.C., Burgette, R.J., Guerrero, E.F., and Wiley, T.J., in press, Geology of the southern Oregon Coast between Coos Bay and the California Border, Coos and Curry Counties, Oregon: Oregon Department of Geology and Mineral Industries Bulletin 109.

Mohney, C.E., Racker, D.R., (2004), Whaleshead Cove landslide repair engineering geology report, Curry County Oregon, Geo/Hydro Services section region 3 geology unit

Montaño, J., Coco, G., Antolínez, J.A.A. et al. Blind testing of shoreline evolution models. Sci Rep 10, 2137 (2020). https://doi.org/10.1038/s41598-020-59018-y

NGS. (2018). "Guidelines for New and Existing Continuously Operating Reference Stations (CORS)", National Geodetic Survey, National Ocean Survey, NOAA, Solver Spring, MD 20910.

Niem, A.R., (1975). The Ore bin; Vol. 37 No. 2, Oregon Department of Geology and Mineral Industries.

Niem, A.R., Niem, W.A., Martin, M.W., Kadri, M.M., McKeel, D.R., (1985). Oil and gas investigation of the Astoria basin, Clatsop and northernmost Tillamook Counties, northwest Oregon. State of Oregon, Department of Geology and Mineral Industries.

NRC, 2012. Sea-Level Rise for the Coasts of California, Oregon, and Washington: Past, Present, and Future, *National Research Council, Washington, D.C.*

ODOT: Oregon Department of Transportation(1995). Phase II: Arizona Inn Landslide geotechnical investigation, Curry County, Oregon

Olsen M.J., (2009). "Methodology for assessing coastal change using terrestrial laser scanning," PhD dissertation, University of California, San Diego, Available online at: http://escholarship.org/uc/item/49z2x13x

Olsen, M. J., Allan J., Dundas, S. J., Krivova, M., Leshchinsky, B. A.,. Senogles, A., Hermann, J. Parrish, C., and Mackenzie, A. L. (2024). US Highway 101 Coastal Hazard Vulnerability and Risk Assessment for Mitigation Prioritization (No. FHWA-OR-RD-21-01). Oregon Department of Transportation. Research Section., ODOT-FHA Project SPR-843, 242p

Olsen, M. J., E. Johnstone, and F. Kuester (2013), Hinged, pseudo-grid triangulation method for long, near linear cliff analysis, *Journal of Surveying Engineering*, *139*(2), 105-109.

Olsen, M. J., E. Johnstone, N. Driscoll, S. A. Ashford, and F. Kuester (2009), Terrestrial Laser Scanning of Extended Cliff Sections in Dynamic Environments: Parameter Analysis, *Journal of Surveying Engineering*, *135*, 161-169.

Olsen, M., Johnstone, E., Kuester, F., Driscoll, N., and Ashford, S. (2011). "New Automated Point-Cloud Alignment for Ground-Based Light Detection and Ranging Data of Long Coastal Sections." *Journal of Surveying Engineering*, *137*(1), 14–25

Olsen, M.J. (2015). In Situ Change Analysis and Monitoring through Terrestrial Laser Scanning. *Journal of Computing in Civil Engineering*, 29(2), 04014040.

Olsen, M.J., Allan, J.C., & Priest, G.R. (2012), Johnson Creek landslide movement and erosion quantification through 3D laser scanning, ASCE GeoCongress 2012, Oakland, California.

Olsen, M.J., Allan, J.C., and Priest, G.R., 2012. "Movement and erosion quantification of the Johnson Creek Landslide through 3D laser scanning," Proc. ASCE Geocongress 2012: State of the Art and Practice in Geotechnical Engineering, pp. 3050-3059.

Olsen, M.J., Butcher, S., and Silvia, E.P., (2012). Real-time change and damage detection of landslides and other earth movements threatening public infrastructure, OTREC Final Report 2011-22 and ODOT Final Report RS 500-500, 80p.

Olsen, M.J., J. Wartman, M. McAlister, H. Mahmoudabadi, M.S. O'Banion, L. Dunham, K. Cunningham, (2015). To Fill or Not to Fill: Sensitivity Analysis of the Influence of Resolution and Hole Filling on Point Cloud Surface Modeling and Individual Rockfall Event Detection. *Remote Sensing, 7*, 12103-12134.

Olsen, M.J., Young, A.P, & Ashford, S.A. (2012). "TopCAT – Topographical Compartment Analysis tools for ArcGIS®," *Computers and Geosciences*, 45, 284-292.

Orr, E. L., W. N. Orr, and E. M. Baldwin (1992), *Geology of Oregon*, 4th ed., Kendall/Hunt Dubuque, Iowa.

Peponi, A., Morgado, P., and Trindade, J. (2019). Combining artificial neural networks and GIS fundamentals for Coastal Erosion Prediction Modeling. Sustainability, 11(4), 975. doi:10.3390/su11040975

Peterson, C. D., E. Stock, D. M. Price, R. Hart, F. Reckendorf, J. M. Erlandson, and S. W. GHostetler (2007), Ages, distributions, and origins of upland coastal dune sheets in Oregon, USA, *Geomorphology*, *91*, 80-102.

Petley, D. (2012). "Global patterns of loss of life from landslides." *Geology.* 40(10): 927-930.

Prasad, D. and Kumar, N., 2014. Coastal Erosion Studies — A Review. International Journal of Geosciences, 5, 341-345. doi:10.4236/ijg.2014.53033

Priest, G. R., and J. C. Allan (2004), Evaluation of coastal erosion hazard zones along dune and sea cliff backed shorelines in Lincoln County, Oregon: Cascade Head to Seal Rock. Technical report to Lincoln County, *Open file report O-04-09*, Oregon Department of Geology and Mineral Industries, Portland, Oregon.

Priest, G.R., (1999). Coastal shoreline change study northern and central Lincoln county, Oregon. Journal of Coastal Research, pp.140-157

Priest, G.R., Allan, J.C. and Sonnevil, R., 2004. Evaluation of coastal erosion hazard zones from Sisters Rocks to North Gold Beach, Curry County, Oregon: Technical report to Curry County. Open file report O-04-20, Oregon Department of Geology and Mineral Industries, Portland, Oregon.

Priest, G. R., Allen, J., Niem, A., Christie, S. R., & Dickenson, S. E. (2006). Interim Report: Johnson Creek Landslide Project, Lincoln County, Oregon. Oregon Department of Geology and Mineral Industries Open-File Report O-06, 2.

Priest, G. R., Allan, J. C., Niem, A. R., Niem, W. A., & Dickenson, S. E. (2008). Johnson Creek Landslide Research Project, Lincoln County, Oregon (No. FHWA-OR-RD-08-13).

Priest, G. R., Schulz, W. H., Ellis, W. L., Allan, J. A., Niem, A. R., & Niem, W. A. (2011). Landslide stability: role of rainfall-induced, laterally propagating, pore-pressure waves. Environmental & Engineering Geoscience, 17(4), 315-335.

Ramp, L., Schlicker, H.G. and Gray, J.J., (1977). Geology, mineral resources, and rock material of Curry County, Oregon (No. 93). State of Oregon, Dept. of Geology and Mineral Industries.

Robinson, B.A., (1988). "Coastal cliff sediments- San Diego region, Dana Point to the mexican border (1887-1947)," Coast of California Storm and Tidal Wave Study, 88-8, U.S. Army Corps of Engineers, Los Angeles District, 275pp.

Rosser, N.J., Lim, M., Norman, E., and Petley, D.N., 2008. "Exploring variations in and controls upon cliff, platform and coastline geometry." Geophysical Research Abstracts, Vol. 10, European Geosciences Union, EGU2008-A-10318.

Rosser, N.J., Petlety, D.N., Lim, M., Dunning, S.A., and Allison, R.J., 2005. "Terrestrial laser scanning for monitoring the process of hard rock coastal cliff erosion." Quarterly J. of Eng. Geology and Hydrology, 38, 363-375.

Ruggerio, P., Kratzmann, M.G., Himmelstoss, E.A., Reid, D., Allan, J. and Kaminsky, G., (2013). National assessment of shoreline change: historical shoreline change along the Pacific Northwest coast (No. 2012-1007). US Geological Survey.

Ruggiero, P. (2012). Is the intensifying wave climate of the US Pacific Northwest increasing flooding and erosion risk faster than sea-level rise?. *Journal of Waterway, Port, Coastal, and Ocean Engineering*, *139*(2), 88-97.

Ruggiero, P., Kratzmann, M. G., Himmelstoss, E. A., Reid, D., Allan, J., & Kaminsky, G. (2013). National assessment of shoreline change: historical shoreline change along the Pacific Northwest coast. US Geological Survey. Open-File Report 2012–1007, 62 pp., http://dx.doi.org/10.3133/ofr20121007.

Ruggiero, P., P. D. Komar, et al. (2001). "Wave runup, extreme water levels and the erosion of properties backing beaches." Journal of Coastal Research 17(2): 407-419.

Ruggiero, P., Komar, P.D. and Allan, J.C. (2010), Increasing wave heights and extreme value projections: The wave climate of the U.S. Pacific Northwest. *Coastal Engineering*, 57(5): 539-552.

Ruggiero, P., P. D. Komar, W. G. McDougal, and R. A. Beach (1996), Extreme water levels, wave runup and coastal erosion, paper presented at Proceedings of the 25th Conference on Coastal Engineering, ASCE, Orlando, Florida.

Sallenger, A.H, Krabill, W.B., Swift, R.N., Brock.J, List, J., Hansen, M., Holman, R.A., Manizade, S., Sontag, J., Meredith, A., Morgan, K., Yunkel, J.K., Frederick, E.B., and Stockdon, H., 2003. "Evaluation of airborne topographic LIDAR for quantifying beach changes," Journal of Coastal Research, 19(1), 125-133.

Schlicker, H., R. Deacon, J. Beaulieu, and G. Olcott (1973), Environmental geology of Lincoln County, Oregon, *B-081*, 171 pp, Portland, Oregon.

Schlicker, H.G., (1972). Environmental geology of the coastal region of Tillamook and Clatsop Counties, Oregon (Vol. 74). State of Oregon, Dept. of Geology and Mineral Industries.

Schulz, W. H., & Ellis, W. L. (2007). Preliminary results of subsurface exploration and monitoring at the Johnson Creek landslide, Lincoln County, Oregon (No. 2007-1127). Geological Survey (US).

Schulz, W. H., & Wang, G. (2014). Residual shear strength variability as a primary control on movement of landslides reactivated byearthquake-induced ground motion: Implications for coastal Oregon, U.S.Journal of Geophysical Research: Earth Surface,119,1617–1635. https://doi.org/10.1002/2014JF003088

Schulz, W. H., Galloway, S. L., & Higgins, J. D. (2012). Evidence for earthquake triggering of large landslides in coastal Oregon, USA. *Geomorphology*, *141*, 88-98.

Schuster, Robert L., and Lynn Highland. (2001). *Socioeconomic and environmental impacts of landslides in the western hemisphere*. US Department of the Interior, US Geological Survey,

Shadrick, J. R. et al. Sea-level rise will likely accelerate rock coast cliff retreat rates. Nat. Commun. 13, 1–12 (2022).

Shannon & Wilson Inc, 2015, Spencer Creek Bridge Geotechnical Case Study, FHWA Northwest Geotech Workshop

Squier, L.R., Inc., (1974), Subsurface investigation, Silver Point landslide, Oregon Coast Highway 9, MP 32, Clatsop county, Oregon, unpublished report prepared for the Oregon State Highway Department, 27 p., figures and appendices paginated separately

Squier, L.R., Scofield, D.H., Peterson, G.L., (1994), Phase I Arizona Inn Landslide Geotechnical Investigation, Curry County, Oregon, Oregon Dept of Transportion.

Stark, T. D., & Choi, H. (2008). Slope inclinometers for landslides. *Landslides*, *5*(3), 339.

Stockdon, H. F., R. A. Holman, P. A. Howd, and A. H. Sallenger (2006), Empirical parameterization of setup, swash, and runup, *Coastal Engineering*, *53*(7), 573-588.

Storlazzi, C. D., & Griggs, G. B. (2000). Influence of El Niño–Southern Oscillation (ENSO) events on the evolution of central California's shoreline. *Geological Society of America Bulletin*, *112*(2), 236-249.

Sunamura, T. (1992), *Geomorphology of Rocky Coasts*, John Wiley and Sons, New York.

Sweet, W.V., Hamlington, B.D., Kopp, R.E., Weaver, C.P., Barnard, P.L., Bekaert, D., Brooks, W., Craghan, M., Dusek, G. and Frederikse, T., 2022. Global and regional sea level rise scenarios for the United States: updated mean projections and extreme water level probabilities along US coastlines. National Oceanic and Atmospheric Administration. NOAA Technical Report NOS 01, Silver Spring, MD, 111 p.

Swirad, Z. M., & Young, A. P. (2021). Automating coastal cliff erosion measurements from large-area LiDAR datasets in California, USA. Geomorphology, 389, 15. https://doi.org/10.1016/j.geomorph.2021.107799

Swirad, Z. M., & Young, A. P. (2022). Spatial and temporal trends in California coastal cliff retreat. Geomorphology, 412, 108318. https://doi.org/10.1016/j.geomorph.2022.108318

Thieler, E.R., Himmelstoss, E.A., Zichichi, J.L., and Miller, T.L., 2005, "Digital Shoreline Analysis System (DSAS) version 3.0: An ArcGIS extension for calculating shoreline change," U.S. Geological Survey Open-File Report 2005-1304.

Trenhaile, A. S. (1989). Sea level oscillations and the development of rock coasts. In Elsevier Oceanography Series (Vol. 49, pp. 271-295). Elsevier.

Trenhaile, A. S. (2010). Modeling cohesive clay coast evolution and response to climate change. *Marine Geology*, *277*(1), 11-20.

Utili, S., & Crosta, G. B. (2011). Modeling the evolution of natural cliffs subject to weathering: 1. Limit analysis approach. *Journal of Geophysical Research: Earth Surface*, *116*(F1).

Witter, R.C., Allan, J.C. and Priest, G.R., 2007. Evaluation of coastal erosion hazard zones along dune and sea cliff backed shorelines: Southern Lincoln County, Oregon: Seal Rock to Cape Perpetua. Open-file-report O-07-03, Oregon Department of Geology and Mineral Industries, Portland, Oregon.

Witter, R.C., Horning, T. and Allan, J.C., (2009). Coastal Erosion Hazard Zones in Southern Clatsop County, Oregon: Seaside to Cape Falcon. State of Oregon, Department of Geology and Mineral Industries.

Young, A. P., & Ashford, S. A. (2008). Instability investigation of cantilevered sea cliffs. *Earth Surface Processes and Landforms*, *33*(11), 1661-1677.

Young, A. P., Guza, R. T., Dickson, M. E., O'Reilly, W. C., & Flick, R. E. (2013). Ground motions on rocky, cliffed, and sandy shorelines generated by ocean waves. Journal of Geophysical Research: Oceans, 118(12), 6590-6602.

Young, A. P., P. N. Adams, W. C. O'Reilly, R. E. Flick, and R. T. Guza(2011), Coastal cliff ground motions from local ocean swell and infra-gravity waves in southern California,J. Geophys. Res.,116, C09007,doi:10.1029/2011JC007175.

Young, A. P., R. T. Guza, P. N. Adams, W. C. O'Reilly, and R. E. Flick(2012), Cross-shore decay of cliff top ground motions driven by localocean swell and infragravity waves,J. Geophys. Res.,117, C06029, doi:10.1029/2012JC007908.

Young, A. P., R. T. Guza, R. E. Flick, W. C. O'Reilly, and R. Gutierrez (2009), Rain, waves, and short-term evolution of composite sea cliffs in southern California, *Marine Geology*, *267*, 1-7.

Young, A.P. and Ashford, S.A., (2006a). "Application of airborne LIDAR for sea cliff volumetric change and beach sediment budget contributions," *J. of Coastal Research*, 22(2), 307-318.

Young, A.P. and Ashford, S.A., (2007). "Quantifying sub-regional sea cliff erosion using mobile terrestrial LIDAR." Shore and Beach, 75(3), 38-43.

Young, A.P., (2006c). "Quantifying Short-Term Sea cliff Morphology of a Developed Coast: San Diego County, California." PhD Dissertation, University of California, San Diego (UCSD), San Diego, CA, 208pg.

Young, A.P., and Ashford, S.A., (2006b). Performance Evaluation of Sea cliff Erosion Control Methods*, Shore and Beach*, 74(4), 16-24

Young, A.P., Flick, R.E., Gutierrez, R., and Guza, R.T., (2009). Comparison of Short-Term Sea cliff Retreat Measurement Methods in Del Mar, California, Geomorphology 112, 318-323.

Young, A.P., Guza, R.T., Flick, R.E., O'Reilly, W.C., and Gutierrez, R., (2009). Rain, Waves, & Short-Term Sea cliff Evolution, Marine Geology 267, 1-7.

Young, A.P., Guza, R.T., O'Reilly, W.C., Flick, R.E., and Gutierrez, R., (2011). Short-term retreat statistics of a slowly eroding coastal cliff, Natural Hazards and Earth Systems Sciences 11, 205-217.

Young, A.P., Olsen, M.J., Driscoll, N., Flick, R.E, Gutierrez, R., Guza, R.T., Johnstone, E., and Kuester, F., (2010). Comparison of airborne and terrestrial LIDAR estimates of sea cliff erosion in southern California. Photogrammetric Engineering and Remote Sensing 76(4), 421-427.

Young, A.P., Raymond, J.H., Sorenson, J., Johnstone, E.A., Driscoll, N.W., Guza, R.T., Flick, R.E., (2010). Coarse Sediment Yields from Sea cliff Erosion in the Oceanside Littoral Cell, Journal of Coastal Research 26(3), 580-585.

Young, AP, Guza RT, O'Reilly WC, Burvingt O, Flick RE. 2016. Observations of coastal cliff base waves, sand levels, and cliff top shaking. Earth Surface Process and Landforms.

Young, AP. 2015. Recent deep-seated coastal landsliding at San Onofre State Beach, California. Geomorphology. 228:200-212. 10.1016/j.geomorph.2014.08.005

Young, A., 2018, Decadal-scale coastal cliff retreat in southern and central California, Geomorphology, 300, 164-175. ss